

Nonlinear excitations in Bose-Einstein condensates

Dissertation

zur Erlangung des Doktorgrades

des Department Physik

der Universität Hamburg

vorgelegt von

Stephan Middelkamp

aus Ankum

Hamburg

2010

Gutachter der Dissertation:	Prof. Dr. Schmelcher Prof. Dr. Kevrekidis
Gutachter der Disputation:	Prof. Dr. Schmelcher Prof. Dr. Moritz
Datum der Disputation:	23.07.2010
Vorsitzende des Prüfungsausschusses:	Prof. Dr. Hagner
Vorsitzender des Promotionsausschusses:	Prof. Dr. Bartels
Dekan der Fakultät für Mathematik, Informatik und Naturwissenschaften:	Prof. Dr. Graener

Zusammenfassung

Gegenstand dieser Arbeit ist die Untersuchung nichtlinearer Anregungen von Bose-Einstein Kondensaten mit Schwerpunkt auf ein- und zweidimensionalen Systemen. Unterschiedliche Fallenpotentiale und Effekte von einer ortsabhängigen Streulänge werden studiert. Mittels der Gross-Pitaevskii Gleichung werden sowohl Grundzustand als auch kollektive Anregungen untersucht.

Als Erstes präsentieren wir Auswirkungen einer ortsabhängigen Streulänge für ein quasi eindimensionales Kondensat, welches in einem Doppeltopfpotential gefangen ist. Das inhomogene Streuverhalten führt zu einer Sattelpunktbifurkation von zwei Zweigen von Lösungen, die für konstante Streulänge nicht existieren. Des Weiteren ist der Übergang von Josephson Schwingungen zum nichtlinear induziertem Selbstfangen verschoben. Wir entwickeln ein angepasstes Zweimodenmodell, welches diese Effekte exakt beschreibt. In einem zweiten Schritt werden die Auswirkungen einer ortsabhängigen Streulänge auf dunkle und helle Materiewellen Solitonen untersucht. In beiden Fällen lässt sich die Solitonendynamik durch entsprechende Störungstheorie für Solitonen exakt beschreiben. Darüber hinaus zeigen wir, dass die örtliche Modulation der Wechselwirkung dazu verwendet werden kann, um sogenannte Vortex Zustände bei endlicher Temperatur zu stabilisieren.

Ein zweiter Schwerpunkt dieser Arbeit ist die Untersuchung kohärenter angeregter Zustände von Bose-Einstein Kondensaten, sog. Soliton und Vortex Zustände. Die Existenz und Stabilität von einzelnen oder mehreren dunklen Solitonen in quasi-eindimensionalen Kondensaten, gefangen in einem Doppeltopf, sowie von einzelnen und mehreren Vortex Zuständen in quasi-zweidimensionalen Kondensaten werden systematisch untersucht. Wir veranschaulichen den Zusammenhang von dunklen Soliton-Streifen und mehreren Vortex Zuständen. Ein Quasi-Teilchen-Ansatz ermöglicht es uns, Potentiale für die Wechselwirkung von mehreren Solitonen und Vortices auf einem inhomogenen Hintergrund herzuleiten und die entsprechende Dynamik durch einfache gewöhnliche Differentialgleichungen zu beschreiben. Als Erweiterung zu den Untersuchungen von dunklen und hellen Solitonen studieren wir sogenannte dunkel-hell Solitonen in Zweikomponenten-Bose-Einstein Kondensaten. Eine starke Abhängigkeit der Schwingungsfrequenz und der Stabilität der dunkel-hell Solitonen von der Atomzahl in ihren Komponenten wird gefunden.

Darüber hinaus werden Methoden zum Fangen von ultrakalten Atomen entwickelt. Wir präsentieren einen Weg zum Fangen von magnetisch unempfindlichen Atomen durch atomare Stöße mit Atomen der gleichen Art, die magnetisch eingeschlossen werden. Die kontrollierte Auskopplung der gefangenen Atome durch entsprechende Gestaltung der Kondensatwellenfunktion wird erforscht. Dies führt zu einer gepulsten Emission von Atomen aus der gefangenen Region, die an einen Atom-Laser erinnert. Darüber hinaus präsentieren wir eine Möglichkeit zum Fangen von Atomen durch die Anwendung von nahresonantem Laserlicht in einer Raman-Konfiguration in Kombination mit einer Ioffe-Pritchard Magnetfeld-Konfiguration. Die entstehende Potenzialflächen sind flexibel einstellbar und können zum gleichzeitigen Fangen zweier interner Atomzustände verwendet werden.

Abstract

We investigate nonlinear excitations of Bose-Einstein condensates focusing on quasi one and two dimensional condensates. Different geometries of the external potential and effects of a spatial modulation of the interatomic interaction are studied. Our investigations incorporate the ground state and collective excitations of the condensate on a mean-field level by employing the Gross-Pitaevskii equation augmented by effective low-dimensional approaches.

Firstly, we demonstrate the effects of a spatially inhomogeneous scattering length on quasi-one-dimensional condensates trapped in a double-well potential. The collisional inhomogeneity produces a saddle-node bifurcation scenario between two additional solution branches. Moreover, the threshold of transition from Josephson matter-wave oscillations to nonlinearly induced self-trapping is shifted due to the collisional inhomogeneity. We develop an adjusted two-mode model which describes these effects accurately. In a second step, the effects of a collisional inhomogeneity on dark and bright matter-wave solitons are explored. In both cases appropriate versions of the soliton perturbation theory are shown to accurately describe the soliton dynamics. Moreover, we illustrate that modulating the interaction can be used to stabilize vortices against excitations due to finite temperature effects.

A second focal point of this thesis is the investigation of coherent excited states of Bose-Einstein condensates, i.e., solitonic and vortex states. The existence and stability of single and multiple dark soliton states in quasi-one-dimensional condensates trapped in a double-well potential and single as well as multiple vortex states in quasi-two-dimensional condensates are investigated systematically. We illustrate the connection of dark soliton stripes and multiple vortex states. Using a quasi-particle approach enables us to predict the motion of multiple solitons and vortices on an inhomogeneous background by simple ordinary differential equations. As an extension to the investigations of dark and bright solitons, we study dark bright solitons in two component Bose Einstein condensates. A strong dependence of the oscillation frequency and of the stability of the dark-bright soliton on the atom number of its components is found theoretically and has been verified experimentally as well.

Moreover, methods for trapping of ultracold atoms are developed. We depict a way of trapping magnetically insensitive atoms by inter atomic collisions with atoms of the same species which are trapped magnetically. The controlled outcoupling of the trapped atoms by shaping the condensate's wave function is explored leading to a pulsed emission of atoms from the trapping region reminiscent of an atom laser. Moreover, we present a way of trapping atoms by applying near resonant laser light in a Raman configuration on a Ioffe-Pritchard like magnetic field configuration leading to versatile atom traps. The emerging potential surfaces are widely tunable and can be used for trapping two internal states.

Contents

1	Introduction	1
2	Basic Mean-Field Theory	13
2.1	The Gross Pitaevskii Mean-Field Model	13
2.1.1	Derivation and Basic Properties of the Gross Pitaevskii Equation	13
2.1.2	The External Potential	15
2.1.3	Feshbach Resonances	16
2.2	Dimensionality Reduction	18
2.2.1	Effectively 2d Condensates	19
2.2.2	Effectively 1d Condensates	20
2.2.3	Cigar-Shaped Condensates	21
2.3	Stationary Solutions of the Gross Pitaevskii Equation	24
2.3.1	The Ground State	24
2.3.2	Excited States	25
2.4	Small-Amplitude Excitations and Bogoliubov Analysis	31
3	Collisionally Inhomogeneous Bose-Einstein Condensates in Double-Well Potentials	35
3.1	The Model and its Semi-Analytical Consideration	36
3.2	Numerical Results	41
3.3	Two-Mode Dynamics	46
3.4	Conclusions	49
4	Matter-Wave Solitons in the Presence of Collisional Inhomogeneities: Perturbation Theory and the Impact of Derivative Terms	51
4.1	Perturbed Gross Pitaevskii Equation and the Derivative-Only Case	51
4.2	Dark Matter-Wave Solitons	53
4.2.1	Full Perturbative Approach	53
4.2.2	Approximations	54
4.2.3	Numerical Results	56
4.3	Bright Matter-Wave Solitons	58
4.3.1	Full Perturbative Approach	58
4.3.2	Approximations	59
4.3.3	Numerical Results	59
4.4	Conclusions	61
5	Dark Solitons in Cigar-Shaped Bose-Einstein Condensates in Double-Well Potentials	63
5.1	Model and Theoretical Framework	64
5.1.1	The Effective 1D Mean-Field Model and Bogoliubov Analysis	64
5.1.2	Dark Soliton States	65

5.2	Bifurcation and Bogoliubov Analysis	67
5.3	Statics vs. Dynamics of Dark Soliton States	72
5.3.1	The One-Soliton State	72
5.3.2	Two Dark-Soliton States	76
5.4	Dark Soliton Dynamics: Numerical Results	80
5.5	Conclusions	83
6	Stability and Dynamics of Matter-Wave Vortices in the Presence of Collisional Inhomogeneities and Dissipative Perturbations	85
6.1	Analytical Results	86
6.2	Numerical Results	89
6.2.1	Bogoliubov-de Gennes Analysis	89
6.2.2	Direct Numerical Simulations	94
6.3	Conclusions	97
7	Bifurcations, Stability and Dynamics of Multiple Matter-Wave Vortex States	99
7.1	Theoretical Analysis	100
7.1.1	Dark Soliton Stripe Bifurcation Picture	100
7.1.2	Vortex Particle Complementary Picture	103
7.2	Soliton and Vortex States and their Stability	105
7.2.1	The Dark Soliton State	105
7.2.2	The Vortex Dipole State	107
7.2.3	The Vortex Tripole State	109
7.2.4	The Aligned Quadrupole State	110
7.2.5	The Vortex Quadrupole State	112
7.2.6	The Vortex Quintopole State	113
7.3	Vortex Dynamics: Numerical Results	114
7.3.1	Microscopical Displacements	114
7.3.2	Macroscopical Displacements	116
7.4	Conclusions	117
8	Dynamics of Dark-Bright Solitons in Cigar-Shaped Bose-Einstein Condensates	119
8.1	Effective 1D Theory	119
8.2	Dark Bright Solitons	121
8.3	Numerical Results	123
8.3.1	Comparison of quasi-1D and 3D Results	123
8.3.2	Departure from the quasi-1D Behavior	124
8.3.3	Interaction of Dark-Bright Solitons	124
8.4	Experimental Results	126
8.5	Conclusions	126
9	Interaction Induced Trapping and Pulsed Emission of a Magnetically Insensitive Bose-Einstein Condensate	129
9.1	Spinor Equations	130
9.2	Effective 1D Equations	131
9.3	Setup	132

9.4	Trapping of the $m = 0$ Component	133
9.5	Loss Mechanism	134
9.6	Backaction of the $m = 0$ Component on the $m = 1$ Component	136
9.7	Outcoupling of Atoms	137
10	Creating Versatile Atom Traps by Applying Near Resonant Laser Light in Magnetic Traps	141
10.1	Analytical Considerations	142
10.1.1	Hamiltonian and Setup	142
10.1.2	Rotating Wave Approximation	144
10.1.3	Van Vleck Perturbation Theory	144
10.2	Numerical Results	146
10.2.1	Overview Over All Components	146
10.2.2	$m_F = 0$ Component	147
10.2.3	$m_F = -1$ Component	149
10.3	Semi-Analytical Interpretation of the Potential	149
10.3.1	Principal Axis Transformation	149
10.3.2	Effective Potential for the $m_F = 0$ Component	150
10.3.3	Discussion of the Effective Potential	152
10.3.4	Effective Potential for a Single Laser	154
10.4	Loss Mechanisms	154
10.4.1	Lifetime of the Intermediate State	154
10.4.2	Inelastic Collisions	155
10.5	Conclusions and Physical Applications	155
11	Conclusions	157
A	Numerical Methods for Solving the Gross Pitaevskii Equation	161
A.1	Representing the Derivative Term	161
A.2	Time Propagation	162
A.3	Methods for Finding Eigenstates	162
A.3.1	Relaxation	163
A.3.2	The Newton Algorithm	163
B	Numerical Methods for Solving the Vector Gross Pitaevskii Equation	165
B.1	Methods for Finding Eigenstates	165
B.1.1	Relaxation	166
B.1.2	The Newton Algorithm	166
B.1.3	Newton Augmented	168
B.2	Bogoliubov de Gennes Analysis	168
C	Two-Mode Approximation	173
D	Van Vleck Perturbation Theory	179
E	Spinor Condensate Exposed to Raman Lasers	181
E.1	Multicomponent Gross-Pitaevskii Equations	181

E.2 Raman Potential	182
E.3 Augmented Spinor Equations	183
Acknowledgements	206

Chapter 1

Introduction

The path to Bose-Einstein condensation

The experimental creation of atomic Bose-Einstein condensates (BECs) has been one of the most fundamental developments in quantum and atomic physics over the past two decades. The impressive progress in this field due to intense experimental and theoretical studies has been already summarized in various books [1–3] and reviews [4,5] to which we refer the reader at this point.

Bose-Einstein condensation was first proposed as a theoretical concept in the first half of the last century. By investigating the statistics of photons, the Indian physicist Satyendra N. Bose discovered that the thermal distribution of photons is not of the Maxwell-Boltzmann type [6]. Nowadays, particles that obey the distribution function derived by Bose are known as bosons. Albert Einstein extended the work of Bose to a gas of massive, noninteracting particles [7] and realized that for sufficiently low temperatures a large fraction of particles occupies the state of lowest energy. Below a critical temperature, all particles “condense” consequently into the lowest energy state and hence behave all in the same manner. Importantly, this critical temperature turns out to be finite. The idea of Bose-Einstein condensation was born and the search for Bose-Einstein condensates began.

First approaches for realizing a BEC used superfluid liquid ^4He , as suggested by F. London in 1938 [8,9]. However, due to the strong interactions between the Helium atoms, in contrast to Einstein’s assumption of noninteracting particles, no BEC could be realized. Theoretical results and modern experiments suggest that even at zero temperature the fraction of condensed particles in superfluid liquid ^4He is less than about 7% [10–12].

In the 1980s novel laser and magnetic based cooling techniques were developed that allowed experimentalists to cool dilute gases of neutral atoms down to extremely low temperatures, see Refs. [14–16] for overviews of these techniques. These developments lead to the achievement of Bose-Einstein condensation in dilute alkali gases in 1995 for the first time in a series of experiments using Rubidium in the group of Eric Cornell and Carl Wieman, Lithium in the group of Randall Hulet and Sodium in the group of Wolfgang Ketterle [13,17,18]. Fig. 1.1 shows experimental evidence for the occurrence of a BEC from the experiment of Eric Cornell and Carl Wieman [13]. The experimental data of the Lithium experiment had to be reanalyzed and unambiguous results were published only in 1997 [19]. Only six years after the first realization of Bose-Einstein condensates in experiments, Wieman, Cornell and Ketterle were awarded the Nobel Prize in Physics “for the achievement of Bose-Einstein condensation in dilute gases of alkali atoms, and for early fundamental studies of the properties of the condensates”. For a more detailed account of the history of the first Bose-Einstein condensates, see Ref. [20].

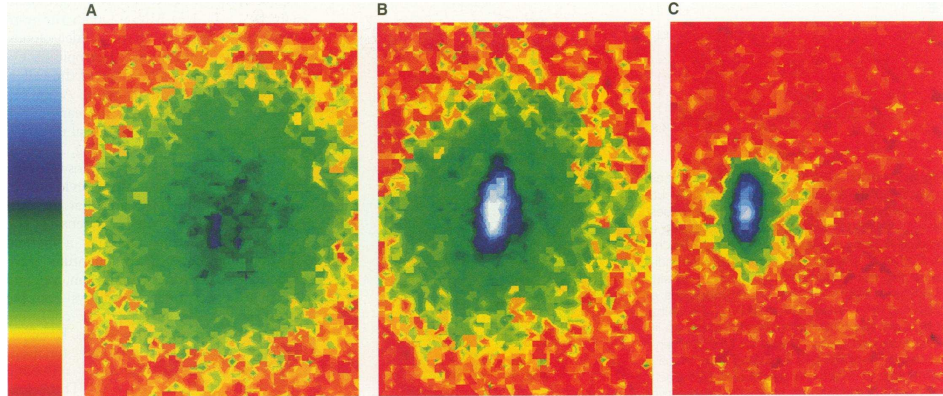


Figure 1.1: Occurrence of a BEC. False-color images display the velocity distribution of the cloud (A) just before the appearance of the condensate, (B) just after the appearance of the condensate, and (C) after further evaporation has left a sample of nearly pure condensate. The circular pattern of the noncondensate fraction (mostly yellow and green) is an indication that the velocity distribution is isotropic, consistent with thermal equilibrium. The condensate fraction (mostly blue and white) is elliptical indicative that it is a highly nonthermal distribution. The elliptical pattern is in fact an image of a single, macroscopically occupied quantum wave function. From [13].

Trapping ultracold atoms

In the first BEC experiments magnetic fields coupling to the magnetic moments of the atoms were used to trap the atoms at ultracold temperatures [20, 21]. A standard technique in today's experiments is to apply static inhomogeneous magnetic fields [4, 22–24] with a minimum of the magnetic field configuration leading to an attractive potential for the atoms. Magnetic trapping relies on the coupling of the total angular momentum to the magnetic field vector. If the polarization vector of the atom is always parallel to the direction of the magnetic field (which is usually granted for ultracold atoms), the resulting potential is proportional to the magnetic quantum number. The magnetically insensitive state can therefore not be trapped magnetically. Moreover, states with different magnetic quantum numbers are exposed to different potentials.

In order to circumvent these limitations, optical traps making use of the polarizability of the atoms were used in later experiments [25, 26]. Optical trapping relies on the coupling of two internal states by a laser which is far detuned with respect to the transition frequency of these states. Since the energy gap between the different states of one hyperfine manifold is much smaller than the typical detuning of the laser the states are exposed to approximately the same potential and one can consequently trap the different internal states of an hyperfine manifold by an optical trap. Moreover, optical traps have got the advantage that one can shape the trapping potential by changing the intensity profile of the applied laser. A prominent example for traps exploiting this feature are optical lattices formed by counter propagating light waves which facilitate the observation of effects like the Mott-Insulator phase transition [27], second-order tunneling [28] or Josephson oscillations [29]. In a generalization of a standard optical trap two lasers in a Raman configuration were used to trap atoms and to create thus an optical lattice with a reduced lattice spacing compared to standard optical lattices [30].

In more recent approaches, combinations of static and oscillating magnetic fields [31, 32], leading to the so-called radio-frequency dressed adiabatic potentials [33, 34], are used in order

to coherently manipulate matter-waves [35] and to investigate the decoherence dynamics of one-dimensional Bose gases [31]. Other approaches use combinations of optical and magnetic fields for trapping atoms, leading to the so called hybrid traps [36, 37].

The double-well potential

One interesting type of potential that has drawn a considerable amount of attention is the double-well potential. This may originate, for instance, from combining a harmonic trap with a repulsive barrier potential, induced by a blue-detuned laser beam [38]. It may also be formed by the combination of a parabolic with a periodic potential. Its experimental realization was featured in Ref. [29], where a variety of interesting phenomena are studied; these include Josephson oscillations and tunneling for a small number of atoms, or macroscopic quantum self-trapping and an asymmetric partition of the atoms between the wells for sufficiently large numbers of atoms. In parallel to these experimental findings, numerous theoretical insights on this topic have emerged [39–49]. These concern finite-mode reductions, analytical results for specially designed shapes of the potential, quantum depletion effects, and other theoretical aspects. Interestingly, double-well potentials have also been studied in applications arising in the context of nonlinear optics, including twin-core self-guided laser beams in Kerr media [50], optically induced dual-core waveguiding structures in a photorefractive crystal [51], and trapped light beams in a structured annular core of an optical fiber [52]. It is relevant to point out here that double-well settings have been examined not only in one-component systems, but also in multi-component cases, i.e., with atoms in different internal states. In particular, a recent study motivated by two-component BECs can be found in [53], while similar attempts have been made in the context of the so-called spinor BECs (where it is possible to have three, and even five components) in the works of [54, 55]. These works examined not only finite-mode reductions of the multi-component case, but also phenomena beyond the level of the mean-field description such as quantum entanglement and spin-squeezing properties.

Tuning the interatomic interaction

Moreover, nonlinear matter-waves have not only been studied in a variety of external potentials, but also in the presence of temporally or spatially varying external fields manipulating the interatomic interactions. Indeed, the s-wave scattering length (which characterizes the interaction strength in ultracold atom collisions) can be adjusted experimentally by employing either magnetic [56–60], optical [61, 62] or more recently a combination of optical and magnetic [63] Feshbach resonances in a very broad range. Magnetic Feshbach resonances apply a bias magnetic field for changing the scattering length whereas optical Feshbach resonances apply a laser beam for doing so. The flexibility of manipulating the interatomic interactions has motivated a significant number of studies both on the theoretical and on the experimental front. In particular, on the experimental side, a tuning of the interatomic interactions from repulsive to attractive was used for the formation of bright matter-wave solitons (cf. Section 2.2 for a definition of a soliton and a discussion of its basic properties) and soliton trains for ^7Li [64, 65] and ^{85}Rb [66]. Also, this type of manipulations was instrumental in achieving the formation of molecular condensates [67, 68], and the probing of the BEC-BCS crossover [69, 70]. On the other hand, theoretical studies have predicted

that a time-dependent modulation of the scattering length can be used to stabilize attractive higher-dimensional BECs against collapse [71–73], or to create robust matter-wave breathers in lower-dimensional BECs [74–78]. While the above studies focused on temporal variations of the interaction strength, more recently spatial variations of the nonlinearity have come to be of interest in the so-called “collisionally inhomogeneous” environments. These have been realized in a recent experiment on a nanometer length scale [79] and have been found to lead to a variety of interesting developments including (but not limited to) adiabatic compression of matter-waves [80, 81], Bloch oscillations of matter-wave solitons [80], atomic soliton emission and atom lasers [82, 83], enhancement of transmittivity of matter-waves through barriers [84, 85], dynamical trapping of matter-wave solitons [84], stable condensates exhibiting both attractive and repulsive interatomic interactions [86], the delocalization transition of matter waves [87]. Many different types of spatial variations of the nonlinearity have been considered, including linear [80, 84], parabolic [88], random [89], periodic [87, 90–93], and localized (step-like) [82, 94, 95] ones. Furthermore, a number of detailed mathematical studies [96–98] have appeared, addressing aspects such as the effect of a “nonlinear lattice potential” (i.e., a spatially periodic nonlinearity) on the stability of matter-wave solitons and the interplay between drift and diffraction/blow-up instabilities. More recently, the interplay of nonlinear and linear potentials has been examined in both continuum [99] and discrete [100] settings.

Solitonic states

The progress in the field of ultracold atoms has been, to a considerable extent, fueled by the fact that, in a mean-field picture, BECs can be described by a macroscopic wave function obeying the Gross-Pitaevskii equation (GPE). The macroscopic wave function has got the form of a single particle wave function, i.e., it depends on a single spatial coordinate, but serves as an effective description for a many-body system. The GPE is an equation of the nonlinear Schrödinger (NLS) type; a Schrödinger equation augmented by a nonlinear term. The nonlinear term stems from the effective mean-field description and models the interatomic interaction of the atoms.

On the one hand the GPE describes accurately the ground-state [1–5], but on the other hand also macroscopic nonlinear excitations of BECs, such as matter-wave dark and bright solitons. These have been studied theoretically (see, e.g., Refs. [3, 5, 101] and references therein) and were observed in a series of experiments [102–112]. Solitons are localized nonlinear structures which preserve their shapes while propagating due to the cancellation of the dispersive effects caused by the nonlinear effects. Moreover, solitons occur as analytical solutions of the NLS equation without an external potential leading to a remarkable robustness of solitons with respect to perturbations. Fig. 1.2 shows the evolution of a dark soliton (the density dip) in a harmonically confined condensate. One clearly observes the oscillatory behavior. Solitons have attracted much attention as they arise spontaneously upon crossing the BEC phase-transition [113, 114], while their properties may be used as diagnostic tools probing properties of BECs [115]. Additionally, applications of matter-wave dark solitons have been proposed: the dark soliton position can be used to monitor the phase acquired in an atomic matter-wave interferometer in the nonlinear regime [116, 117]. As matter-wave dark solitons are known to be more robust in the quasi one-dimensional (1D) geometry, the majority of relevant

theoretical studies have been performed in the framework of the 1D GPE and, particularly, in the so-called Thomas-Fermi (TF)-1D regime (see, e.g., Ref. [110]). More specifically, many works are devoted to the stability [118–120] and dynamical properties of dark solitons, such as their oscillations [118–127] and sound emission [125, 128] in the presence of a harmonic trapping potential. In the TF-1D regime, matter-wave dark solitons have also been studied in periodic (optical lattice) potentials [129–133], as well as in combinations of harmonic traps and optical lattices [134–138]. Nevertheless, the TF-1D regime has not been practically

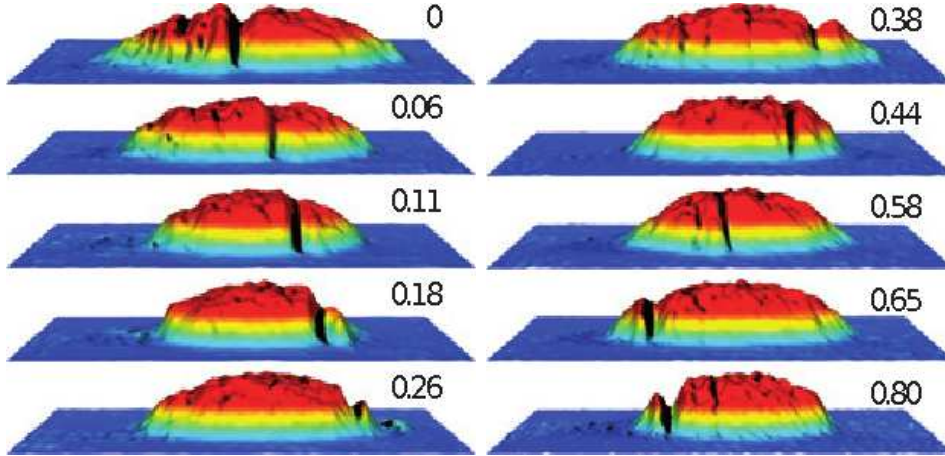


Figure 1.2: A set of absorption images showing the soliton position at various times after phase imprinting. The soliton propagates to the right and is reflected off the edge of the condensate after $t = 80$ ms. The corresponding evolution time for each image is given in units of the oscillation period T . From [108].

accessible in real experiments, yet: In fact, in most relevant experiments the condensates were usually elongated (alias “cigar-shaped”) three-dimensional (3D) objects, while only two recent experiments [110, 112] were conducted in the so-called dimensionality crossover regime from 1D to 3D [139]. The observations of these experiments were found to be in very good agreement with the theoretical predictions [110, 112] (see also Ref. [140], based on the use of an effective 1D mean-field model devised in Refs. [141–145]). This model, which has the form of a GP-like equation with a non-cubic nonlinearity, was also successfully used in Ref. [112] to analyze dark soliton statics and dynamics observed in the experiment.

Vortex states

One of the most fundamental and thoroughly studied type of excitations in the realm of BECs is the matter-wave vortex ([1–3, 5, 146, 147]). Matter-wave vortices represent fundamental nonlinear macroscopic excitations of BECs and are characterized by their nonzero topological charge S and a vanishing of the BEC density at the vortex core. The topological charge stems from the phase dislocation and jump by $2\pi S$ induced by the vorticity.

In two- (but also often in higher-) dimensional settings these structures are also of particular interest in nonlinear optics [148–151], and more broadly in nonlinear field theories in various branches of science [152]. Nevertheless, BECs represent a pristine setting where numerous features of the exciting nonlinear dynamics of single- and multi-charge vortices as well as of

vortex crystals and vortex lattices can be not only theoretically studied, but also experimentally observed. More specifically the first experimental observation of vortices [153] by means of a phase-imprinting method between two hyperfine spin states of a ^{87}Rb BEC [154] paved the way for a systematic investigation of their dynamical properties. Stirring the BECs [155] above a certain critical angular speed [156–158] led to the production of few vortices [158] and even of robust vortex lattices [159]. Fig. 1.3 shows the experimental observation of such vortex lattices. Other vortex-generation techniques were also used in experiments, including the breakup of the BEC superfluidity by dragging obstacles through the condensate [160], as well as nonlinear interference between condensate fragments [161].

In the above studies, vortices were singly-charged, i.e., with a topological charge of $S = 1$; higher-charged vortices with $S > 1$ may also be created experimentally [162, 163] and could, in principle, be stable under appropriate conditions [163–165]. Considerable effort has been dedicated to the investigation of the stability of such higher charge structures [166–169]. Nevertheless, such higher-charged vortices are typically far less robust than the fundamental $S = 1$ vortex.

In the BEC context, a theme that has received somewhat lesser attention, chiefly from

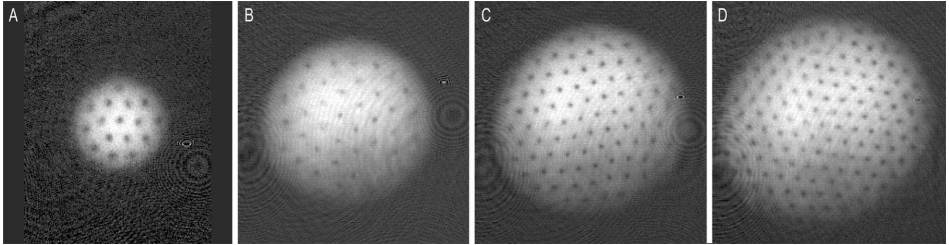


Figure 1.3: Observation of vortex lattices. The examples shown contain approximately (A) 16, (B) 32, (C) 80, and (D) 130 vortices. The vortices have “crystallized” in a triangular pattern. From [170].

the theoretical point of view, is that of “crystals” or clusters consisting of small numbers of vortices. In an important earlier work [171], the emergence of vortex dipole states from dark soliton stripes via a symmetry-breaking bifurcation was illustrated. Furthermore, in Refs. [165, 172] more complicated states such as vortex dipoles, tripoles and quadrupoles were illustrated, and energetic arguments concerning their instability were provided; in particular, it was argued that all these states correspond to energy maxima. Later, in Ref. [172], a linear stability analysis of these states led to the result that they are, in fact, unstable through different types of mechanisms. A dynamical perspective, focusing especially on the vortex evolution and the vortex interactions, was adopted in Ref. [173]; note that in this work, the vortices were considered in the vicinity of the linear/weakly-interacting limit. More recently, in Ref. [174], the bifurcation of the vortex dipole state from the dark soliton stripe was reproduced and a relevant explanation was attempted through a variational approximation; additionally, in the same work, the precessional dynamics of the vortex dipole near its equilibrium (as well as the potential for more complicated large-amplitude trajectories) was revealed. It should also be noted that similar vortex clusters have been considered in other settings, including toroidal traps [175, 176], rotating condensates with pinning sites of laser beams [177], or rotating anisotropic traps which may enforce a linear arrangement of the vortices [178].

At this point, it is also relevant to discuss the connection of vortex dipoles with the states

out of which they were shown to emerge, namely the dark solitons. The earlier experiments demonstrated the existence of these structures in BECs with repulsive interatomic interactions. However, dark solitons were found to be unstable, therefore exhibiting short lifetimes mainly due to thermal [102, 103] and dimensionality [105] effects. Regarding the latter, Ref. [105] reported the experimental observation of the onset of the transverse modulational instability of dark soliton stripes, as well as their concomitant decay into vortex structures, in accordance to the theoretical predictions [120, 179] and similar findings in nonlinear optics [150, 180, 181]. The transverse instability of dark solitons exhibiting radial symmetry [182] was also systematically studied [183, 184]. Other theoretical works investigated the possibility of avoiding the transverse instability of dark solitons, e.g., by using sufficiently tight traps [185, 186], highly-anisotropic traps, i.e., quasi one-dimensional (1D) traps, or narrow external potential sheets [187] that would enable the persistence of dark solitons [188]. The use of quasi-1D traps eventually allowed the recent experimental observation of robust, long-lived dark soliton states [108–110, 189].

In recent experiments even the observation of robust vortex dipoles [190, 191] and of three-vortex states [192] was reported. As far as the latter are concerned, in Ref. [190], vortex dipoles were produced by dragging a localized light beam with appropriate speed through the BEC, while in Ref. [191] they were distilled through the Kibble-Zurek mechanism [193–195] that was first experimentally reported for vortices in Ref. [196]. Note that in Ref. [191] near-equilibrium dynamics of the vortices were also observed along with small amplitude “epicyclic” motions of the dipole constituents, as well as large (distinct) amplitude, nearly decoupled precessional motions thereof.

Multi-component BECs

Up to now we discussed properties of the scalar GPE describing a condensate consisting of indistinguishable atoms, i.e. atoms of the same species in the same internal state. Let us in this section briefly discuss the case of multi-component BECs, i.e., BECs consisting of atoms in different internal states or even of atoms of different species. Experimentally, one can use optical traps in order to trap atoms in different internal states with the same potential. Note, in case of atoms of different species one needs to adjust the laser potential in such a way that the different masses are taken into account. It is as well worth mentioning that one can use magnetic traps for trapping atoms in different internal states in the same potential as well, when the states couple in the same way to magnetic fields. Indeed, this fact was exploited for trapping two different hyperfine components of different hyperfine manifolds of ^{87}Rb in one of the first multi-component BEC experiments [197]. The first multi-component BEC in an optical trap was realized with ^{23}Na [198]. For the description of multi-component BECs one has to distinguish two different cases: The case where an exchange of population between the components is possible and the case where no population exchange is possible.

The previous one is realized when the different internal states of one hyperfine manifold are trapped and can be described by the so-called spinor GPE consisting of three (five) coupled partial differential equations for the $F = 1$ ($F = 2$) manifold denoting the dynamics of three (five) wave functions with each wave function representing one spin component. The spin mixing dynamics between the different components has been studied theoretically [199, 200] and experimentally [198, 201–205].

The case without population transfer is described by the pseudo-spinor or vector GPE. Usually two component system are described by the vector GPE leading to two coupled partial differential equations [3]. The vector equations conserve the norm of the two wave functions individually thus reflecting the fact that particle exchange is prohibited. Experimentally a BEC consisting of a mixture of atoms in different internal states but of the same species has already been realized in 1997 [197]. Later a BEC of two different atomic species has been demonstrated in a harmonic potential [206] and moreover in [207] it was demonstrated how to tune the inter species interaction in a two component BEC consisting of two species. The ability to tune the inter species interaction allows the formation of ultracold heteronuclear molecules [208] which is the first step for achieving a BEC consisting of dipolar molecules.

Nonlinear excitations in multi-component systems

Excited states of multi-component systems of nonlinear waves are a fascinating topic with a rich and diverse history spanning a variety of areas, including Bose-Einstein condensates (BECs) in atomic physics [3], optical fibers and crystals in nonlinear optics [209], and integrable systems in mathematical physics [210]. Of particular interest are the so-called “symbiotic solitons”, namely structures that do otherwise not exist in one-component settings but can be supported by the interaction between the optical or atomic species components. A prototypical example of such a structure is the dark-bright (DB) soliton in self-defocusing, two-component systems, whereby the dark soliton (density dip) which typically arises in self-defocusing media [3, 101, 209, 210] creates through nonlinearity a trapping mechanism that localizes a density hump (bright soliton) in the second component.

Dark-bright solitons were experimentally created in photorefractive crystals [211], while their interactions were partially monitored in [212]. Upon realization of multi-component atomic BECs [197, 213, 214], it was predicted that similar structures would exist therein [121]. While theoretical developments along this direction were extended in even more complex settings (such as the spinor system of Ref. [215]), stable DB solitons were observed only recently in two-component BECs [108], leading to a renewed interest in this area. Relevant recent works include the interaction between DB solitons [216, 217] and their higher-dimensional generalizations [218].

Objective of this work

In this dissertation we investigate nonlinear excitations of BECs. We especially focus on condensates trapped in double-well potentials, on the effects of a spatial modulation of the interatomic interaction on solitonic and vortex states, and on trapping magnetically insensitive atoms. On the one hand, we perform continuations in the nonlinear parameter of the GPE starting from the linear limiting case. On the other hand, we investigate the occurrence of nonlinear states which do not exist in the linear limiting case. Subsequently, we investigate the stability of these states by small-amplitude excitations and verify our findings by direct numerical integration of the GPE. For the soliton and vortex dynamics we develop effective equations of motion describing the motion of solitons and vortices as the motion of quasi-particles. Moreover, we demonstrate two novel ways of trapping magnetically insensitive atoms: The one relies on interatomic collisions of the atoms with magnetically trappable

atoms and the other on applying near resonant laser light in a magnetic trap.

Scope of this work

In detail, the current work is structured as follows.

Chapter 2 is devoted to a brief theoretical introduction into basic mean field theory in the context of BECs. We derive the Gross Pitaevskii mean field model and discuss its basic properties. Moreover, we present the most important types for the confining potential and describe how one can vary the interaction between ultracold atoms by Feshbach resonances. We explicitly perform the reduction of the three dimensional (3D) GPE to effective lower dimensional equations and discuss the ground state solution of the 3D GPE and excited states of the lower dimensional equations, i.e., solitonic states for the one dimensional case and vortex states for the two dimensional case. Finally, we present a stability analysis of solutions of the GPE by the Bogoliubov de Gennes analysis.

In Chapter 3 we consider quasi-one-dimensional Bose-Einstein condensates (BECs), with spatially varying collisional interactions, trapped in double-well potentials. In particular, we study a setup in which such a collisionally inhomogeneous BEC has the same (attractive-attractive or repulsive-repulsive) or different (attractive-repulsive) type of inter particle interactions. Our analysis is based on the continuation of the symmetric ground state and anti-symmetric first excited state of the non-interacting (linear) limit into their nonlinear counterparts.

In Chapter 4 we study the dynamics of bright and dark matter-wave solitons in the presence of a spatially varying nonlinearity. When the spatial variation does not involve zero crossings, a transformation is used to bring the problem to a standard nonlinear Schrödinger form, but with two additional terms: an effective potential one and a non-potential term. We illustrate how to apply perturbation theory of dark and bright solitons to the transformed equations. We develop the general case, but primarily focus on the non-standard special case where the potential term vanishes, for an inverse square spatial dependence of the nonlinearity. In both cases of repulsive and attractive interactions, appropriate versions of the soliton perturbation theory are shown to accurately describe the soliton dynamics.

In Chapter 5 we study the statics and dynamics of dark solitons in a cigar-shaped Bose-Einstein condensate confined in a double-well potential. Using a mean-field model with a non-cubic nonlinearity, appropriate to describe the dimensionality crossover regime from one to three dimensional, we obtain branches of solutions in the form of single- and multiple-dark soliton states and study their bifurcations and stability. It is demonstrated that there exist dark soliton states which do not have a linear counterpart and we highlight the role of anomalous modes in the excitation spectra. Particularly, we show that anomalous mode eigenfrequencies are closely connected to the characteristic soliton frequencies as found from the solitons' equations of motion. Moreover, we demonstrate how the anomalous modes are related to the emergence of instabilities. We also analyze in detail the role of the height of the barrier in the double-well setting, which may lead to instabilities or decouple multiple dark soliton states.

Chapter 6 is devoted to the spectral properties of a singly-charged vortex in a Bose-Einstein condensate confined in a highly anisotropic (disk-shaped) harmonic trap. Special emphasis is given on the analysis of the anomalous mode of the Bogoliubov spectrum. We use analytical

and numerical techniques to illustrate the connection of the anomalous mode to the precession dynamics of the vortex in the trap. Effects due to inhomogeneous interatomic interactions and dissipative perturbations motivated by finite temperature considerations are explored. We find that both of these effects may give rise to oscillatory instabilities of the vortex, which are suitably diagnosed through the perturbation-induced evolution of the anomalous mode and being monitored by direct numerical simulations.

Chapter 7 offers a unifying perspective between the dark soliton stripe and the vortex multipole (dipole, tripole, aligned quadrupole, quintopole, etc.) states that emerge in the context of quasi-two-dimensional Bose-Einstein condensates. In particular, we illustrate that the multi-vortex states with the vortices aligned along the (former) dark soliton stripe sequentially bifurcate from the latter state in a supercritical pitchfork manner. Each additional bifurcation adds an extra mode to the dark soliton instability and an extra vortex to the configuration; also, the bifurcating states inherit the stability properties of the soliton prior to the bifurcation. The critical points of this bifurcation are computed analytically via a few-mode truncation of the system, which clearly showcases the symmetry-breaking nature of the corresponding bifurcation. We complement this small(er) amplitude, few mode bifurcation picture with a larger amplitude, particle-based description of the ensuing vortices. The latter enables us to characterize the equilibrium position of the vortices, as well as their intrinsic dynamics and anomalous modes, thus providing a qualitative description of the non-equilibrium multi-vortex dynamics.

In Chapter 8 we explore the stability and dynamics of dark-bright solitons in two-component elongated Bose-Einstein condensates by applying effective 1D vector equations as well as solving the corresponding 3D Gross-Pitaevskii equations. A strong dependence of the oscillation frequency and of the stability of the dark-bright soliton on the atom number of its components is found. Spontaneous symmetry breaking leads to oscillatory dynamics in the transverse degrees of freedom for a large occupation of the component supporting the dark soliton. Moreover, the interactions of two dark-bright solitons are investigated with special emphasis on the importance of their relative phases. Finally, we compare our results with experimental results showcasing dark-bright soliton dynamics and collisions in a Bose-Einstein condensate consisting of two hyperfine states of ^{87}Rb confined in an elongated optical dipole trap.

Chapter 9 is devoted to the investigation of a multi-component BEC. We demonstrate that atoms in magnetically insensitive hyperfine states ($m = 0$) can be trapped efficiently by a Bose-Einstein Condensate of the same atomic species occupying a different hyperfine state. The latter is trapped magnetically. Hyperfine state changing collisions, and therefore loss of the trapped ($m = 0$) atoms, are shown to be strongly inhibited in case of a low density of the confined atomic cloud. We monitor the transition from a 'soft' to a 'hard' effective potential by studying the backaction of the trapped ($m = 0$) atoms onto the condensate which provides their confinement. The controlled outcoupling of the trapped atoms by shaping the condensate's wave function is explored. We observe a pulsed emission of atoms from the trapping region reminiscent of an atom laser.

In Chapter 10 we discuss explicitly a way how one can trap atoms by applying external fields. We utilize the combination of two standard trapping techniques, a magnetic trap and an optical trap in a Raman setup, to propose a versatile and tunable trap for cold atoms. The created potential provides several advantages over conventional trapping potentials. One can easily convert the type of the trap, e.g., from a single well to a double-well trap. Atoms in different internal states can be trapped in different trap types, thereby enabling the realization

of experiments with multi-component Bose-Einstein condensates. Moreover, one can achieve variations of the trapping potential on small length scales without the need of microstructures. We present the potential surfaces for different setups, demonstrate their tunability, give a semi-analytical expression for the potential, and propose experiments which can be realized within such a trap.

Finally, in Chapter 11 we present our conclusions and an outlook for future studies.

Chapter 2

Basic Mean-Field Theory

This chapter is devoted to a brief theoretical introduction into the mean field description of a Bose-Einstein condensate (BEC). In particular, we present the derivation of the Gross Pitaevskii equation (GPE) in section 2.1 and discuss there some of its basic features as well. We describe typical shapes of external potentials used to confine ultracold atoms and present how one can tune the interaction parameter, which describes the interatomic interactions in BECs, via Feshbach resonances. In section 2.2 we discuss the reduction of the three dimensional (3D) GPE to effective lower dimensional equations for highly anisotropic trapping potentials. Subsequently, we investigate the ground state solution of the 3D GPE and collective excitations of BECs in one dimensional (1D) and two dimensional (2D) setups in section 2.3. Finally, we present in section 2.4 a stability analysis of solutions of the GPE using small amplitude linear excitations by the Bogoliubov de Gennes (BdG) analysis. The concepts presented in this chapter have already partly been published in textbooks [1–3] or review articles [4, 5, 101].

2.1 The Gross Pitaevskii Mean-Field Model

2.1.1 Derivation and Basic Properties of the Gross Pitaevskii Equation

We consider an ultracold dilute atomic gas of N interacting bosons of mass M confined in a potential $V^{\text{ext}}(\mathbf{r})$. We assume that two body collisions are dominant in the system. Then the many body Hamiltonian can be expressed in second quantized form with the bosonic annihilation and creation field operators $\hat{\Psi}^\dagger(\mathbf{r}, t)$ and $\hat{\Psi}(\mathbf{r}, t)$:

$$\hat{H} = \int d\mathbf{r} \hat{\Psi}^\dagger(\mathbf{r}, t) \hat{H}_0 \hat{\Psi}(\mathbf{r}, t) + \frac{1}{2} \int d\mathbf{r} d\mathbf{r}' \hat{\Psi}^\dagger(\mathbf{r}, t) \hat{\Psi}^\dagger(\mathbf{r}', t) V(\mathbf{r} - \mathbf{r}') \hat{\Psi}(\mathbf{r}', t) \hat{\Psi}(\mathbf{r}, t) \quad (2.1)$$

$\hat{H}_0 = -(\hbar^2/2M)\nabla^2 + V_{\text{ext}}(\mathbf{r})$ denotes the single atom Hamiltonian and $V(\mathbf{r} - \mathbf{r}')$ the two body interaction potential. Applying the standard boson commutator relations one can deduce with the Heisenberg equation $i\hbar\partial_t = [\hat{\Psi}^\dagger, \hat{H}]$ the equation of motion

$$i\hbar\partial_t \hat{\Psi}(\mathbf{r}, t) = \left[\hat{H}_0 + \int d\mathbf{r}' \hat{\Psi}^\dagger(\mathbf{r}', t) V(\mathbf{r} - \mathbf{r}') \hat{\Psi}(\mathbf{r}', t) \right] \hat{\Psi}(\mathbf{r}, t). \quad (2.2)$$

Eq. (2.2) can in principle be solved exactly within statistical errors using Monte Carlo methods. However, the calculations become heavy and impracticable for large atom numbers N . In order to circumvent solving the full many body Schrödinger equation (2.2) mean field models were developed. These have got the advantage of being less heavy to calculate and furthermore they consist of few parameters allowing for physical interpretations of the

results. In the mean field approach, formulated by Bogoliubov (1947), one assumes that the condensate fraction can be separated from the non-condensed fraction. In general, the field operator $\hat{\Psi}(\mathbf{r})$ can be decomposed as $\hat{\Psi}(\mathbf{r}) = \sum_i \psi_i(\mathbf{r}) a_i$ with the single particle wave function $\psi_i(\mathbf{r})$ and the bosonic annihilation operator a_i . The annihilation and creation operators a_i and a_i^\dagger are defined in the standard way acting on Fock states annihilating and creating a particle in the state i

$$a_i^\dagger |n_0, n_1, \dots, n_i, \dots\rangle = \sqrt{n_i + 1} |n_0, n_1, \dots, n_i + 1, \dots\rangle \quad (2.3)$$

$$a_i |n_0, n_1, \dots, n_i, \dots\rangle = \sqrt{n_i} |n_0, n_1, \dots, n_i - 1, \dots\rangle \quad (2.4)$$

with n_i being the eigenvalue of the operator $\hat{n}_i = a_i^\dagger a_i$. n_i denotes the number of atoms in the single particle state i . One speaks of the occurrence of Bose-Einstein condensation if one of the single particle states i becomes macroscopically occupied, i.e., the atom number $n_0 \equiv N_0$ becomes large for fixed atom number N . Then one can treat the operators a_i and a_i^\dagger as c numbers since the physical configurations with N_0 and $N_0 \pm 1 \approx N_0$ can be treated as approximately identical. This approximation allows us to write the time dependent field operator as

$$\hat{\Psi}(\mathbf{r}, t) = \phi(\mathbf{r}, t) + \partial \hat{\Psi}(\mathbf{r}, t). \quad (2.5)$$

Here $\phi(\mathbf{r}, t)$ is a complex function defined as the expectation value of the field operator $\langle \hat{\Psi}(\mathbf{r}, t) \rangle$. $\phi(\mathbf{r}, t)$ is a classical field and describes the condensed part of the atoms. Therefore we will often refer to it as the wave function of the condensate. Its modulus fixes the condensate's density $\rho = |\phi(\mathbf{r}, t)|^2$. $\partial \hat{\Psi}(\mathbf{r}, t)$ describes the non-condensed part and can be neglected for temperature well below T_c , the temperature where Bose-Einstein condensation occurs.

Next, considering a dilute ultracold gas one can assume that the low energy collision are dominated by s-wave scattering and can therefore be described by a single parameter: the s-wave scattering length. This allows to describe the two body interaction potential as $V(\mathbf{r} - \mathbf{r}') = g\delta(\mathbf{r} - \mathbf{r}')$ with the coupling coefficient $g = 4\pi\hbar^2 a/M$ with the s-wave scattering length a . Replacing the interaction potential and the operator $\hat{\Psi}(\mathbf{r}, t)$ by the classical field $\phi(\mathbf{r}, t)$ leads to the Gross-Pitaevskii equation

$$i\hbar\partial_t\phi(\mathbf{r}, t) = \left[-\frac{\hbar^2}{2M}\nabla^2 + V_{\text{ext}}(\mathbf{r}) + g|\phi(\mathbf{r}, t)|^2 \right] \phi(\mathbf{r}, t). \quad (2.6)$$

The s-wave scattering length a can be negative or positive, leading to a repulsive or attractive interaction between the atoms. The sign and the value of the scattering length depend on the atomic species but can be tuned as well using so called Feshbach resonances which we will describe in more detail below. An alternative way to derive the GPE (2.6) is by using a variational principal

$$i\hbar\partial_t\phi(\mathbf{r}, t) = \frac{\partial E}{\partial\phi^*(\mathbf{r}, t)} \quad (2.7)$$

with the energy functional

$$E[\phi] = \int d\mathbf{r} \left[-\frac{\hbar^2}{2M} |\nabla\phi(\mathbf{r}, t)|^2 + V_{\text{ext}}(\mathbf{r}) |\phi(\mathbf{r}, t)|^2 + \frac{1}{2} g |\phi(\mathbf{r}, t)|^4 \right]. \quad (2.8)$$

The individual terms can be assigned to the kinetic energy E_{kin} , the potential energy E_{pot}

and the interaction energy E_{int} . For time independent external potentials $V_{\text{ext}}(\mathbf{r})$ the energy of the system $E = E[\phi]$ is conserved. A second conserved quantity is given by the total number of atoms

$$N = \int d\mathbf{r} |\phi(\mathbf{r}, t)|^2. \quad (2.9)$$

2.1.2 The External Potential

The external potential $V_{\text{ext}}(\mathbf{r})$ is used to trap the atoms of the condensate. The potential is usually created by magnetic, electric or optical fields. Magnetic trapping relies on the coupling of the total angular momentum \mathbf{F} to the magnetic field vector $V^{\text{mag}} = g_F \mu_B \mathbf{F} \cdot \mathbf{B}$. In the adiabatic approximation, i.e., when one assumes that the polarization vector of the atom is always parallel to the direction of the magnetic field, the resulting potential is proportional to the magnetic projection quantum number m ranging from $-F$ to F and can be described as $V^{\text{mag}} = g_F \mu_B m |\mathbf{B}|$. Let us briefly discuss some consequences of the magnetic field potential. The $m = 0$ state is insensitive to the magnetic field and can therefore not be trapped magnetically. Moreover, states with different coefficients $g_F m$ are exposed to different potentials. Furthermore, one cannot trap states with negative $g_F m$ since it is not possible to create maxima of the magnetic field using a superposition of static magnetic fields. Optical trapping relies on the coupling of two internal states by a laser which is far detuned with respect to the transition frequency of these states. In optical dipole traps the potential is proportional to the intensity profile of the laser.

In Chapter 10 we describe in detail how to confine atoms by applying near resonant laser light in magnetic traps and derive the corresponding potential. At this point we briefly mention the most important trap types and the corresponding potentials.

The most simple trapping potential created by the 'traditional' magnetic traps or optical dipole traps with Gaussian intensity profiles is the harmonic trap. The corresponding potential can be described approximately by a harmonic potential

$$V_{\text{HT}} = \frac{1}{2} M (\omega_x^2 x^2 + \omega_y^2 y^2 + \omega_z^2 z^2), \quad (2.10)$$

where the three oscillator frequencies $(\omega_x, \omega_y, \omega_z)$ may differ from each other. Another important type of potentials are the optical lattice potentials. These are imposed by a pair of laser beams in each direction forming a standing wave which generates a periodic potential of the following form

$$V_{\text{OL}} = V_0 [\cos^2(k_x x + \phi_x) + \cos^2(k_y y + \phi_y) + \cos^2(k_z z + \phi_z)] \quad (2.11)$$

with arbitrary phases ϕ_x, ϕ_y, ϕ_z , wave vectors k_x, k_y, k_z depending on the wavelength of the standing waves and on the angles between the different standing waves [219]. It is also possible to realize experimentally superpositions of optical lattices with different periods or superpositions of harmonic dipole traps and optical lattices. This allows for example the creation of an optical lattice potential in one direction and a harmonic potential in the other directions. Moreover, the superposition of a harmonic and an optical lattice potential in the

same direction leads in one dimension to the potential

$$V_{\text{DW}} = \frac{1}{2}M\omega_z^2 z^2 + V_0 \cos^2(k_z z + \phi_z). \quad (2.12)$$

By a proper choice of the parameters the potential may readily lead to a trapping potential that has the form of an effective double-well potential [29], i.e., a potential which constitutes of two wells which are separated by a barrier. In this case the height of the barrier is given by V_0 . Note, one often finds different implementations of double-well potentials as well, e.g., a superposition of a harmonic potential and a Gaussian or a Sech potential, or a superposition of a harmonic and a quartic potential. These stem from different experimental realization or are used in theoretical works out of convenience since they are for some applications easier to tune and represent the general behavior of a double-well potential correctly.

2.1.3 Feshbach Resonances

The s-wave scattering length a sets the nonlinearity strength in Eq. (2.6). The value of the scattering length depends on the atomic species and of the internal state of the atom. It can be positive, e.g., for rubidium or negative e.g., for lithium leading to a repulsive or attractive interaction, respectively. Moreover, one can tune the value of the scattering length by the means of Feshbach resonances (for a detailed description see the recent review [220] and ref. therein). A Feshbach resonance occurs when the threshold collision energy of two single atoms is resonant with the energy of a bound state. Fig. 2.1 shows a basic level scheme of the potential of the unbound entrance channel and of one closed bound channel. The threshold energy of the unbound state is indicated by the dashed line and the energy of the bound state E_C by the solid line. If the energies become degenerate, a Feshbach resonance will occur. Pictorially speaking, the atoms stay for a longer time together since they can be reflected at the potential of the closed channel, leading to a larger scattering length.

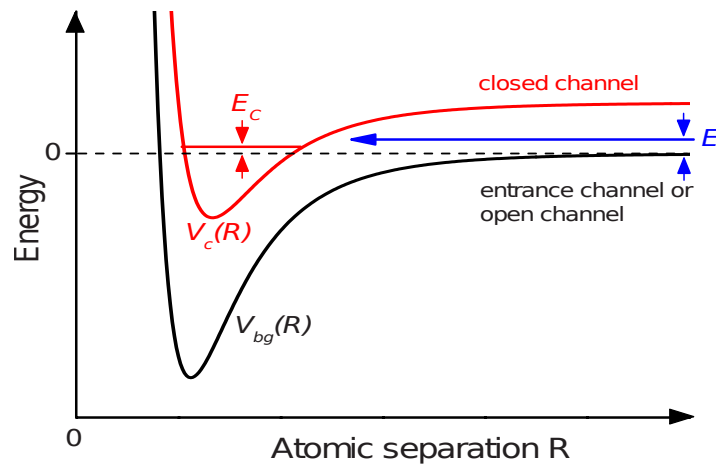


Figure 2.1: Basic two-channel model for a Feshbach resonance. From Ref. [220].

There are different ways of changing the energy difference between the bound and unbound state. The different states couple differently to magnetic fields thereby allowing to shift the relative energy of the states by applying a magnetic field leading to the so called magnetically

induced Feshbach resonances. A magnetically induced Feshbach resonance can be described by the simple expression for the s-wave scattering length

$$a(B) = a_{\text{bg}} \left(1 - \frac{\Delta}{B - B_0}\right) \quad (2.13)$$

where a_{bg} is the value of the scattering length far from the resonance, B_0 and Δ are position and width of the resonance, respectively.

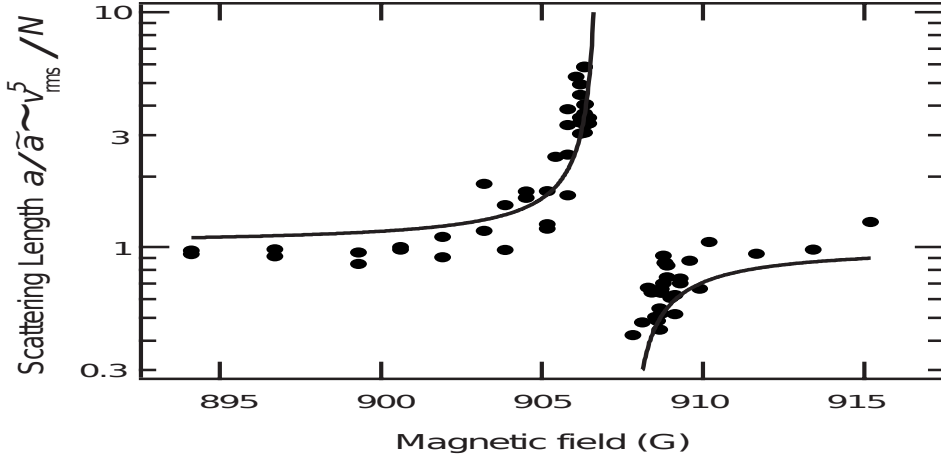


Figure 2.2: Shape of the scattering length a for Na atoms near a Feshbach resonance determined from measurements. Here a is normalized to the value of the background scattering length a_{bg} . From Ref. [57].

Fig. 2.2 shows the shape of the scattering length for Na in dependence of the magnetic field close to a Feshbach resonance. The points indicate experimental data and the solid line the theoretical prediction. One clearly observes that the value of the scattering length is widely tunable. Since the atoms have got multiple bound states one obtains multiple Feshbach resonances for different values of the magnetic field. This can lead to more complex shapes of the scattering length due to overlapping resonances.

By applying a spatially dependent magnetic field one can consequently achieve a spatially varying scattering length. The drawback of using magnetic Feshbach resonances is that a spatially dependent magnetic field creates a spatially dependent external potential for most of the atoms used in ultra cold experiments as well thus making it difficult to observe the pure effect of the spatially varying scattering length.

Therefore another approach uses an optical potential [61, 62] in order to achieve that the open and closed channel become energetically degenerate by coupling the state of the closed channel to an highly excited state and thereby changing its energy. This coupling can be done optically by applying an off-resonant laser with respect to the transition of the bound state to the excited state. In principle one can by increasing the intensity of the laser shift the energy of the bound state in a wide region by admixing the excited state. Additionally, the ability to vary the laser intensity offers a broader flexibility to tune the scattering length than in the case of the magnetic Feshbach resonances. However, the admixture of the excited state leads to a finite probability to populate the excited state and thereby to loose atoms by light-induced inelastic collisions. This loss rate increases with increasing laser intensity.

Therefore a combination of magnetic and optical fields was used in a recent approach [63].

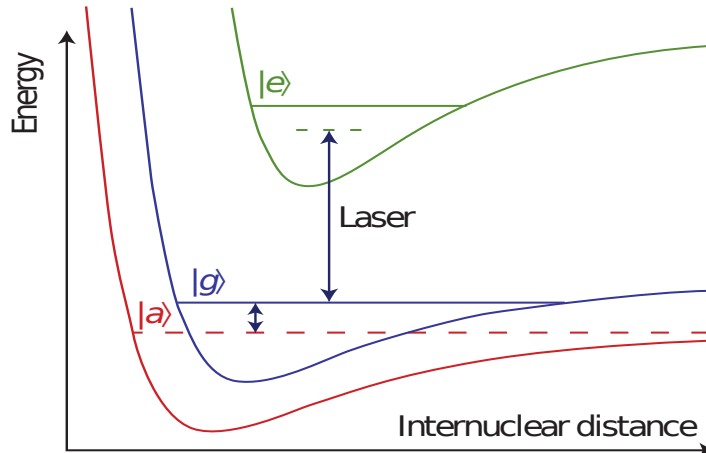


Figure 2.3: Level scheme for a combined magnetic and optical Feshbach resonance. From Ref. [63].

The corresponding level scheme is shown in Fig. 2.3. A magnetic field is used to shift the relative energy between the incoming channel $|a\rangle$ and a bound state $|g\rangle$ in such a way that they are almost degenerate. By coupling the bound state $|g\rangle$ to an excited state $|e\rangle$ the energy of the bound state is shifted optically in such a way that it becomes degenerate with the threshold energy of the unbound state. This procedure has got the advantage that the energy shift caused by the laser is small and thus only small laser intensities are needed. Nevertheless the condition that the energies are degenerate, i.e., that a Feshbach resonance occurs, is achieved optically. Thus one can tune the interaction strength with laser light allowing a spatial modulation of the scattering length by using a laser with a spatial dependent intensity distribution.

2.2 Dimensionality Reduction

The ability to vary the oscillation frequencies in a harmonic trap in the different directions individually allows the creation of very elongated or highly flattened condensates. These condensates can be regarded as effectively one-dimensional (1D) or two-dimensional (2D). One speaks of effectively 1D (2D) condensates if the shape of the wave function in the other directions does not change, i.e., the other directions are frozen out. There exist different criteria for a dimension to be regarded as frozen out depending on the quantities one wants to observe and the accuracy needed. However, we should note, the dimensionality reduction we perform in the following is an approximation and the resulting equations should be considered as effective 1D or 2D equations and not as the results of genuinely 1D or 2D theories. However, they are extremely useful since equation (2.6) is a 3D nonlinear partial differential equation and therefore considerable numerical effort is needed in order to find its solutions. The numerical effort decreases notably for lower dimensional equations. The minimal condition for a dimension to be frozen out is that the energy gap between the ground state and the first excited state in the corresponding direction is much larger than the typical energy in the system thus making it impossible to excite the state in the corresponding direction. A stricter criterion can be deduced from the length scales in the system. On the one hand the

length scale of the trap is given by the harmonic oscillator length $a_{\text{HO}} = \sqrt{\hbar/(M\omega)}$, on the other hand a typical length scale introduced by the effective mean-field nonlinearity is the so-called healing-length $\xi = (8\pi\rho a)^{-1/2}$ with the s-wave scattering length a and the local density ρ . The name healing length results from the fact that ξ is the length scale over which the condensate wave function heals over defects. Therefore the width of nonlinear excitation such as solitons or vortices is of order $O(\xi)$ as well. For $a_{\text{HO}} < \xi$ one consequently assumes that no excitations in the corresponding directions are possible and that one can consider the direction as frozen out.

2.2.1 Effectively 2d Condensates

Let us assume that $\omega_x = \omega_y \equiv \omega_r$ and $\omega_z \gg \omega_r$. Then one can consider the condensate according to the criterion presented above as effectively 2D, if the axial harmonic oscillator length $a_z < \xi$. In order to perform a reduction to an effective 2D system we decompose the wave function $\phi(\mathbf{r})$ in a axial part (along z) and a transverse component depending on (x, y) .

$$\phi(\mathbf{r}, t) = f(x, y, t)\psi(z, t)\exp(-i\gamma t/\hbar) \quad (2.14)$$

with the chemical potential γ . The axial wave function should be normalized to unity, i.e., $\int dz|\psi(z)|^2 = 1$. Substitution of the ansatz (2.14) in the GPE (2.6) leads to

$$\begin{aligned} & \left[i\hbar\partial_t f(x, y, t) + \frac{\hbar^2}{2M}\nabla_{\perp}^2 f(x, y, t) - \frac{1}{2}M\omega_r^2 r^2 f(x, y, t) \right] \psi(z) \\ &= \left[-\frac{\hbar^2}{2M}\partial_z^2 \psi(z) + \frac{1}{2}M\omega_z^2 z^2 \psi(z) - \gamma\psi(z) + g|\psi(z)|^2|f(x, y, t)|^2\psi(z) \right] f(x, y, t). \end{aligned} \quad (2.15)$$

Here we have neglected the time variation of the axial wave function $\psi(z)$ which is justified by the strong axial confinement leading to a suppression of excitations as we have argued above. One can now multiply both sides of Eq. (2.15) from the left with $\psi^*(z)$ and formally integrate out the axial wave function leading to

$$i\hbar\partial_t f(x, y, t) = \left[-\frac{\hbar^2}{2M}\nabla_{\perp}^2 + \frac{1}{2}M\omega_r^2 r^2 + \mu_z[f(x, y, t)] \right] f(x, y, t) \quad (2.16)$$

with the functional

$$\mu_z[f(x, y, t)] = \int dz\psi^*(z) \left[-\frac{\hbar^2}{2M}\partial_z^2 + \frac{1}{2}M\omega_z^2 z^2 - \gamma + g|\psi(z)|^2|f(x, y, t)|^2 \right] \psi(z). \quad (2.17)$$

Note, μ_z is a functional $\mu_z = \mu_z[f(x, y, t)]$ depending on the transversal part of the wave function and of course on the axial part of the wave function. So far we have only separated the wave functions in an axial and a transversal part and neglected time variations of the axial part. Let us now assume that due to the strong harmonic axial confinement the axial wave function obeys the differential equation corresponding to the harmonic oscillator problem

$$0 = \left(-\frac{\hbar^2}{2M}\partial_z^2 + \frac{1}{2}M\omega_z^2 z^2 - \gamma \right) \psi(z), \quad (2.18)$$

thereby we neglect interaction effects in the axial direction. Furthermore, it is reasonable to assume that the axial wave function is in its ground state leading to

$$\psi(z) = \frac{1}{\pi^{1/4} \sqrt{a_z}} \exp\left(-\frac{z^2}{2a_z^2}\right) \quad (2.19)$$

with the harmonic oscillator length a_z in the z -direction. Substitution of Eq. (2.19) in Eq. (2.16,2.17) leads to the effective 2d equation

$$i\hbar\partial_t f(x, y, t) = \left[-\frac{\hbar^2}{2M} \nabla_{\perp}^2 + \frac{1}{2} M \omega_r^2 r^2 + g_{2D} |f(x, y, t)|^2 \right] f(x, y, t) \quad (2.20)$$

with the effective 2D coupling coefficient $g_{2D} = g/(\sqrt{2\pi}a_z)$. Note, the effective 2D equation (2.20) has got the same structure as the 3D GPE (2.6). The only differences are the modified coupling coefficient and that the wave function is a two dimensional wave function $f = f(x, y, t)$ and consequently the Laplacian operator is the 2D Laplacian. One can perform the same reduction for an arbitrary external potential $V_{\text{ext}}(x, y)$ in the x - y plane instead of the harmonic one.

2.2.2 Effectively 1d Condensates

One can perform a similar reduction as in the previous subsection of the 3D GPE (2.6) to an effective 1D equation for $\omega_x = \omega_y \equiv \omega_r \gg \omega_z$ and $a_r < \xi$. Following the lines of the previous subsection we use the separation ansatz

$$\phi(\mathbf{r}) = f(z, t)\psi(x, y, t) \exp(-i\gamma t/\hbar) \quad (2.21)$$

leading to

$$i\hbar\partial_t f(z, t) = -\frac{\hbar^2}{2M} \partial_z^2 f(z, t) + \frac{1}{2} M \omega_z^2 z^2 f(z, t) + \mu_{\perp}[f(z, t)] f(z, t) \quad (2.22)$$

with the functional

$$\mu_{\perp}[f(z, t)] = \int dx dy \psi^*(x, y) \left(-\frac{\hbar^2}{2M} \nabla_{\perp}^2 + \frac{1}{2} M \omega_r^2 r^2 - \gamma + g |\psi(x, y)|^2 |f(z, t)|^2 \right) \psi(x, y) \quad (2.23)$$

Let us at this point neglect the interaction in the transversal direction and assume that the transversal wave function is and remains in the ground state of the transverse quantum harmonic oscillator

$$\psi(x, y) = \frac{1}{\pi^{1/2} a_r} \exp\left(-\frac{r^2}{2a_r^2}\right) \quad (2.24)$$

with the harmonic oscillator length a_r in the transversal direction. Substitution of Eq. (2.24) in Eqs. (2.22,2.23) leads to the effective 1D equation

$$i\hbar\partial_t f(z, t) = \left[-\frac{\hbar^2}{2M} \partial_z^2 + \frac{1}{2} M \omega_z^2 z^2 + g_{1D} |f(z, t)|^2 \right] f(z, t) \quad (2.25)$$

with the effective 1D coupling coefficient $g_{1D} = g/(2\pi a_r^2)$. Once again the structure of the effective 1D equation is equal to the structure of the 3D GPE with a modified interaction parameter.

2.2.3 Cigar-Shaped Condensates

In the previous section we derived an effective 1D equation by separating the wave function in an axial and a transversal part and assuming that the transversal part is given by the 2D harmonic oscillator ground state eigenfunction. This effective 1D equation is valid for $a_r < \xi$. However, in fact, most relevant experiments were conducted in the so-called dimensionality crossover regime from 1D to 3D [139] where the condensate is cigar-shaped but $a_r < \xi$ is not fulfilled. There do not exist strict conditions for the different regimes and the ranges of validity of the corresponding equations depends on the observables one investigates. For investigating the dimensionality crossover regime, let us make an adiabatic approximation and use the more general ansatz for factorizing the wave function

$$\phi(\mathbf{r}, t) = f(z, t)\psi(x, y, t; z) \exp(-i\gamma t/\hbar). \quad (2.26)$$

Here we allow ψ to depend parametrically on z . Substitution of Eq. (2.26) in Eq. (2.6) leads to

$$\begin{aligned} & \left[i\hbar\partial_t f(z, t) + \frac{\hbar^2}{2M}\partial_z^2 f(z, t) - \frac{1}{2}M\omega_z^2 z^2 f(z, t) \right] \psi(x, y; z) \\ &= \left[-\frac{\hbar^2}{2M}\nabla_\perp^2 \psi(x, y; z) + \frac{1}{2}M\omega_r^2 r^2 \psi(x, y; z) - \gamma\psi(x, y; z) \right. \\ & \quad \left. + g|\psi(x, y; z)|^2 |f(z, t)|^2 \psi(x, y; z) \right] f(z, t) \end{aligned} \quad (2.27)$$

We have neglected axial and time variation of the transversal wave function $\psi(x, y; z)$, ending up with a similar equations as previously. One can now formally integrate out the transversal wave function leading to

$$\left[i\hbar\partial_t + \frac{\hbar^2}{2M}\partial_z^2 - \frac{1}{2}M\omega_z^2 z^2 \right] f(z, t) = \mu_\perp[f(z, t)] f(z, t) \quad (2.28)$$

with the functional

$$\mu_\perp[f(z, t)] = \int d^2\mathbf{r}_\perp \psi^*(x, y; z) \left[-\frac{\hbar^2}{2M}\nabla_\perp^2 + \frac{1}{2}M\omega_r^2 r^2 - \gamma + g|\psi(x, y; z)|^2 |f(z, t)|^2 \right] \psi(x, y; z) \quad (2.29)$$

Once again we assume that the wave function should have a Gaussian shape due to the strong, harmonic transversal confinement.

$$\psi(x, y; z) = \frac{1}{\sqrt{\pi}\sigma[f(z, t)]} \exp\left(-\frac{r^2}{2(\sigma[f(z, t)])^2}\right). \quad (2.30)$$

In contrast to the previous ansatz we allow here the width σ to be a variational parameter $\sigma = \sigma[f(z, t)]$. There are mainly two different approaches how to determine σ leading to the Gerbier equation (GE) [141, 144] and the non-polynomial Schrödinger equation (NPSE) [142].

Gerbier Equation

For the previous one, one determines σ by minimizing the chemical potential μ_{\perp} with respect to σ . Substitution of the ansatz (2.30) in Eq. (2.29) leads to

$$\mu_{\perp}[f(z, t)] = \frac{\hbar^2}{2M}(\sigma[f(z, t)])^{-2} + \frac{M\omega_r^2}{2}(\sigma[f(z, t)])^2 + \frac{1}{2\pi}g|f(z, t)|^2(\sigma[f(z, t)])^{-2}. \quad (2.31)$$

Here we have set the constant offset $\gamma = 0$. Eq. (2.31) is minimal for

$$(\sigma[f(z, t)])^2 = a_r^2\sqrt{1 + 4a|f(z, t)|^2} \quad (2.32)$$

This compact expression allows a physical interpretation of the variational process. For $4a|f(z)|^2 \ll 1$ one can neglect interaction effects and the width is given by a_r leading to the ground state eigenfunction of the 2D harmonic oscillator for ψ . This is exactly the case discussed previously. Otherwise the interaction leads for a repulsive condensate ($a > 0$) to a broadening of the width and for an attractive condensate ($a < 0$) to a reduction of the width. Note, σ depends on the axial component z . So the width of the Gaussian function in the transversal direction depends on the axial coordinate. Finally, the minimal chemical potential is given by

$$\mu_{\perp}[f(z, t)] = \hbar\omega_r\sqrt{1 + 4a|f(z, t)|^2} \quad (2.33)$$

leading to the effective equation of motion for the axial wave function

$$i\hbar\partial_t f(z, t) = \left[-\frac{\hbar^2}{2M}\partial_z^2 + \frac{1}{2}M\omega_z^2 z^2 + \hbar\omega_r\sqrt{1 + 4a|f(z, t)|^2} \right] f(z, t). \quad (2.34)$$

As demonstrated in Refs. [143–145], equation (2.34) provides accurate results in the dimensionality crossover regime and in the limit of large chemical potentials, thus describing the axial dynamics of cigar-shaped BECs in a very good approximation to the 3D GPE. It is worth mentioning that in the weakly-interacting limit, $4a|\psi|^2 \ll 1$, Eq. (2.34) is reduced to the usual 1D GPE with a cubic nonlinearity, characterized by an effective 1D coupling constant $g_{1D} = 2a\hbar\omega_r$ (see, e.g., discussion and references in Ref. [5]). This is consistent with the picture that the interaction leads to a modification of the width in the transversal direction and that for small densities this modification can be neglected.

Non-polynomial Schrödinger Equation

The second approach for determining σ makes use of the fact that the 3D GPE (2.6) can be obtained by using the quantum least action principle, i.e., Eq. (2.6) is the Euler-Lagrange equation of the functional

$$S = \int dt d\mathbf{r} \phi^*(\mathbf{r}, t) \left[i\hbar\partial_t + \frac{\hbar^2}{2M}\nabla^2 - V_{\text{ext}}(\mathbf{r}) - \frac{g}{2}|\phi(\mathbf{r}, t)|^2 \right] \phi(\mathbf{r}, t). \quad (2.35)$$

Substitution of the ansatz (2.26,2.30) and integration along x and y leads to the action functional

$$S = \int dt dz f^*(z, t) \left[i\hbar\partial_t + \frac{\hbar^2}{2M} \partial_z^2 - \frac{1}{2} M\omega_z^2 z^2 - \frac{g}{2} \frac{1}{2\pi(\sigma[f(z, t)])^2} |f(z, t)|^2 \right. \\ \left. - \frac{\hbar^2}{2M(\sigma[f(z, t)])^2} - \frac{M\omega_r^2}{2} (\sigma[f(z, t)])^2 \right] f(z, t) \quad (2.36)$$

The Euler-Lagrange equation with respect to f^* then reads

$$i\hbar\partial_t f(z, t) = \left[-\frac{\hbar^2}{2M} \partial_z^2 + \frac{1}{2} M\omega_z^2 z^2 + g \frac{1}{2\pi(\sigma[f(z, t)])^2} |f(z, t)|^2 + \frac{\hbar^2}{2M(\sigma[f(z, t)])^2} \right. \\ \left. + \frac{M\omega_r^2}{2} (\sigma[f(z, t)])^2 \right] f(z, t). \quad (2.37)$$

σ can be determined by the corresponding Euler-Lagrange equation with respect to σ leading to

$$\frac{g}{2} \frac{1}{2\pi(\sigma[f(z, t)])^3} |f(z, t)|^2 + \frac{\hbar^2}{2M(\sigma[f(z, t)])^3} - \frac{M\omega_r^2}{2} \sigma[f(z, t)] = 0 \quad (2.38)$$

with a one to one correspondence between σ and f

$$(\sigma[f(z, t)])^2 = a_r \sqrt{1 + 2a|f(z, t)|^2}. \quad (2.39)$$

Note, Eq. (2.32), which determines the width within the Gerbier approach, has got a similar form but a factor of 4a instead of 2a, which we obtain here. Finally, one obtains the following effective 1D equation

$$i\hbar\partial_t f(z, t) = \left[-\frac{\hbar^2}{2M} \frac{\partial^2}{\partial z^2} + \frac{1}{2} M\omega_z^2 z^2 + \hbar\omega_r \frac{\sqrt{1 + 3a|f(z, t)|^2}}{\sqrt{1 + 2a|f(z, t)|^2}} \right] f(z, t). \quad (2.40)$$

In the low density limit this model is reduced to Eq. (2.25).

Equations (2.34,2.40) have been used in studies of dark solitons in the dimensionality crossover between 1D and 3D, yielding excellent quantitative agreement with experimental observations [110, 112, 140]. The results of both equations were similar. In general one would expect equations (2.34) to provide better results in the limit of large chemical potentials since it was derived by minimizing the chemical potential and equation (2.40) for larger aspect ratio ω_z/ω_r of the trap frequencies since it was determined by minimizing the energy. The investigation of the oscillation frequencies of dark solitons in the quasi-1D regime revealed differences between experimental results and the prediction of Eq. (2.25), which could be explained by applying equation (2.34) or (2.40). However, qualitatively the results of the 1D GPE were correct. We note in passing that for negative a Eqs. (2.34) and (2.40) collapse for sufficiently large densities due to the negative discriminant and indeed such a collapse of an attractive BEC was observed experimentally [221, 222] for larger densities. From the GPE one obtains the prediction of the collapse of the wave function out of energy considerations [1] but not directly from the equation.

2.3 Stationary Solutions of the Gross Pitaevskii Equation

In order to obtain eigensolutions of Eq. (2.6) one can write the condensate wave function as $\phi(\mathbf{r}, t) = \phi(\mathbf{r}) \exp(-i\mu t/\hbar)$ where $\mu = \partial E / \partial N$ is the chemical potential and $\phi(\mathbf{r})$ is a time independent function normalized to the total number of atoms. This ansatz leads to the steady state equation:

$$\mu\phi(\mathbf{r}) = [-\frac{\hbar^2}{2M}\nabla^2 + V_{\text{ext}}(\mathbf{r}) + g|\phi(\mathbf{r})|^2]\phi(\mathbf{r}). \quad (2.41)$$

Note, in case of $\phi(\mathbf{r})$ being the ground state wave function $\phi(\mathbf{r})$ is a real function however for excited states $\phi(\mathbf{r})$ can be complex. Let us make a few comments concerning the nature of Eq. (2.41). Eq. (2.41) is, in contrast to the Schrödinger equation, a nonlinear differential equation. Therefore a solution depends on its norm or in other words when one changes the norm of a solution the corresponding function is no longer a solution. Moreover, different solutions, solutions with different chemical potentials, do not need to be orthogonal, i.e., $1/N \int d\mathbf{r} \phi_a^* \phi_b$ can be nonzero even if ϕ_a and ϕ_b are solutions of the GPE. At first glance this seems to be surprising since the GPE was derived from quantum mechanical principles and quantum mechanics respects the orthogonality condition of different eigenfunctions. However, one has to bear in mind that the condensate wave functions ϕ are approximations to the multi particle wave functions which would be solution of the many body Schrödinger equations. The latter form a set of orthogonal solutions. In fact, even if two solutions of the GPE are not orthogonal the corresponding many body wave function $\psi_{a,b}(\mathbf{r}_1, \dots, \mathbf{r}_N) = \prod_{i=1}^N \phi_{a,b}(\mathbf{r}_i)$ are orthogonal in the thermodynamical limit (for $N \rightarrow \infty$). The scalar product of the two many body wave functions then reads $(\psi_a, \psi_b) = (1/N \int d\mathbf{r} \phi_a^* \phi_b)^N$. This quantity tends to zero for $N \rightarrow \infty$ since $1/N \int d\mathbf{r} \phi_a^* \phi_b < 1$ for $\phi_a \neq \phi_b$.

In general, there are no obvious analytical solution of Eq. (2.41). Numerically one can solve the equation for example by a Newton-Raphson method. In appendix A we describe in detail an algorithm for solving a nonlinear equation numerically. Once a solution is found one can vary the chemical potential and subsequently find a solution with a different norm. For small variations of the chemical potential one finds (in most cases) a solution of the same 'kind' (symmetry, number of nodes). Thus one can build up a continuation diagram showing the dependence of the atom number (the norm of the condensate wave function) on the chemical potential for different branches. The different branches correspond to solutions of different kinds.

2.3.1 The Ground State

Let us consider for reasons of concreteness and due to the experimental importance the external potential to be harmonic. Even in this case, there is in general no obvious analytical solution of Eq. (2.41). One can nevertheless investigate some limiting cases in order to get some insights into the shape of the ground state. For $g = 0$ equation (2.41) reduces to the linear Schrödinger equation which has the following solution for an harmonic external potential

$$\phi(\mathbf{r}) = \sqrt{N} \left(\frac{M\omega_{\text{HO}}}{\pi\hbar} \right)^{3/4} \exp\left[-\frac{M}{2\hbar}(\omega_x x^2 + \omega_y y^2 + \omega_z z^2)\right] \quad (2.42)$$

with the geometric average of the trap frequencies $\omega_{\text{HO}} = (\omega_x \omega_y \omega_z)^{1/3}$.

Let us discuss now at first the case of repulsive interaction $g > 0$. For small values of the interaction parameter one can perform a variational calculation. Therefore one replaces the trap frequencies in Eq. (2.42) by variational parameters and minimizes the energy functional (2.8) with Eq. (2.42) with substituted variational parameters as trial function [1]. This leads to a broadening of the Gaussian trial function with increasing interaction parameter g due to the increasing interaction energy. This variational calculation is valid for small values of g . For large values of g the dominant term in the energy functional (2.8) is the interaction energy. Therefore one can perform a different simplification and neglect the kinetic Laplacian term in equation (2.41) leading to the so called Thomas-Fermi (TF) approximation and the density profile

$$\rho_{\text{TF}}(\mathbf{r}) = \frac{\mu - V_{\text{ext}}}{g} \quad (2.43)$$

for $\mu > V_{\text{ext}}$ and zero elsewhere. The TF approximation is valid for large N as well. Since the interaction energy scales with N^2 whereas the kinetic energy scales with N . Therefore one can neglect for large N the kinetic term in comparison to the interaction term. In typical experimental setups the TF approximation is fulfilled very well.

For an isotropic harmonic trap $\omega = \omega_x = \omega_y = \omega_z$ the size of the condensate is thus given by the Thomas-Fermi radius $R_{\text{TF}}^2 = \frac{2\mu}{M\omega^2}$. Furthermore, one obtains due to the normalization condition a relation between the chemical potential and the atom number

$$N_{\text{TF}} = \frac{8\pi}{15} \left(\frac{2\mu}{M\omega^2} \right)^{3/2} \frac{\mu}{g}. \quad (2.44)$$

For attractive interatomic interaction $g < 0$ the width of the Gaussian (2.42) decreases with decreasing g (leading to a stronger interaction). So the density at the center tends to increase. The kinetic energy tends to balance this effect. However, above a critical atom number N_{cr} for fixed $g < 0$ the system is subject to collapse. The critical number of atoms necessary for collapse in an isotropic harmonic trap is given by $N_{\text{cr}} = 0.575 \sqrt{\hbar/M\omega^2}$ with the s-wave scattering length a . This collapse was observed experimentally as well [221, 222].

2.3.2 Excited States

The GPE (2.6) does not only describe the ground state of the condensate but collective excitations as well. We will restrict our investigations of the excited states to the effective lower dimensional setups described by equations (2.20, 2.25).

Solitonic States

The effective 1D equation (2.25) reads in the homogeneous case (without axial external potential, i.e., $\omega_z = 0$) in a dimensionless form

$$i\partial_t f(z, t) = \left[-\frac{1}{2}\partial_z^2 + s|f(z, t)|^2 \right] f(z, t) \quad (2.45)$$

with $s = \pm 1$ for repulsive and attractive interaction, respectively. After the rescaling to the dimensionless form density $|f(z, t)|^2$, length, time and energy are measured in units of $2a$, a_r ,

$1/\omega_r$ and $\hbar\omega_r$, respectively. Eq. (2.45) is the completely integrable non-linear Schrödinger (NLS) equation possessing an infinite number of conserved quantities [101, 223]. The lowest integrals of motion are the number of particles

$$N = \int dz |f(z, t)|^2, \quad (2.46)$$

the momentum,

$$P = \frac{i}{2} \int dz [f(z, t) \partial_z f^*(z, t) - f^*(z, t) \partial_z f(z, t)] \quad (2.47)$$

and the energy,

$$E = \int dz [|\partial_z f(z, t)|^2 + s|f(z, t)|^4]. \quad (2.48)$$

For attractive BECs ($s = -1$) the NLS possesses a bright soliton solution of the form [224]

$$\psi_{\text{BS}}(z, t) = \eta \operatorname{sech}[\eta(z - vt)] \exp[i(kz - \omega t)] \quad (2.49)$$

with the inverse spatial width and amplitude η of the soliton, the soliton wavenumber k , frequency

$$\omega = \frac{1}{2}(k^2 - \eta^2) \quad (2.50)$$

and velocity $v \equiv \partial\omega/\partial k = k$. Note, the soliton is characterized by only two independent parameters.

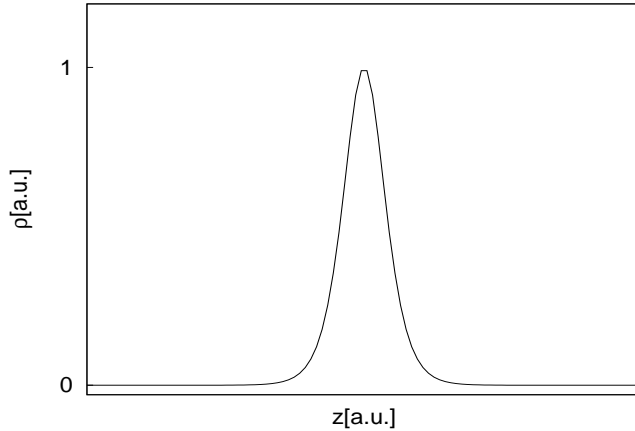


Figure 2.4: Density profile of a bright soliton.

Fig. 2.4 shows the density profile of a bright soliton in arbitrary units. A bright soliton is a localized wave packet with a width characterized by the condensates healing length ξ .

Evaluation of the conserved quantities (2.46-2.48) for a bright soliton solution leads to

$$N = 2\eta \quad (2.51)$$

$$P = 2\eta k \quad (2.52)$$

$$E = \eta k^2 - \frac{1}{3}\eta^3 \quad (2.53)$$

implying that a bright soliton behaves like a classical particle with mass

$$M_{\text{BS}} = 2\eta, \quad (2.54)$$

momentum

$$P_{\text{BS}} = Mv, \quad (2.55)$$

and energy

$$E_{\text{BS}} = \frac{1}{2}Mv^2 - \frac{1}{24}M^3. \quad (2.56)$$

The first term in the energy can be associated to its kinetic energy and the second one to the binding energy of the quasi-particles associated to the soliton. Another indicator for the particle like behavior of a bright soliton is given by the relation

$$\frac{\partial E_{\text{BS}}}{\partial P_{\text{BS}}} = v. \quad (2.57)$$

In practice this particle like behavior is reflected in the fact that the soliton propagates without changing its shape. One can consider a bright soliton as a wave packet where the dispersion of the wave packet due to the kinetic term is balanced by the nonlinear term. This fact leads to a surprisingly stable state. For small perturbations the functional form of the soliton is conserved and the perturbation leads only to a modification of the parameters of the soliton.

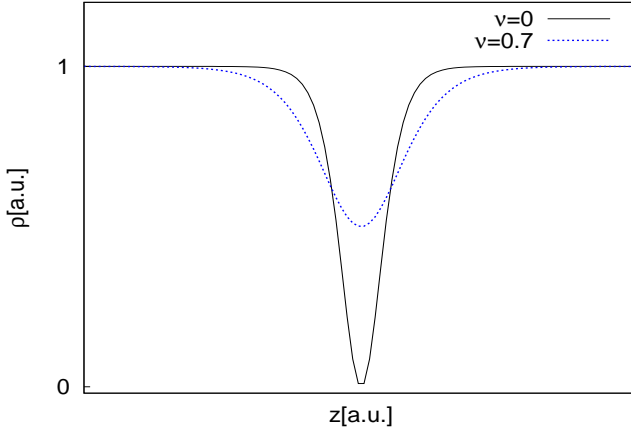


Figure 2.5: Density profile of a black (solid line) and a grey (dashed line) soliton.

For repulsive BECs ($s = 1$) the NLS supports dark soliton solutions on a homogeneous background $\psi = \sqrt{n_0} \exp(-i\mu t)$. Here we assumed for reasons of simplicity that the back-

ground is at rest. Then a single dark soliton solution has the form [225],

$$\psi_{\text{DS}}(z, t) = \sqrt{n_0} [iA + B \tanh(\eta)] \exp(-i\mu t), \quad (2.58)$$

where $\eta = \sqrt{n_0}B[z - z_0(t)]$, $z_0(t) = vt + z_0$ is the soliton center, z_0 an arbitrary real constant representing the initial location of the soliton, v is the relative velocity between the soliton and the background given by $v = dz_0/dt = \sqrt{n_0}A$, the parameter $B \equiv \sqrt{1 - A^2}$ sets the soliton depth given by $\sqrt{n_0}B$. One can introduce the soliton phase angle ϕ by the relations $A = \sin \phi$ and $B = \cos \phi$. This clarifies that the dark soliton possesses two independent parameters: the phase ϕ defining the soliton width, velocity and depth and the chemical potential μ defining the background phase and density. Note that for $A = 0$ the dark soliton becomes a black soliton (alias a stationary kink), with the following representation

$$\psi_{\text{black}} = \sqrt{n_0} \tanh(\sqrt{n_0}z) \exp(-i\mu t). \quad (2.59)$$

The black soliton has a π phase jump across its density minimum. The magnitude of the phase jump decreases with decreasing depth of the soliton. This phase jump across the soliton density minimum is exploited for generating dark solitons experimentally by the phase-imprinting method. Therefore a phase jump is imprinted in the condensate by illuminating part of the condensate by a short laser pulse. Subsequently the corresponding density profile is formed by itself. This underlines the stability of a soliton. In Fig. 2.5 examples of the density profiles of a black soliton and a grey soliton (a soliton with finite velocity) are illustrated. The grey soliton has a smaller depth and larger width compared to the black soliton.

When evaluating the integrals of motion (2.46-2.48) one has to bear in mind that these refer to the background and the soliton. Therefore one may follow the lines of Ref. [101] and renormalize the integrals of motion. For a detailed calculation how to determine the integrals of motion we refer to the review article [101]. In conclusion one obtains similar to the case of the bright soliton that the dark soliton behaves like a classical particle, for example it obeys the relation

$$\frac{\partial E_{\text{DS}}}{\partial P_{\text{DS}}} = v. \quad (2.60)$$

Moreover, one can associate the dark soliton to an effective mass

$$M_{\text{DS}} = \frac{\partial P_{\text{DS}}}{\partial v} = -4\sqrt{n_0}B \quad (2.61)$$

showing that the dark soliton is characterized by a negative effective mass. Pictorially speaking, this can be understood by the fact that the dark soliton represent a lack in the background density.

Aside from the single-dark-soliton, multiple dark soliton solutions of the cubic NLS equation are also available [225–227]. In the simplest case of a two-soliton solution, with the two solitons moving with opposite velocities, $A_1 = -A_2 = A$, the wave function can be expressed as [227] (see also Ref. [228]):

$$\psi_{\text{2sol}}(z, t) = \frac{F(z, t)}{G(z, t)} \exp(-i\mu t), \quad (2.62)$$

with $F = 2(n_0 - 2n_{\min}) \cosh(T) - 2n_0 A \cosh(Z) + i \sinh(T)$, $G = 2\sqrt{n_0} \cosh(T) + 2\sqrt{n_{\min}} \cosh(Z)$,

while $Z = 2\sqrt{n_0}Bz$, $T = 2\sqrt{n_{\min}(n_0 - n_{\min})}t$, and $n_{\min} = n_0 - n_0B^2 = n_0A^2$ is the minimum density (i.e., the density at the center of each soliton).

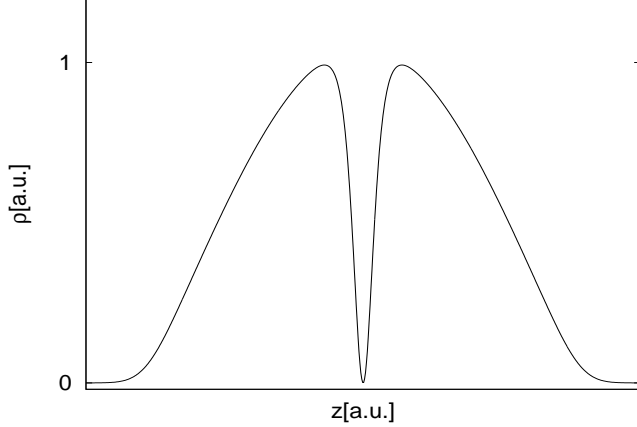


Figure 2.6: Density profile of a solitonic state in a harmonically confined condensate.

In the case of an external potential, leading to an inhomogeneous condensate background, there does not exist an analytical soliton solution anymore. However, the existence and dynamics of matter-wave dark solitons can be studied analytically by applying perturbation theory methods, assuming that the trapping potential is smooth and slowly varying on the soliton scale. Then one can make a local density like approximation and replace the constant background wave function $\psi_0 = \sqrt{n_0}$ by the corresponding background wave function ψ_{bg} . The shape of the background wave function is given by the ground state wave function of the condensate in the external potential. Fig. 2.6 illustrates the density of a condensate confined in a harmonic potential carrying a stationary black soliton. The corresponding wave function can be approximated by the product of the background wave function and a wave function describing the soliton

$$\psi(z) = \psi_{\text{bg}}(z)\psi_{\text{DS}}(z)\exp(-i\mu t). \quad (2.63)$$

For large chemical potentials one can approximate the background wave function by the Thomas-Fermi solution $\psi_{\text{bg}}(z) = \sqrt{(\mu - \frac{1}{2}M\omega_z^2 z^2)/g}$. The Thomas Fermi solution can be considered as constant close to the center of the trap (for small z) for large chemical potentials. Therefore $\psi_{\text{DS}}(z)$ can be approximated by the wave function of a dark soliton on a constant background with density $n_0 = \mu/g$ for large chemical potentials. One can use this ansatz as initial condition to find the exact eigenstate numerically by an iterative solver and afterwards perform a continuation in the chemical potential in order to find the corresponding solution for smaller chemical potentials.

Alternatively, one can start a continuation from the linear limiting case, the case of small atom numbers and chemical potentials as well. In the case of negligible nonlinearity (for $N \rightarrow 0$) the dark soliton state can be approximated by the first excited state of the linear problem (the problem without the nonlinear term) with the chemical potential being defined by the energy of the state. Using this state as initial state for an iterative solver one can find numerically the exact soliton state and subsequently one can perform numerically a continuation in the chemical potential towards larger values of the chemical potential. In the same manner one

can find the two (three, ...) soliton state by starting with the second (third, ...) excited state of the linear problem. For the case of a 1D harmonic trap there do not exist nonlinear states without a linear counterpart. Therefore one can find each nonlinear state by performing a continuation in the chemical potential (atom number) from the corresponding linear state. However, this situation changes for more complicated potentials, e.g., a double-well potential as we show in Chapter 5.

Vortices

In the higher dimensional cases the NLS equation is not longer integrable. However, in the 2D repulsive case Eq. (2.20) possesses excited stationary solutions of the form (in units so that $\hbar = M = 1$)

$$\psi_{\text{vor}}(r, \theta, t) = \psi_{\text{bg}}(r)U(r) \exp(iS\theta - i\mu t) \quad (2.64)$$

for a rotationally symmetric harmonic external potential; r and θ are the polar coordinates. $\psi_{\text{bg}}(r)$ denotes the background density defined by the external potential. The wave function (2.64) is an eigenstate of the angular momentum operator with $l_z = S$, so that it carries a total angular momentum $L_z = NS$. The wave function represent a gas rotating around the z -axis with tangential velocity

$$v_s = \frac{s}{r} \quad (2.65)$$

leading to the circulation of the velocity field over a closed contour around the z -axis

$$\int \mathbf{v}_s d\mathbf{l} = 2\pi S, \quad (2.66)$$

which is quantized and independent on r .

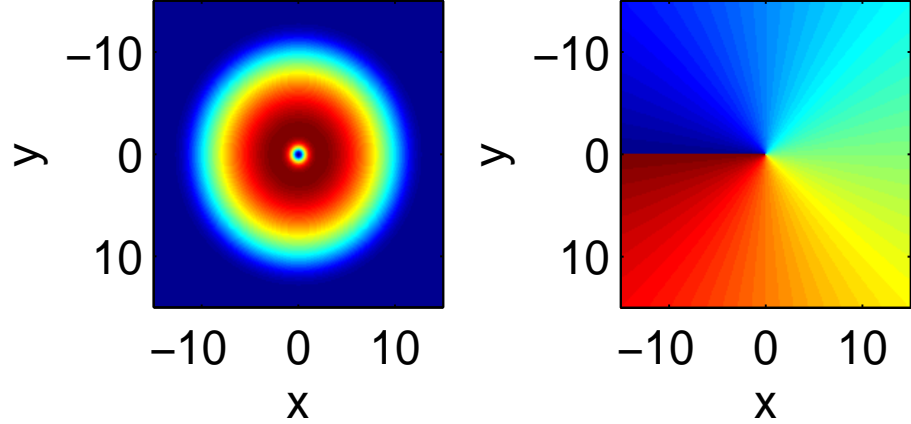


Figure 2.7: Density (left) and phase (right) of a singly charged vortex. Left panel: Blue represents zero density and red maximal. Right panel: Blue to red represents a phase from 0 to 2π .

$U(r) \exp(iS\theta)$ is called a vortex with vorticity S . Vortices are characterized by their non-zero topological charge or vorticity S whereby the phase of the wave function has a phase jump of $2\pi S$ along a closed contour surrounding the core of the vortex as shown by Eq. (2.66).

The Equation for U takes the form

$$\partial_r^2 U(r) + \frac{1}{r} \partial_r U - \frac{S^2}{r^2} U(r) + [\mu - V(r) - U^2(r)] U(r) = 0 \quad (2.67)$$

with the boundary conditions $U(0) = 0$ and $U(\infty) = \sqrt{\mu}$. Unfortunately, one can not solve the differential equation (2.67) for $U(r)$ analytically. In contrast to the soliton case this is even impossible for the homogeneous case $V = 0$. However, one can predict the asymptotical behavior of the vortex profile from equation (2.67): $U(r) \sim r^{|S|}$ for $r \rightarrow 0$ and $U(r) \sim \sqrt{\mu} - S^2/(2r^2)$ as $r \rightarrow \infty$. The width of a single charged vortex is of the order of the healing length of the condensate, while higher charged vortices have a wider width.

In the linear limiting case ($|\psi|^2 \rightarrow 0$), a state analogous to the vortex state can be seen in a superposition of the two energetically degenerate first excited states, i.e., the wave function is given by one of the states plus the imaginary unit times the other state. In the nonlinear case a vortex state can be found by performing a continuation from such a linear state. Fig. 2.7 shows a contour plot of the density and the phase of a singly charged vortex in a harmonically confined condensate. The shape of the density for large distances from the center is given by the background wave function. For a large distance from the center, the density increases with decreasing distance to the center monotonically. Without a vortex this would hold for the whole condensate. However, due to the vortex located at the center of the condensate, the density vanishes at the center. The phase modulation of the condensate's wave function is granted by the relation of the vortex.

Singly charged vortices are extremely robust due to their inherent topological charge. The 2π phase jump cannot be eliminated by continuous deformations of the density profile, unless the density of the background condensate is close to zero. Therefore one can, for systems where the typical length scale is larger than the width of the vortex, often treat a vortex as a particle localized at the center of the vortex. Pictorially speaking, as long as one does not need to resolve the inner structure of the vortex one can treat the vortex as a point-like particle, similar to the case of solitons. However, due to the long range phase relation of the vortex states it turns out that there occur crucial differences for the dynamics of dark solitons and vortices, despite their similar density profiles.

2.4 Small-Amplitude Excitations and Bogoliubov Analysis

Let us now consider small amplitude excitations on eigenstates of the 3D GPE (2.6). This allows to analyze the stability of the nonlinear modes of Eq. (2.6). In particular, once a numerically exact — up to a prescribed tolerance — stationary state, $\psi_0(\mathbf{r})$, is found (e.g., by a Newton-Raphson method), we consider small perturbations of this state of the form,

$$\psi(\mathbf{r}, t) = [\psi_0(\mathbf{r}) + \epsilon \left(u(\mathbf{r}) e^{-i\omega t} + v^*(\mathbf{r}) e^{i\omega^* t} \right)] e^{-i\mu t}, \quad (2.68)$$

where ϵ is a small number. Substitution of the ansatz (2.68) in (2.6) leads in first order in ϵ to the following system of equations.

$$[\hat{H}_0 - \mu + 2g|\psi_0(\mathbf{r})|^2]u(\mathbf{r}) + g\psi_0(\mathbf{r})^2v(\mathbf{r}) = \hbar\omega u(\mathbf{r}), \quad (2.69)$$

$$[\hat{H}_0 - \mu + 2g|\psi_0(\mathbf{r})|^2]v(\mathbf{r}) + g[\psi_0^*(\mathbf{r})]^2u(\mathbf{r}) = -\hbar\omega v(\mathbf{r}), \quad (2.70)$$

In the case of the effective 1D and 2D equations (2.20,2.25) one has to replace the coupling coefficient g by the corresponding effective coupling coefficient and the 3D Laplacian by the corresponding lower dimensional operator. Equations (2.69-2.70) are known as the Bogoliubov-de Gennes (BdG) equations (see, e.g., Ref. [2]). Note, equations (2.69-2.70) are nonlinear in ψ_0 but linear in u, v . However, ψ_0 is the (known) solution of the 3D GPE. Therefore one needs to solve a linear system of equations for the stability analysis, i.e., diagonalize in this case a anti-hermitian matrix

$$\mathbf{M} = \begin{pmatrix} L_1 & L_2 \\ -L_2^* & -L_1 \end{pmatrix},$$

where $L_1 = \hat{H}_0 - \mu + 2g|\psi_0(\mathbf{r})|^2$ and $L_2 = g\psi_0(\mathbf{r})^2$. Solving equations (2.69,2.70) by diagonalizing the above matrix, we determine the eigenfrequencies $\omega \equiv \omega_r + i\omega_i$ and the amplitudes u and v of the normal modes of the system. Note that if ω is an eigenfrequency of the Bogoliubov spectrum, so are $-\omega$, ω^* and $-\omega^*$ (due to the Hamiltonian nature of the system; this can be used as a test for the correctness of the numerical code). Consequently, the occurrence of a complex eigenfrequency always leads to a dynamic instability due to the presence of a real and positive exponent in equation (2.68) leading to an exponential increase of the initially small perturbation. Thus, a linearly stable configuration is tantamount to $\omega_i = 0$, i.e., all eigenfrequencies being real.

An important quantity resulting from the BdG analysis is the amount of energy carried by the normal mode with eigenfrequency ω , namely

$$E = \int d\mathbf{r}(|u(\mathbf{r})|^2 - |v(\mathbf{r})|^2)\hbar\omega. \quad (2.71)$$

The sign of this quantity, known as *Krein sign* [229], is a topological property of each eigenmode. Modes with negative energy (Krein sign) are called *anomalous modes* (see, e.g., Sec. 5.6 of Ref. [2]). The presence of anomalous modes in the excitation spectrum is a direct signature of an energetic instability, which is particularly relevant to the case of vortices and dark solitons [118]. Importantly, if the normal mode eigenfrequencies with opposite energy (Krein) signs become resonant then, in most cases, there appear complex frequencies in the excitation spectrum, i.e., a dynamical instability occurs [229]. In order to further elaborate on such a possibility, it is relevant to note that modes with complex or imaginary frequencies carry zero energy (due to the condition $(\omega - \omega^*) \int dz(|u|^2 - |v|^2) = 0$, which must hold for each BdG mode).

Let us make at this point some comments concerning anomalous modes in general, which we found empirically in this work. In the case of solitonic and vortex states the number of anomalous modes plus oscillatory unstable modes (appearing due to collisions of anomalous modes with normal modes) is equal to the number of solitons or vortices, respectively. The BdG spectrum is in the linear limit equal to the spectrum of the linear problem. Then one can assign to each Bogoliubov mode an eigenstate of the linear spectrum. Consequently, if one calculates the BdG spectrum of an excited state, modes corresponding, in the linear limit, to lower excited states occur as well. These modes have got a negative energy.

One can obtain a physical interpretation of the individual Bogoliubov modes by perturbing the GPE eigenstate with the corresponding mode and propagate this state, which is no

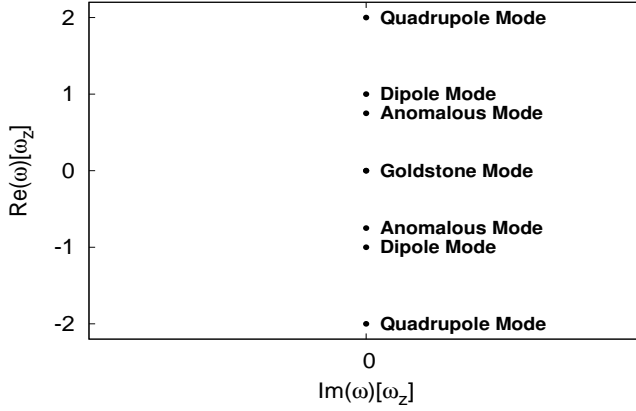


Figure 2.8: The lowest characteristic eigenfrequencies of the Bogoliubov excitation spectrum for a dark soliton state confined in a harmonic trap with frequency ω_z .

longer an eigenstate, in time using the time dependent GPE. A typical example for the lowest eigenvalues of the BdG spectrum of a single dark soliton state supported by a harmonically confined condensate is shown in Fig. 2.8. All eigenvalues are real, showing that the state is dynamically stable, i.e., small perturbations remain small. There exist a pair of zero eigenvalues. The mode corresponding to these is called Goldstone mode. It is connected to the fact that the GPE is gauge invariant (which is reflected in the norm conservation as well) and should always be present for norm conserving systems (another test). The second lowest eigenvalues have got a negative energy according to the definition (2.71). It is connected to the oscillation of the soliton around the center of the trap. Perturbing the eigenstate with the corresponding mode leads to an oscillation of the soliton around the center with the oscillation frequency being determined by the magnitude of the eigenvalue. Since the eigenvalue is real, the amplitude of the oscillation is constant and determined by the initial state. If the eigenvalue was complex the amplitude would increase. The magnitude of the third eigenvalue is determined by the trap frequency. The corresponding mode is called dipole mode (or Kohn mode) and the perturbation of the eigenstate with the corresponding mode leads to an oscillation of the whole condensate with the trap frequency. The value of the dipole mode is independent of the nonlinearity and thus of the chemical potential. Therefore this excitation is often used in experiments as a way to determine the harmonic frequencies of the trap. Finally, the mode at $2\omega_z$ corresponds to the quadrupole mode and is independent of the chemical potential as well. Note, the oscillation frequency of the soliton is smaller than the trap frequency and is therefore the lowest excitation of the system. If the condensate is in its ground state the lowest excited mode is the dipole mode.

Chapter 3

Collisionally Inhomogeneous Bose-Einstein Condensates in Double-Well Potentials

In this chapter, we consider quasi-one-dimensional BECs, with spatially varying collisional interactions, trapped in double-well potentials. In particular, we study a setup in which such a “collisionally inhomogeneous” BEC has the same (attractive-attractive or repulsive-repulsive) or different (attractive-repulsive) type of interparticle interactions. As, arguably, one of the simplest forms of this combination, we select a coefficient of the nonlinearity which is piecewise constant, in line with the suggestions of [82, 95, 230] and can vary between two (smoothly connected) pieces with the same sign, or even two pieces with opposite signs. The latter form of a spatially dependent nonlinearity appears to be one that should be straightforwardly experimentally realizable [231], through the use of magnetic field gradients of moderate size for atom chips (see also the relevant discussion in [230]). The phenomenology that we observe in this setting appears to be *remarkably different* from that of the standard double-well. In particular, as was detailed in Ref. [48], the linear states of the underlying potential can be continued into nonlinear ones in the presence of the pertinent cubic nonlinearity. As prototypical examples of these linear states one can consider the symmetric ground state and the anti-symmetric first excited state of the double-well potential. A remarkable feature, however, which takes place for sufficiently strong nonlinearity (to the symmetric state for attractive interactions and to the anti-symmetric state for repulsive interactions) is a symmetry-breaking bifurcation of the pitchfork type. This bifurcation generates two new asymmetric solutions (which exist for sufficiently large nonlinearity). What we find here is that even a weak inhomogeneity in the collisional properties of the condensate changes the nature of this bifurcation from a pitchfork to a saddle-node one. This may be anticipated given the “non-parametrically robust” nature of the pitchfork bifurcation which will yield similar changes in the presence of different asymmetries (see also [48]). In addition to that, increasing the inhomogeneity strength shifts (eventually to infinity) the turning point of the saddle-node bifurcation. Thus, for sufficiently large variation of the nonlinear coefficient between the two wells, only two nonlinear states emanate from the ground and first excited states of the linear problem. Furthermore, for one of these states, the monotonicity of the number of particles changes as a function of its nonlinear eigenvalue parameter (i.e., the chemical potential). This is a rather unusual feature that leads to a bifurcation diagram entirely different from those of the homogeneous interatomic interactions (i.e., homogeneous nonlinearity) limit of either the one-component [48] or of the multi-component system (see e.g., [53]).¹ These traits are captured accurately, as we will show below, by a two-mode, Galerkin-type approximation [47, 48]

¹We note in passing that for the multi-component system the diagram is also substantially different (in that case, more involved) than that of the single component one, due to the presence of “mixed states”, mixing the symmetric and anti-symmetric nonlinear states of *each* of the two components (and bifurcations thereof).

applied to the present collisionally inhomogeneous double-well setting. The content of this chapter has been published partly in Ref. [232].

The chapter is structured as follows. The model and the semi-analytical predictions regarding its stationary solutions are presented in section 3.1. Our corresponding directly numerical findings and their comparison with the analysis are given in section 3.2. In section 3.3, we present an alternative theoretical viewpoint more akin to the model dynamics and compare its results to the full results of the partial differential equation. Finally, in section 3.4, we present a brief summary of the chapter.

3.1 The Model and its Semi-Analytical Consideration

We investigate in this chapter the dynamics of a quasi one-dimensional (1D) condensate. The dynamics of a quasi 1D condensate, oriented along the x -axis, can be described by the following GP equation (cf. section 2.2.2),

$$i\hbar\partial_t\Psi = \left(-\frac{\hbar^2}{2m} + V(x) + g|\Psi|^2 - \mu\right)\Psi, \quad (3.1)$$

where $\Psi(x, t)$ is the mean-field order parameter, m is the atomic mass, and μ is the chemical potential of the effectively 1D system. The nonlinear coefficient g arises from the interatomic interactions and has an effective 1D form, namely $g = 2\hbar\omega_{\perp}a$, where ω_{\perp} is the transverse confining frequency and a is the three-dimensional (3D) s-wave scattering length (the cases $a > 0$ or $a < 0$ correspond, respectively, to repulsive or attractive interatomic interactions). The external potential $V(x)$ in the GP Eq. (3.1) consists of a regular harmonic trap and a repulsive potential localized at the harmonic trap center, namely,

$$V(x) = \frac{1}{2}m\omega_x^2x^2 + V_0\operatorname{sech}^2\left(\frac{x}{w_B}\right), \quad (3.2)$$

where ω_x is the longitudinal confining frequency, while V_0 and w_B are, respectively, the strength and width of the localized potential; the latter is in fact a barrier potential that may be created by a blue-detuned laser beam, repelling the atoms in the condensate. It is clear that the combination of the harmonic trap and the barrier potential is in fact a double-well potential.

Moreover, we assume that the collisional properties of the condensate are spatially inhomogeneous, i.e., $a = a(x)$ (cf. section 2.1.3), with the function $a(x)$ taking different, but smoothly connected, values in the two wells of the external potential. In particular, we consider that an external magnetic or optical field modifies the scattering length of the condensate as follows,

$$a(x) = a_0 + a_1\tanh\left(\frac{x}{W}\right), \quad (3.3)$$

where a_0 and a_1 are constant values of the condensate's scattering length in the absence and in the presence of the external field, respectively, which are smoothly connected through the tanh function (here, W is the spatial length scale on which the transition between the two values a_0 and a_1 takes place). Apparently, far away from the harmonic trap center at $x = 0$ (or, in other words, far away from the barrier), the scattering length takes the values

$a = a_0 \pm a_1$, for $x \rightarrow \pm\infty$ respectively. Such an inhomogeneity of the scattering length may be realized in practice upon employing a bias homogeneous field and imposing a steep localized gradient on top of it. In such a case, in a quasi 1D configuration (as is the case under consideration) this will lead to a constant scattering length with value $a = a_1$ in the left well, which is followed by a localized change of a , finally ending up with a second value $a = a_2$ in the right well. Notice that in our model we choose the function \tanh to analytically describe the transition between these different constant values of a since there are no ideal steps, but rather close approximations to it. Also, we naturally assume that we are relatively close to a Feshbach resonance, in order to easily manipulate the scattering length with the external field.

Next, measuring time in units of the inverse transverse trapping frequency ω_\perp^{-1} , length in units of the transverse oscillator length $l_\perp \equiv \sqrt{\hbar/m\omega_\perp}$, energy in units of $\hbar\omega_\perp$, and introducing the normalized wave function $u(x, t) = (2|a_r|)^{1/2}\Psi(x, t)$ (where a_r is a reference value of the scattering length), we reduce the GP Eq. (3.1) to the following dimensionless form:

$$i\partial_t u = Hu + \Gamma(x)|u|^2u - \mu u. \quad (3.4)$$

In the above equation,

$$H \equiv -\frac{1}{2}\partial_x^2 + V(x) \quad (3.5)$$

is the “single-particle” operator in the normalized external potential

$$V(x) = \frac{1}{2}\Omega^2 x^2 + V_0 \operatorname{sech}^2\left(\frac{x}{w}\right), \quad (3.6)$$

with $\Omega \equiv \omega_x/\omega_\perp$ being the normalized harmonic trap strength and $w = w_B/l_\perp$. The nonlinearity coefficient $\Gamma(x)$ in Eq. (3.4) is given by

$$\Gamma(x) = \alpha + \beta \tanh(bx), \quad (3.7)$$

where $\alpha = a_1/|a_r|$, $\beta = a_2/|a_r|$, and $b = l_\perp/W$. Apparently, the cases $\Gamma > 0$ or $\Gamma < 0$ correspond to repulsive or attractive interactions, respectively. We finally mention that the number of particles in the condensate \mathcal{N} is now defined as $\mathcal{N} = (l_\perp/2|a_r|)N$, where

$$N = \int_{-\infty}^{+\infty} |u(x, t)|^2 dx \quad (3.8)$$

is an integral of motion (normalized number of particles) of the GP Eq. (3.4). Also, in our analysis (and particularly in the typical numerical results that will be presented below) we will assume fixed parameter values $\Omega = 0.1$, $V_0 = 1$, $w = 0.5$ and $b = 1$.

In the non-interacting limit [i.e., for $\Gamma(x) = 0$], the spectrum of the underlying linear Schrödinger equation consists of a ground state, $u_0(x)$, and excited states, $u_l(x)$ ($l \geq 1$). Our analytical investigation of the nonlinear problem (at the stationary level) in the weakly nonlinear regime consists of applying a Galerkin-type, two-mode approximation to Eq. (3.4). In particular, we assume that the wave function $u(x, t)$ can be decomposed as

$$u(x, t) = c_0(t)u_0(x) + c_1(t)u_1(x), \quad (3.9)$$

where $c_0(t)$ and $c_1(t)$ are unknown time-dependent complex prefactors. Substituting Eq. (3.9) into Eq. (3.4) and projecting the resulting equation to eigenfunctions u_0 and u_1 , we obtain the following equations:

$$\begin{aligned} i\dot{c}_0 = & (\omega_0 - \mu)c_0 + A_0|c_0|^2c_0 + D_0(2|c_0|^2c_1 + c_0^2c_1^*) \\ & + B(2|c_1|^2c_0 + c_1^2c_0^*) + D_1|c_1|^2c_1, \end{aligned} \quad (3.10)$$

$$\begin{aligned} i\dot{c}_1 = & (\omega_1 - \mu)c_1 + A_1|c_1|^2c_1 + D_1(2|c_1|^2c_0 + c_1^2c_0^*) \\ & + B(2|c_0|^2c_1 + c_0^2c_1^*) + D_0|c_0|^2c_0. \end{aligned} \quad (3.11)$$

In these equations, dots denote time derivatives, stars denote complex conjugates, and $\omega_{0,1}$ are the eigenvalues corresponding to the eigenstates $u_{0,1}$; in the numerical examples presented herein, ω_0 and ω_1 can be numerically found to be 0.133 and 0.156 respectively. We should note in passing here that although $\omega_{0,1}$ and $u_{0,1}$ are numerically obtained through a simple eigensolver of the underlying linear Schrödinger problem, it is also, in principle, possible to develop a perturbative approach towards obtaining such eigenvalues and eigenvectors following the work of [233], rendering our semi-analytical approach developed below more proximal to a fully analytical one. The overlap integrals $A_0 = \int \Gamma(x)u_0^4(x)dx$, $A_1 = \int \Gamma(x)u_1^4(x)dx$, $B = \int \Gamma(x)u_0^2(x)u_1^2(x)dx$, $D_0 = \int \Gamma(x)u_0^3(x)u_1(x)dx$ and $D_1 = \int \Gamma(x)u_0(x)u_1^3(x)dx$ are constants. Notice that $u_0(x)$ and $u_1(x)$ are both real functions (due to the Hermitian nature of the underlying linear Schrödinger problem) and are also orthonormal. In what follows, in the definition of $\Gamma(x)$ in Eq. (3.7), we will set

$$\alpha + \beta = -1, \quad \alpha - \beta = -1 + \varepsilon, \quad (3.12)$$

with $0 \leq \varepsilon \leq 2$, as shown in the left panel of Fig. 3.1. Notice that in the limiting case $\varepsilon = 0$, the nonlinearity coefficient takes a constant value, $\Gamma(x) = -1$, and the problem is reduced to the study of a collisionally homogeneous condensate with attractive interatomic interactions in a double-well potential; this problem was studied in detail in Ref. [48] by means of the considered two-mode approximation for both symmetric and asymmetric double-well potentials. As a result of this choice and of fixing the rest of the parameters, the above overlap integrals A_0 , A_1 , B , D_0 and D_1 are functions of ϵ and their dependence on this parameter is shown in the right panel of Fig. 3.1.

We now introduce in Eqs. (3.10-3.11) the amplitude-phase variables $c_j = \rho_j e^{i\varphi_j}$, $j = 0, 1$ (the functions ρ_j and φ_j are assumed to be real and are time-dependent) and derive from Eqs. (3.10) and (3.11) the equations for ρ_0 and φ_0 :

$$\dot{\rho}_0 = B\rho_0\rho_1^2 \sin(2\varphi) + (D_0\rho_0^2\rho_1 + D_1\rho_1^3) \sin(\varphi), \quad (3.13)$$

$$\dot{\varphi}_0 = (\mu - \omega_0) - A_0\rho_0^2 - B(2\rho_1^2 + \rho_1^2 \cos(2\varphi)) - (3D_0\rho_0\rho_1 + D_1\frac{\rho_1^3}{\rho_0}) \cos(\varphi), \quad (3.14)$$

where $\varphi = \varphi_0 - \varphi_1$ is the relative phase between the two modes. The equations for ρ_1 and φ_1 can directly be obtained by interchanging indices 1 and 0 in Eqs. (3.13) and (3.14).

Focusing on real solutions of Eq. (3.4), we consider the steady solutions, i.e., $\dot{\rho}_0 = \dot{\varphi}_0 = 0$ [associated to the fixed points of the dynamical system of Eqs. (3.13-3.14)], with $\varphi = k\pi$ with k an integer. In such a case, the equations for ρ_0 [Eq. (3.13)] and ρ_1 are automatically satisfied, while the equations for φ_0 [Eq. (3.14)] and φ_1 are reduced to the following algebraic

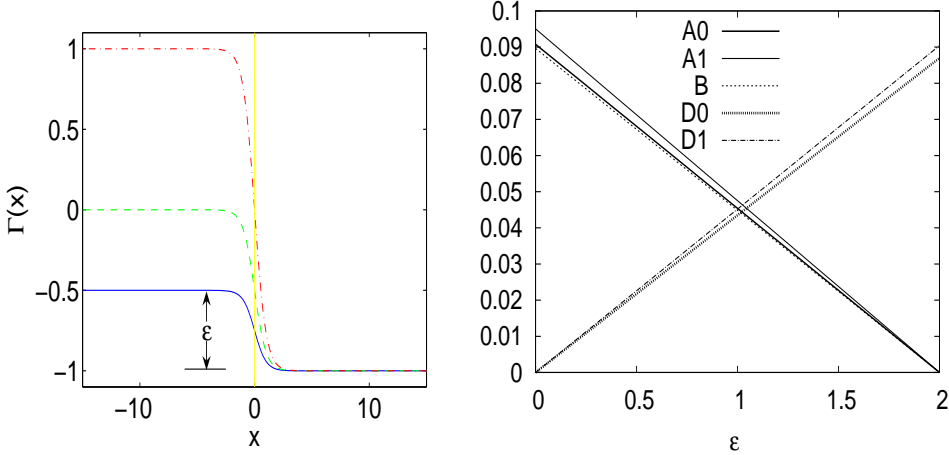


Figure 3.1: Left panel: The nonlinearity coefficient $\Gamma(x) = \alpha + \beta \tanh(bx)$ with parameters $\alpha + \beta = -1$, $\alpha - \beta = -1 + \epsilon$, and $b = 1$. The panel displays some examples of the shape of $\Gamma(x)$ for different values of ϵ (i.e., the inhomogeneity parameter): $\epsilon = 0.5$ (blue solid line), $\epsilon = 1$ (green dashed line) and $\epsilon = 2$ (red dashed-dotted line.) Right Panel: The dependence of the overlap integrals A_0, A_1, B, D_0 and D_1 on ϵ (for our choice of the rest of the parameters of the potential and of $\Gamma(x)$).

system:

$$(\mu - \omega_0) - A_0 \rho_0^2 - 3B \rho_1^2 - 3D_0 \rho_0 \rho_1 - D_1 \frac{\rho_1^3}{\rho_0} = 0, \quad (3.15)$$

$$(\mu - \omega_1) - A_1 \rho_1^2 - 3B \rho_0^2 - 3D_1 \rho_1 \rho_0 - D_0 \frac{\rho_0^3}{\rho_1} = 0. \quad (3.16)$$

The semi-analytical part of our considerations will consist of solving these algebraic conditions for given linear potential $V(x)$ and nonlinear spatial dependence $\Gamma(x)$ parameters (as mentioned above) and we will compare the findings from this two-mode, Galerkin-type truncation with the full numerical results in what follows.

It is interesting to briefly address the case where $\phi \neq k\pi$ (hence $n(\phi) \neq 0$). In that case, the stationary form of Eq. (3.13) leads to:

$$\cos(\phi) = -\frac{D_0 \rho_0^2 + D_1 \rho_1^2}{2B \rho_0 \rho_1}. \quad (3.17)$$

Then it is straightforward to observe that since $D_0 < D_1$, for all ϵ , and $B < D_1$ for $\epsilon > 0.995$ (from Fig. 3.1), for such values of ϵ , the fraction of the right-hand-side of Eq. (3.17) can be shown to be < -1 and, hence, there are no other solutions satisfying Eq. (3.13). For $\epsilon < 0.995$ we could not perform a similar semi-analytical calculation. However, we confirmed numerically the non-existence of additional solutions (to the ones with $\phi = k\pi$) for this domain.

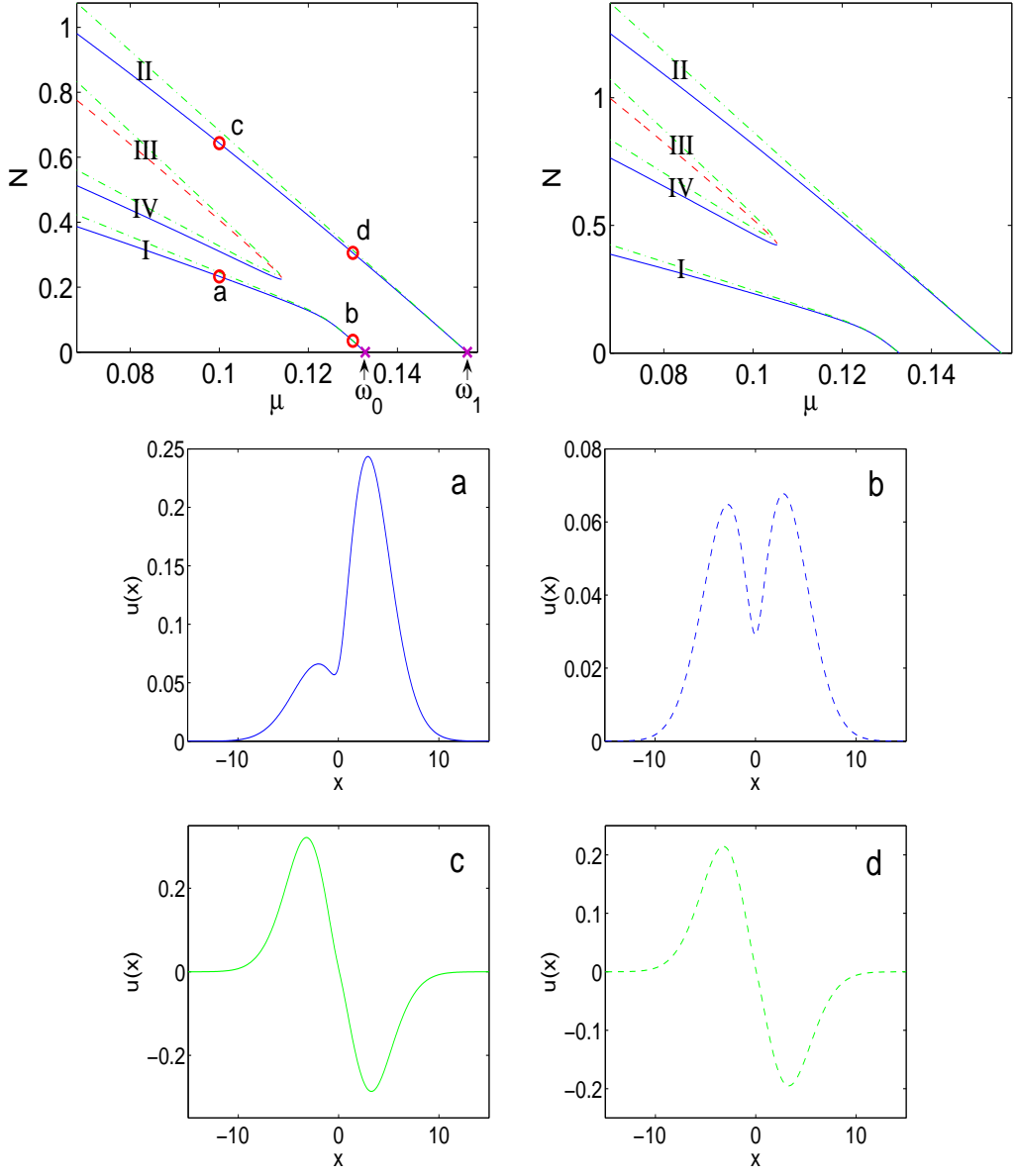


Figure 3.2: Top panels: The normalized number of atoms N [see Eq. (3.8)] of the solutions of Eq. (3.4) for the case of attractive interatomic interactions, i.e., for a nonlinearity coefficient $\Gamma(x)$ with parameters $\alpha + \beta = -1$ and $\alpha - \beta = -1 + \varepsilon$, with $\varepsilon = 0.25$ (top left) and $\varepsilon = 0.5$ (top right), as a function of the normalized chemical potential μ . The blue solid lines and red dashed lines denote the stable and unstable numerically found solutions. The green dashed-dotted lines depict the result of the two-mode approximation. Notice that as $N \rightarrow 0$, the spatial profiles of the two branches tend to the linear eigenmodes $u_{0,1}$ and accordingly $\mu \rightarrow \omega_{0,1}$. Bottom panels: The profiles of the wave functions corresponding to branch I (upper blue) and II (lower green). Along each branch, the profiles are shown for two values of μ , i.e., $\mu = 0.1$ (left solid) and $\mu = 0.13$ (right dashed); the corresponding labels are a) and b) for the symmetric (in the linear limit) branch shown above, while c) and d) are for the antisymmetric (in the linear limit) branch shown below.

3.2 Numerical Results

We begin the exposition of our numerical results by considering $0 < \varepsilon < 1$, in which case $\Gamma(x) < 0$, i.e., attractive interatomic interactions. The top panels of Fig. 3.2 show two examples: $\varepsilon = 0.25$ (left) and $\varepsilon = 0.5$ (right). Each of these panels presents the complete diagram of the numerically generated solutions (blue solid lines correspond to stable solutions and red dashed lines to unstable ones) to Eq. (3.4) and the corresponding analytical predictions (green dashed-dotted lines), namely, the results of the two mode approximation obtained by solving Eqs. (3.15) and (3.16). The solutions are expressed in terms of the normalized number of atoms N [see Eq. (3.8)] as a function of the normalized chemical potential μ . The branches are obtained using a fixed-point Newton iteration (cf. appendix A) and numerical continuation from the non-interacting limit of the system (i.e., in the absence of nonlinearity). Then, numerical linear stability analysis is performed to determine whether each branch does or does not possess real eigenvalues (which result in instability as described in section 2.4). It is readily observed that the analytical predictions for the different branches through Eqs. (3.15-3.16) are in very good agreement with the numerically found solutions.

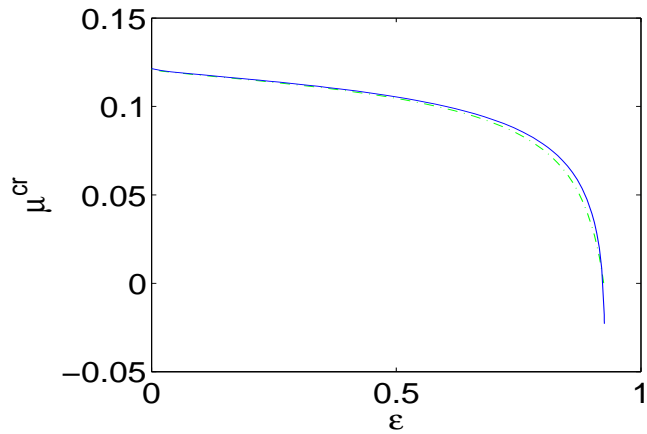


Figure 3.3: The value of μ at which branches III and IV disappear as a function of ε with respect to Fig. 3.2. The blue solid lines and the green dashed-dotted lines denote the numerically found solutions and the result of the two-mode approximation, respectively.

Let us now discuss the various branches appearing in the bifurcation diagrams in more detail. Branch I corresponds to the asymmetric (due to the collisional inhomogeneity) solution starting at $\mu = \omega_0$, the eigenvalue corresponding to the symmetric ground eigenstate u_0 . The asymmetry arises immediately after the deviation from the linear limit of $N \rightarrow 0$, and becomes increasing as one drifts further away. Similarly, branch II starts from $\mu = \omega_1$, the eigenvalue of the anti-symmetric first excited eigenstate, and becomes increasingly asymmetric as it gets away from its linear limit, i.e., when N gets larger. The four bottom panels of Fig. 3.2 provide specific examples of the profiles of this continuation.

Branches III and IV correspond to a pair of two other asymmetric solutions which collide at some critical value of $\mu \equiv \mu^{cr}$ and disappear from then on through a saddle-node bifurcation. As for the two examples in Fig. 3.2, the critical points are 0.1140 and 0.1054, for the cases $\varepsilon = 0.25$ and $\varepsilon = 0.5$, respectively. Moreover, branch IV is observed to move towards branch

I as $\varepsilon \rightarrow 0$. Specifically, when $\varepsilon = 0$, branch IV merges into branch I and the diagram turns into a pitchfork bifurcation (the two asymmetric branches are mirror images of each other and both bifurcate from the symmetric solution in that case), which is the case with attractive interactions analyzed in Ref. [48]. As ε increases, the critical point μ^{cr} of the saddle-node bifurcation decreases and tends to negative infinity rapidly, especially as ε gets closer to 1; then, branches III and IV keep moving to the left of the diagram and disappear finally when ε is close enough to 1. Also, the stability analysis indicates that branch III is the only unstable one among the four solutions, while the other three are all stable for any value of μ .

As a stringent test of our analytical two-mode approximation, in Fig. 3.3 we show the critical point of the saddle-node bifurcation μ^{cr} as a function of the collisional inhomogeneity parameter ε . We observe that the solid line of the fully numerical results is almost identical to the dashed line yielding the theoretical prediction for the occurrence of this bifurcation. This figure demonstrates excellent agreement between the analytical results and the numerical findings.

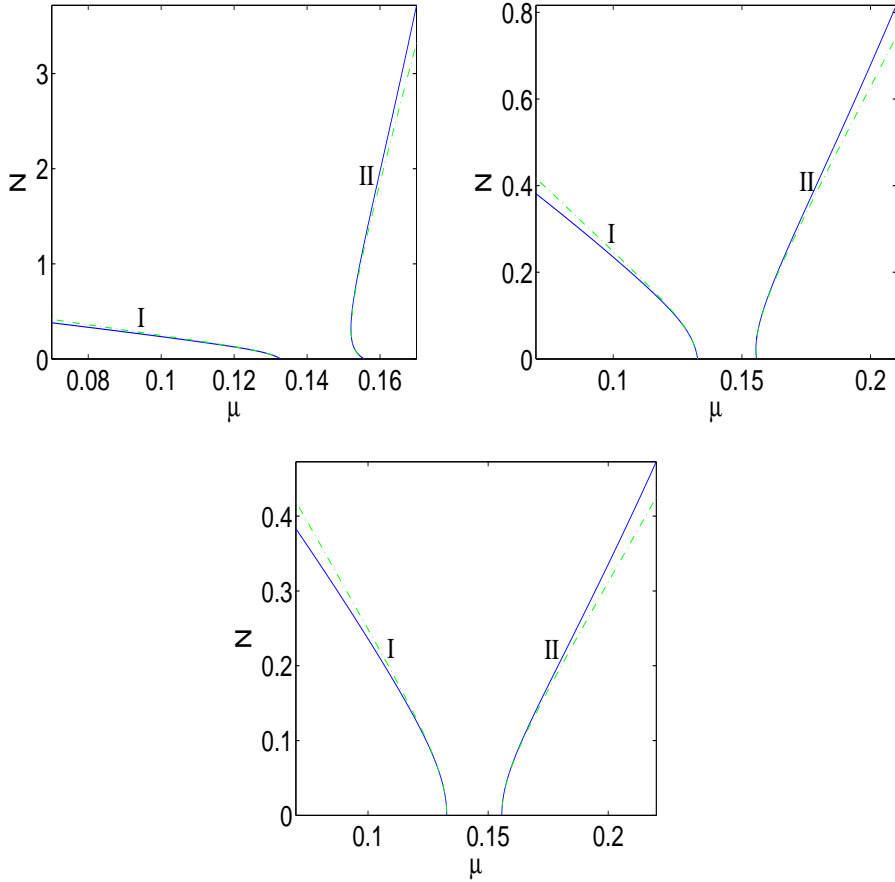


Figure 3.4: The norm of the solutions of Eq. (3.4) for a nonlinearity coefficient $\Gamma(x)$ with parameters such that $\alpha + \beta = -1$ and $\alpha - \beta = -1 + \varepsilon$, with $\varepsilon = 1.05$ (top left), $\varepsilon = 1.5$ (top right) and $\varepsilon = 2$ (bottom), as a function of μ . The notation is the same as in Fig. 3.2.

Next, we study the behavior of the solutions when $\varepsilon > 1$, in which case the nonlinearity

is no longer purely attractive. Remarkably, in this case, only two solutions, branch I and II, still survive for all the examined values of $\varepsilon > 1$. We realize that when ε grows larger from 0 to 1, both branches I and II move 'clockwise' and branch II appears to be almost vertical when ε passes the value 1. As ε continues to increase from 1 to 2, we find an interesting new phenomenon: within a certain small range of N , the solution II only exists for chemical potentials μ slightly less than the eigenvalue ω_1 (corresponding to the eigenstate u_1) before it meets a turning point; the latter occurs, for example, at $\mu = 0.1520$ or 0.1554 for the cases $\varepsilon = 1.05$ or 1.5 , respectively. After the turning point, the solution exists when μ gets larger. This phenomenon is shown in Fig. 3.4, in which it is observed that branch II starts at the linear limit, persists with $dN/d\mu < 0$ for a narrow interval of chemical potentials, before turning to the right with and acquiring $dN/d\mu > 0$. It is also worth mentioning that both branches I and II are still asymmetric and *stable* in this case; thus, here we observe an interesting deviation from the well-known Vakhitov-Kolokolov criterion [234] (see, e.g., a relevant discussion in Ref. [235]) about the slope of the branch determining its linear stability. We present an explanation of the relevant feature at the end of this section (after observing similar features in the principally defocusing case below).

Now let us consider the case in which the parameters involved in the nonlinearity coefficient $\Gamma(x)$ are such that

$$\alpha + \beta = 1 - \varepsilon, \quad \alpha - \beta = 1, \quad (3.18)$$

with $0 \leq \varepsilon \leq 2$, as shown in Fig. 3.5. Notice that Eqs. (3.12) and (3.18) produce the same results when $\varepsilon = 2$.

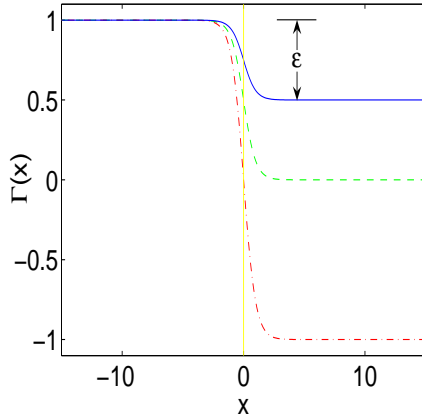


Figure 3.5: Similar to Fig. 3.1, but with a nonlinearity coefficient $\Gamma(x)$ such that $\alpha + \beta = 1 - \varepsilon$, $\alpha - \beta = 1$ and $b = 1$, with $\varepsilon = 0.5$ (blue solid line), $\varepsilon = 1$ (green dashed line) and $\varepsilon = 2$ (red dashed-dotted line).

Figure 3.6 shows some prototypical examples of the bifurcation diagram of the relevant solutions when $0 < \varepsilon < 1$, i.e., in the case of a purely repulsive nonlinearity (notice that the branches turn to the opposite direction than in Fig. 3.2). Similar to the previous case, four solutions are found, two of which disappear through a saddle node bifurcation, allowing only two to survive in the non-interacting (linear) limit of $N \rightarrow 0$. As before, the saddle-node bifurcation becomes a pitchfork one (but now emerging from the anti-symmetric branch) in the case of a collisionally homogeneous environment, i.e., for $\varepsilon \rightarrow 0$. Preserving the original

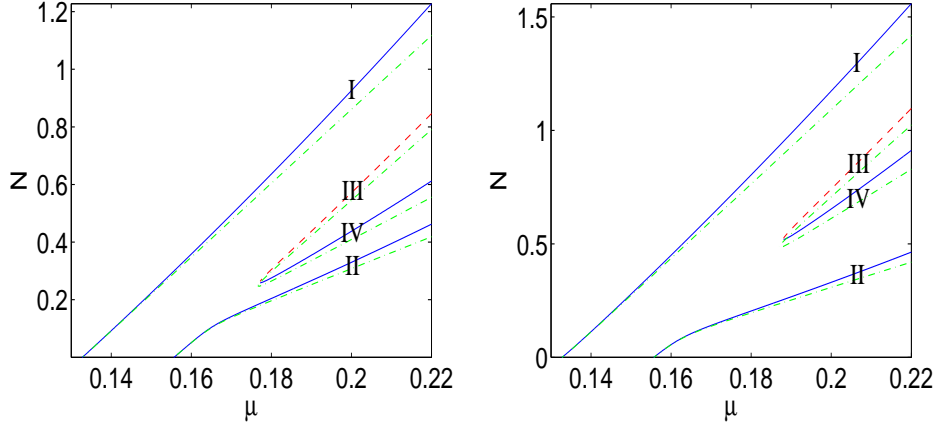


Figure 3.6: The normalized number of particles N for the solutions of Eq. (3.4) as a function of μ in the case of repulsive interatomic interactions, namely, for a nonlinearity coefficient $\Gamma(x)$ with parameters such that $\alpha + \beta = 1 - \varepsilon$ and $\alpha - \beta = 1$, with $\varepsilon = 0.25$ (left) and $\varepsilon = 0.5$ (right). The notation is the same as in Fig. 3.2.

notations, branches I and II are the two asymmetric solutions extending to the linear limit, and starting at $\mu = \omega_0$ and $\mu = \omega_1$, respectively. Once again branches III and IV disappear when μ decreases to some critical value μ^{cr} , which goes up to infinity as ε increases to 1. The dependence of μ^{cr} on the inhomogeneity parameter ε is shown in Fig. 3.7. It is important once again to highlight the good qualitative and even quantitative (apart from the case of very large ε) agreement of the two-mode prediction for μ^{cr} with the full numerical results.

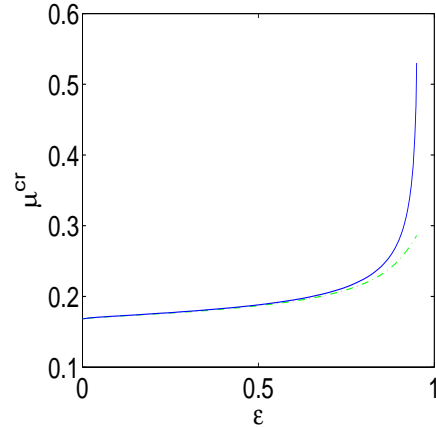


Figure 3.7: The critical value μ^{cr} of the normalized chemical potential at which branches III and IV disappear as a function of ε with respect to Fig. 3.5. The blue solid lines and the green dashed-dotted lines denote the numerically found solutions and the prediction of the two-mode approximation, respectively.

It is interesting to note that in this case as ε increases and one of the wells becomes less repulsive (and eventually attractive for $\varepsilon > 1$), the branches I and II keep rotating 'counterclockwise'. For $\varepsilon > 1$, the turning of the branch arises again, on branch I this time, as shown in Fig. 3.8. In this case, the bifurcation diagram contains only two branches which, for sufficiently large ε , feature opposite monotonicity of the dependence of N on the chemical

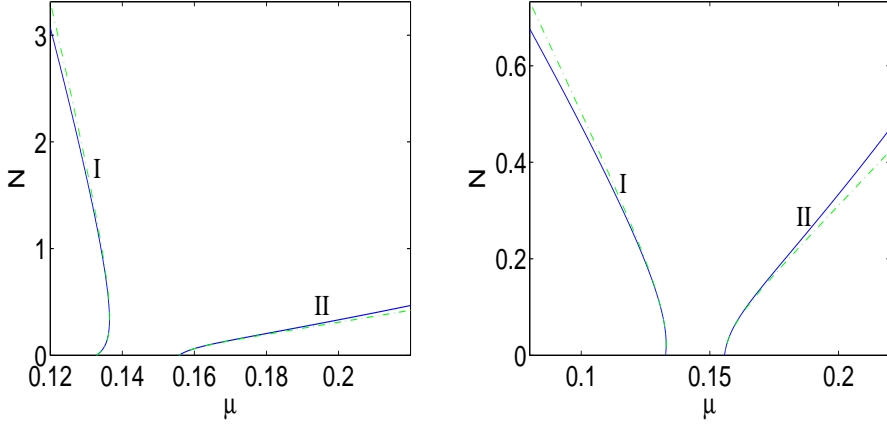


Figure 3.8: The normalized number of particles N of the solutions of Eq. (3.4) as a function of μ , for a nonlinearity coefficient $\Gamma(x)$ with parameters such that $\alpha + \beta = 1 - \varepsilon$ and $\alpha - \beta = 1$, with $\varepsilon = 1.05$ (left) and $\varepsilon = 1.5$ (right). The notation is the same as in Fig. 3.2.

potential μ (although both branches are linearly stable). Similarly to the previous case, branch III is the unstable solution, while the other three remain stable. In all the cases (and even these of large ε), we again note the strong agreement between the bifurcation diagram predicted by the two-mode approximation, in comparison with the numerical results.

We observe that in Fig. 3.4 (e.g., in its top left panel) for the case where the nonlinearity is principally focusing, as well as in Fig. 3.8 (e.g., in its left panel), where it is principally defocusing, one of the branches changes its monotonicity, as a result of the spatially dependent nonlinearity. As indicated previously, given the slope condition of the Vakhitov-Kolokolov criterion [234], it appears to be rather surprising that this change of monotonicity is not accompanied by a change of stability. However, we argue here that it is not. Defining the well known linearization operators

$$L_+ = -\frac{1}{2}\partial_x^2 + V(x) + 3g(x)|u|^2 - \mu \quad (3.19)$$

$$L_- = -\frac{1}{2}\partial_x^2 + V(x) + g(x)|u|^2 - \mu, \quad (3.20)$$

it is known from the work of [236, 237] that when $|n(L_+) - n(L_-)| = 1$ [i.e., the number of negative eigenvalues of L_+ minus the negative eigenvalues of L_- is in absolute value equal to 1], instability arises when the slope condition of Vakhitov-Kolokolov is violated. Since, when $|n(L_+) - n(L_-)| > 1$, the relevant theory indicates that the solution is always unstable, we argue that what should be happening here is that the violation of the slope condition of Vakhitov-Kolokolov is not associated with an instability because it occurs at the same time as the change of the count of $|n(L_+) - n(L_-)|$ (from 1 to 0 or vice versa). This is precisely what we numerically illustrate in Fig. 3.9. In particular, the left panel concerns the principally focusing case associated to the first excited state “turning branch” of Fig. 3.4. There, given the fact that $n(L_-) = 1$ (due to the one zero-crossing of the configuration itself, which is an eigenfunction of L_- with a 0 eigenvalue), we expect the count of eigenvalues $n(L_+)$ to change from 2 to 1 exactly at the critical point, precisely as observed in the figure. On the

other hand, the right panel concerning the ground state branch of Fig. 3.8 for the principally defocusing case, corresponds to a case with $n(L_-) = 0$. Hence, when the slope condition is violated (near the linear limit in this case), it has to be true that $n(L_+) = 0$, while after the turning point of the branch, the slope condition is satisfied and then $n(L_+) = 1$, which again is consonant with the observed stability. These features are clearly illustrated in the right panel of Fig. 3.9. We believe that similar considerations and counts may resolve apparent paradoxes that seem to be encountered e.g. in [235, 238].

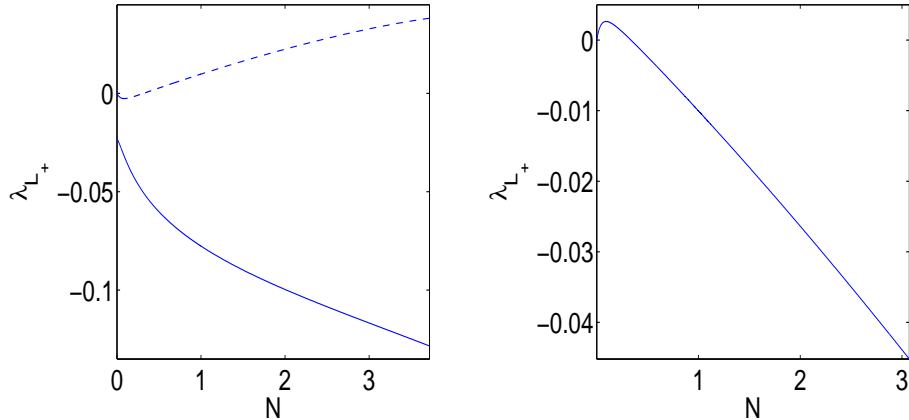


Figure 3.9: The eigenvalues of the operator $L_+ = -\frac{1}{2}\partial_x^2 + V(x) + 3g|u|^2 - \mu$, which involve negative parts, as a function of N . The left and right panels relate to the two “turning branches”, i.e. branch II in Fig. 3.4 and branch I in Fig. 3.8, respectively, for the case that $\varepsilon = 1.05$.

3.3 Two-Mode Dynamics

So far, we have considered the two-mode reduction as a tool for identifying (quite successfully, as shown above) the stationary states of the underlying problem. However, here we illustrate how the same tool can be used to understand the system dynamics. The two principal dynamical features of the (symmetric) double-well system involve the oscillations of matter between the two wells (for low population asymmetries between the wells) and the nonlinearly induced self-trapping regime (for high population asymmetries between the wells); see e.g., [39–41, 45]. For this reason, although our setting here is inherently asymmetric (due to the nature of $\Gamma(x)$), it is of interest to develop a variant of the two-mode approximation that accounts for the population imbalance between the wells.

In order to formulate the problem based on the populations of the left and right well, one can reformulate our two-mode decomposition as

$$u(x, t) = c_R(t) \frac{1}{\sqrt{2}}(u_0(x) + u_1(x)) + c_L(t) \frac{1}{\sqrt{2}}(u_0(x) - u_1(x)), \quad (3.21)$$

where it is clear that c_L and c_R are connected with c_0 and c_1 through a simple linear transformation. If we then decompose $c_i = \rho_j e^{i\phi_j}$ $j = R, L$ and define the phase difference $\Delta\phi = \phi_L - \phi_R$, and the population imbalance $z = \rho_R^2 - \rho_L^2$ (recall that $N = \rho_L^2 + \rho_R^2$), one

can then project the equation to $(u_0 + u_1)$, as well as to $(u_0 - u_1)$ and eventually obtain the dynamical equations for the conjugate variables z and $\Delta\phi$. These read:

$$\begin{aligned}\dot{\Delta\phi} = & -\frac{z}{4}(A_0 - 10B + A_1) + N(D_0 + D_1) - \cos(\Delta\phi)\frac{z}{\sqrt{N^2 - z^2}}\left[\mu_0 - \mu_1 + \frac{N}{2}(A_0 - A_1)\right] \\ & + \cos(\Delta\phi)\frac{N^2 - 2z^2}{\sqrt{N^2 - z^2}}(D_0 - D_1) - \cos(2\Delta\phi)\frac{z}{4}(A_0 - 2B + A_1)\end{aligned}\quad (3.22)$$

$$\begin{aligned}\dot{z} = & \sqrt{N^2 - z^2}\sin(\Delta\phi)\left[\mu_0 - \mu_1 + \frac{N}{2}(A_0 - A_1) + z(B_0 - B_1)\right] \\ & + \frac{N^2 - z^2}{4}\sin(2\Delta\phi)(A_0 - 2B + A_1)\end{aligned}\quad (3.23)$$

For a detailed derivation of the above equations we refer the interested reader to Appendix C. It is interesting to examine the dynamical evolution of these equations (their stationary states are identical to the ones identified above), and to compare their dynamics with the corresponding PDE dynamics. In the latter, one can also make similar projections to $(u_0 + u_1)$, as well as to $(u_0 - u_1)$ and define accordingly $c_{L,R}$, as well as thereafter z and $\Delta\phi$. A comparison of the $(z, \Delta\phi)$ phase space for different ϵ of such canonically conjugate variables can be found in Fig. 3.10. It can be clearly observed that for non-zero ϵ the reflection symmetry around $z = 0$ is broken. For increasing ϵ the population imbalance of the stationary states shifts towards larger values of z (see also Fig. 3.11), denoting a larger occupation of the right well compared to the left one. This can be understood by taking into account that we consider the case of repulsive interaction. There, an increase of ϵ implies a reduction of interaction in the right well (see Fig. 3.5). So, pictorially speaking, the atoms feel less repulsion in the right well than in the left one, leading to the observed population imbalance. For small populational asymmetries (around the nonzero stationary ones), the system executes inter-well matter-transfer oscillations. On the other hand, beyond a critical asymmetry in the initial populations, we enter the self-trapping regime, as is shown both in the partial differential equation of the full dynamics and in the above reduced two-mode description of Eqs. (3.22-3.23). For non-zero ϵ the value of this critical points taken at $\delta\phi = 0$ depend also on their sign, in contrary to the symmetric case for $\epsilon = 0$. For small values of ϵ there are two critical points, which increase with increasing ϵ . Eventually, the positive one ceases to exist as one can see by inspecting Fig. 3.10 for $\epsilon = 0.5$.

A detailed discussion of the dynamical comparison of the two-mode approximation with the corresponding results of the full system can be found in [45]. There, it is highlighted how the effect of a reduced barrier height of the trapping potential or increased interactions can deteriorate the dynamical effectiveness of the two-mode reduction.

Here we explore the role of the collisional inhomogeneity in affecting the accuracy of this reduction, by illustrating a prototypical diagnostic, namely the critical population imbalance threshold beyond which self-trapping occurs, as this is identified in the full dynamical equation and as it is obtained within the two-mode reduction. This is shown in Fig. 3.11. It can be seen that as ϵ increases, both critical points (the positive and the negative one) increase. The positive one vanishes when it is equal to the total number of atoms. By comparing the results obtained by solving the PDE with the results of the ODEs one observes that the two-mode approximation becomes less accurate, as ϵ increases, in capturing the corresponding threshold, a feature that we have also seen regarding stationary state properties; see e.g. Fig. 3.7.

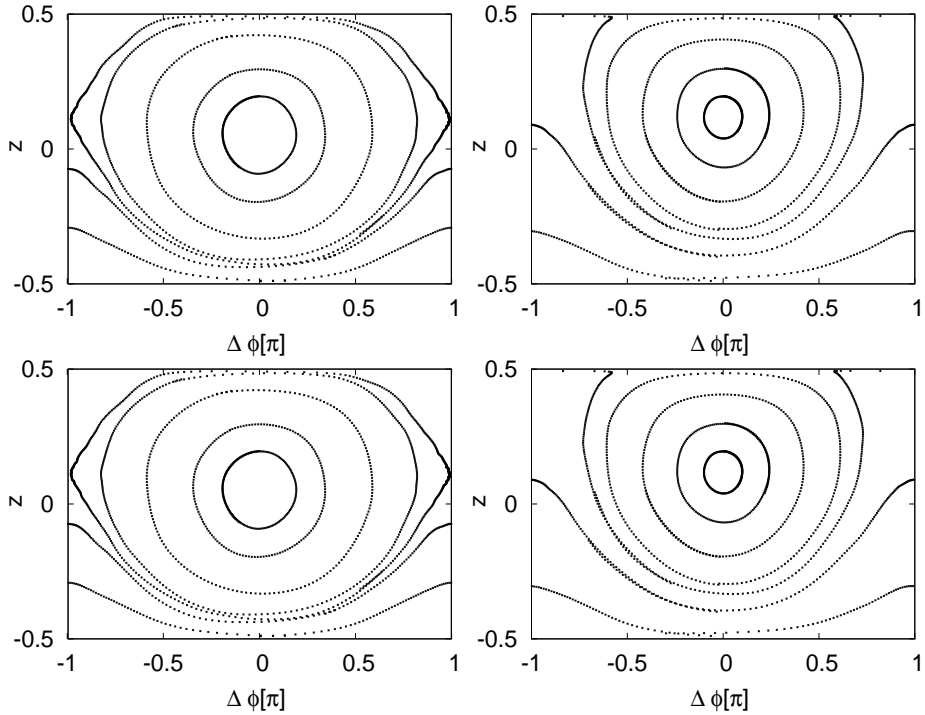


Figure 3.10: Phase diagrams for $\epsilon = 0.25$ (left column) and $\epsilon = 0.5$ (right column) and $N = 0.5$. The results from the ordinary differential equations (3.22-3.23) are shown in the top row, while the corresponding results from the partial differential equation are shown in the bottom row.

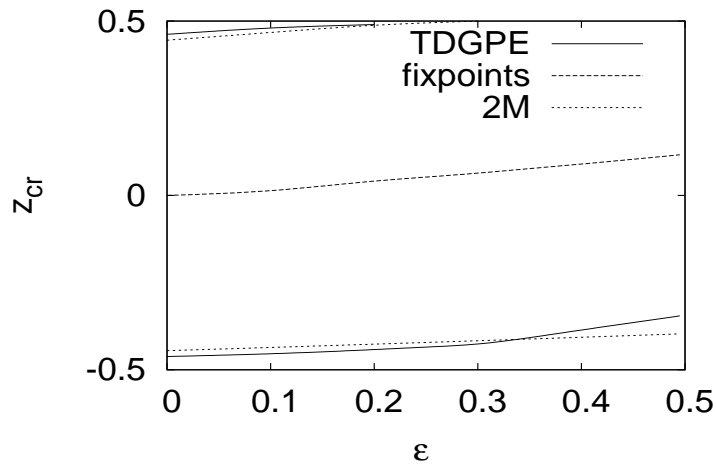


Figure 3.11: The critical points z_{cr} of population imbalance above which there exists self-trapping are shown in the time-dependent Gross-Pitaevskii equation (TDGPE) and in the two-mode approximation (2M) for $N = 0.5$. Notice that in this setting, the population imbalance becomes nonzero when $\epsilon \neq 0$ due to the asymmetry (as shown by the dashed line).

3.4 Conclusions

In this chapter, we studied in detail the nature of the most fundamental matter-waves (emitting from the linear limit of the problem) that emerge from a quasi-1D collisionally inhomogeneous Bose-Einstein condensate trapped in a double-well potential. We specifically considered a setup which features distinct scattering lengths between the two wells, including also the case where the nonlinearity coefficient of the pertinent Gross-Pitaevskii equation has different signs in the two wells. We observed that the relevant phenomenology is different in the considered collisionally inhomogeneous environment in comparison to the collisionally homogeneous case studied previously. In particular, even for weak inhomogeneities, the asymmetry (that the spatial dependence of the nonlinearity introduces) induces a modification of the bifurcation picture of the double-well potential and a change in the nature of the symmetry-breaking bifurcation from a pitchfork to a saddle-node; this is reminiscent of similar modifications to the bifurcation picture due to asymmetries of the linear potential [48]. On the other hand, it was found that as the strength of the inhomogeneity is increased, even this saddle-node “recollection” of the symmetry-breaking bifurcation eventually disappears (the corresponding critical point is pushed to infinity) and only one nonlinear branch persists that corresponds to each state of the problem’s linear limit. Interestingly also, as the inhomogeneity acquires opposite sign values of the scattering length, the monotonicity of the number of atoms’ dependence on the chemical potential may change (and may even be different between the two branches), although they do maintain their stability (which presents an interesting deviation –in this spatially inhomogeneous case– from the well-known Vakhitov-Kolokolov criterion that we rationalized in detail above). All of this phenomenology, including the detailed bifurcation diagram and other specific features, such as the critical point of the saddle-node bifurcation and its dependence on the degree of inhomogeneity, are captured remarkably accurately by a Galerkin-type, two-mode approximation and a resulting simple set of algebraic equations. Finally, we also briefly discussed dynamical aspects of the system including a phase space reduction in the population imbalance-interwell phase difference space. We have illustrated that despite the ensuing asymmetry in the phase space (for positive vs. negative population imbalances), the two-mode reduction can accurately capture the threshold of transition from Josephson matter-wave oscillations to nonlinearly induced self-trapping (especially so for weak collisional inhomogeneities).

Our investigation herein presents some testable predictions for the original physical system and its realization in atomic physics or, also possibly, in nonlinear optics [51]; in particular, as the nonlinearity becomes increasingly different in the two wells, the emergence of additional states should be occurring for increasingly larger number of atoms and eventually, such additional states (in particular, the stable one among them) should no longer be observable.

Chapter 4

Matter-Wave Solitons in the Presence of Collisional Inhomogeneities: Perturbation Theory and the Impact of Derivative Terms

Our aim in this chapter is to study the dynamics of matter-wave solitons in the presence of a spatially-dependent nonlinearity in quasi-one-dimensional BECs. We consider both dark solitons in repulsive BECs, as well as bright solitons in attractive BECs. In the case where the sign of the nonlinearity coefficient (hereafter referred to as $g(x)$) does not change, we first show that a change of variables can convert the spatially variable nonlinearity problem into a “regular” one where the nonlinearity has a constant prefactor. This transformation results in the emergence of two additional perturbation terms: one of them can be considered as an effective potential term (i.e., a spatially-dependent function multiplying the macroscopic wave function u), while the other one can not (it consists of a spatially-dependent function multiplying the *derivative* of the wave function $\partial_x u$, for an elongated BEC along the x -direction). We use this transformation as a starting point in order to develop perturbation theory for the soliton dynamics in the presence of $g(x)$ for the case of arbitrary $g(x)$. However our focus is on the case where $g(x)$ is such that the potential term completely vanishes. The reason for this selection is that it appears to be the less physically intuitive case (due to the derivative nature of the corresponding perturbation). Moreover, the effect of a perturbation induced by a “standard” potential term has been studied fairly extensively in the BEC context (see, e.g., [1–3, 5]), also in the particular case of collisionally inhomogeneous BECs (see, e.g., [80, 81, 84]). The results of this chapter are published in Ref. [239].

Our investigation is structured as follows. In the next section, we give the general setting and analyze the relevant transformation. In section 4.2, we focus on dark solitons, first providing the general theory, and then applying it to the particular case of interest. In section 4.3, we follow a similar path for the case of bright solitons. Finally, in section 4.4, we summarize our findings and present our conclusions.

4.1 Perturbed Gross Pitaevskii Equation and the Derivative-Only Case

In this chapter we will restrict ourselves to an effective 1D description accounting only for the longitudinal dynamics of the condensate. In the transverse directions the atoms should be tightly confined by an isotropic harmonic potential with a trap frequency ω_\perp (associated with the harmonic oscillator length a_\perp). The longitudinal motion takes place in the x -direction and should not be confined. Then, the corresponding mean-field equation is given by (cf.

section 2.2.2)

$$i\hbar\partial_t\Psi = -\frac{\hbar^2}{2m}\partial_x^2\Psi + g(x)|\Psi|^2\Psi \quad (4.1)$$

where $\Psi(x, t)$ is the macroscopic wave function, m the atomic mass and $g(x) = g^{(3D)}(x)/2\pi a_{\perp}^2$ the effective 1D interaction coefficient. $g^{(3D)}(x) = 4\pi\hbar^2 a/m$ characterizes the two-particle interaction in 3D with the s-wave scattering length a . The value of the scattering length can be tuned by the use of Feshbach resonances (cf. section 2.1.3). Measuring x in units of $\sqrt{\hbar/(M\omega)}$, t in units of $1/\omega$ and energy in units of $\hbar\omega$ allows us to express Eq. (4.1) in the following form:

$$i\partial_t\Psi = -\frac{1}{2}\partial_x^2\Psi + s|g(x)||\Psi|^2\Psi, \quad (4.2)$$

where the coefficient $s = \text{sgn}(g) = \pm 1$ for attractive and repulsive condensates, respectively. Note, ω is a scaling frequency which has to be adjusted for a concrete problem in such a way that the real (physical) coupling coefficient $g_{\text{phys}} = g/(\hbar\omega)$. Applying the transformation $\Psi = \frac{u}{\sqrt{g}}$ allows us to rewrite Eq. (4.2) in the following way:

$$i\partial_t u = -\frac{1}{2}\partial_x^2 u + s|u|^2 u + \tilde{V}_{\text{eff}}(x)u - \sqrt{g}\partial_x \frac{1}{\sqrt{g}}\partial_x u, \quad (4.3)$$

with the effective potential term $\tilde{V}_{\text{eff}}(x) = -\frac{1}{2}\sqrt{g}\partial_x^2 \frac{1}{\sqrt{g}}$. Equation (4.3) can be written as the usual NLS equation (with a defocusing or focusing nonlinearity for $s = \pm 1$, respectively) with an external spatially-dependent perturbation $P[u(x, t); x]$, namely:

$$i\partial_t u + \frac{1}{2}\partial_x^2 u - s|u|^2 u = P[u(x, t); x]. \quad (4.4)$$

The perturbation can be expressed as $P[u(x, t); x] = P_L[u(x, t); x] + P_{NP}[u(x, t); x]$, i.e., it consists of a linear effective potential contribution $P_L[u(x, t); x] = \tilde{V}_{\text{eff}}(x)u(x, t)$, as well as of a non-potential perturbation of the form $P_{NP}[u(x, t); x] = -\sqrt{g}\partial_x \frac{1}{\sqrt{g}}\partial_x u$. In this chapter we are mainly interested in the effects of the less standard, non-potential type of perturbation. Therefore, we assume the collisionally inhomogeneous interaction to be of the form

$$g(x) = \frac{1}{(D + Cx)^2}, \quad (4.5)$$

with arbitrary constants C and D . For such a particular selection of $g(x)$, $\tilde{V}_{\text{eff}}(x)$ vanishes leading to the perturbation

$$P[u(x, t); x] = -\frac{C}{D + Cx}\partial_x u, \quad (4.6)$$

consisting only of the non-potential contribution in the right hand side. Thus we can investigate the pure effects of the latter, non-standard contribution (the effects of a standard linear potential have been studied fairly extensively; see e.g. [1–3, 5]). We choose $C = 1$ and $D = -200$; thereby the singularity in the perturbation occurs at $x_0^{\text{sing}} = 200$ (which will be outside the region of interest in our domain). For this choice, the spatial dependence of the coefficient $g(x)$ is shown in Fig. 4.1.

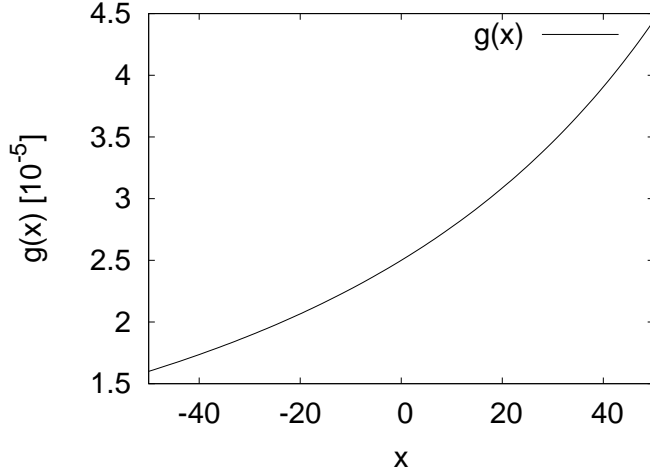


Figure 4.1: Spatial dependence of the interaction parameter $g(x)$ for $C = 1$ and $D = -200$ for a repulsive condensate.

4.2 Dark Matter-Wave Solitons

4.2.1 Full Perturbative Approach

Let us first consider the case of dark matter-wave solitons for $s = 1$. In order to treat effects of the perturbation (4.6) on a dark soliton analytically we employ the adiabatic perturbation theory assuming that the functional form of the soliton remains unchanged by the perturbation (an assumption that in our setting will be justified a posteriori). We first use the transformation $u \rightarrow u \exp(-it)$ to put Eq. (4.4) in the form

$$i\partial_t u + \frac{1}{2}\partial_x^2 u - (|u|^2 - 1)u = P[u(x, t); x] \quad (4.7)$$

and use as an ansatz for the soliton, the following expression,

$$u = B \tanh(B(x - x_0)) + iA, \quad (4.8)$$

which is the exact dark soliton solution of the above mentioned unperturbed NLS equation (cf. section 2.3.2). According to the above discussion, the soliton depth A , velocity B (with $A^2 + B^2 = 1$), and center x_0 are assumed to be unknown functions of time. The Lagrangian density of an unperturbed dark soliton is given by [124]:

$$\mathcal{L}(u) = \frac{i}{2}(u^\star \partial_t u - u \partial_t u^\star)(1 - \frac{1}{|u|^2}) - \frac{1}{2}|\partial_x u|^2 - \frac{1}{2}(|u|^2 - 1)^2, \quad (4.9)$$

while the averaged Lagrangian, $L = \int dx \mathcal{L}(u)$, can be calculated by substituting (4.8) in Eq. (4.9) yielding:

$$L(A, x_0) = 2\partial_t x_0 \left[-AB + \tan^{-1}(\frac{B}{A}) \right] - \frac{4}{3}B^3. \quad (4.10)$$

In [240] it was shown that, within the framework of the adiabatic perturbation theory for small perturbations, the parameters of the soliton $\alpha_j = \{x_0, A\}$ obey the the Euler-Lagrange equations

$$\partial_{\alpha_j} L - \frac{d}{dt} \partial_{\alpha'_j} L = 2Re \left\{ \int dx P^*(u) \partial_{\alpha_j} u \right\} \quad (4.11)$$

with $\alpha'_j = \partial_t \alpha_j$. This leads to a system of ordinary differential equations (ODE) for A and x_0 :

$$\begin{aligned} \partial_t A &= \frac{1}{2} B^3 \int dx \sqrt{g} \partial_x \frac{1}{\sqrt{g}} \operatorname{sech}^4[B(x - x_0)] \\ &\quad + \frac{1}{4} B^2 \int dx \sqrt{g} \partial_x^2 \frac{1}{\sqrt{g}} \tanh[B(x - x_0)] \operatorname{sech}^2[B(x - x_0)], \end{aligned} \quad (4.12)$$

$$\begin{aligned} \partial_t x_0 &= A - \frac{1}{2} A \int dx \sqrt{g} \partial_x \frac{1}{\sqrt{g}} \operatorname{sech}^2[B(x - x_0)] \left[\tanh[B(x - x_0)] \right. \\ &\quad \left. + B(x - x_0) \operatorname{sech}^2[B(x - x_0)] \right] \\ &\quad - \frac{1}{4} \int dx \sqrt{g} \partial_x^2 \frac{1}{\sqrt{g}} \left[\left[\frac{1}{B} \tanh^2[B(x - x_0)] - 1 \right] \right. \\ &\quad \left. + (x - x_0) \tanh[B(x - x_0)] \operatorname{sech}^2[B(x - x_0)] \right]. \end{aligned} \quad (4.13)$$

For an interaction obeying Eq. (4.5), the terms arising from the linear potential vanish, leading to the system:

$$\partial_t A = \frac{1}{2} B^3 \int dx \frac{C}{D + Cx} \operatorname{sech}^4[B(x - x_0)], \quad (4.14)$$

$$\begin{aligned} \partial_t x_0 &= A - \frac{1}{2} A \int dx \frac{C}{D + Cx} \operatorname{sech}^2[B(x - x_0)] \left[\tanh[B(x - x_0)] \right. \\ &\quad \left. + B(x - x_0) \operatorname{sech}^2[B(x - x_0)] \right]. \end{aligned} \quad (4.15)$$

4.2.2 Approximations

We can simplify the general framework of Eqs. (4.12,4.13) by performing a Taylor expansion of the interaction around $x = x_0$, leading in first order to

$$\partial_t A \approx \frac{2}{3} (1 - A^2) \sqrt{g(x_0)} \partial_x \frac{1}{\sqrt{g(x)}} \Big|_{x=x_0} \quad (4.16)$$

$$\partial_t x_0 \approx A + \frac{1}{4} \frac{A}{B^2} \sqrt{g(x_0)} \partial_x^2 \frac{1}{g(x)} \Big|_{x=x_0}. \quad (4.17)$$

The Taylor expansion around x_0 can be justified in most settings due to the exponential localization of the soliton around its center. Dropping higher-order terms essentially implies that the interaction does not change on the scale of the width of the soliton (if the latter assumption is invalid, then we can not resort to this approximation). In the special case of

the interaction (4.5) the following evolution equations are obtained:

$$\partial_t A \approx \frac{2}{3}(1 - A^2) \frac{C}{D + Cx_0} \quad (4.18)$$

$$\partial_t x_0 \approx A \quad (4.19)$$

By combination of Eqs. (4.18) and (4.19), we obtain a single second-order ODE

$$\partial_t^2 x_0 = \frac{2}{3} \frac{C}{D + Cx_0} [1 - (\partial_t x_0)^2] \quad (4.20)$$

for the center of the soliton. If the velocity of the soliton is small, $\partial_t x_0 \ll 1$, one can neglect the second term in the right hand side of Eq. (4.20) leading to:

$$\partial_t^2 x_0 = \frac{2}{3} \frac{C}{D + Cx_0}. \quad (4.21)$$

We will discuss the validity of this approximation in our numerical results below. Equation (4.21) is the equation of motion (EOM)

$$\partial_t^2 x_0 = -\partial_{x_0} V^{eff}(x_0), \quad (4.22)$$

of a particle in the presence of the effective potential

$$V^{eff}(x_0) = -\frac{2}{3} \ln(|Cx_0 + D|). \quad (4.23)$$

Therefore, we will denote Eq. (4.20) as EOM and Eq. (4.21) as EOM_a in the next section. As an interesting aside, we should note that even in the presence of the kinetic term (i.e., if $(\partial_t x_0)^2$ is not neglected), one can rewrite Eq. (4.20) as a Hamiltonian system (see Ref. [241]) using a generalized momentum $P = g(x_0)\partial_t x_0$. With this momentum one finds for a system

$$\partial_t^2 x_0 = f(x_0)[1 - (\partial_t x_0)^2], \quad (4.24)$$

the equations of motion

$$\partial_t x_0 = \frac{P}{g(x_0)}, \quad (4.25)$$

$$\partial_t P = g(x_0)f(x_0) + P^2 \left[\frac{\partial_{x_0} g(x_0)}{(g(x_0))^2} - \frac{f(x_0)}{g(x_0)} \right], \quad (4.26)$$

which correspond to the Hamiltonian

$$H(x_0, P) = \frac{1}{2} \frac{P^2}{g(x_0)} + F(x_0), \quad (4.27)$$

with

$$g(x_0) = A \exp \left[2 \int^{x_0} dx'_0 f(x'_0) \right], \quad (4.28)$$

$$F(x_0) = -\frac{1}{2} g(x_0). \quad (4.29)$$

In the particular case of $f(x_0) = \frac{2}{3} \frac{C}{D+Cx_0}$, one obtains for the momentum

$$P = A(D + Cx_0)^{\frac{4}{3}} \partial_t x_0, \quad (4.30)$$

and for the Hamiltonian

$$H(x_0, P) = \frac{P^2}{2A} (D + Cx_0)^{-\frac{4}{3}} - \frac{1}{2} A(D + Cx_0)^{\frac{4}{3}}. \quad (4.31)$$

4.2.3 Numerical Results

In this section we present and compare the numerical results obtained by solving the full partial differential equation (PDE) of the GP type (4.4), as well as the ODEs (4.14,4.15), the EOM (4.20) and the simplified EOM_a (4.21). We have confirmed that throughout our simulations the soliton is localized in a region with a well defined perturbation avoiding the singularity. Since the soliton is exponentially localized, the spatial integrations in Eqs. (4.14,4.15) can be restricted to a region around the center of the soliton with a finite perturbation and a well defined integrand. The time evolution is performed by the Adams-Bashforth-Moulton predictor-corrector method (cf. Appendix A).

Figure 4.2 shows the time evolution of the density profile of a dark soliton with $x_0(0) = 0$ for different initial velocities obtained by solving Eq. (4.4). Black represents the highest density, while white corresponds to the lowest density. The dotted lines are the results for x_0 (the center of the soliton) as obtained by solving the ODEs (4.14,4.15). The results agree very well, showing that the adiabatic perturbation theory describes the motion of the center of the soliton accurately. For $A_{init} = 0$ (lowest curve) the soliton gets accelerated to the negative half-plane and moves immediately into this direction. For $A_{init} = 0.25$ and $A_{init} = 0.5$ (middle and top curve, respectively), the soliton also gets accelerated into the direction of the negative half-plane but starts moving to the positive one due to its initial velocity until it reaches a turning point of zero velocity and changes direction. By investigation of Fig. 4.1 one observes that in the considered region the value of the interaction parameter decreases for decreasing x . Thus, the soliton gets accelerated into the direction with a smaller interaction parameter. Due to the fact that the interaction is repulsive, the interaction energy decreases with decreasing interaction parameter. So the soliton tends to move into the region with less interaction energy. This happens despite the fact that the interaction parameter does not enter explicitly in the perturbation as a potential but rather through the product of its first derivative and the first derivative of the scaled wave function.

Figure 4.3 shows the time evolution for $x_0(0) = 0$, $A_{init} = 0$ (a) and $A_{init} = 0.5$ (b) of the differences between the results for the center of the soliton obtained by solving the PDE, and the ODE, EOM and EOM_a, respectively. We calculated the center of mass of the PDE

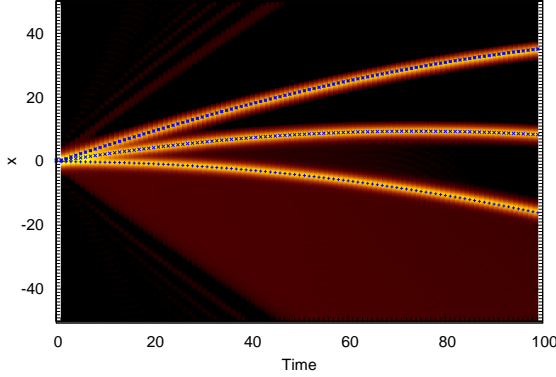


Figure 4.2: Time evolution of the density of dark solitons with $x_0(0) = 0$ and $A_{init} = 0, 0.25, 0.5$ (from bottom to top). The dotted line is the CM parameter (x_0) obtained by solving the ODEs (4.14-4.15).

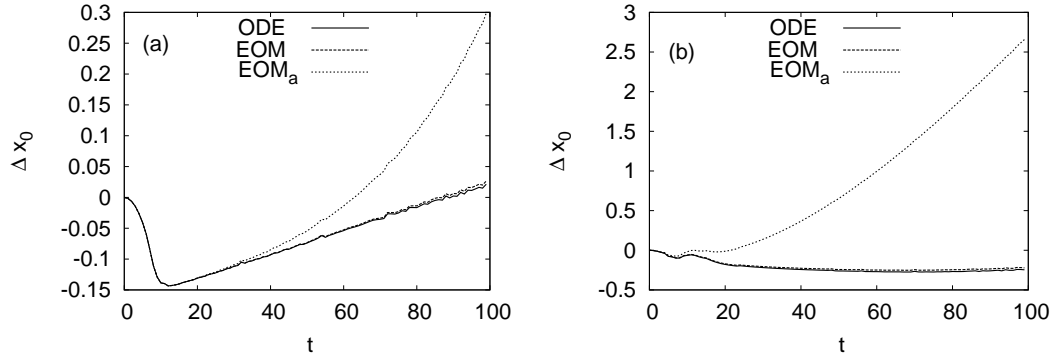


Figure 4.3: Difference of the soliton center Δx_0 calculated by solving the PDE with the result of the ODEs, EOM and EOM_a for $A_{init} = 0.0$ (a) and $A_{init} = 0.5$ (b).

solution by performing the integration

$$x_0 = \int x(b - |u|^2)dx / \int (b - |u|^2)dx, \quad (4.32)$$

with $b = |u(x_b)|^2$ being the background density evaluated far away from the center of the soliton. The thus calculated center of mass position denotes the position of the soliton. The differences for the ODEs and the EOM are almost equal and small for both initial velocities. So the adiabatic perturbation theory works fine for describing the center of the soliton. The results obtained by solving EOM_a coincide for a small time period with the result of the PDE. For longer times, they deviate from these results. For a larger initial velocity the deviation is even larger. The reason for this is that we neglected the impact of the velocity in EOM_a and, thus, the approximation gets worse for larger velocities. However, the qualitative behavior is described correctly even within this approximation. Hence, one can understand the behavior of the soliton as a particle moving in the effective potential (4.23) and thus can explain the acceleration observed in Fig. 4.2.

4.3 Bright Matter-Wave Solitons

4.3.1 Full Perturbative Approach

In the case of attractive interactions ($s = -1$), Eq. (4.4) reads after substitution of $\tau = t/2$

$$i\partial_\tau u + \partial_x^2 u + 2|u|^2 u = 2\epsilon P(u). \quad (4.33)$$

In the absence of perturbations, it is well known that Eq. (4.33) possesses a bright soliton solution of the form (cf. section 2.3.2)

$$u(z, t) = 2i\eta \exp(-2i\xi z - i\Phi) \operatorname{sech}(z), \quad (4.34)$$

where $z = 2\eta(x - \zeta)$, while η represents the amplitude, Φ the phase and ζ the center of the soliton, and ξ is related to the velocity of the soliton. For a small perturbation, we can now employ the adiabatic perturbation theory for bright solitons [242] to treat the perturbation effects analytically. Then, the soliton parameters become slowly-varying functions of time, however the shape of the soliton remains unchanged (once again this is a principal assumption that will be justified a posteriori). With the general perturbation arising due to a spatially-dependent scattering length, one arrives at the following system of ordinary differential equations for the parameters of the soliton:

$$\partial_\tau \eta = 8\eta^2 \xi \int dx \sqrt{g} \partial_x \frac{1}{\sqrt{g}} \operatorname{sech}^2[2\eta(x - \zeta)], \quad (4.35)$$

$$\begin{aligned} \partial_\tau \xi = & 8\eta^3 \int dx \sqrt{g} \partial_x \frac{1}{\sqrt{g}} \tanh^2[2\eta(x - \zeta)] \operatorname{sech}^2[2\eta(x - \zeta)] \\ & - 2\eta^2 \int dx \sqrt{g} \partial_x^2 \frac{1}{\sqrt{g}} \tanh[2\eta(x - \zeta)] \operatorname{sech}^2[2\eta(x - \zeta)], \end{aligned} \quad (4.36)$$

$$\partial_\tau \zeta = -4\xi + 8\eta\xi \int dx \sqrt{g} \partial_x \frac{1}{\sqrt{g}} (x - \zeta) \operatorname{sech}^2[2\eta(x - \zeta)], \quad (4.37)$$

$$\begin{aligned} \partial_\tau \Phi = & 4(\xi^2 - \eta^2) + 8\eta^2 \int dx \sqrt{g} \partial_x \frac{1}{\sqrt{g}} \operatorname{sech}^2[2\eta(x - \zeta)] \tanh[2\eta(x - \zeta)] \\ & [1 - 2\eta x \tanh[2\eta(x - \zeta)]] \\ & - 2\eta \int dx \sqrt{g} \partial_x^2 \frac{1}{\sqrt{g}} \operatorname{sech}^2[2\eta(x - \zeta)] [1 - 2\eta x \tanh[2\eta(x - \zeta)]]. \end{aligned} \quad (4.38)$$

For an interaction parameter of the form (4.5) one obtains:

$$\partial_\tau \eta = 8\eta^2 \xi \int dx \frac{C}{D + Cx} \operatorname{sech}^2[2\eta(x - \zeta)] \quad (4.39)$$

$$\partial_\tau \xi = 8\eta^3 \int dx \frac{C}{D + Cx} \tanh^2[2\eta(x - \zeta)] \operatorname{sech}^2[2\eta(x - \zeta)] \quad (4.40)$$

$$\partial_\tau \zeta = -4\xi + 8\eta\xi \int dx \frac{C}{D + Cx} (x - \zeta) \operatorname{sech}^2[2\eta(x - \zeta)] \quad (4.41)$$

$$\partial_\tau \Phi = 4(\xi^2 - \eta^2) + 8\eta^2 \int dx \frac{C}{D + Cx} \operatorname{sech}^2[2\eta(x - \zeta)] \tanh[2\eta(x - \zeta)] [1 - 2\eta x \tanh[2\eta(x - \zeta)]]. \quad (4.42)$$

4.3.2 Approximations

From the above equations it is clear that Eq. (4.42) describes the time evolution of the phase of the soliton which, however, does not emerge in the equations determining the other parameters. Therefore, we will restrict our considerations to Eqs. (4.39-4.41). Since the soliton is exponentially localized around $x = \zeta$ we can perform a Taylor expansion around ζ and thus simplify Eqs. (4.35-4.37) as follows:

$$\partial_\tau \eta = 8\eta \xi \sqrt{g(\zeta)} \partial_x \frac{1}{\sqrt{g(x)}} \Big|_{x=\zeta} \quad (4.43)$$

$$\partial_\tau \xi = \frac{8}{3}\eta^2 \sqrt{g(\zeta)} \partial_x \frac{1}{\sqrt{g(x)}} \Big|_{x=\zeta} \quad (4.44)$$

$$\partial_\tau \zeta = -4\xi. \quad (4.45)$$

The physical interpretation of this approximation is that the interaction parameter does not vary over the width of the soliton. Focusing more specifically on a collisional inhomogeneity of the form of Eq. (4.5) where these contributions vanish exactly, leads to

$$\partial_\tau \eta = \eta \xi \frac{8C}{D + C\zeta} \quad (4.46)$$

$$\partial_\tau \xi = \frac{8}{3}\eta^2 \frac{C}{D + C\zeta} \quad (4.47)$$

$$\partial_\tau \zeta = -4\xi. \quad (4.48)$$

We can solve the simplified Eq. (4.46) directly by using Eq. (4.48):

$$\eta = \eta(0) \frac{[C\zeta(0) + D]^2}{[C\zeta + D]^2}. \quad (4.49)$$

Combination of Eqs. (4.47-4.49) and back transformation to the real time t leads to the equation of motion for the soliton center:

$$\partial_t^2 \zeta = -\frac{8}{3}C\eta(0)^2 \frac{[C\zeta(0) + D]^4}{[C\zeta + D]^5}, \quad (4.50)$$

with an associated effective potential:

$$V^{eff}(\zeta) = \frac{2}{3}\eta(0)^2 \frac{[C\zeta(0) + D]^4}{[C\zeta + D]^4}. \quad (4.51)$$

4.3.3 Numerical Results

Figure 4.4 shows the time evolution of the density of the bright soliton (note that, in contrary to before, black represent zero density, while white represents high density). The results are

obtained by integration of Eq. (4.4) with an initial state given by Eq. (4.34) with parameters initialized as $\eta = 0.5$, $\Phi = \zeta = 0$ and $\xi_{init} = 0, 0.25, 0.5$ (from top to bottom). The dotted line shows the corresponding results for the center of the soliton ζ obtained by solving Eqs. (4.39-4.42). The results of the perturbation theory once again agree very well with the results of the PDE. In the case of zero initial velocity (top curve), the soliton gets accelerated to the positive half-plane and starts moving into this direction immediately. For positive ξ_{init} the initial velocity is negative, according to Eq. (4.40), leading to a motion towards the negative half-plane. However, the soliton still moves toward the direction of the positive half-plane, due to its initial speed, yet eventually it acquires a zero velocity and a change of the direction of motion occurs. The direction of the acceleration is the direction of increasing interaction parameter as can be seen by comparing the results with Fig. 4.1, as this minimizes the energy of the system (even though the interaction does not act, strictly speaking, as a potential).

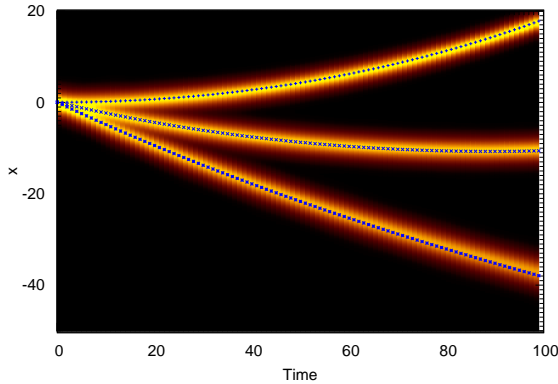


Figure 4.4: Time evolution of the density of a bright soliton with initial parameter $\eta = 0.5$, $\Phi = \zeta = 0$ and $\xi_{init} = 0, 0.25, 0.5$ (from top to bottom). The dotted line shows the result for ζ (the center of the soliton) from the adiabatic perturbation theory.

Figure 4.5 shows the difference of the center of the soliton calculated by the PDE with the results of the ODEs (4.39-4.41) and the EOM (4.50). The center of the soliton of the PDE solution is determined by the quotient

$$\zeta = \int x|u|^2 dx / \int |u|^2 dx. \quad (4.52)$$

Figure 4.5a shows the differences for $\eta = 0.5$, $\Phi = \zeta = 0$ and $\xi_{init} = 0$. The difference of the EOM result from the PDE result is slightly larger than the difference of the ODE result. Both differences increase with time but they are still very small for the time period considered. Fig. 4.5b shows the differences for $\eta = 0.5$, $\Phi = \zeta = 0$ and $\xi_{init} = 0.5$. In this case, the absolute differences are an order of magnitude larger than in the previous case. However, compared to the position and width of the soliton one can still regard them as small. The results of the ODEs and the EOM are almost equal. A conclusion of this investigation is that the dynamics of the soliton is described fairly accurately by the model of a particle subject to the effective potential (4.51).

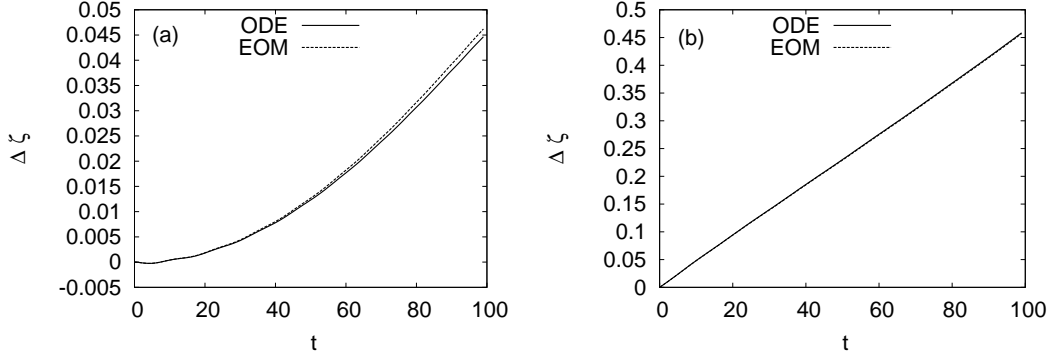


Figure 4.5: Difference of the soliton center calculated by solving the ODE and EOM to the result of the PDE with initial parameter $\eta = 0.5$, $\Phi = \zeta = 0$ and $\xi_{init} = 0$ (a) or $\xi_{init} = 0.5$ (b).

4.4 Conclusions

In this chapter, we considered the effect of (slowly-varying) spatially dependent nonlinearities of a definite sign on both dark and bright matter-wave solitons of repulsive and attractive Bose-Einstein condensates, respectively. We have shown that a relevant transformation can be employed to convert the spatially dependent nonlinear problem into one of spatially uniform nonlinearity, at the expense of introducing two perturbative terms. One of the latter is in the form of a linear potential (which have been considered extensively previously), while the other constitutes a non-potential type of perturbation, being proportional to the spatial derivative of the field. To especially highlight the non-potential nature of the second term, we considered collisional inhomogeneities of inverse square spatial dependence, whereby the linear potential perturbation identically vanishes, and the purely non-potential one has to be considered. Even in these settings (but also more generally), we found that soliton perturbation theory provides a powerful tool towards describing such collisional inhomogeneities.

Chapter 5

Dark Solitons in Cigar-Shaped Bose-Einstein Condensates in Double-Well Potentials

In this chapter we study the statics and dynamics of dark solitons in a cigar-shaped Bose-Einstein condensate confined in a double-well potential. So far, there exist only a few studies on matter-wave dark solitons in double-well potentials [243, 244]. In particular, Ref. [243] was devoted to the study of nonlinearity-assisted quantum tunneling and formation of dark solitons in a matter-wave interferometer, which is realized by the adiabatic transformation of a double-well potential into a single-well harmonic trap. On the other hand, in Ref. [244], the stability of the first excited state of a quasi-1D BEC trapped in a double-well potential was studied and regimes of (in)stability were found; note that in the nonlinear regime, the first excited state of the BEC is nothing but the stationary “black” soliton — alias “kink” — solution of the pertinent 1D GP equation.

We study dark soliton states in cigar-shaped BECs — being in the dimensionality crossover regime from 3D to 1D — confined in double-well potentials that are formed by a combination of a harmonic trap and an optical lattice. Our aim is to systematically study, apart from the single stationary dark soliton (see Ref. [244] for a study in the TF-1D regime), multiple dark soliton states as well; such a study is particularly relevant, as many dark solitons can be experimentally created by means of the matter-wave interference method, as demonstrated in Refs. [110, 112]. Our study starts from the non-interacting (linear) limit, where we obtain the pertinent excited states of the BEC and, then, using continuation in the chemical potential (number of atoms), we find all branches of purely nonlinear solutions, including the ground state and single or multiple dark solitons, and their bifurcations. An important finding of our analysis is that the optical lattice (which sets the barrier in the double-well setting) results in the emergence of nonlinear states that do not have a linear counterpart, such as dark soliton states, with solitons located in one well of the double-well potential. As concerns the bifurcations of the various branches of solutions, we show that particular states emerge or disappear for certain chemical potential thresholds, which are determined analytically, in some cases, by using a Galerkin-type approach [48]. For each branch, we also study the stability of the pertinent solutions via a Bogoliubov-de Gennes (BdG) analysis. Furthermore, based on the weakly-interacting limit of the model, we study analytically small-amplitude oscillations of the one- and multiple-dark-soliton states. Particularly, we obtain equations of motion for the single and multiple solitons from which we determine the characteristic soliton frequencies; the latter, are found to be, in many cases in good agreement with the eigenfrequencies found in the framework of the BdG analysis. The results of this chapter are published partly in Ref. [245].

The chapter is organized as follows. We present our model in section 5.1 and provide the theoretical framework of our analysis. In Sec. 5.2, we study the bifurcations of the branches of the solutions of the model and study their stability via the BdG equations. In Sec. 5.3, we

provide some analytical estimates for the soliton frequencies based on the dynamics of solitons and compare our findings to the ones obtained by the BdG analysis. Sec. 5.4 is devoted to a study of the soliton dynamics numerically, and shows the manifestation of instabilities when they arise. Finally, in Sec. 5.5, we present our conclusions.

5.1 Model and Theoretical Framework

5.1.1 The Effective 1D Mean-Field Model and Bogoliubov Analysis

We consider a BEC confined in a highly elongated trap, with longitudinal and transverse confining frequencies (denoted by ω_z and ω_{\perp} , respectively) such that $\omega_z \ll \omega_{\perp}$. In contrary to the previous chapters we do not apply the 1D GPE in this chapter for describing the condensate. Most experiments investigating solitons are not in the 1D regime and importantly this leads to a modification of the soliton oscillation frequency in a trap (cf. section 5.3.1 for a detailed discussion). Therefore we apply the effectively 1D mean-field model describing cigar shaped condensates with a non-cubic interaction derived in section 2.2.3. In this chapter we apply the Gerbier equation (2.34), however applying the non-polynomial Schrödinger equation (2.40) would lead to similar results. The Gerbier equation reads

$$i\hbar\partial_t\psi = \left[-\frac{\hbar^2}{2m}\partial_z^2 + V_{\text{ext}}(z) + \hbar\omega_{\perp}\sqrt{1+4a|\psi|^2} \right] \psi, \quad (5.1)$$

where $\psi(z, t)$ is normalized to the number of atoms, i.e., $N = \int_{-\infty}^{+\infty} |\psi|^2 dz$, a is the s -wave scattering length, m is the atomic mass, and $V_{\text{ext}}(z)$ is the longitudinal part of the external trapping potential.

Let us now assume that the trapping potential is a superposition of a harmonic trap and an optical lattice, characterized by an amplitude V_0 and a wavenumber k , namely,

$$V_{\text{ext}}(z) = \frac{1}{2}m\omega_z^2 z^2 + V_0 \cos^2(kz). \quad (5.2)$$

It is clear that a proper choice of the potential parameters (and the number of atoms) may readily lead to a trapping potential that has the form of an effective double well potential; in such a setting, the height of the barrier can be tuned by the amplitude of the optical lattice. In our considerations below, we consider the case of a ^{87}Rb condensate, confined in a harmonic trap with frequencies $\omega_{\perp} = 10\omega_z = 2\pi \times 400\text{Hz}$ (these values are relevant to the experiments of Refs. [110, 112]); furthermore, we will vary the optical lattice strength in the range of $V_0 = 0$ to $V_0 = 1.16 \times 10^{-12} \text{ eV}$, thereby changing the trapping potential from a purely harmonic form to a double-well potential. Finally, we will assume a fixed value of the optical lattice wavenumber, namely $k = \pi/5.37 \mu\text{m}^{-1}$.

Next, assuming that the density, length, time and energy are measured, respectively, in units of a , $\alpha_{\perp} \equiv \sqrt{\hbar/m\omega_{\perp}}$ (transverse harmonic oscillator length), ω_{\perp}^{-1} , and $\hbar\omega_{\perp}$, we express Eq. (5.1) in the following dimensionless form,

$$i\partial_t\psi = \hat{H}\psi + \sqrt{1+4|\psi|^2}\psi, \quad (5.3)$$

where $\hat{H} = -(1/2)\partial_z^2 + (1/2)\Omega^2 z^2 + V_0 \cos^2(kz)$, is the usual single-particle Hamiltonian and

$\Omega \equiv \omega_z/\omega_{\perp}$ is the normalized harmonic trap strength (note that the normalized optical lattice strength V_0 is measured in the units of energy $\hbar\omega_{\perp}$).

Below, we will analyze the stability of the nonlinear modes of Eq. (5.3) by means of the BdG equations. It is clear that the BdG equations derived from the Gerbier equation differ from the 'standard' BdG equations (2.69-2.70) derived from the GPE. However one can use the same scheme as described in section 2.4 for deriving the following BdG equations:

$$[\hat{H} - \mu + f]u + gv = \omega u, \quad (5.4)$$

$$[\hat{H} - \mu + f]v + gu = -\omega v, \quad (5.5)$$

where μ is the chemical potential, and the functions f and g are given by $f = g + \sqrt{1 + 4n_0}$, and $g = 2\psi_0^2/\sqrt{1 + 4n_0}$ (with $n_0 \equiv |\psi_0|^2$).

Then, solving Eqs. (5.4-5.5), we determine the eigenfrequencies $\omega \equiv \omega_r + i\omega_i$ and the amplitudes u and v of the normal modes of the system. Note, the system possesses again an Hamiltonian structure and therefore holds if ω is an eigenfrequency of the Bogoliubov spectrum, so are $-\omega$, ω^* and $-\omega^*$, and consequently the occurrence of a complex eigenfrequency leads again to a dynamic instability. Thus, a linearly stable configuration is tantamount to $\omega_i = 0$, i.e., all eigenfrequencies being real. Moreover, one can define the Krein sign of a mode in the same way as described in section 2.4.

5.1.2 Dark Soliton States

Exact analytical dark soliton solutions of non-linear Schrödinger (NLS) equations with a generalized defocusing nonlinearity, such as Eq. (5.3), are not available. In fact, in such cases, dark solitons may only be found in an implicit form (via a phase-plane analysis) or in an approximate form (via the small-amplitude approximation) [246]. Nevertheless, exact analytical dark soliton solutions of Eq. (5.3) can be found in the weakly-interacting limit ($4|\psi|^2 \ll 1$), and in the absence of the external potential: in this case, Eq. (5.3) is reduced to the completely integrable cubic NLS model, which possesses single- and multiple-dark-soliton solutions on top of a background with constant density $n = n_0 = \mu$ (cf. section 2.3.2).

Generally, the single dark soliton, as well as all higher-order dark soliton states, can be obtained in a stationary form from the *non-interacting* (linear) limit of Eq. (5.3), corresponding to $N \rightarrow 0$ [247, 248]. In this limit, Eq. (5.3) is reduced to a linear Schrödinger equation for a confined single-particle state, namely the equation of the quantum harmonic oscillator, together with the contribution of the optical lattice. However, due to the presence of the harmonic trap, the problem is characterized by discrete energy levels and corresponding localized eigenmodes. In the *weakly-interacting* limit, where Eq. (5.3) is reduced to the cubic NLS equation, all these eigenmodes exist for the nonlinear problem as well [247, 248], describing an analytical continuation of the linear modes to a set of nonlinear stationary states. Recent analysis and numerical results [249] (see also Ref. [112]) suggest that there are no solutions of Eq. (5.3) without a linear counterpart, at least in the case of a purely harmonic potential. However, as we will show below, the presence of the optical lattice in the model results in the occurrence of additional states, for sufficiently large nonlinearity (large atom numbers), which do not have a linear counterpart.

Next, let us discuss the dynamics of dark solitons in the considered setup with an external potential in the weakly-interacting limit ($4|\psi|^2 \ll 1$). Therefore, we factorize the total wave

function $\psi = n_0 u$ into the background density n_0 and the soliton wave function u . We assume that the background density is given by the ground state wave function of the condensate and that we can use the TF approximation to describe the latter. Then Eq. (5.3) may be expressed as a perturbed NLS equation for the soliton wave function u , namely,

$$i\partial_t u + \frac{1}{2}\partial_z^2 u - \mu(|u|^2 - 1)u = P(u), \quad (5.6)$$

where the effective perturbation $P(u)$ is given by:

$$P(u) = (1 - |u|^2)Vu + \frac{1}{2} \frac{1}{\mu - V(z)} \frac{dV}{dz} \frac{\partial u}{\partial z}. \quad (5.7)$$

Here, $V(z) = (1/2)\Omega^2 z^2 + V_0 \cos^2(kz)$ is the trapping potential, and all terms of $P(u)$ are assumed to be of the same order. Furthermore, assuming that the length scale of the trap is much larger than the width of the soliton, one can apply the adiabatic perturbation theory for dark solitons devised in Ref. [122, 250] to derive the following equation of motion for the slowly-varying dark soliton center $z_0(t)$ [138]:

$$\frac{d^2 z_0}{dt^2} = -\frac{1}{2} \frac{dV_{\text{eff}}}{dz_0}, \quad (5.8)$$

where the effective potential felt by the soliton is given by:

$$V_{\text{eff}}(z) = \frac{1}{2}\Omega^2 z^2 + \frac{1}{2}V_0 \left[1 - \left(\frac{\pi^2}{3} - 2 \right) \frac{k^2}{6\mu} \right] \cos(2kz). \quad (5.9)$$

At this point we should make the following remarks. First, for the derivation of Eq. (5.8), it was assumed that the background density of the condensate can be described via the TF approximation; this actually means that Eq. (5.8) is valid only for sufficiently large number of atoms. At the same time, however, the derivation of Eq. (5.8) was done in the framework of the cubic NLS model, i.e., the weakly-interacting limit of Eq. (5.3), which is valid for sufficiently small number of atoms. Nevertheless, Eq. (5.8) may still be relevant to provide some estimates. It is known that the soliton oscillation frequency (for a BEC confined in a harmonic trap) is up-shifted for large number of atoms due to the dimensionality of the system (i.e., the effect of transverse dimensions, which are taken into regard in the derivation of Eq. (5.3)) [140]. Particularly, one should expect that in the case of a purely harmonic trap the soliton oscillates with a frequency $\omega_{\text{ds}} > \Omega/\sqrt{2}$, which can be found numerically in the absence of the optical lattice (note that $\Omega/\sqrt{2}$ is the characteristic value of the soliton oscillation frequency in a 1D harmonic trap of strength Ω in the TF limit [118–126]). For a more detailed discussion see section 5.3.1. Moreover, for sufficiently small optical lattice wave numbers (such as the chosen value of $k = \pi/5.37\mu\text{m}^{-1}$), and large chemical potentials (TF limit) the effective potential of Eq. (5.9) can be simplified to the following form:

$$V_{\text{eff}}(z) = \omega_{\text{ds}}^2 z^2 + \frac{1}{2}V_0 \cos(2kz). \quad (5.10)$$

We complete this section by mentioning that the case of two (or more) spatially well separated solitons can also be treated analytically, taking into account the repulsive interaction

potential between two solitons. In the case of two spatially separated solitons located at z_1 and z_2 , on top of a constant background with density n_0 , the interaction potential takes the form [112],

$$V^{\text{int}}(z_1, z_2) = \frac{n_0}{\sinh^2(\sqrt{n_0}(z_2 - z_1))}. \quad (5.11)$$

5.2 Bifurcation and Bogoliubov Analysis

Let us now proceed by investigating the existence, the stability and possible bifurcations of the lowest macroscopically excited states of Eq. (5.3). We fix the parameter values as follows: $\Omega = 0.1$, $k = \pi/5.37 \mu\text{m}^{-1}$ and $V_0 = 1.16 \times 10^{-12} \text{ eV}$; for such a choice, the four lowest eigenvalues of the operator $1 + \hat{H}$ (corresponding to the linear problem) are found to be:

$$\omega_0 = 2.138 \times 10^{-12} \text{ eV}, \omega_1 = 2.142 \times 10^{-12} \text{ eV}, \omega_2 = 2.634 \times 10^{-12} \text{ eV}, \omega_3 = 2.700 \times 10^{-12} \text{ eV}, \quad (5.12)$$

and the energy of the first excited state is almost degenerate with that of the ground state, i.e., $\omega_0 \sim \omega_1$.

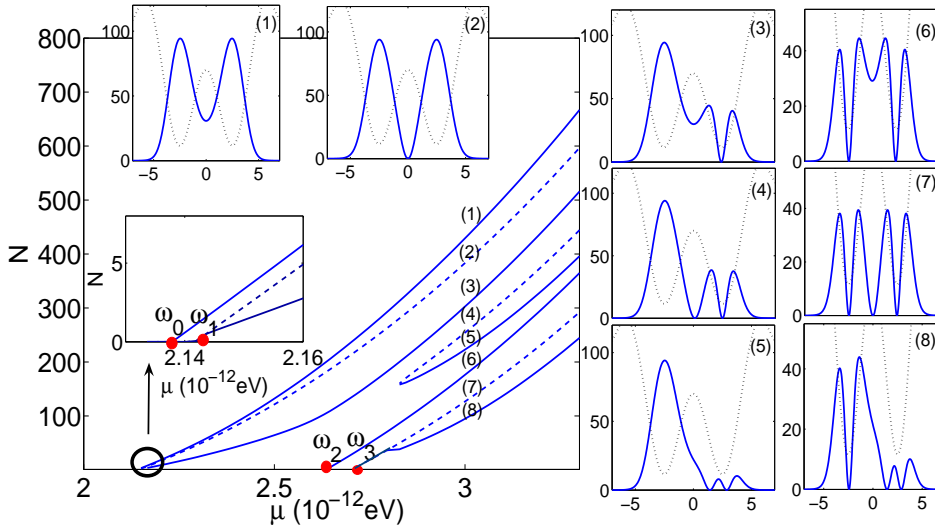


Figure 5.1: Number of atoms as a function of the chemical potential for the different states. The potential parameters are $\Omega = 0.1$, $k = \pi/5.37 \mu\text{m}^{-1}$ and $V_0 = 1.16 \times 10^{-12} \text{ eV}$. The inset shows the spatial density profiles for $\mu = 3 \times 10^{-12} \text{ eV}$.

Fig. 5.1 shows the number of atoms as a function of the chemical potential for different branches of solutions. The insets show the spatial density profiles for $\mu = 3 \times 10^{-12} \text{ eV}$, with the units of the horizontal and vertical axes being given by μm and $1/\mu\text{m}$, respectively.

Branch (1) corresponds to the states with the largest number of atoms, for fixed chemical potential. The respective states are symmetric and have no nodes. Continuation of this symmetric branch to the linear limit ends at the eigenvalue ω_0 , corresponding to the ground state of the linear problem.

The second branch [branch (2)] starts from the first excited state in the linear limit, $\mu \rightarrow \omega_1$ as $N \rightarrow 0$. The wave functions of the states of this branch are *antisymmetric* and have a node

at the center of the barrier, while their densities are symmetric. From this density symmetric one-soliton branch, two asymmetric one-soliton branches, namely branch (3) and its mirror image with respect to the $z = 0$ axis, bifurcate close to the linear limit, at $\mu \simeq 2.144 \times 10^{-12}$ eV – see the close-up inset. Let us define a local occupation number, i.e., number of atoms in the different wells, as the integral over the density up to the center of the barrier (see also section 5.4). The occupation number in the well with the node is then smaller than the occupation number without the node. This can be explained by the fact that the state with one node is the first excited state, characterized by a higher energy than the one without a node, which is the ground state. Thus, in order to balance the chemical potential in both wells one needs a larger interaction energy (i.e., more atoms) in the well without a node. Note that the macroscopic quantum self-trapping (MQST) state as predicted in Ref [39–41] and discussed in chapter 3 is not considered in what follows. The reason for that is that the MQST is a running phase state while our bifurcation analysis below focuses on the stationary states of the system. Branches (4) and (5) have no linear counterparts since at $\mu \simeq 2.828 \times 10^{-12}$ eV they “collide” and disappear. The states that belong to these branches are asymmetric, exhibiting two nodes. The state with larger number of atoms (for a fixed chemical potential) has one node approximately at the barrier and one node in one well. The other state has both nodes in one well. Once again, the occupation number in the well with two nodes is less than the one of the well with one node, so as to balance the chemical potential.

Branch (6) starts from the second excited state of the linear problem, hence $\mu \rightarrow \omega_2$ as $N \rightarrow 0$. Therefore, the density of the respective state is symmetric and there is one node in each well.

Branch (7) starts from the third excited state of the linear problem, and $\mu \rightarrow \omega_3$ as $N \rightarrow 0$. The states belonging to this branch have three nodes, one located in each well and one at the barrier, and are symmetric. Close to the linear limit, at $\mu \simeq 2.795 \times 10^{-12}$ eV, two asymmetric three-soliton branches, namely branch (8) and its mirror image with respect to the $z = 0$ axis, bifurcate from this state. This state has two nodes in one well and one in the other. The occupation number in the well with more nodes is smaller than in the well with just one node in order to balance the chemical potential. Notice that there exist two more three-soliton branches without linear counterparts, but they only occur at higher chemical potentials — where the BEC has occupied four-wells rather than two — so they will not be considered here.

Next, let us study the stability of the states belonging to the above mentioned branches by considering the respective excitation spectra, shown in Fig. 5.2. In this figure, the (blue) $*$ symbol denotes a positive Krein sign mode (or a zero one for a vanishing frequency), the (green) \times symbol a negative Krein sign mode, i.e., a negative energy *anomalous mode*, and the (red) $(+)$ symbol a vanishing Krein sign, i.e., an eigenmode associated with complex/imaginary eigenfrequency. Generally speaking, there are two different kinds of instability, corresponding to the cases of either a purely imaginary eigenfrequency, or a genuinely complex eigenfrequency. The latter case gives rise to the so-called oscillatory instability, stemming from the collision of a negative energy mode with one of positive energy.

The first panel of Fig. 5.2 shows the BdG spectra along the first branch. The imaginary part is zero for every value of the chemical potential, a fact reflecting the stability of this state. The absence of negative energy modes is expected, as this state is actually the ground state of the system. Since the BdG spectrum refers to all excitations of the state, one can attribute in the linear limit to each mode an excited state of the linear problem. The energy

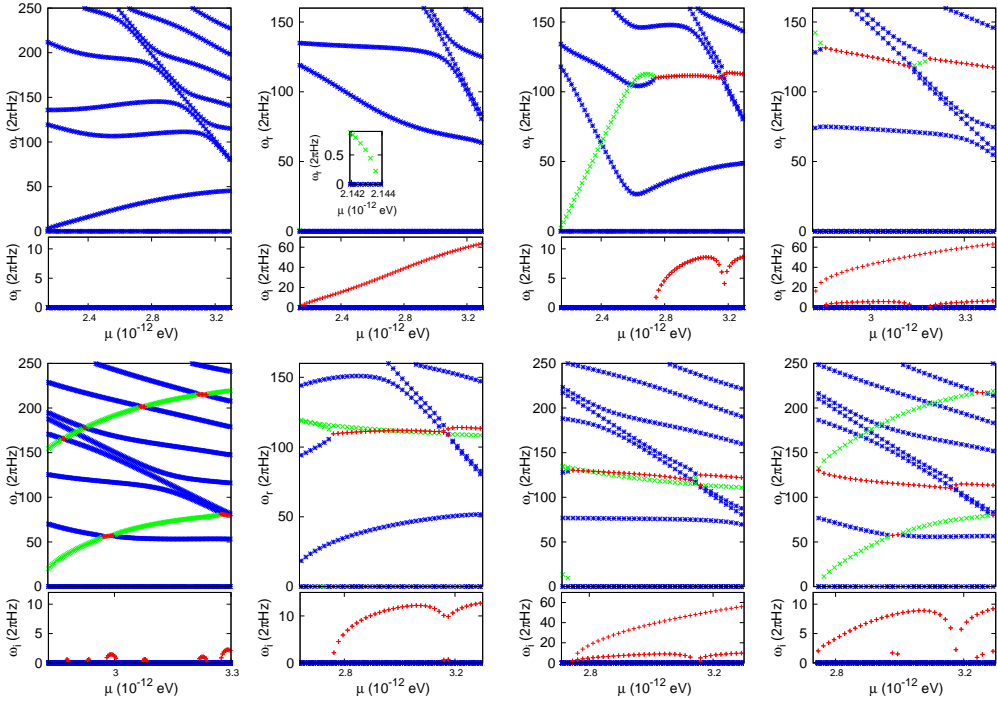


Figure 5.2: BdG Spectrum of the states shown in Fig. 5.1. First panel shows the spectrum of the first branch, second panel the spectrum of the second branch and so forth. The (blue) \ast symbol denotes an eigenmode of positive Krein sign (or zero Krein sign for a vanishing eigenfrequency), the (green) \times symbol an eigenmode of negative Krein sign, and the (red) $+$ symbol an eigenmode associated to a vanishing Krein sign with complex/imaginary eigenfrequency.

gap between the ground state and the first excited state corresponds to the energy of the first mode. Since the frequency of the so-called *bosonic Josephson junction*, namely the oscillation frequency characterizing the transfer of atoms between the two wells, is equal to this frequency in the linear limit, this mode is connected to the oscillation of atoms between the two wells. We investigate this fact in more detail below (see Sec. 5.4) by direct simulations in the framework of Eq. (5.3). The frequency value of the second nonzero BdG mode of the ground state spectrum is correspondingly equal to the energy gap between the ground state and the second excited state in the linear limit, and so forth. We define the difference in the way that these frequency differences are positive.

The second panel shows the BdG spectra along the second branch, solutions of which represent states with a density minimum at the center of the barrier. In the linear limit one can assign to each mode an energy difference of the linear problem similar as in the BdG spectrum of the ground state. However in this case the frequency difference of the first excited state to the ground state is negative (according to our definition) leading to a negative energy mode. As one can see in the inset, the lowest mode has negative energy close to the linear limit. However, increasing the chemical potential the eigenfrequency of this mode is moving rapidly towards the origin of the spectrum and, at $\mu = 2.1437 \times 10^{-12}$ eV, becomes and remains purely imaginary, thus carrying zero energy (red $+$ symbols). This happens exactly at the point where the third branch bifurcates as one can see in the inset of Fig. 5.1. For the above mentioned potential parameters, this bifurcation happens in the

weakly-interacting regime, where Eq. (5.3) reduces to the cubic NLS equation. Thus, one can apply the Galerkin-type approach of Ref. [48] and find that the critical value of the norm N at which the bifurcation occurs is given by

$$N_{\text{cr}} = \frac{\omega_1 - \omega_0}{3B - A_1}, \quad (5.13)$$

where $\omega_{0,1}$ are the first two lowest eigenvalues of the operator $1 + \hat{H}$, $A_1 = \int \psi_1^4 dz$, $B = \int \psi_0^2 \psi_1^2 dz$, while $\psi_{0,1}$ denote the ground state and the first excited state of the operator $1 + \hat{H}$, respectively. One can also determine the critical chemical potential at which the symmetry breaking is expected to occur, namely $\mu_{\text{cr}} = 1 + \omega_0 + 3BN_{\text{cr}}$ [48] leading for (these parameter values) to $\mu_{\text{cr}} = 2.1436 \times 10^{-12}$ eV, which is in very good agreement with our numerical findings.

The third panel shows the BdG spectra along the third branch which bifurcates at $\mu = 2.1437 \times 10^{-12}$ eV from the second one. All the eigenfrequencies of the arising asymmetric state are real close to the linear limit, thus it is concluded that this state is linearly stable and that the bifurcation is a supercritical pitchfork. This state has one negative energy mode as well, since it is a one-soliton state. The eigenfrequency of the negative energy mode increases with increasing chemical potential, passes through the mode corresponding to the second excited state of the linear limiting case, and finally collides at some critical value of the chemical potential, $\mu = 2.76 \times 10^{-12}$ eV, with the mode corresponding to the third excited state; this results in the generation of a quartet of unstable eigenfrequencies and, at this point, the state becomes oscillatory unstable. However, the magnitude of the instability is much smaller than in the previous case of the purely imaginary eigenfrequency.

The fourth and fifth panel show the spectra along the fourth and fifth branch, the solutions of which correspond to asymmetric two-soliton states having no linear counter-part. The previous one has got one imaginary and one negative energy mode and the latter one has two negative energy modes. These modes result from the presence of two dark solitons. The state considered in the fourth panel has two dark solitons, one soliton located approximately at the barrier and one soliton in one well. The eigenfrequency corresponding to the former one is purely imaginary and looks similar to the mode of the symmetric one soliton state of the second panel. The eigenfrequency of the other anomalous mode decreases with increasing chemical potential and collides with a mode with positive energy, thus generating a quartet of complex eigenfrequencies. The magnitude of the imaginary part is again much smaller than the magnitude of the purely imaginary eigenfrequency. The generation of dynamic instabilities is illustrated, e.g., in panel five. The collision of one of the anomalous modes with a mode of positive Krein sign could lead to the emergence of a quartet of complex eigenfrequencies, resulting in the concurrent presence of an apparent level crossing in the real part of the eigenfrequency along with a nonzero imaginary part of the relevant eigenfrequency mode.

At $\mu \simeq 2.828 \times 10^{-12}$ eV, the states of the fourth and fifth branch collide and disappear as can be seen in Fig. 5.1. Just before the collision (for slightly larger μ), the state of the fourth branch is unstable due to the presence of a mode with imaginary eigenfrequency in the BdG spectrum, while the state of the fifth branch is linearly stable since all the BdG eigenfrequencies have only real parts. Thus, it can be concluded that, at this critical point, a saddle-node bifurcation occurs, readily destroying these two states.

The sixth panel shows the BdG spectra along the sixth branch, the solutions of which correspond to symmetric two-soliton states. This branch has a linear counterpart, and we can assign to each mode in the linear limit an energy difference of the linear problem. The negative energy modes occur for negative energy differences, e.g., at the energy difference to the ground state and the first excited state. The anomalous modes here are close to being degenerate. Physically speaking, this reflects the fact that the dark solitons are essentially decoupled at the linear limit due to the presence of the optical lattice. The negative energy modes are not the modes with the lowest eigenfrequency. The energy gaps between the second excited state and the third and fourth excited state, respectively, are smaller than the gaps between the ground state and the first excited state. Therefore, these modes with positive energy occur in the linear limit at lower frequencies. One of the negative energy modes collides at some critical value of the chemical potential with the mode stemming from the fourth excited state and forms a quartet of complex frequencies, thus leading to an oscillatory instability.

The seventh panel shows the BdG spectra along the seventh branch, the solutions of which corresponds to the symmetric three-soliton state exhibiting a linear counterpart. The negative energy modes occur at the energy gaps to the ground state, the first and the second excited states. The eigenfrequency of the latter becomes, for increasing μ , purely imaginary at the point where the eighth branch bifurcates. The other two anomalous modes are almost degenerate, reflecting again the fact that the solitons in the different wells are almost decoupled. One of the negative energy modes collides with a mode with positive energy and forms a quartet of complex frequencies. However, the magnitude of the imaginary part is much smaller than the magnitude of the purely imaginary mode. The behavior of the purely imaginary mode is similar to the behavior of the mode in panel two (describing a single soliton at the center of the barrier). The behavior of the other two modes is similar to the modes in panel six describing one soliton in each well.

Finally, the eighth panel shows the BdG spectra along the eighth branch, the solutions of which corresponds to the asymmetric three-soliton state. This state, which has two solitons in one well and one soliton in the other well, emerges at $\mu \sim 2.74 \times 10^{-12}$ eV, where the seventh state (i.e., the one corresponding to the nonlinear continuation of the third excited state), becomes unstable. The critical value of the number of atoms for which the bifurcation occurs can be predicted in the same way as for the bifurcation of the one soliton branch; the result is:

$$N_{\text{cr}}^{(3)} = \frac{\omega_3 - \omega_2}{3D - C_1}, \quad (5.14)$$

where $\omega_{2,3}$ are the third and fourth lowest eigenvalues of operator $1 + \hat{H}$, $C_1 = \int \psi_3^4 dz$, $B = \int \psi_2^2 \psi_3^2 dz$, while $\psi_{2,3}$ denote the second and third excited state of the operator $1 + \hat{H}$, respectively. The corresponding critical chemical potential is then given by $\mu_{\text{cr}}^{(3)} = 1 + \omega_2 + 3BN_{\text{cr}}^{(3)}$ leading (for these parameters) to $\mu_{\text{cr}}^{(3)} = 2.7420 \times 10^{-12}$ eV, which is in very good agreement with the numerical critical point given above.

Right after the bifurcation, the asymmetric three soliton states are stable and, thus, we can conclude that the bifurcation is of the supercritical pitchfork type. Two modes look similar to the negative energy modes in panel five describing a two-soliton state in one well and the third mode looks similar to a mode of one-soliton in a harmonic trap.

From the above analysis, we can readily derive some general conclusions concerning dark

soliton states in a double well potential. The sum of negative energy modes and imaginary eigenfrequency modes is equal to the number of nodes in the wave function profile which, for large values of the chemical potential, represent dark solitons. In the linear limit, the BdG eigenfrequencies of a state correspond to the energy differences between that and other states of the linear system. For a negative energy difference the corresponding mode has a negative energy. Dark solitons located at the center of the barrier are known to be linearly unstable (for sufficiently high chemical potential) associated with a purely imaginary eigenfrequency [134, 135, 244]. Thus, symmetric states with an odd number of nodes always have a mode which, above a critical value of the chemical potential, becomes purely imaginary. At this critical point additional stable asymmetric dark-soliton states emerge through supercritical pitchfork bifurcations.

5.3 Statics vs. Dynamics of Dark Soliton States

5.3.1 The One-Soliton State

Having investigated in detail the statics of matter-wave dark solitons in double-well potentials, we now proceed to compare these results to the soliton dynamics, using the theoretical background exposed in section 5.1.2. Particularly, considering the case of a single dark soliton, we can readily obtain from Eqs. (5.8) and (5.10) the following approximate equation of motion for the dark soliton center:

$$\frac{d^2 z_0}{dt^2} = -\omega_{ds}^2 z_0 + \frac{1}{2} k V_0 \sin(2kz_0). \quad (5.15)$$

It is straightforward to find the fixed points $z_o, p_o \equiv dz_o/dt$ of the above dynamical system, which are given by

$$p_o = 0, \quad z_o = \frac{kV_0}{2\omega_{ds}^2} \sin(2kz_o). \quad (5.16)$$

It is clear that the fixed points correspond to intersections of the straight line $f_1(z_o) = z_o$ and the sinusoidal curve $f_2(z_o) = \frac{kV_0}{2\omega_{ds}^2} \sin(2kz_o)$. The fixed point at $(z_o, p_o) = (0, 0)$ exists for all choices of (Ω, V_0, k) . This equilibrium corresponds to the symmetric one-soliton state, namely a stationary black soliton located at the center of the potential. In the absence of the optical lattice (i.e., for $V_0 = 0$) this is the only existing fixed point, i.e., in the case of a purely harmonic trap, only a symmetric one-soliton state can exist, which originates from the first excited state of the linear problem. On the other hand, when the optical lattice is present (i.e., for $V_0 \neq 0$), this situation changes and more fixed points arise when the slope of the curve $f_2(z_o)$ at the origin becomes larger than the one of the straight line $f_1(z_o)$, namely when $k^2 V_0 / \omega_{ds}^2 > 1$, two new fixed points appear through a supercritical pitchfork, with the newly emerging states corresponding to the bifurcating asymmetric one-soliton states. Therefore, the bifurcating state appears only for a sufficiently strong optical lattice, such that $V_0 > V_{0,cr} \equiv \omega_{ds}^2/k^2$. Note that for even larger values of the parameter $k^2 V_0 / \omega_{ds}^2$ more fixed points appear, corresponding to solitons located in further (i.e., more remote from the trap center) wells of the optical lattice; for this reason, these states are not considered herein.

Let us now investigate the spectral stability of the fixed points employing the linearization technique (see, e.g., Ref. [251]). Particularly, we first find the corresponding Jacobian matrix

(evaluated at the fixed points), which is given by:

$$\mathbf{J} = \begin{pmatrix} 0 & 1 \\ -\omega_{ds}^2 + k^2 V_0 \cos(2kz_0) & 0 \end{pmatrix}.$$

When evaluated at the trivial fixed point $(z_0, p_0) = (0, 0)$, the corresponding eigenvalue problem for the Jacobian, $\det(\mathbf{J} - \lambda \mathbf{I}) = 0$, leads to eigenvalues $\lambda^2 = -\omega_{ds}^2 + k^2 V_0$. It is clear that in the case of $k^2 V_0 / \omega_{ds}^2 < 1$, the eigenvalues are imaginary (note that, accordingly, the eigenfrequencies are real since $\omega = i\lambda$) and, thus, the fixed point $(0, 0)$ is a center. In this case, if the dark soliton is weakly displaced from the center of the trap, it performs harmonic oscillations around the center with an oscillation frequency given by $\omega_{osc} = \sqrt{\omega_{ds}^2 - k^2 V_0}$. On the other hand, if $k^2 \frac{V_0}{\omega_{ds}^2} > 1$ then the eigenvalues become real (and, accordingly, the eigenfrequencies are imaginary), hence $(0, 0)$ becomes a saddle point, while the respective imaginary eigenfrequency is given by $\omega_{osc} = i\sqrt{|\omega_{ds}^2 - k^2 V_0|}$. For the newly bifurcating (stable, since $V_0 > \omega_{ds}^2/k^2$) fixed points one can obtain the following eigenfrequency

$$\omega_{osc} = \sqrt{\omega_{ds}^2 - k^2 V_0 \cos(2kz_0)}. \quad (5.17)$$

From the above analysis it is clear that the supercritical pitchfork occurs at

$$V_{0,cr} = \frac{\omega_{ds}^2}{k^2}. \quad (5.18)$$

Based on the above, one can make the following estimates and comparisons to numerical results: in the TF limit, and in the weakly-interacting case (i.e., in the framework of the 1D cubic GP equation), the dark soliton oscillation frequency is predicted to be $\omega_z/\sqrt{2} = 28.28$ Hz. However, as mentioned in Sec. 5.1.2, a larger value of this frequency is expected in the framework of Eq. (5.3), due to the effect of the dimensionality of the system. Employing a BdG analysis in the case of a pure harmonic trap, we find that the anomalous mode eigenfrequency (i.e., the soliton oscillation frequency) decreases with increasing chemical potential and asymptotically reaches the value $\omega_{ds} = 30.36$ Hz (see first panel of Fig. 5.4 below). Using this value (and for $k = \pi/5.37\mu m^{-1}$), one obtains $V_{0,cr} = 9.6 \times 10^{-14}$ eV.

In the top panel of Fig. 5.3, we show the fixed points of the dynamical system (5.15) as a function of the optical lattice strength V_0 . The dash-dotted (green) line denotes the non-zero fixed point calculated from Eq. (5.16) with $\omega_{ds} = \omega_z/\sqrt{2}$, while the solid (black) line denotes the non-zero fixed point calculated from Eq. (5.16) with $\omega_{ds} = 30.36$ Hz. Furthermore, the circles denote the position of the node of the nonlinear stationary state — i.e., the position of the dark soliton — obtained by numerical integration of Eq. (5.3) with $\mu = 3.8 \times 10^{-12}$ eV (in the TF limit). Clearly, at $V_{0,cr} \simeq 9.6 \times 10^{-14}$ eV, the asymmetric one-soliton branch bifurcates through a supercritical pitchfork bifurcation; notice the excellent agreement between the two approaches.

The bottom left and right panels of Fig. 5.3 show the BdG spectra of the symmetric and asymmetric one soliton state, respectively, as a function of the optical lattice strength (for a fixed chemical potential, $\mu = 3.8 \times 10^{-12}$ eV). For sufficiently small lattice strength, $V_0 < V_{0,cr}$, the symmetric state is stable, while when the lattice strength V_0 is increased, the magnitude

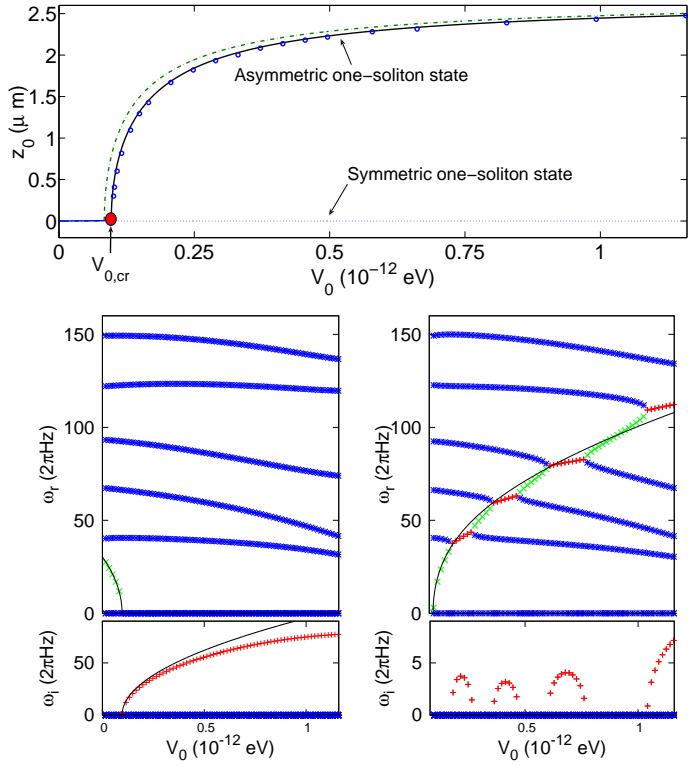


Figure 5.3: Top panel: Fixed points (lines) of the dynamical system (5.15) and position of the soliton (open circles) calculated by the Eq. (5.3) with $\mu = 3.8 \times 10^{-12}$ eV. Bottom left (right) panel: BdG spectra of the symmetric (asymmetric) one-soliton state for $\mu = 3.8 \times 10^{-12}$ eV as a function of V_0 .

of the instability grows and the prediction of Eq. (5.17) deviates from the results obtained from the integration of Eq. (5.3). To explain this discrepancy, it is relevant to recall that the result of the perturbation theory of Sec. 5.1.2 is valid only if all perturbation terms are small and of the same order. Nevertheless, for the symmetric one soliton state — with the soliton located at zero — the magnitude of the perturbation term corresponding to the harmonic trap (optical lattice) has its smallest (largest) value; thus, for large V_0 , these perturbations cannot be of the same order. As concerns the asymmetric state, the prediction of Eq. (5.17) is in fairly good agreement to the results obtained from the numerical integration of Eq. (5.3). However, Eq. (5.17) cannot predict oscillatory instabilities (associated with the existence of complex eigenfrequencies), which occur when the anomalous mode collides with a mode of the background condensate. This can readily be understood by the fact that the derivation of the equation of motion of the dark soliton relies on the assumption that the soliton is decoupled from the background (see, e.g., Refs. [122] and [5] for details), which is not the case for oscillatory instabilities.

Next, let us study the continuation of both symmetric and asymmetric one-soliton states with increasing chemical potential for various values of the optical lattice strength.

First, we consider the symmetric one-soliton state and in Fig. 5.4 we show the BdG spectra along the corresponding branch. The first panel shows the case of a pure harmonic trap, i.e., $V_0 = 0$, and the dashed line is the prediction from Eq. (5.17) using $\omega_{ds} = \omega_z/\sqrt{2}$. It is clear

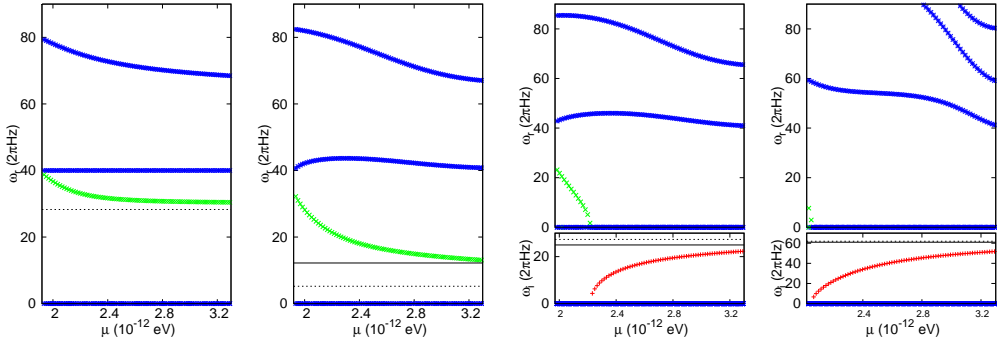


Figure 5.4: BdG spectra for four different values of the optical lattice strength for the symmetric dark soliton state (with the soliton located at the trap center): from left to right, $V_0 = 0$, $V_0 = 8.3 \times 10^{-14}$ eV, $V_0 = 1.65 \times 10^{-13}$ eV and $V_0 = 4.96 \times 10^{-13}$ eV. The solid lines correspond to the predictions of Eq. (5.17). Symbol * (blue) denotes a positive (or zero for a vanishing eigenfrequency), symbol \times (green) a negative and symbol + (red) a vanishing Krein sign mode (for non-zero eigenfrequencies).

that the eigenfrequencies are real, indicating the stability of this state for all values of the chemical potential. The figure shows the constant eigenfrequency of the dipolar mode [see straight (blue) line] at the value of the trap frequency ω_z and the anomalous mode bifurcating from the dipolar mode in the linear limit. As mentioned above, the eigenfrequency of the anomalous mode reaches asymptotically the value $\omega_{ds} = 30.36$ Hz.

The second panel of Fig. 5.4 shows the BdG spectrum for $V_0 = 8.3 \times 10^{-14}$ eV. All eigenfrequencies are real, so the state is still stable. The dashed line is the prediction by Eq. (5.17) using $\omega_{ds} = \omega_z/\sqrt{2}$, while the solid line is the prediction with $\omega_{ds} = 30.36$ Hz. The dipole mode remains approximately constant for such a small optical lattice strength. However, the degeneracy of the anomalous mode and the dipole mode in the linear limit disappears.

The third panel shows the spectra for $V_0 = 1.65 \times 10^{-13}$ eV. In this case, the anomalous mode becomes purely imaginary for increasing chemical potential, reflecting the fact that the state becomes unstable. Notice that the numerical result and the analytical prediction, $\omega_{ODE} = i\sqrt{|\omega_{ds}^2 - k^2 V_0|}$, are in a good agreement for large values of the chemical potential, where the TF limit is reached and Eq. (5.15) is valid. Since $V_0 > V_{0,cr}$, this state is expected to be unstable in the TF limit.

The fourth panel shows the spectra for $V_0 = 4.96 \times 10^{-13}$ eV. In this case, the anomalous mode becomes purely imaginary already at small chemical potentials. Furthermore, the dipole mode eigenfrequency is now significantly modified, upon the reported interval of changes of the chemical potential. The analytical prediction agrees again well with the numerical BdG result in the TF limit.

Next, we consider the continuation with increasing chemical potential of the asymmetric states bifurcating from the symmetric one when the latter becomes unstable. Fig. 5.5 shows the BdG spectra along the asymmetric one-soliton state for $V_0 = 1.65 \times 10^{-13}$ eV and $V_0 = 8.3 \times 10^{-13}$ eV. The analytical predictions of Eq. (5.17) with $\omega_{ds} = \omega_z/\sqrt{2}$ and $\omega_{ds} = 30.36$ Hz, respectively plotted with dashed and solid lines are in good agreement with the respective anomalous mode eigenfrequencies. In the case of $V_0 = 8.3 \times 10^{-13}$ eV, the difference between the result of Eq. (5.17) using $\omega_{ds} = \omega_z/\sqrt{2}$ and $\omega_{ds} = 30.36$ Hz is small, showing that the dynamics is mostly governed by the potential term stemming from the optical lattice.

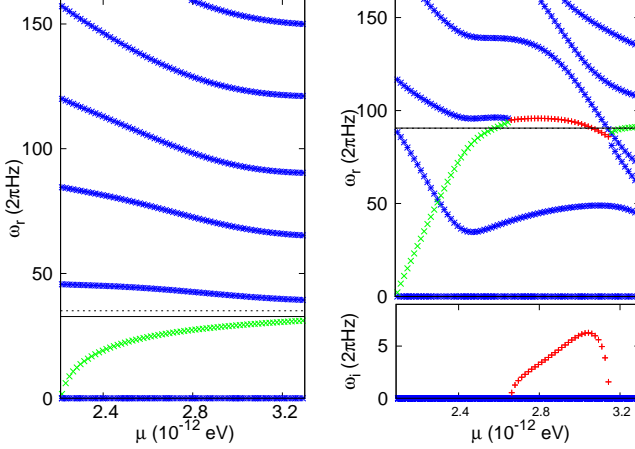


Figure 5.5: BdG spectra for $V_0 = 1.65 \times 10^{-13}$ eV (left panel) and $V_0 = 8.3 \times 10^{-13}$ eV (right panel) for the asymmetric dark soliton state, bifurcating from the symmetric one. The notation of eigenstates is the same as in Fig. 5.4.

5.3.2 Two Dark-Soliton States

We now consider the case of the two-soliton state, for which we need to incorporate the interaction potential in order to describe their dynamics. Particularly, according to the theoretical framework of Sec. 5.1.2, the effective potential describing the dynamics of two solitons located at z_1 and z_2 has the following form:

$$V_{\text{eff}}(z_1, z_2) = \omega_{\text{ds}}^2(z_1^2 + z_2^2) + \frac{V_0}{2}[\cos(2kz_1) + \cos(2kz_2)] + \frac{2n_0}{\sinh^2[\sqrt{n_0}(z_2 - z_1)]}. \quad (5.19)$$

Using $d^2z_i/dt^2 = -(1/2)dV_{\text{eff}}(z_1, z_2)/dz_i$ (with $i = 1, 2$) as per Eq. (5.8), it is straightforward to derive the following system of equations of motion,

$$\frac{d^2z_1}{dt^2} = -\omega_{\text{ds}}^2 z_1 + \frac{1}{2}kV_0 \sin(2kz_1) - 2n_0^{3/2} \coth[\sqrt{n_0}(z_2 - z_1)] \operatorname{csch}^2[\sqrt{n_0}(z_2 - z_1)], \quad (5.20)$$

$$\frac{d^2z_2}{dt^2} = -\omega_{\text{ds}}^2 z_2 + \frac{1}{2}kV_0 \sin(2kz_2) + 2n_0^{3/2} \coth[\sqrt{n_0}(z_2 - z_1)] \operatorname{csch}^2[\sqrt{n_0}(z_2 - z_1)], \quad (5.21)$$

which, accordingly, leads to the following system for the fixed points $(z_o^{(1)}, z_o^{(2)})$:

$$z_o^{(1)} = \frac{V_0 k}{2\omega_{\text{ds}}^2} \sin(2kz_o^{(1)}) - \frac{n_0^{3/2}}{\omega_{\text{ds}}^2} \coth[\sqrt{n_0}(z_o^{(2)} - z_o^{(1)})] \operatorname{csch}^2[\sqrt{n_0}(z_o^{(2)} - z_o^{(1)})], \quad (5.22)$$

$$z_o^{(2)} = \frac{V_0 k}{2\omega_{\text{ds}}^2} \sin(2kz_o^{(2)}) + \frac{n_0^{3/2}}{\omega_{\text{ds}}^2} \coth[\sqrt{n_0}(z_o^{(2)} - z_o^{(1)})] \operatorname{csch}^2[\sqrt{n_0}(z_o^{(2)} - z_o^{(1)})]. \quad (5.23)$$

Thus, the fixed points for the two soliton states depend on the density of the background cloud and thereby on the chemical potential. Due to the presence of the external potentials, the density of the background is inhomogeneous. In our analysis, we replace the inhomogeneous density, with the density of the background at $z = 0$ using the TF approximation; namely,

$$n_0 \rightarrow n_0(z=0) = ((\mu - V_0)^2 - 1)/4.$$

Considering small deviations from the fixed points, i.e., $z_i = z_o^{(i)} + \epsilon \eta_i \exp(i\omega t)$ (with $i = 1, 2$), leads to the eigenvalue problem for the normal modes:

$$\omega^2 \eta = \begin{pmatrix} A(z_o^{(1)}) + B(z_o^{(1)}, z_o^{(2)}) & -B(z_o^{(1)}, z_o^{(2)}) \\ -B(z_o^{(1)}, z_o^{(2)}) & A(z_o^{(2)}) + B(z_o^{(2)}, z_o^{(1)}) \end{pmatrix} \eta \quad (5.24)$$

with

$$A(x) = \omega_{ds}^2 - V_0 k^2 \cos(2kx) \quad (5.25)$$

$$B(x, y) = 4n_0^2 \coth^2(\sqrt{n_0}(x-y)) \operatorname{csch}^2[\sqrt{n_0}(x-y)] + 2n_0^2 \operatorname{csch}^4[\sqrt{n_0}(x-y)]. \quad (5.26)$$

Diagonalizing the above matrix, we obtain the eigenfrequencies of the two anomalous modes of the two-soliton states. Notice that since different two soliton states lead to different fixed points, the oscillation frequencies for the two solitons will differ as well. Negative eigenvalues of this 2×2 system lead to imaginary frequencies describing unstable states; however, as mentioned in the previous section, one cannot describe oscillatory instabilities.

In the top panel of Fig. 5.6, we show the fixed points of the system (5.22-5.23) and the zero points of the solutions with two nodes of Eq. (5.3) corresponding to the positions of the two solitons as a function of V_0 (the chemical potential is fixed: $\mu = 3.6 \times 10^{-13}$ eV). For small V_0 there exists only the symmetric solution with two nodes. However, for $V_{0,cr} = 3.4 \times 10^{-12}$ eV, two asymmetric states appear stemming from a saddle-node bifurcation. For all three states, the agreement between the fixed points obtained from Eqs. (5.22-5.23) and the position of the solitons is excellent.

The bottom panels of Fig. 5.6 show the BdG spectra for the symmetric and the two asymmetric two soliton states as a function of V_0 for fixed $\mu = 3.8 \times 10^{-12}$ eV. The solid lines correspond to the normal modes of Eqs. (5.20-5.21) around the corresponding fixed points. For a small optical lattice strength V_0 , the two anomalous modes of the symmetric states have a different magnitude, which indicates that the solitons are coupled. However, for increasing V_0 , this difference decreases and, thus, the coupling between the solitons becomes weaker. Notice that for an optical lattice strength $V_0 \simeq 3.6 \times 10^{-12}$ the two modes become of the same order, a fact that indicates that the two solitons become eventually decoupled. The prediction of Eqs. (5.20-5.21) agrees very well with the numerical results obtained via the BdG analysis for the anomalous modes. The second panel shows the BdG spectrum of the asymmetric state with one soliton located approximately at the center of the barrier. The latter, leads to a purely imaginary mode with an increasing magnitude with increasing V_0 . The increase of the magnitude of this mode results from the increase of the height of the barrier. For large V_0 the prediction of Eqs. (5.20-5.21) deviates from the result obtained in the framework of Eq. (5.3): the contributions of the perturbation terms are not of the same order and, thus, perturbation theory fails in this case. The third panel shows the BdG spectrum for the second asymmetric state with two solitons in one well. The difference between the modes is always large, a fact indicating the strong coupling between the two solitons. With increasing lattice strength V_0 , the eigenfrequencies of the anomalous modes increases too. The predictions of Eqs. (5.20-5.21) agree once again well with the BdG results; nevertheless, as in previous cases, Eqs. (5.20-5.21) cannot predict oscillatory instabilities.

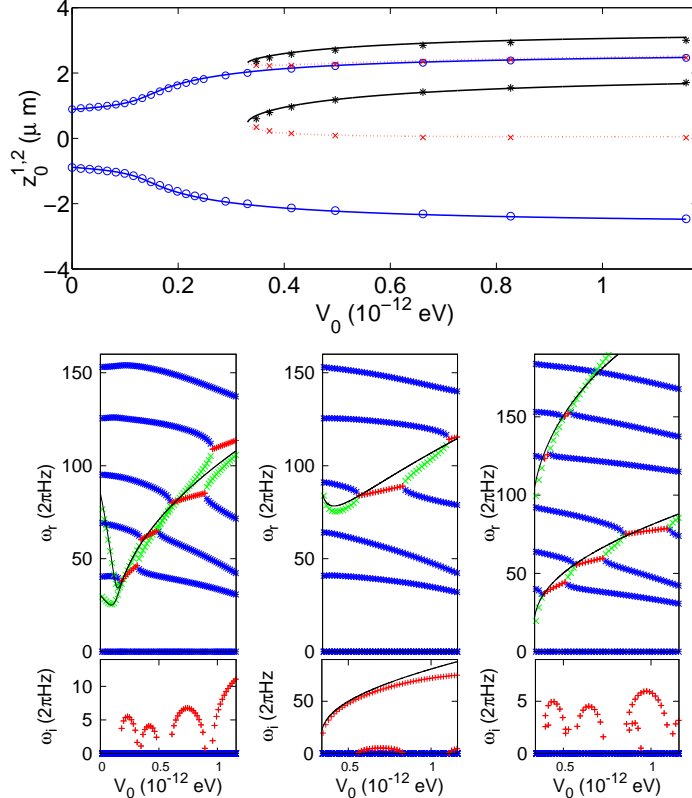


Figure 5.6: Top panels: Fixed points (lines) of the system (5.22-5.23) and position of the solitons (circles for the symmetric two-soliton state, \times for the two-soliton branch with one soliton near the center and one in one well, and stars for the state with both dark solitons in the same well) calculated by the numerical integration of Eq. (5.3) for $\mu = 3.8 \times 10^{-12}$ eV. Bottom panels: BdG spectra of the two-soliton states for $\mu = 3.8 \times 10^{-12}$ eV as a function of V_0 ; left corresponds to the symmetric two-soliton state, middle to the always unstable state with one soliton near the center and one in one well, while the right corresponds to the state with both dark solitons in the same well. Notice also the agreement of the theoretically predicted modes from Eq. (5.24) with the numerical ones.

Next, let us consider a continuation with respect to the chemical potential. Fig. 5.7 shows the BdG spectra, and the predicted oscillation frequencies, for the symmetric two soliton state for different values of the optical lattice strength: $V_0 = 0$, $V_0 = 8.3 \times 10^{-14}$ eV, $V_0 = 1.65 \times 10^{-13}$ eV and $V_0 = 4.96 \times 10^{-13}$ eV. In the case of a purely harmonic potential, $V_0 = 0$, one observes the constant eigenfrequency of the dipolar mode at ω_z , as well as the eigenfrequency of one anomalous mode bifurcating from the dipolar mode in the linear limit. The eigenfrequency at $2\omega_z$ is imaginary due to a degeneracy of a negative and a positive Krein sign mode. The former one corresponds to the second anomalous mode and the latter one to the quadrupole mode. This degeneracy is lifted for increasing chemical potential. The predictions of Eqs. (5.20-5.21) agree very well with the BdG results for the anomalous modes in the case of large chemical potentials.

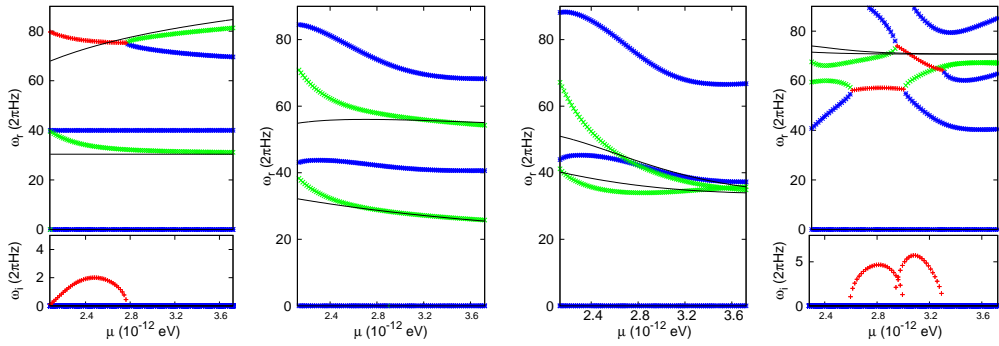


Figure 5.7: BdG spectra for different values of the optical lattice strength; from left to right, $V_0 = 0$, $V_0 = 8.3 \times 10^{-14}$ eV, $V_0 = 1.65 \times 10^{-13}$ eV and $V_0 = 4.96 \times 10^{-13}$ eV. The solid lines are the predictions of Eqs. (5.20-5.21) with a numerically determined oscillation frequency (ω_{ds}).

For $V_0 = 8.3 \times 10^{-14}$ eV the degeneracy between the anomalous modes and the dipolar and the quadrupole mode is lifted in the linear limit. Thus, there exists an energy gap between the anomalous mode and the dipolar mode and, more importantly, an energy gap between the second anomalous mode and the quadrupole mode. A particularly useful conclusion stemming from the above findings is that the two soliton state can be stabilized in a harmonic trap by adding a small optical lattice.

For $V_0 = 1.65 \times 10^{-13}$ eV the system is stable as well. The anomalous modes decrease with increasing chemical potential and reach similar values for a large chemical potential. This denotes that the two solitons are decoupled for a large chemical potential. This can be understood at least in the framework of the effective potential (5.19): the range of the interaction potential scales with the density n_0 of the background atom cloud and thereby with the chemical potential as well. Thus, for a large chemical potential, i.e., a large density, the interaction between solitons is strong but of short range too.

For $V_0 = 4.96 \times 10^{-13}$ eV the anomalous modes have similar values even in the linear limit. Thus, the two solitons are already almost decoupled in the linear limit due to their large separation. The two anomalous modes collide with the dipolar and quadrupole modes for increasing chemical potential, leading to oscillatory instabilities, and bifurcate from these modes again for a larger chemical potential. Although the predictions of Eqs. (5.20-5.21) agree qualitatively with the BdG results, there is no quantitative agreement due to the crossings and collisions of the soliton modes with the modes of the condensate.

5.4 Dark Soliton Dynamics: Numerical Results

So far, we have examined the existence, stability and bifurcations of the branches of dark-solitonic states in the double-well potential setting. We now proceed to investigate the dynamics of these states by direct numerical integration of Eq. (5.3), using as initial conditions stationary soliton states, perturbed along the direction of eigenvectors associated with particular eigenfrequencies (especially ones associated with instabilities). To better explain the above, we should recall that anomalous modes are connected to the positions and oscillation frequencies of the solitons; therefore, perturbations of stationary dark soliton states along the directions of the eigenvectors of the anomalous modes result in the displacement of the positions of the solitons, thus giving rise to interesting soliton dynamics.

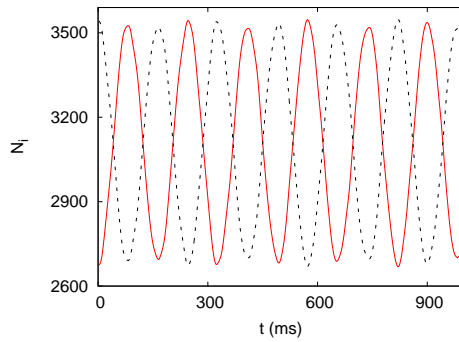


Figure 5.8: Time evolution of the number of atoms N_L (solid line) and N_R (dashed line) in the left and right well of the double-well potential, respectively, for the ground state of the system perturbed by the lowest BdG mode. Parameter values are $\mu = 3 \times 10^{-12}$ eV and $V_0 = 1.12 \times 10^{-12}$ eV.

Before proceeding with the dynamics of the (excited) soliton states, let us make a remark concerning the ground state of the system. As mentioned above, the value of the lowest BdG mode of the ground state is given, in the linear limit, by the energy difference between the ground state and the first excited state. However, this energy gap determines the oscillation frequency of atoms between the wells of the double-well potential, which suggests that the lowest BdG mode is connected to an oscillation between the wells. Let us define the atom numbers N_L and N_R in the left and right well, respectively, as $N_L = \int_{-\infty}^0 |\psi|^2 dz$ and $N_R = \int_0^{+\infty} |\psi|^2 dz$ (the total number of atoms is $N = N_L + N_R$). In Fig 5.8, we show the time evolution of N_L (solid line) and N_R (dashed line) for the ground state, when perturbed by the eigenvector corresponding to the lowest BdG mode (parameter values are $\mu = 3 \times 10^{-12}$ eV and $V_0 = 1.12 \times 10^{-12}$ eV). One can clearly observe the oscillation of the atom numbers in the different wells, with a characteristic frequency known as Josephson oscillation frequency [39–41], determined by the magnitude of the respective BdG eigenmode.

Let us now proceed with the one-soliton states. Fig. 5.9 shows the time evolution of the symmetric one soliton state perturbed by the eigenvector corresponding to the unstable mode, for $\mu = 3 \times 10^{-12}$ eV and $V_0 = 4.96 \times 10^{-13}$ eV. The instability manifests itself as a drift of the soliton from the trap center to the rims of the background atom cloud, where the soliton is reflected back and forth. One clearly observes that the soliton is located at an unstable position, since a small perturbation leads to a large amplitude oscillation of the soliton. On the other hand, Fig. 5.10 shows the time evolution of the asymmetric one soliton

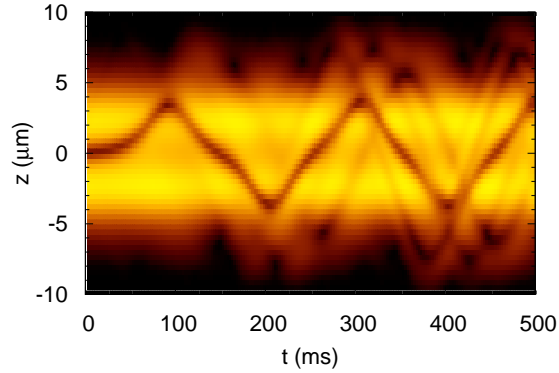


Figure 5.9: Contour plot showing the space-time evolution of the density of the condensate, which carries the symmetric one-soliton state; dark corresponds to minimal and white to maximal density. The soliton is unstable and departs from the trap center after a short time period, performing subsequently large amplitude oscillations. Parameter values are $\mu = 3 \times 10^{-12}$ eV and $V_0 = 4.96 \times 10^{-13}$.

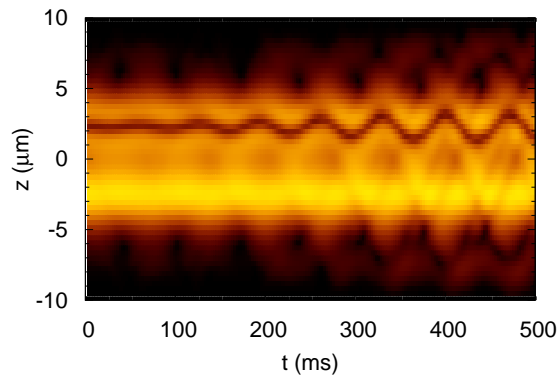


Figure 5.10: Same as in Fig. 5.9, but for the asymmetric one-soliton state, for $\mu = 3 \times 10^{-12}$ eV for $V_0 = 8.27 \times 10^{-13}$ eV.

state perturbed by the eigenvector corresponding to the unstable mode for $\mu = 3 \times 10^{-12}$ eV for $V_0 = 8.27 \times 10^{-13}$ eV. The corresponding state is subject to an oscillatory instability, which results in a growing amplitude of the soliton oscillation. However, in comparison to the previous case, the magnitude of the instability is much smaller and, thus, the increase of the amplitude is smaller (for the same time scale) as well.

Next, we consider the multi-soliton states and start with the symmetric two-soliton state which, for $\mu = 3.3 \times 10^{-12}$ eV and $V_0 = 8.27 \times 10^{-14}$ eV, is found to be linearly stable. Numerical simulations, using as initial conditions this state perturbed by the eigenvectors corresponding to both anomalous modes, reveal that the two solitons perform oscillations with a constant amplitude and different frequencies. Specifically, the mode with smaller amplitude performs an in-phase oscillation (with the two solitons moving towards the same direction), whereas the mode with larger amplitude performs an out-of-phase oscillation (with the two solitons moving towards opposite directions) with a larger oscillation frequency. The existence of two different oscillation frequencies indicates the coupling of the dark solitons. This situation changes for a large optical lattice strength (e.g., $V_0 = 1.65 \times 10^{-13}$ eV): in this case, the two dark solitons are decoupled, since the numerical simulations show that both the in-phase and out-of phase oscillations are characterized by almost the same frequency.

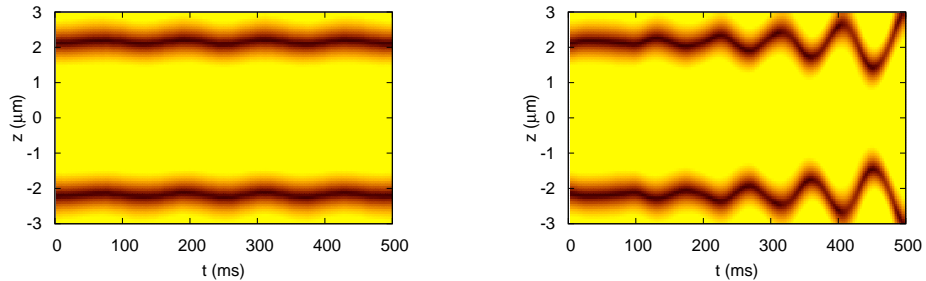


Figure 5.11: Same as in Fig. 5.9, but for the symmetric two-soliton state with in-phase (left) anomalous mode and out-of-phase (right) imaginary mode perturbations, for $\mu = 3.1 \times 10^{-12}$ eV and $V_0 = 4.96 \times 10^{-13}$ eV. The former anomalous eigenmode is stable, while the latter is unstable (as concluded also from the BdG analysis).

Fig. 5.11 shows the time evolution of the symmetric two-soliton state for $\mu = 3.1 \times 10^{-12}$ eV and $V_0 = 4.96 \times 10^{-13}$ eV perturbed by the eigenvector corresponding to the anomalous mode associated with in-phase (left panel) and by the eigenvector corresponding to the imaginary mode out-of-phase (right panel) oscillations of the dark solitons. For these parameters, the BdG analysis predicts that the former mode is stable while the latter is unstable. This is confirmed by the direct simulations: it is clearly observed that the amplitude of the out-of-phase oscillation increases whereas the amplitude of the in-phase oscillation remains constant.

Finally, in Fig. 5.12 we show the time evolution of the symmetric two soliton state for $\mu = 2.8 \times 10^{-12}$ eV and $V_0 = 4.96 \times 10^{-13}$ perturbed by the eigenvector corresponding to the anomalous mode with in-phase (left panel) and by the eigenvector corresponding to the imaginary mode out-of-phase (right panel) oscillations. For these parameters, the simulations show that the out-of-phase oscillation of the solitons is stable and the in-phase oscillation unstable, in agreement with the predictions of the BdG analysis.

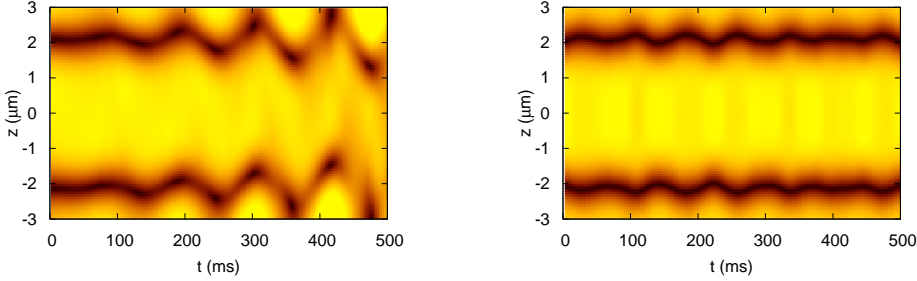


Figure 5.12: Same as in Fig. 5.11, but for the symmetric two-soliton state, for $\mu = 2.8 \times 10^{-12}$ eV and $V_0 = 4.96 \times 10^{-13}$ eV. Notice the reversal of stability of the two anomalous modes with respect to Fig. 5.11.

5.5 Conclusions

In this chapter, we have performed a detailed study of the statics and dynamics of matter-wave dark solitons in a cigar-shaped Bose-Einstein condensate confined in a double-well potential. The latter, was assumed to be formed as a combination of a usual harmonic trap and a periodic (optical lattice) potential. For our analysis, we have adopted and used an effectively 1D mean-field model, namely a Gross-Pitaevskii-like equation with a non-cubic nonlinearity, which has been used successfully in other works to describe dark solitons in BECs in the dimensionality crossover regime between 1D and 3D.

As a first step in our analysis, we studied the existence and stability of both the one- and multiple-dark soliton states. In particular, starting from the respective linear problem, we have used the continuation with respect to the chemical potential (number of atoms) to reveal the different branches of purely nonlinear solutions, including the ground state, as well as excited states, in the form of single or multiple dark solitons. We have shown that the presence of the optical lattice is crucial for the existence of nonlinear states that do not have a linear counterpart: these are actually asymmetric dark soliton states, with solitons located in one well (rather than in both wells) of the double-well potential, and do not exist in the non-interacting — linear — limit. We have systematically studied the bifurcations of the various branches of solutions and showed how each particular state emerges or disappears for certain chemical potential thresholds; the latter were determined analytically, in some cases, by using a Galerkin-type approach, in very good agreement with the numerical results. For each branch, we have also studied the stability of the pertinent solutions via a Bogoliubov-de Gennes analysis. This way, we have discussed the role of the anomalous (negative energy) modes in the excitation spectra and revealed two types of instabilities of dark solitons, corresponding to either purely imaginary or genuinely complex eigenfrequencies; the latter were found to occur due to the collision of an anomalous mode with a positive energy mode and are associated with the so-called oscillatory instabilities of dark solitons.

We have also adopted a simple analytical model to study small-amplitude oscillations of the one- and multiple-dark-soliton states. Particularly, equations of motion for the single and multiple solitons were presented in the weakly-interacting limit (where the model becomes the usual cubic 1D GPE), and modified them to take into regard the dimensionality of the system (i.e., the effect of transverse directions). The analysis of these equations of motion

led to the determination of the characteristic soliton frequencies, which were then compared to the eigenfrequencies found in the framework of the BdG analysis; the agreement between the two was generally found to be very good. Perhaps even more importantly, the simple physical (i.e., particle) picture we adopted allowed us to reveal the role of the optical lattice strength (i.e., the height of the barrier in the double-well setting) in the stability of the dark solitons, as well as its role on the coupling between solitons. Particularly, it was found that sufficiently strong barriers lead to instability of symmetric and asymmetric soliton states, while it results in an effective decoupling of multi-solitons: the coupling between neighboring solitons as described by an effective repulsive potential, becomes negligible for sufficiently strong barriers. We should also note that generally the states possessing a dark soliton at the center of the trap were found to be most strongly unstable, due to the emergence of a progressively larger (the larger the nonlinearity) imaginary eigenfrequency.

Finally, we have performed systematic numerical simulations, based on direct numerical integration of the quasi-one-dimensional model, to investigate the dynamics of dark solitons in the double-well setup. We studied the manifestation of instabilities, when present, and found in all cases, a very good agreement between the predictions based on the BdG analysis and the numerical results. Instabilities have been observed to manifest themselves through the exponential divergence of the soliton from its initial location (when associated with an imaginary pair of eigenfrequencies) or the oscillatory growth (when associated with a complex quartet of eigenfrequencies).

Chapter 6

Stability and Dynamics of Matter-Wave Vortices in the Presence of Collisional Inhomogeneities and Dissipative Perturbations

So far we investigated cigar-shaped quasi 1D BECs and solitons as the emerging excited states. In this chapter we systematically study singly-charged vortices in a two-dimensional (2D) — disk-shaped— BEC from a spectral (i.e., Bogoliubov-de Gennes) point of view. In particular, first we focus on the so-called anomalous mode of the Bogoliubov theory, characterized by negative energy or Krein-sign, and elucidate its connection with the precessional motion of the vortex, if displaced from its equilibrium position, i.e., the trap center. Next, we will study how this mode is affected by the presence of different kinds of perturbations. The perturbations we consider here arise from inhomogeneous interatomic interactions and finite-temperature induced dissipation.

We will examine how harmonic spatial variations of the scattering length, inducing a sort of a nonlinear optical lattice in the system, affect the stability and ensuing dynamics of the vortex. Interestingly, we find that the anomalous mode of the vortex (located at the origin) is differently affected by cosinusoidally (the vortex is located at a maximum of the nonlinearity) and sinusoidally (the vortex is located at a local minimum of the nonlinearity) varying nonlinearities, i.e., the phase of the nonlinearity's spatial variation at the vortex location plays a crucial role in the ensuing stability properties. This turns out to be the most critical element of influence within this setting. In the former case the vortex is stable, while in the latter the vortex is subject to an oscillatory instability, emerging by the collision of the anomalous mode with another eigenmode of the system.

We also consider in our study the effect of dissipative perturbations on the vortex dynamics motivated by considerations of the coherent structure's interaction with the thermal cloud. Here we will adopt a simple phenomenological model relying on the inclusion of a phenomenological damping in the mean-field model, first introduced by Pitaevskii and subsequently used in various works to describe, e.g., decoherence [252] and growth [253] of BECs, damping of collective excitations of BECs [254], vortex lattice growth [255, 256], vortex dynamics [257–261]), and decay of dark solitons [262]. Importantly, inclusion of such a phenomenological damping in the GPE can be justified from a microscopic perspective (see, e.g., the recent review [263]). Herein, we will show how such a finite-temperature motivated dissipation affects the statics and dynamics of the vortex, by leading its anomalous mode to become immediately unstable. Despite the relatively simple and phenomenological nature of the model, we will see that its results will bear significant similarities to the phenomenology of more complex dynamical models of the relevant interactions, allowing us to understand qualitatively the origin of the observed dynamical features. We will also present some interesting twists that may arise when the combined effect of thermal dissipation and spatially-dependent interatomic interactions

is considered. The results presented in this chapter are partly published in Ref. [264].

The chapter is structured as follows. In section 6.1, we present our analytical considerations in connection to the spectrum of a $S = 1$ vortex and its precession frequency in the trap. In section 6.2, we examine numerically the validity of the analytical predictions, but also how these are modified in the presence of additional perturbations such as the spatially dependent nonlinearity, or the finite-temperature induced dissipative perturbation. This is done both through a systematic analysis of the Bogoliubov-de Gennes equations, as well as through the direct numerical simulations of the pertinent GPE models. Finally, in section 6.3, we summarize our results.

6.1 Analytical Results

We first consider the simplest case in our study, namely a matter-wave vortex in a 2D BEC confined in a harmonic trap. The singly charged vortex possesses precisely one anomalous mode [265]; this mode, characterized by a negative energy, is also known as mode of negative Krein sign (or signature) in the mathematical literature [266]; see also Eq. (2.71) in section 2.4 for an explicit definition of the Krein signature of a mode. In Ref. [265] (see also the review [147]), it was argued that the single negative energy mode with $S = 1$ (which is of interest here) is responsible for the precessional motion of the vortex in the trap (in addition to being relevant for other processes such as vortex nucleation).

One of the key purposes in our study is to consider the precession in the setting described above. The three-dimensional (3D) analogue of this setting has been considered and studied analytically by means of the matched asymptotics technique in Ref. [267], while the 2D case has been studied by means of a variational approach in Ref. [268] (see more details below). Here, employing the matched asymptotics method, we derive an expression for the precession frequency in the 2D case, and provide a detailed comparison of this result with numerics pertaining to the study of the anomalous mode.

We consider a disk-shaped BEC confined in the in-plane and transverse direction by a harmonic potentials with frequencies ω_r and ω_z , respectively. For $\omega_z \gg \omega_r$ the emerging model under consideration is the $(2 + 1)$ -dimensional GPE (cf. section 2.2.1),

$$i\hbar\partial_t u = -\frac{\hbar^2}{2m}\Delta' u + V(r')u + g_{2D}|u|^2u - \mu'u. \quad (6.1)$$

Here, $u(x', y', t')$ is the macroscopic wave function of the disk-shaped BEC, Δ' is the 2D Laplacian, $r' \equiv \sqrt{x'^2 + y'^2}$ is the radial variable, $V(r') = \frac{1}{2}\omega_r^2 r'^2$ is the harmonic trapping potential in the in-plane direction, μ' the chemical potential and $g_{2D} = g_{3D}/2\pi a_z = 2\sqrt{2\pi}aa_z\hbar\omega_z$ is the effectively 2D nonlinear coefficient where a is the scattering length and a_z , ω_z are the transverse (strongly confining) harmonic oscillator length and trapping frequency, respectively. Measuring length in units of a_z and frequencies in units of ω_z Eq. (6.1) can be expressed in the following dimensionless form,

$$i\partial_t u = -\frac{1}{2}\Delta u + V(r)u + g|u|^2u - \mu u. \quad (6.2)$$

Here, Δ is the 2D Laplacian of the rescaled variables, r is the rescaled radial variable, $V(r) = \frac{1}{2}\Omega^2 r^2$ is the harmonic trapping potential with Ω being measured in units of ω_z , g is the

normalized strength of the interatomic interactions (which we set to $g = 1$ for the analytical considerations of this section), and μ is the chemical potential measured in units of $\hbar\omega_z$. In order to study the effect of the potential on the vortex, we will follow the lines of Ref. [269] (see also Ref. [148] for similar work in the context of optics) and use a matched asymptotics approach between an inner and an outer perturbative solution. The former one is of the form:

$$u(r, \theta) = [u_0(r) + \varepsilon\chi(r) \cos(\theta)] e^{i[S\theta + \varepsilon\eta(r) \sin(\theta)]}, \quad (6.3)$$

where ε is a formal small parameter associated with the slow speed of precession and $u_0(r)$ is the radial vortex profile, while χ and η are functions of r , whose asymptotics have been detailed in Refs. [148, 269] (see also Ref. [267]). The outer perturbative solution can be obtained by a lowest-order equation for the phase, resulting from a rescaling of space, $r \rightarrow \varepsilon r$, and time, $t \rightarrow \varepsilon^2 t$, namely:

$$\Delta\theta + \mathbf{F} \cdot \nabla\theta = 0, \quad (6.4)$$

where $\mathbf{F} = \nabla \log(|u_b|^2)$ and $|u_b|^2$ is the (background, hence the relevant subscript) BEC density in the absence of the vortex; notice that the density can be approximated in the Thomas-Fermi (TF) limit as $|u_b|^2 = \mu - V(r)$.

Interestingly, the similarity of Eq. (6.4) to Eq. (20) of Ref. [148] could lead to the impression that the detailed formalism of Ref. [148] could be blindly followed giving rise to the precessional motion of Eq. (27) therein. However, this turns out to be incorrect. Particularly, in Ref. [148], it was non-generically assumed that \mathbf{F} of the outer expansion can be accurately approximated by a constant. In our case where $\mathbf{F} \approx -\Omega^2 \mathbf{r}/\mu$ (for small and intermediate distances where the matching with the inner expansion is performed), this approximation is clearly not an appropriate one. Instead, we follow the original formulation of Ref. [269], which employs the change of variables $\phi(x, y) \rightarrow \theta(x, y)$:

$$\theta_x = -S \left(\phi_y - \phi \frac{\Omega^2}{\mu} y \right), \quad (6.5)$$

$$\theta_y = S \left(\phi_x - \phi \frac{\Omega^2}{\mu} x \right), \quad (6.6)$$

(we will suppress the S -dependence hereafter, focusing on singly-charged vortices). Then, the equation for ϕ reads:

$$\Delta\phi - \frac{\Omega^2}{\mu} (x\phi_x + y\phi_y) - 2\frac{\Omega^2}{\mu}\phi = 0, \quad (6.7)$$

which, upon using the transformation $\phi = H(r)/\sqrt{\mu - V(r)}$, yields

$$\Delta H - \frac{\Omega^2}{\mu} H = 2\pi\delta(\mathbf{r} - \mathbf{r}_0), \quad (6.8)$$

assuming a point vortex source at \mathbf{r}_0 . This leads to the asymptotic behavior $H = -K_0(m|\mathbf{r} - \mathbf{r}_0|)$, where K_0 is the modified Bessel function and $m = \Omega/\sqrt{\mu}$. This should be directly compared with Eq. (23) of Ref. [148], showcasing that instead of $F^r/2$ in the latter equation, here we have the constant factor m multiplying the distance from the vortex core. Once this *critical* modification is made, the rest of the calculation of Ref. [148] can be followed directly,

yielding the final result (in the presence of the trap):

$$\dot{x}_v = \frac{\Omega^2}{2\mu} \log\left(A \frac{\mu}{\Omega}\right) y_v, \quad (6.9)$$

$$\dot{y}_v = -\frac{\Omega^2}{2\mu} \log\left(A \frac{\mu}{\Omega}\right) x_v, \quad (6.10)$$

where the pair (x_v, y_v) defines the location of the vortex center, A is an appropriate numerical factor (detailed comparison with numerics yields very good agreement in the TF regime e.g. for $A \approx 8.88 \approx 2\sqrt{2}\pi$, see below).

It should be noted that this equation is valid for small displacements from the trap center which lends further support to the connection of this dynamics with the relevant mode of the BdG analysis. For larger displacements from the vortex center, this expression should be appropriately corrected [270].

Eqs. (6.9-6.10) suggest a precession of the vortex in the harmonic trap with a frequency

$$\omega_{\text{an}} = \frac{\Omega^2}{2\mu} \log\left(A \frac{\mu}{\Omega}\right), \quad (6.11)$$

which, as suggested by the subscript (“an” stands for anomalous), should coincide with the eigenfrequency of the anomalous mode of the Bogoliubov spectrum. The anomalous mode eigenfrequency can readily be obtained through a standard Bogoliubov-de Gennes (BdG) analysis (cf. section 2.4).

In order to compare our results to the ones obtained in earlier works, we should mention that a similar setup was investigated in Ref. [270] for finite displacements of the vortex from the center of the trap and in Ref. [268] (by means of a variational approximation). In the latter one the frequency of the anomalous mode was derived with a similar functional form. However, in Ref. [268], the case of a BEC unbounded in the axial direction ($\omega_z = 0$) was considered and, as a result, the constant was found to take a different value, $A = 2$. It is also worth noting that the connection between quantum fluctuations and anomalous modes of matter-wave vortices under Magnus forces was considered in Ref. [271].

It is important, at this stage, to make a few comments regarding the nature of the Bogoliubov spectrum resulting from the linearization around the vortex. The system at hand, namely the disk-shaped condensate carrying the vortex, is *not* in the ground state (a similar situation occurs in the 1D analogue of the system, namely a quasi-1D BEC carrying a dark soliton as discussed in the previous chapter). The existence of the anomalous mode, characterized by negative energy, indicates that the vortex (and the dark soliton in the 1D case) is thermodynamically unstable and, in the presence of dissipation, the system is driven towards a lower energy configuration, namely the ground state. Also, the eigenfrequency of the anomalous mode of the vortex (similarly to the case of the dark soliton [272]) bifurcates from its value $\omega = \Omega$ (the linear oscillation with the trap frequency) in the linear limit —where the vortex is represented by the linear superposition $|1, 0\rangle + i|0, 1\rangle$, where $|m, n\rangle$ denotes the m -th linear eigenstate of the quantum harmonic oscillator along the x -direction and n -th one along the y -direction (see discussion in section 6.2.1 and Fig. 6.1). Generally, the anomalous mode (in both 1D and 2D cases) is the *lowest* excitation frequency of harmonically trapped systems and the only one below the trap frequency, which is associated with the doubly de-

generate (in the two-dimensional case) Kohn mode corresponding to the dipolar motion of the condensate [4]. However, in the case of the vortex (and contrary to what is the case for the dark soliton), there is one more frequency, which may be smaller than ω_{an} , at least for small chemical potentials. However the corresponding mode grows monotonically away from the origin and thus becomes larger for increasing chemical potential than the anomalous mode and the Kohn mode. This frequency was described through a small parameter expansion in Section V.B of Ref. [273]. The relevant eigenfrequency is given (in our units) by the following expression,

$$\omega \approx \mu - 2\Omega, \quad (6.12)$$

which becomes increasingly more accurate as $\mu \rightarrow 2\Omega$. This is in contrast to the case for the expression of the precession frequency Eq. (6.11), which should be increasingly more accurate in the Thomas-Fermi (TF) limit, corresponding to large μ .

We now turn to numerical investigations in order to examine the validity of our results in the case of the parabolic trap for constant nonlinearity strength, as well as to generalize them to settings which are less straightforward to consider by analytical means. The results will be partitioned in two subsections: firstly, we will provide bifurcation results from the BdG analysis, and subsequently, we will also test the BdG predictions against full numerical integration of Eq. (6.1).

6.2 Numerical Results

6.2.1 Bogoliubov-de Gennes Analysis

We start with the case of a singly-charged vortex in a harmonically confined BEC with homogeneous interatomic interactions (i.e., $g = 1$). In Fig. 6.1 we show the numerically obtained eigenfrequency ω of the Bogoliubov spectrum as (blue) solid lines as a function of the chemical potential μ and the analytical predictions of Eq. (6.11) (green) dashed-dotted line and Eq. (6.12) (red) dashed line. The numerically obtained frequencies are real denoting that the system is dynamically stable. We observe that in accordance to the analytical predictions, the lowest modes are (i) the one monotonically increasing away from zero and (ii) the anomalous mode, connected to the vortex precession (see previous section), bifurcating from the constant dipolar mode in the liner limit. For the monotonically increasing mode, we notice that the non-radial nature of the solutions at hand (due to their phase profile) leads to the absence of additional symmetries of the eigenvalue problem away from the linear limit. The only symmetry generally present is that of the phase or gauge invariance, associated with the conservation of the number of particles. This sustains a pair of linearization eigenfrequencies at $\omega = 0$, but as discussed in Ref. [273], at the linear limit the dimension of the corresponding kernel is 4, hence an eigenfrequency pair should depart from the origin (at least for small μ) according to Eq. (6.12). As observed in Fig. 6.1, this prediction is in good agreement with the numerical results. Naturally, deviations are observed for larger chemical potentials. On the other hand, as concerns the precession frequency, we notice its monotonically decreasing dependence on μ for given Ω (the latter, was set to $\Omega = 0.2$ in Fig. 6.1), its bifurcation from the Kohn mode eigenfrequency limit and its excellent agreement with the theoretical prediction in the TF limit (for all $\mu > 1$). We note in passing that in this two-dimensional case, a pair of Kohn modes can be seen to be preserved at $\omega = \Omega = 0.2$, being associated with the

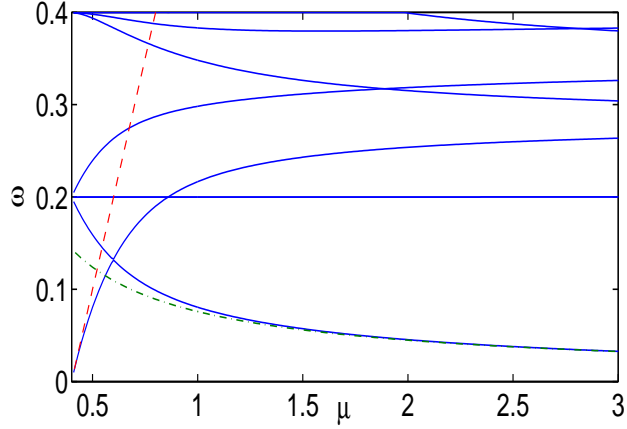


Figure 6.1: The eigenfrequency ω of the Bogoliubov spectrum for a harmonically confined singly-charged vortex as a function of the chemical potential μ (for a trap strength $\Omega = 0.2$). Theoretical predictions are given by $\omega = (\mu - 2\Omega)$ [(red) dashed line] for the mode monotonically increasing from zero and $\omega = (\Omega^2/(2\mu)) \log(A\mu/\Omega)$ [(green) dash-dotted line]; the constant A was chosen to be $2\sqrt{2}\pi \approx 8.886$.

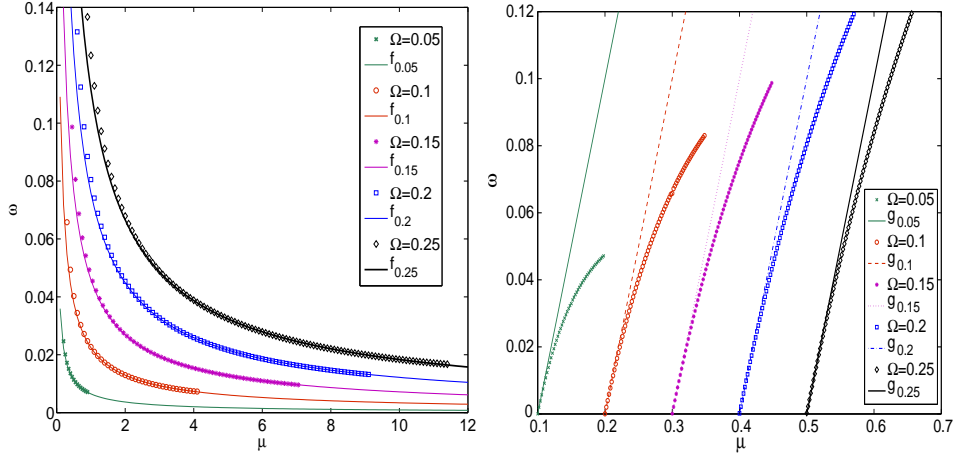


Figure 6.2: Top: dependence of the anomalous mode eigenfrequency on the chemical potential for different trap frequencies Ω . The data points are interpolated by the functions $f_\Omega(\mu) = (\Omega^2/(2\mu)) \log(2\sqrt{2}\pi\mu/\Omega)$. Bottom: similar to top panel, but for the mode bifurcating from zero, as compared to the theoretical prediction $g_\Omega(\mu) = \mu - 2\Omega$.

dipole oscillations of the condensate along the two spatial directions, while the fourth mode at 0.2 in the linear limit results in a monotonically growing eigenfrequency, as μ is increased.

We have also tested the validity of the analytical predictions concerning the two lowest eigenfrequencies for different values of Ω and as a function of μ (see Fig. 6.2). Once again, a very good agreement of the two asymptotic theoretical descriptions in their respective limits is found.

We now consider an interesting modification to this picture, arising from a consideration of inhomogeneous interatomic interactions, described by a spatially-dependent scattering length $a(x, y)$ (cf. section 2.1.3). Here, we will consider the effect of a periodic variation of the

nonlinearity strength, $g \equiv g(x, y)$ (i.e., a sort of a nonlinear optical lattice) on the spectrum of a vortex. We will also draw parallels with similar spectral implications in the setting of a linear periodic potential analyzed in Ref. [274].

In Fig. 6.3, we study the case of a *cosinusoidal* variation of the nonlinearity strength, namely, $g(x, y) = 1 + s(\cos^2(\pi x/4) + \cos^2(\pi y/4))$, monitoring the vortex spectrum as a function of the chemical potential, where s is the strength of the oscillation. In the same figure, the typical form of the density and phase of the wave function (the former showcasing spatial variation dictated by the corresponding variation of the scattering length, and the latter demonstrating the vortex structure of the configuration), as well as the Bogoliubov excitation spectrum, are also illustrated. We notice that while most of the relevant eigenfrequencies are only very weakly affected by the spatially-dependent nonlinearity, the one which is most *dramatically* affected is that of the anomalous mode. The comparison of the $s = 0$ case of Fig. 6.1 (blue solid lines) with the red dashed line of $s = 0.1$ and the green dash-dotted of $s = 0.3$ illustrates that the latter two not only approach zero, but rather cross it at a finite value of μ . For $s = 0.1$, the anomalous mode hits the origin of the spectral plane at $\mu = 2.61$, while for $s = 0.3$ at $\mu = 1.56$. However, it is perhaps even more remarkable that this collision does not produce an instability through an imaginary eigenfrequency (real eigenvalue) pair, but rather maintains the stability of the configuration (the eigenfrequencies appear to go through each other). Generally, it can be seen that the trend of increasing the oscillation strength in the cosinusoidal case leads to a more rapid decrease of the anomalous mode eigenfrequency with μ and an “earlier” collision (i.e., occurring for smaller μ) with the spectral plane origin. The present study focuses on a periodicity (wavelength) of the nonlinearity that is larger than the size (core) of the vortex. All throughout this long wavelength regime the spectral results are qualitatively the same. For the case pertaining to wavelengths of the nonlinearity comparable or smaller than the size of the vortex it can be anticipated that for small enough wavelengths compared to the core of the vortex, the spatial modulation of the nonlinearity will effectively, through spatial homogenization, act as a constant nonlinearity (possibly shifted from its original $g = 1$ value) in a manner akin to the effects of (linear) periodic potentials generated by optical lattices acting on harmonically trapped dark solitons [138].

It is now interesting to turn to the case of the *sinusoidal* modulation of the nonlinearity strength, namely $g(x, y) = 1 + s(\sin^2(\pi x/4) + \sin^2(\pi y/4))$. In this case, as observed in Fig. 6.4, the fundamental difference is that the anomalous mode is larger than that of the homogeneous interactions case ($g = 1$). More importantly perhaps, its dependence can also be non-monotonic, resulting in the increase of the corresponding eigenfrequency for a chemical potential $\mu \gtrsim 1$. Consequently, this raises the possibility of collision of the relevant eigenmode with other modes bifurcating from $\omega = \Omega$ for sufficiently large μ (see [green] cross for $\mu \approx 2.11$ in the case of $s = 0.3$ considered in the figure). This, in turn, produces an instability due to the opposite Krein sign of the colliding modes, yielding a quartet of complex eigenfrequencies. The (positive) imaginary part of the latter, is shown in the bottom panel of Fig. 6.4; see also the second and third row of panels for a typical profile and spectral plane of the relevant configuration.

The above features of the anomalous mode seem structurally similar to the linear periodic potential case, where again the cosinusoidal case was found to be dynamically stable, while the sinusoidal one was unstable beyond a critical lattice strength [146, 274, 275]. These results also motivate an investigation of how this phenomenology may be modified in the presence of a dissipative term.

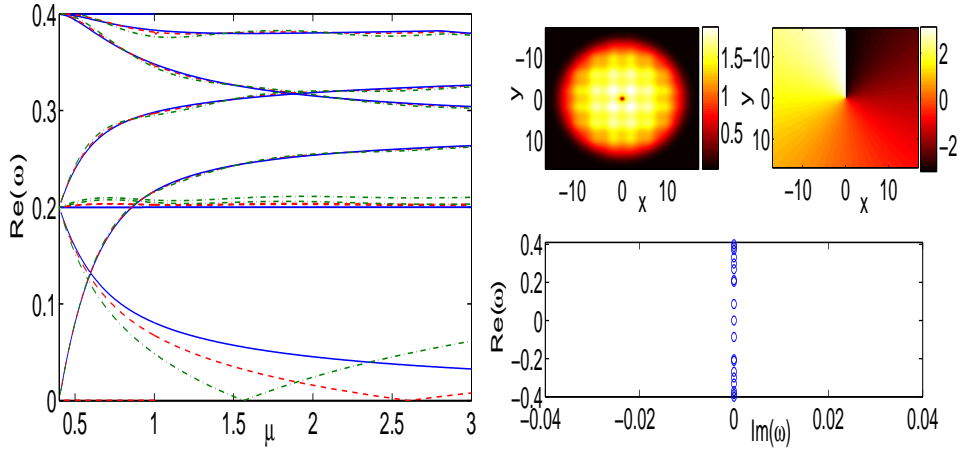


Figure 6.3: The case of a cosinusoidal variation of the nonlinearity strength for a trap strength $\Omega = 0.2$. The left panel is similar to Fig. 6.1 showing the eigenfrequency ω of the Bogoliubov spectrum as a function of the chemical potential μ . Comparison of $g(x,y) = 1 + s(\cos^2(\pi x/4) + \cos^2(\pi y/4))$, with $s = 0.1$ [(red) dashed line] and $s = 0.3$ [(green) dash-dotted line], with the case of $s = 0$ [(blue) solid line]. The upper right panels show contour plots of the density (left) and phase (right) of the wave function, while the bottom panel shows the respective Bogoliubov excitation spectrum (real vs. imaginary part of the eigenfrequency ω , where instability would correspond to the existence of eigenfrequencies with $\text{Im}(\omega) \neq 0$). The chemical potential is $\mu = 4$ (approaching the Thomas-Fermi limit).

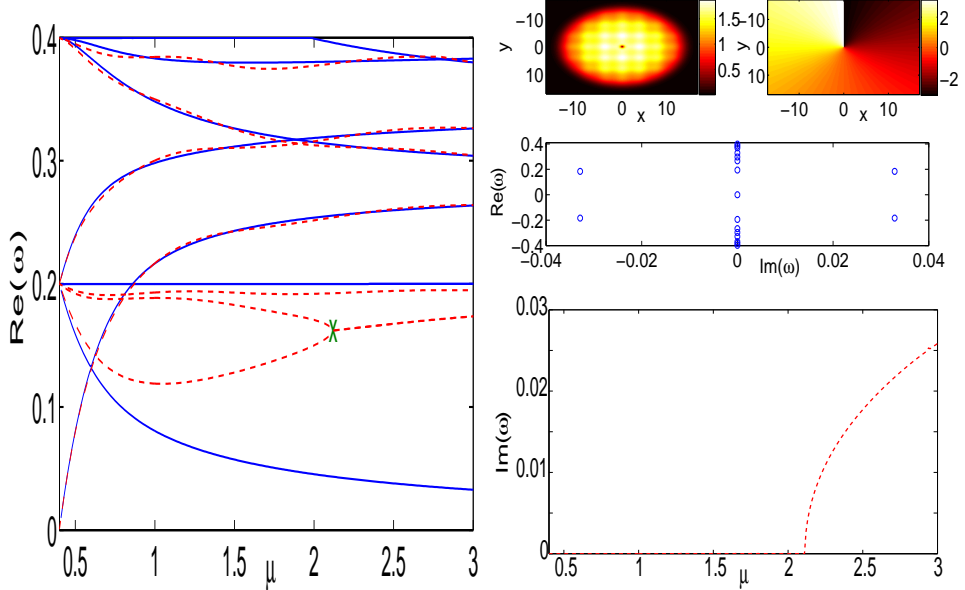


Figure 6.4: Similar to Fig. 6.3, but for the case of a sinusoidal variation of the nonlinearity strength. The left panel and the upper right panels are analogous to the panels of Fig. 6.3. The case of $g(x,y) = 1 + s(\sin^2(\pi x/4) + \sin^2(\pi y/4))$, for $s = 0.3$ [(red) dashed line] is compared to that of $s = 0$ [(blue) solid line]. The bottom right panel shows the imaginary part of the complex eigenfrequency; the oscillatory instability arises for $\mu > 2.11$.

In this case, the pertinent model is the so-called dissipative GPE, which can be expressed in the following dimensionless form:

$$(i - \gamma)u_t = -\frac{1}{2}\Delta u + V(r)u + |u|^2u - \mu u, \quad (6.13)$$

where the dimensionless parameter γ can be associated with the system's temperature in SI units according to [253, 256] (see also [263])

$$\gamma = G \times \frac{4ma^2k_B T}{\pi\hbar^2}, \quad (6.14)$$

with k_B being Boltzmann's constant and the heuristically introduced dimensionless prefactor $G \approx 3$. Note that in the dissipative model the interaction between the thermal cloud and the condensate is only modeled by particle exchange resulting in the dissipative factor γ ; we should note that physically, the relevant case is that of $\gamma \ll 1$, although for illustration purposes we will occasionally show also the results away from that regime. The chemical potential and trap strength in Eq. (6.13) are set to the values $\mu = 1$ and $\Omega = 0.2$ (per the above discussion, it is understood how different μ and Ω will modify the relevant phenomenology).

In Fig. 6.5, we show the BdG spectrum of a vortex for a case of $\gamma = 0$ (zero temperature, i.e., no dissipation) and for the case of $\gamma = 0.2$ (finite temperature, i.e., dissipation). It is clear that the lowest frequency mode of the condensate (which for $\mu = 1$ is the anomalous mode) is the one that, for nonzero values of γ , immediately acquires a positive imaginary eigenfrequency, contrary to what is the case for all other eigenmodes of the system. In fact, precisely this property was rigorously proved in Ref. [266] for negative Krein sign eigenmodes, namely that their bifurcation upon such dissipative perturbations happens *oppositely* to that of all other modes (of positive energy) of the system. This remarkable feature is directly consonant with the property of this excited state of the system resulting, via the effect of dissipation (and through the complex nature of the relevant eigenmode) eventually into the ground state of the system. Moreover, notice that this complex eigenmode also implies the combination of growing amplitude with the previously analyzed precessional motion, leading to the spiraling of the vortex core toward the edges of the TF cloud and its eventual disappearance, in favor of the ground state of the system (see below).

Lastly, let us investigate the effect of a periodic modulation of the nonlinearity on the stability of the system for the finite-temperature case. For a periodic cosinusoidal modulation of the nonlinearity the imaginary part of all eigenfrequencies vanishes and the system is stable for $\gamma = 0$ as discussed above. The top panel of Fig. 6.6 shows the maximal imaginary part of the eigenfrequency as a function of γ for different chemical potentials μ for $g(x, y) = 1 + s(\cos^2(\pi x/4) + \cos^2(\pi y/4))$, with $s = 0.3$. For $\gamma = 0$ the imaginary part of the eigenfrequency vanishes for all cases. However, for small μ the imaginary part of the eigenfrequency becomes non-zero immediately, similar to the case of a constant nonlinearity strength. On the other hand, for large chemical potential the maximal imaginary part of the eigenfrequencies remains zero *independent* of γ . Thus, the system remains stable even in the presence of dissipation. This behavior can be understood by investigation of Fig. 6.4. The occurrence of a positive imaginary part of the eigenfrequencies is due to the fact that the anomalous mode is of negative Krein sign. However, for the case of a cosinusoidal modulation of the nonlinearity one observes that the value of the frequency of the anomalous mode decreases with increasing

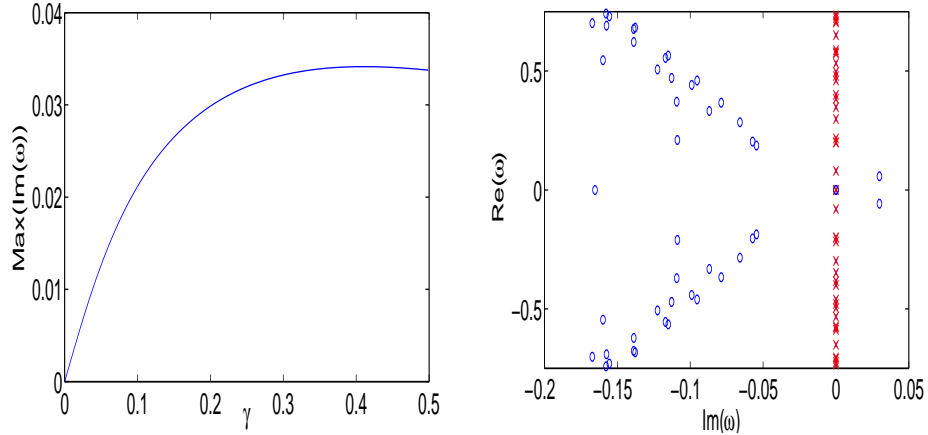


Figure 6.5: The left panel shows the immediate acquisition of a non-vanishing imaginary part of the eigenfrequency associated with the anomalous mode, as soon as the temperature-dependent dissipative prefactor γ becomes nonzero. The right panel highlights the special behavior of the anomalous mode by illustrating the BdG spectrum for the cases of $\gamma = 0$ (red crosses) and that of $\gamma = 0.2$ (blue circles). Notice how in the latter case the eigenfrequencies form nearly two symmetric arcs in the negative imaginary half-plane.

μ and, finally, even crosses the origin. At that critical point, the frequency curve shows a crossover with its opposite-value companion (of the same pair). However the latter mode has a positive Krein sign and therefore (since all negative signatures arise for negative frequencies, and positive signatures for positive frequencies), the imaginary parts of the eigenfrequencies become negative in the case of nonzero γ . The bottom panel in Fig. 6.6 provides an overview of the eigenfrequencies for $\gamma = 0.2$ and $\mu = 1.6$. All eigenfrequencies were shifted further into the negative imaginary half-plane in comparison to the corresponding panel in Fig. 6.5. Importantly, the eigenfrequencies corresponding to the (formerly) anomalous mode got shifted into the negative imaginary half-plane as is shown in the inset.

6.2.2 Direct Numerical Simulations

In this section we show results obtained by direct numerical integration of Eq. (6.1) starting with different initial states containing a single vortex. In order to determine the position of the vortex as a function of time we first compute the fluid velocity [276]

$$\mathbf{v}_s = -\frac{i}{2} \frac{u^* \nabla u - u \nabla u^*}{|u|^2}. \quad (6.15)$$

The fluid vorticity is then defined as $\omega_{\text{vor}} = \nabla \times \mathbf{v}_s$. Due to our setup, the direction of the fluid vorticity is always the z -direction and, therefore, we can treat this quantity as a scalar. Furthermore, we investigate single vortex states leading to a single maximum of the fluid vorticity at the position of the vortex. This allows us to determine the position of the vortex by determining the center of mass of the vorticity ω_{vor} .

Figure 6.7 shows the evolution of a single vortex for $g = 1$. We displaced the vortex initially from the center of the trap to $(x_0, y_0) = (-1.5, 0)$ and propagated the state numerically using Eq. (6.1). The thus obtained results are compared to the solutions of Eqs. (6.9-6.10)

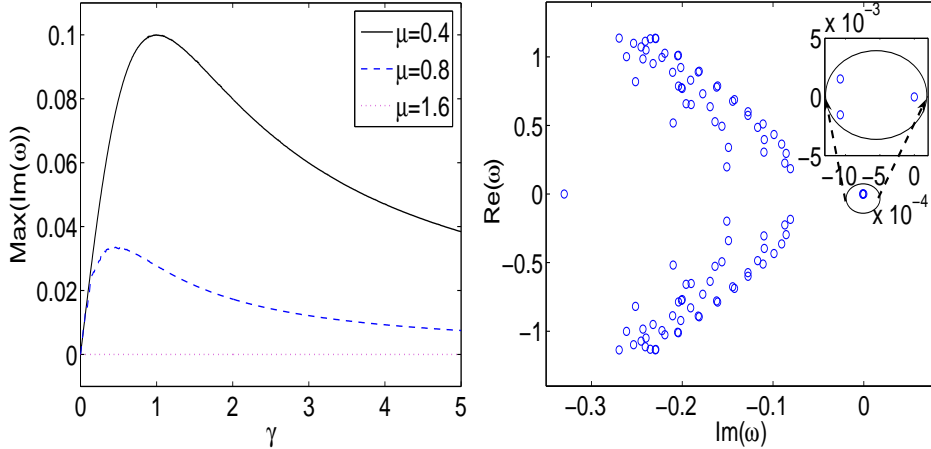


Figure 6.6: The left panel shows the immediate acquisition of a non vanishing imaginary part of the eigenfrequency associated with the anomalous mode, as soon as the temperature-dependent dissipative prefactor γ is nonzero for small chemical potentials, but no acquisition of an imaginary part for large chemical potentials. The right panel gives an overview of the eigenfrequencies for $\gamma = 0.2$ and $\mu = 1.6$. The maximum imaginary part is zero. The inset shows that the eigenfrequencies corresponding to the anomalous mode got shifted into the negative imaginary half-plane.

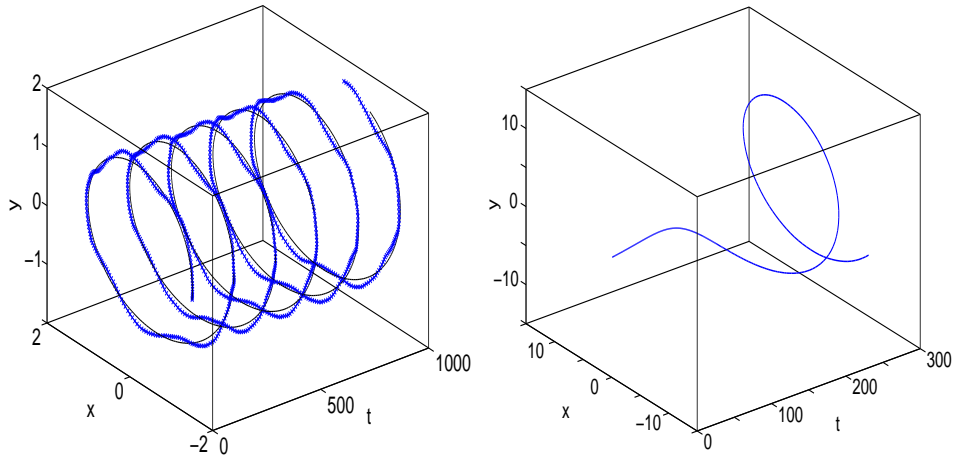


Figure 6.7: The left panel shows the trajectory of the vortex for $g = 1$ and $\mu = 3$ obtained by direct integration (crosses) and the theoretical prediction (solid line) obtained by solving Eqs. (6.9-6.10). Notice the excellent agreement between the two. The right panel shows the corresponding trajectory for the case taking into account dissipation, namely integrating Eq. (6.13) with $\gamma = 0.2$.

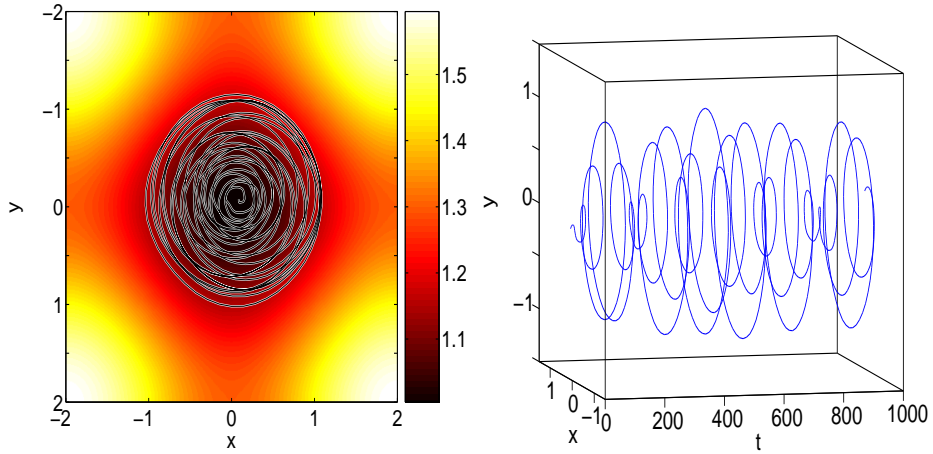


Figure 6.8: The trajectory of a vortex for $\mu = 3$ for the case $g(x, y) = 1 + s(\sin^2(\pi x/4) + \sin^2(\pi y/4))$ with $s = 0.3$. In the left panel the trajectory is plotted on top of the profile of the coupling $g(x, y)$, whereas the right panel shows the trajectory as a function of time.

$x = x_0 \cos(Ct)$ and $y = y_0 \sin(Ct)$ with $C = (\Omega^2/(2\mu)) \log(A\mu/\Omega)$ and the initial position (x_0, y_0) . The theoretical predictions agree very well with our numerical findings: the vortex oscillates around the center of the trap with constant frequency and radius (see left panel). The right panel shows the trajectory for the case of constant nonlinearity $g = 1$ but for finite temperature (i.e., including dissipation). The results shown were obtained by direct numerical integration of Eq. (6.13) for $\gamma = 0.2$, with the initial condition being a slightly perturbed eigenstate of the system. Due to the instability of the system this small perturbation leads to the spiraling out of the vortex, as is physically anticipated in the presence of finite temperature [277]; we note in passing that this work contains a detailed model from microscopic first principles that illustrates a similar phenomenology upon a spatially dependent inclusion of the coupling of the condensate with the thermal cloud.

Figure 6.8 shows the trajectory of a vortex for the case of a periodically modulated sinusoidal nonlinearity, $g(x, y) = 1 + s(\sin^2(\pi x/4) + \sin^2(\pi y/4))$. The initial configuration is a slightly perturbed eigenstate leading to a small shift of the position of the vortex. Due to the instability of the sinusoidal $g(x, y)$ landscape, the vortex spirals outwards initially, but then spirals inwards after reaching a region with approximately constant nonlinearity. Subsequently the vortex follows a series of such alternating (spiraling first outwards, and then inwards) cycles in an apparently quasi-periodic orbit.

Figure 6.9 shows the trajectory of a vortex for the case of a periodically modulated cosinusoidal nonlinearity, $g(x, y) = 1 + s(\cos^2(\pi x/4) + \cos^2(\pi y/4))$, without dissipation (left panel) and with dissipation (right panel). In this case, small perturbations do not get amplified since the system is stable. However, a macroscopic displacement of the vortex to $(x_0, y_0) = (-1.5, 0)$ leads to the trajectories shown in the figure (see left panel). In the case without dissipation the vortex moves outwards (reaching a region outside the “square” of the first minima of the nonlinearity) and oscillates around the center on a trajectory with roughly constant nonlinearity. For the case with cosinusoidal nonlinearity *and* dissipation (see right panel), the vortex remains stable against small perturbations and does not spiral

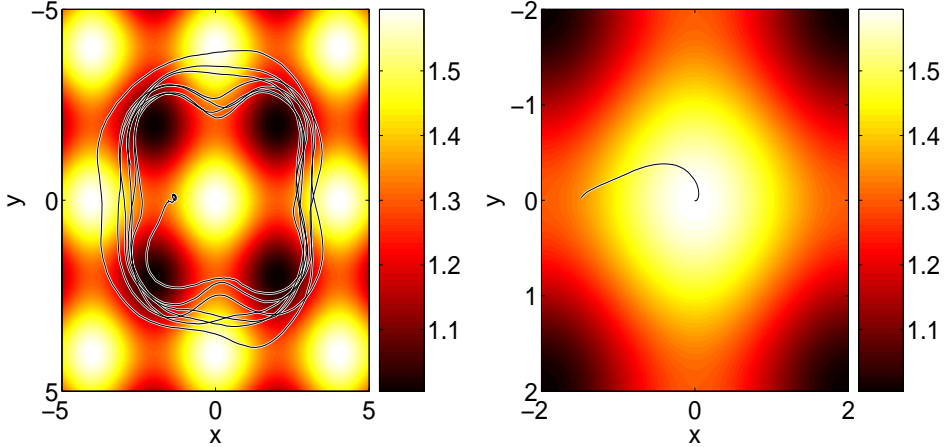


Figure 6.9: The trajectory of the vortex for $\mu = 3$ for the case $g(x, y) = 1 + s (\cos^2(\pi x/4) + \cos^2(\pi y/4))$ with $s = 0.3$ without dissipation (left) and with dissipation (right) with $\gamma = 0.2$. The trajectories are plotted on top of the profile of the coupling $g(x, y)$. Notice the fast inward vortex motion in the presence of dissipation.

out, contrary to the case of a constant nonlinearity. Even for a macroscopical displacement the vortex moves back to the center of the trap and remains stable there. This behavior is possible because the effective potential due to the spatial variation of the nonlinearity creates the possibility for a metastable vortex state *even in the presence of dissipation*.

In conclusion, the modulation of the nonlinearity opens up the possibility to stabilize the vortex against excitations due to finite temperature effects. This can be extremely useful for setups which require stable vortex states for a long period of time as, e.g., in the recent work of Ref. [278] which suggests the use of a superposition of two counter rotating BECs as a gyroscope.

6.3 Conclusions

In summary, in this chapter, we examined the role of anomalous modes in the motion of vortices in harmonically confined condensates. We have also focused on the settings of spatially dependent scattering lengths and of finite temperature (as well as the combination thereof). We found a number of interesting results, including an explicit semi-analytical expression for the precession frequency in the trap (by means of the matched asymptotics technique), which was found to be in excellent agreement with both bifurcation and direct numerical integration results, for different chemical potentials and trap frequencies within the Thomas-Fermi regime.

We subsequently examined how the spectrum (more generally —and the anomalous mode in particular) are affected by the presence of spatially-dependent (harmonic) interatomic interactions. We found that the latter may induce or avoid instabilities depending on the curvature and the strength of the nonlinearity variation. The effect of temperature was examined in a simple phenomenological setting which, however, still enabled us to observe the thermal instability of the vortex and its rapid spiraling towards the edges of the condensate cloud. Intriguingly enough, we also demonstrated that the effect of spatially dependent

nonlinearities may avoid the thermal instability of the vortex by creating a local metastable effective energy minimum wherein the vortex can spiral inwards towards the center of the harmonic trap.

Chapter 7

Bifurcations, Stability and Dynamics of Multiple Matter-Wave Vortex States

In the previous chapter we investigated single vortex states in quasi 2D BECs confined in harmonic, non-rotating traps. Let us now investigate the subject of multiple matter-wave vortex states in disk-shaped BECs thereby connecting dark soliton states and vortex states. Dark soliton states are stable states in 1D BECs confined in harmonic traps and are robust in a quasi (1D) geometry. However in 2D condensates they become unstable. We illustrate that this dimensionality-induced destabilization of the dark soliton leads, through a supercritical pitchfork bifurcation, to the formation of the vortex dipole. Further destabilizations of the dark soliton leads to the formation of the stationary tripole, aligned quadrupole, quintopole, etc. We clarify the relevant nature of such supercritical pitchfork bifurcations and illustrate their symmetry breaking character, through a few mode expansion that enables an *analytical* prediction of the bifurcation point of the emergence of these states. We systematically study the stability of each of these states by elucidating their complete linearization spectrum, anomalous modes and imaginary, as well as complex eigenfrequency instabilities; we also showcase the connections of this spectrum with the bifurcation picture presented through general principles of bifurcation theory. We formulate a complementary physical picture, which considers the vortices as individual particles precessing within the parabolic trap and interacting with each other through the modification of each other's local velocity field. This picture allows us to predict not only the equilibrium position of the vortices, e.g., in a dipole setting, but also (and perhaps even more importantly) the near-equilibrium dynamics, e.g., the anomalous modes of the vortex pair and the epicyclic motions associated with the non-trivial one among these modes. Finally, we use the above particle picture as a guide towards some of the more complex vortex dynamics which we corroborate through direct numerical simulations. The results of this chapter are partly published in Ref. [279].

The chapter is structured in the following way. In section 7.1, we present our theoretical analysis for the few-mode bifurcation picture, which is particularly relevant close to the linear limit. We complement this with a large-amplitude perspective, whereby dynamical equations for two or more isolated vortices are considered, and their static, stability and dynamical implications are examined. Subsequently, in section 7.2, we embark on a detailed numerical bifurcation study of the states emerging from the dark soliton stripe (as well as of a few that do not arise from it). In section 7.3, we corroborate some of the near-equilibrium static/linearization picture with direct numerical simulations; we also consider a few more exotic dynamical implications of the original model [and of its underlying ordinary differential equation (ODE) counterpart]. Finally, in section 7.4, we summarize the content of this chapter.

7.1 Theoretical Analysis

7.1.1 Dark Soliton Stripe Bifurcation Picture

In this chapter we restrict our investigations to zero temperature and a constant scattering length. So the model under consideration can be described by Eq. (6.2). Firstly, let us investigate the existence and possible bifurcations of the lowest macroscopically excited states of Eq. (6.2). Below, we fix the trap strength using $\Omega = 0.2$. In the non-interacting (linear) case, the Hamiltonian describing the stationary states can be written as $\hat{H} = \hat{H}_x + \hat{H}_y$, with \hat{H}_x and \hat{H}_y being the Hamiltonian of a single particle in a harmonic trap oriented along the x - and y - directions, respectively. Therefore, the linear states factorize as well and can be written as $\Psi_{nm}(x, y) = \psi_n(x)\psi_m(y)$ with $\psi_n(x)$ and $\psi_m(y)$ being the states associated to the n -th and m -th eigenvalue of \hat{H}_x and \hat{H}_y , respectively. The resulting states $\Psi_{nm}(x, y)$ with energy $\mu = (n + m + 1)\Omega$ denote the eigenstates of the linear limit. Due to the rotational symmetry of the problem, one can rotate any solution around the center of the trap obtaining another solution. Hence, when we consider in the following a solution with a distinct symmetry direction one needs to have in mind that the direction may be chosen arbitrarily.

The top panel of Fig. 7.1 shows the number of atoms N as a function of the chemical potential for different branches of possible solutions. The bottom panel in this figure shows, for better clarity of exposition, the atom difference $\Delta N = N - N_{\text{ds}}$ between the atom number N of a particular branch and the atom number N_{ds} for the dark soliton branch. We have not shown the branch of the ground state starting at $\mu = \Omega = 0.2$ from the linear limit, as the stable ground state of the system will not be relevant in our discussion hereafter.

The first branch, with the largest atom number (among the ones considered therein) for fixed chemical potential, is the single vortex (sv) state located at the center of the trap. We have shown in the previous chapter that this state is dynamically stable (for zero temperature), despite of the fact that it possesses an anomalous mode in its excitation spectrum. In the linear limit, this state is given by $\Psi_{\text{sv}}(x, y) = \psi_1(x)\psi_0(y) + i\psi_0(x)\psi_1(y)$. Therefore, it is “initialized” at an energy of $\mu = 2\Omega$. For increasing chemical potential the atom number increases monotonically. Furthermore, no other states bifurcate from this one (given its existence properties and its absence of stability changes).

The second (and most critical, for our discussion herein) branch starts from $\mu = 2\Omega$ in the linear limit as well. The wave function of this branch is given in the linear limit by $\Psi_{\text{ds}}(x, y) = \Psi_{10}(x, y) = \psi_1(x)\psi_0(y)$ (without loss of generality we assumed the relevant stripe to be oriented along the y -axis). This state, which has a density minimum along the y -axis and a phase jump across this minimum, is precisely the dark soliton (ds) stripe with the line symmetry that characterizes such a 2D generalization of the 1D dark soliton.

The essence of our discussion lies in the (symmetry-breaking) bifurcations arising from the dark soliton stripe solution. In particular, in the case of $\Omega = 0.2$ considered in Fig. 7.1, and for $\mu \approx 0.68$, the vortex dipole state emerges. This is clearly a supercritical pitchfork bifurcation, as there are two potential installments of such a dipole with opposite, between them, relative positions of their $S = 1$ and $S = -1$ vortex constituents. The location of this bifurcation is sufficiently close to the linear limit so that it can be predicted by using a Galerkin-type approach [48] (see also Refs. [47, 280] for a general discussion). The dark soliton state is given, close to the linear limit, by $\Psi_{\text{ds}}(x, y) = \psi_1(x)\psi_0(y)$. The vortex dipole (vd) state occurs due to an admixture of the $\Psi_{02}(x, y) = \psi_0(x)\psi_2(y)$ state to Ψ_{ds} , but importantly with

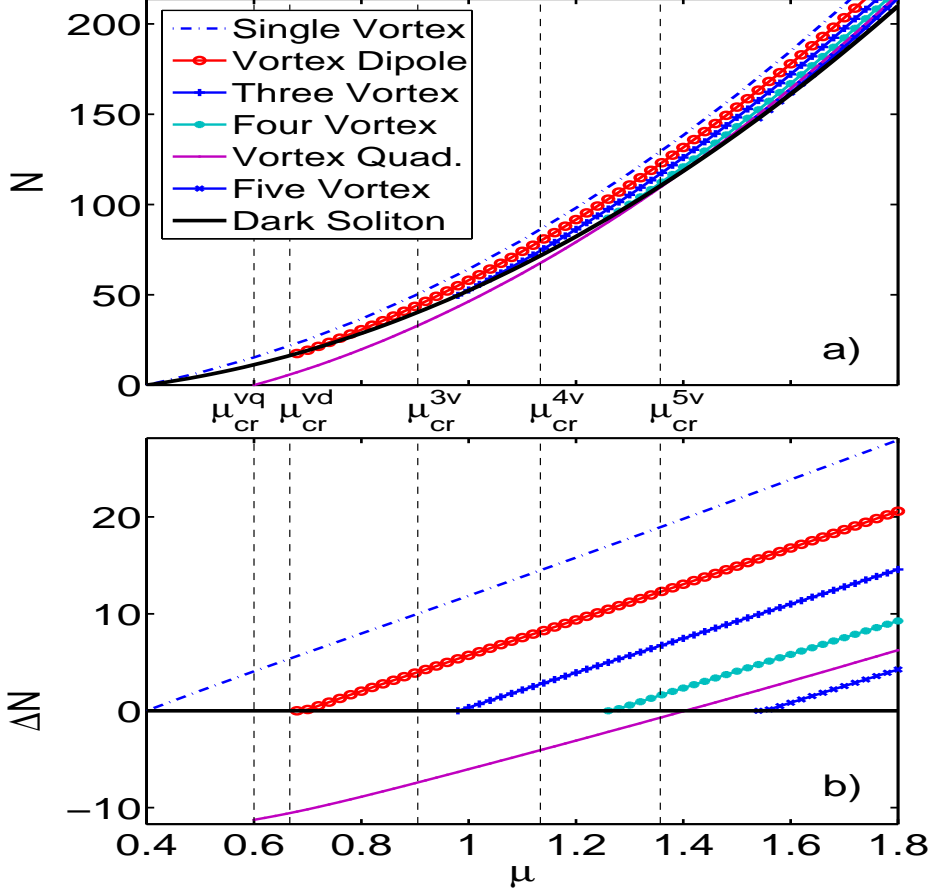


Figure 7.1: Top: Number of atoms as a function of the chemical potential for the different states for $\Omega = 0.2$. Bottom: Corresponding number of atom difference between the different branches and the dark soliton stripe branch.

a phase difference of $\pi/2$ with respect to the Ψ_{ds} . Hence, the bifurcation theory developed in Ref. [48] can be directly applied but with the crucial difference of the relative phase of the symmetry-breaking admixing state (with respect to the original state) of $\phi = \pi/2$. In that case, one can repeat the calculations of Ref. [48] [cf. Eq. (12) therein] to obtain the relevant bifurcation point as:

$$N_{\text{cr}} = \frac{\omega_{10} - \omega_{02}}{I - I_0}, \quad (7.1)$$

where $\omega_{10,02}$ are the eigenvalues corresponding to the states $\Psi_{10}(x, y)$ and $\Psi_{02}(x, y)$, $I_0 = \int \Psi_{10}^4 dx dy$, and $I = \int \Psi_{10}^2 \Psi_{02}^2 dx dy$. One can also determine the critical chemical potential at which the symmetry breaking is expected to occur, namely $\mu_{\text{cr}} = \omega_{10} + I_0 N_{\text{cr}}$ [48]; for these parameter values, this leads to $\mu_{\text{cr}}^{\text{vd}} = \frac{10}{3}\Omega$ ($= 2/3$ for $\Omega = 0.2$, see second vertical thin dashed line in the case shown in Fig. 7.1), which is in excellent agreement with our numerical findings.

For larger chemical potential, at $\mu \approx 0.98$, another branch bifurcates from the dark soliton branch. The wave functions of this branch contain three vortices (3v) oriented along

a line with adjacent vortices having opposite vorticity. It is remarkable that although this bifurcation happens quite far from the linear limit, one can still understand it through the same supercritical pitchfork (symmetry-breaking) theoretical framework. In particular, what is happening in this case is that the Ψ_{03} state is providing the “admixture” element to the “pure” dark soliton stripe state. In light of that, the analysis presented above [and Eq. (7.1)] still holds but now $\omega_{02} \rightarrow \omega_{03} = 3\Omega$ and $I = \int \Psi_{10}^2 \Psi_{03}^2 dx dy$. Repeating the same calculation as above, one finds $\mu_{\text{cr}}^{3v} = 86\Omega/19$ (which in this case is ≈ 0.91 , see the third vertical thin dashed line in Fig. 7.1, in reasonable agreement with the numerical result provided above). Given the substantial departure from the linear limit and the nonlinear deformation of the dark soliton stripe (still represented in the above phenomenology by its linear limit of Ψ_{10}), this slight discrepancy can be well understood. Furthermore, the symmetry-breaking, supercritical pitchfork nature of the bifurcation is again evident since two installments of the same “vortex tripole” (as it will be called below) branch may emerge, one with two $S = 1$ vortices and an $S = -1$ centrally separating them and one with two $S = -1$ vortices with an $S = 1$ between them.

At $\mu \approx 1.26$ a four-vortex (4v) state (an aligned quadrupole), with the vortices oriented along a line, bifurcates from the dark soliton state. At this point, the sequence of symmetry breaking events is clear: now the Ψ_{04} is offering the $\pi/2$ out of phase admixture leading to a critical point through the same procedure and the corresponding reformulation of the above constants of $\mu_{\text{cr}}^{4v} = 890\Omega/157$; in connection to the $\Omega = 0.2$ case of Fig. 7.1, we find $\mu_{\text{cr}}^{4v} \approx 1.13$ (see fourth vertical thin dashed line), with the slight progressive degradation of the critical point attributable again to the further departure from the linear limit. In this case also, the vortex parity variation of $S \rightarrow -S$ for such a four-vortex line configuration whose adjacent vortices possess opposite charges, yields the two bifurcating branches associated with this critical point.

However, we should note in passing here that a state with four vortices exists even in the linear limit as is shown by the branch starting at $\mu = 3\Omega$ in the linear limit: this represents a four vortex state, with vortices located at the vertices of a square, i.e., a vortex quadrupole (vq). This is among the states previously considered in Ref. [165, 172], as well as independently proposed as a member of a larger class of so-called vortex necklace states in Ref. [281]. At the linear limit, this state can be represented as $\Psi_{\text{vq}}(x, y) = C\psi_2(x)\psi_0(y) + C^*\psi_0(x)\psi_2(y)$ with C being a complex number and emerges from the linear limit at $\mu_{\text{cr}}^{\text{vq}} = 3\Omega$ ($= 0.6$ in the case of Fig. 7.1, cf. first vertical thin dashed line in the figure). With increasing chemical potential the number of atoms of the state monotonically increases. At $\mu \approx 1.4$ this branch crosses the branch representing the dark soliton stripe. However, it is important to note that due to the structural disparity of those states, the crossing of the number of atoms (contrary to the previous cases considered above) does *not* constitute a bifurcation and therefore does not lead to any stability change.

Nevertheless, at higher values of μ (e.g., for $\mu \approx 1.54$ in the case of $\Omega = 0.2$ of Fig. 7.1), a five-vortex (5v) state (a vortex quintopole) bifurcates from the dark soliton stripe. Once again, the vortices are oriented along a line and adjacent vortices have opposite vorticities. Furthermore, the bifurcation shares the standard supercritical pitchfork character of the earlier ones, and its characterization through the above analytical tools reveals a critical point at $\mu_{\text{cr}}^{5v} = 726\Omega/107$ (which, for $\Omega = 0.2$, leads to $\mu_{\text{cr}}^{5v} \approx 1.36$, see last vertical thin dashed line in Fig. 7.1). According to the above, the structural progression of these symmetry-breaking events is clear and we will not proceed to characterize higher ones among them, especially

given the dynamical instability of the ones beyond the vortex dipole state (that will be discussed in more detail below).

However, let us add a short note about the physical intuition of the general picture. What is happening in the present setting is that there exists a sequence of supercritical pitchfork bifurcations in which the Ψ_{10} gets mixed progressively with each of the Ψ_{0m} modes. In so doing, the m -fold symmetry of the latter breaks the line symmetry of the former. In addition, the $\pi/2$ relative phase between them introduces a picture which locally at each perpendicular intersection of the m nodal lines of the latter with the nodal line of the former resembles a $\Psi_{10} \pm i\Psi_{01}$ (with the pluses alternating with the minuses due to the field structure of the Ψ_{0m}). As a result, at each of these nodal line intersections, entities with alternating (between adjacent ones) vortices emerge, progressively formulating the dipole, tripole, aligned quadrupole, quintopole, and so on.

7.1.2 Vortex Particle Complementary Picture

The above discussion and bifurcation picture is especially relevant close to the point of emergence of these multi-vortex solution branches. A complementary aspect of our description concerns the case (for larger chemical potentials) where the vortices are well separated, individual entities which can be regarded as interacting particles subject to the precessional effect due to the parabolic confinement. In that picture, it is relevant to develop (kinematic) equations of motion characterizing the vortex dynamical evolution, as well as their potential equilibrium positions and their near-equilibrium behavior. In the previous chapter we derived the equations of motion for the vortex center (x_v, y_v) of a single vortex in an harmonic trap for small displacements of the vortex from the center of the trap, taking the form

$$\dot{x}_v = -S \frac{\Omega^2}{2\mu} \log \left(A \frac{\mu}{\Omega} \right) y_v, \quad (7.2)$$

$$\dot{y}_v = S \frac{\Omega^2}{2\mu} \log \left(A \frac{\mu}{\Omega} \right) x_v, \quad (7.3)$$

where S denotes the topological charge (alias “vorticity”) and A is an appropriate numerical factor, taking the value $A \approx 8.88 \approx 2\sqrt{2}\pi$. Equations (7.2-7.3) suggest a precession of the vortex in the harmonic trap with a frequency

$$\omega_{\text{pr}} = \frac{\Omega^2}{2\mu} \log \left(A \frac{\mu}{\Omega} \right). \quad (7.4)$$

Naturally, the amplitude of the precession is fixed and fully determined by the initial distance $R_0 = \sqrt{x_0^2 + y_0^2}$ of the vortex location from the trap center. While the above results are in excellent agreement with numerical computations for small R_0 as we demonstrated in the previous chapter, it is worth investigating the dependence of the precession frequency on R_0 for intermediate and/or large radii. In that regard, Fig. 7.2 which shows the dependence of A on R_0 (for $\mu = 3$), suggests that the value of the numerical factor A changes for large initial displacements: in fact, up to $R_0 < 1.5$, the value $A \approx 2\sqrt{2}\pi$, (corresponding to infinitesimally small displacements) yields a good approximation, while for larger displacements R_0 , the value of A is increased, indicating the faster rotation of the vortices away from the condensate center.

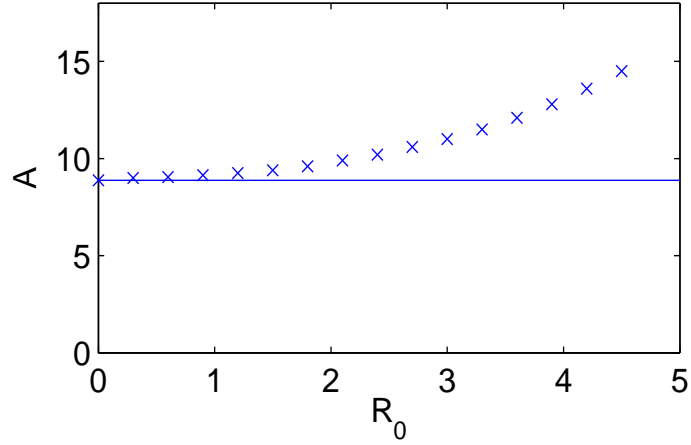


Figure 7.2: Dependence of the numerical factor A [see Eqs. (7.2-7.3)] on the initial displacement R_0 of the vortex from the center of the trap, for $\mu = 3$.

Having discussed the dynamics of a single vortex in the trap, let us now consider the vortex-vortex interaction. Based on the analogy with fluid vortices [282], it has been argued that the superfluid vortices considered herein have similar interaction laws and corresponding kinematic equations. In particular, on a homogeneous background, and for large distances of the vortices compared to the size of the vortex core, the kinematic equations for vortices with centers (x_m, y_m) and (x_n, y_n) take the form [283, 284]

$$\dot{x}_m = -BS_n \frac{y_m - y_n}{2\rho^2}, \quad (7.5)$$

$$\dot{y}_m = BS_n \frac{x_m - x_n}{2\rho^2}, \quad (7.6)$$

with $\rho = \sqrt{(x_m - x_n)^2 + (y_m - y_n)^2}$, $S_n = \pm 1$ the vorticity of the vortex n and an appropriate numerical factor B ; in the case of the homogeneous condensate, the latter takes the value $B \approx 1.95$. Note, S_n is not a typo but the equations of motion for the vortex m depend on the vorticity of the vortex n .

Let us now combine Eqs. (7.2-7.3), describing the interaction of the background density of a condensate in a trap with each single vortex, and Eqs. (7.5-7.6) describing the interaction of (any pair of) two vortices on a homogeneous background, to provide the total contribution to the superfluid local velocity at the vortex location. This way, the vortex motion can be described as follows:

$$\dot{x}_m = -S_m \omega_{\text{pr}} y_m - BS_n \frac{y_m - y_n}{2\rho_{mn}^2}, \quad (7.7)$$

$$\dot{y}_m = S_m \omega_{\text{pr}} x_m + BS_n \frac{x_m - x_n}{2\rho_{mn}^2}. \quad (7.8)$$

It is worth noticing that although these equations refer to the case of two vortices, indexed by m and n , the relevant generalization to an *arbitrary* number of (precessing and interacting) vortices is imminently evident through the conversion of the second term in the right hand

side of Eqs. (7.7-7.8) into a sum over all $n \neq m$.

Focusing on the two-vortex setting for definiteness, the above description yields a number of interesting conclusions. For $S_1 = -S_2 = 1$ the equations possess fixed points at

$$x_1 = x_2 = 0, \quad (7.9)$$

$$y_1 = -y_2 = \sqrt{\frac{B}{4\omega_{\text{pr}}}}. \quad (7.10)$$

These are anticipated to be the equilibrium locations of the vortices within the vortex dipole. Furthermore, the linearization of the dynamical equations (7.7-7.8) around these equilibrium points offers insight into the fate of small perturbations around these steady state locations. Part of the special appeal of this analysis is that it can provide *explicit, analytical* predictions for the *internal modes* of the vortex system. These are in fact, precisely, the anomalous modes of negative Krein signature or the unstable imaginary eigenfrequency modes pertaining to this non-ground-state type of structure, as we will illustrate in our numerical computations of the full system below; see also the corresponding discussion for a single vortex in the previous chapter and for the quasi-1D analog of this picture in the dark soliton setting in chapter 5 and Refs. [110, 127, 285]. The Jacobian matrix of the linearization around the equilibrium vortex dipole location offers the following insights. One of the vortex dipole linearization modes has a vanishing frequency, i.e., a pair of eigenfrequencies at $\omega = 0$. This is natural to expect: this frequency pair merely corresponds to the neutral direction associated with the “rotational freedom” of the vortex dipole pair, i.e., the ability to equivalently locate it at any pair of anti-diametric points located at a distance given by Eq. (7.10) from the trap center. The other non-vanishing pair of linearization eigenmodes (of this 4×4 system) corresponds to a frequency:

$$\omega_{\text{pr}}^{\text{vd}} = \pm \sqrt{2} \omega_{\text{pr}}. \quad (7.11)$$

This frequency characterizes the precessional motion of the vortex pair around this equilibrium position which can be naturally thought of as an “epicyclic” counter-rotation of the oppositely charged vortices. We now turn to the examination of the above analytical findings by applying numerical existence and stability tools.

7.2 Soliton and Vortex States and their Stability

7.2.1 The Dark Soliton State

The top panel of Fig. 7.3 shows contour plots of the density and phase of the dark soliton stripe for $\mu = 3$. The density has a minimum along the y -axis associated with a π phase jump, characteristic of dark solitons. The dark soliton state exists for $\mu > 0.4$. The bottom panel shows the real and imaginary parts of the eigenvalues of the BdG spectrum as a function of the chemical potential. The real parts correspond to oscillation frequencies, whereas the imaginary parts imply dynamical instabilities. We note in passing that at some places some level crossings are observed (accompanied by mergers, e.g., for $\mu \in [1.1, 1.3]$ of the real parts of the corresponding eigenfrequencies). These correspond to collisions of eigenmodes with opposite Krein signatures and lead to complex eigenfrequency quartets. However, because these only happen for small parametric regimes and the instabilities they induce are far weaker

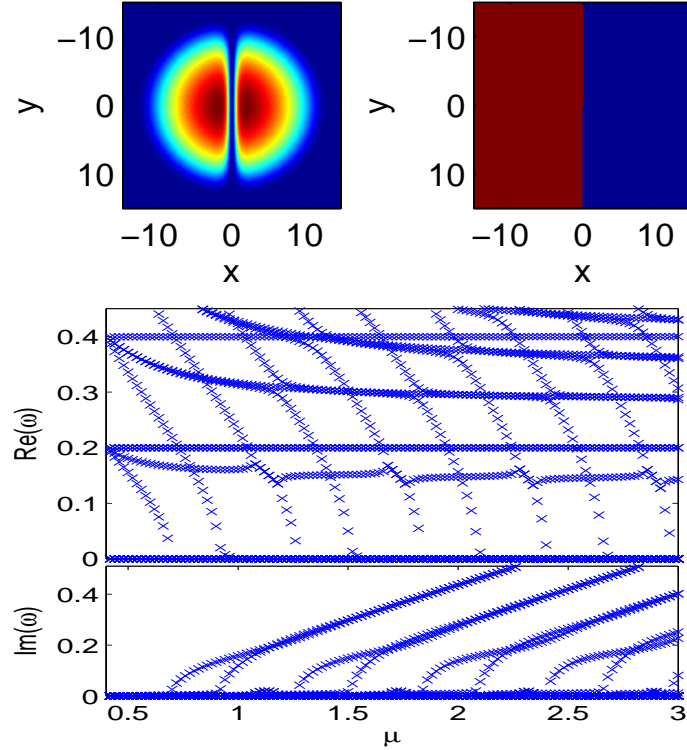


Figure 7.3: The dark soliton state for a trap strength $\Omega = 0.2$. The top panels show contour plots of the density (left) and phase (right) of the wave function for $\mu = 3$, while the bottom panel shows the eigenfrequency ω of the BdG spectrum as a function of the chemical potential μ .

than the ones associated with purely imaginary eigenfrequencies (in fact, they appear as only “small bumps” and are at least an order of magnitude weaker in the bottom panel of Fig. 7.3), they will not be considered further hereafter.

Let us at first investigate the real part of the eigenfrequencies. The mode at $\omega = \Omega$ is twofold degenerate and corresponds to the dipolar mode which describes the oscillation of the whole condensate with the trap frequency. The degeneracy occurs due to the symmetry of the trap, i.e., the trap frequencies in the x - and y - directions are equal. From this mode bifurcate two modes. The mode with smaller magnitude decreases to zero and becomes imaginary leading to a dynamical instability and the symmetry-breaking bifurcation discussed previously. The vanishing of the relevant eigenfrequency denotes the point of bifurcation of the vortex dipole from the dark soliton stripe (cf. Fig. 7.1). The other mode bifurcating from $\omega = \Omega$ also has a negative energy / Krein signature. This mode looks similar to the mode of a dark soliton in a 1D condensate. In the latter setting, this mode is the only one with a smaller magnitude than the dipolar mode. It bifurcates from the dipolar mode and decreases with increasing chemical potential up to a threshold in the Thomas-Fermi limit of large chemical potentials. The general behavior of this mode is similar. However in the 2D case there exist other modes that may acquire a smaller real part than the dipolar modes. These modes bifurcate at the linear limit from $\omega = n\Omega$ (one per multiple of the trap frequency) and, upon decrease of their magnitude, they eventually cross zero and become imaginary leading to additional instabilities. When the negative energy mode collides with these modes, it may

form a band of oscillatory instability manifested in the quartet of complex eigenvalues, e.g., for $1.1 < \mu < 1.2$ (see also the discussion above).

Every time one of these decreasing modes crosses zero, another one of the bifurcations discussed previously will arise. At the critical point of the bifurcation, the kernel of the dark soliton stripe linearization is augmented and becomes four- (instead of two-) dimensional. The additional pair of vanishing eigenfrequencies is associated with a rotational freedom that is, in turn, inherited by the resulting multi-vortex state. It is important to also mention here that given the supercritical pitchfork nature of the bifurcation, the novel emerging state (at *each* step of this bifurcation sequence) inherits the linear stability properties of its dark soliton stripe ancestor just before the bifurcation. In view of that, we have a clear roadmap of what to expect of the multi-vortex states' stability. In particular, the vortex dipole emerging out of the stable dark soliton stripe, should itself be neutrally stable at least close to the bifurcation point. On the contrary, the vortex tripole, aligned quadrupole, quintopole etc. should, respectively, inherit the one-, two-, three- etc., respectively, unstable eigendirections of the dark soliton stripe at the critical parameter point of their bifurcation. We should note in passing here that changing the aspect ratio of the trap leads to a shift of the point where the individual modes of the spectrum cross zero, e.g., a stabilization of the dark soliton stripe. Eventually, the dark soliton becomes stable for quasi-1D traps [185, 186, 188].

It is interesting to parallel the above results with those of Ref. [188], which also considered the destabilization of the dark soliton stripe, although in a waveguide-like trap geometry and through a fully numerical approach. The authors of Ref. [188] recognized the progressive destabilization steps of the dark soliton stripe as they augmented the transverse direction width in their geometry. However, they attributed the instabilities to single- or multi-vortex *decay* indicating that the multi-vortex patterns observed "are by no means stationary but rather form transient states" [188]. We believe that the above picture strongly supports the emergence of stationary bifurcating structures of this multi-vortex type.

7.2.2 The Vortex Dipole State

We now turn to the first by-product of the above bifurcation picture, namely the vortex dipole which is shown in Fig. 7.4. The top panels of the figure show the contour plots of the density and phase of this coherent structure. The middle panel of Fig. 7.4 shows the dependence of the position of the vortices on the chemical potential for $\Omega = 0.1$, $\Omega = 0.15$, and $\Omega = 0.2$ (curves from top to bottom). The lines denote the corresponding prediction by the system of ordinary differential equations (ODEs) for the vortex centers through Eq. (7.10) for $A = 2\sqrt{2}\pi$ and $B = 1.35$. The ODE prediction agrees very well with the results of the full model. The bottom panel shows the real and imaginary part of the eigenfrequencies of the Bogoliubov spectrum as a function of the chemical potential for $\mu > 0.68$ (where the dipole state exists).

Examining in more detail the spectrum of this vortex dipole, we find the following. At $\omega = \Omega$, there exists again the twofold degenerate dipolar modes which are associated with the oscillation of the whole condensate in the x - and y - directions with the trap frequency. From these modes, there bifurcates towards lower frequencies a negative energy mode, similar to the case of a single vortex. However, in this case, the negative energy mode collides with the mode departing from zero and forms a band of complex eigenfrequencies associated with oscillatory instabilities. This is the *sole* (see also discussion below) and predominant, albeit quite weak,

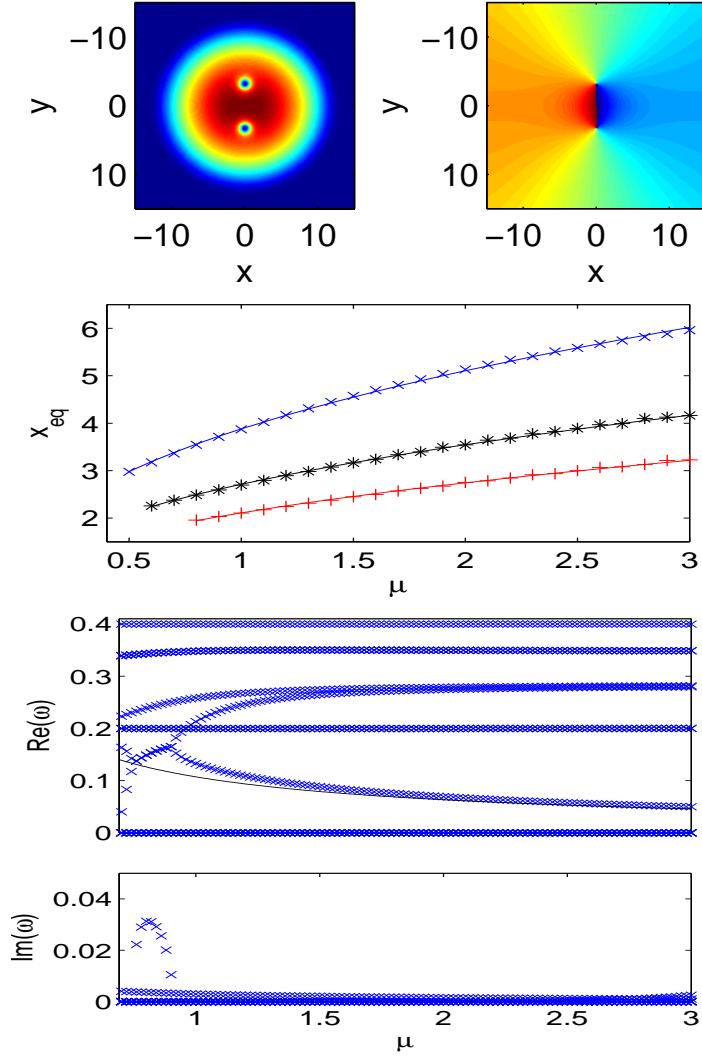


Figure 7.4: The vortex dipole state for a trap strength $\Omega = 0.2$. The top panels show contour plots of the density (left) and phase (right) of the wave function for $\mu = 3$. The middle panel shows the dependence of the position of the vortices on the chemical potential for $\Omega = 0.1$, $\Omega = 0.15$ and $\Omega = 0.2$ (curves from top to bottom). The lines indicate the predictions of the ODE with $A = 2\sqrt{2}\pi$, $B = 1.35$. The bottom panels show the real and imaginary parts of the eigenfrequencies ω of the BdG spectrum as a function of the chemical potential μ . The thin solid line shows the analytical prediction $\omega_{\text{pr}}^{\text{vd}} = \sqrt{2}\omega_{\text{pr}}$.

instability of the vortex dipole state. For larger chemical potentials this degeneracy is lifted and the negative energy mode behaves similarly to the case of the single vortex. However, in the vortex dipole case, the eigenfrequency of this mode for sufficiently large chemical potentials is very accurately predicted by Eq. (7.11), i.e., it is given by $\omega_{\text{pr}}^{\text{vd}} = \pm\sqrt{2}\omega_{\text{pr}}$ and directly reflects the epicyclic counter-rotation of the two vortices around their equilibrium location. The spectrum has two pairs of zero modes associated with the gauge invariance of the model, as well as with the rotational invariance of the dipole location (within the radially symmetric trap).

It is worthwhile to place the above results, and more generally the stability of the vortex

dipole state, in the context of earlier works that had predicted such a structure. The original prediction of Ref. [171] cited the vortex dipoles as “extremely robust”, but only employed direct integration methods (under noisy perturbations); hence, while suggestive, the findings of Ref. [171] could not preclude a potential instability (or trace its parametric regime). The subsequent investigation of Ref. [165] seemed to suggest the opposite, namely that the dipole was, in fact, unstable not only because of its constituting an energy maximum, but also due to a number of (tabulated) values suggesting the presence of non-real eigenfrequencies. This was more systematically considered in Ref. [172], which offered the imaginary parts of the relevant eigenfrequencies indicating two types of instabilities, a universal weak one (for all chemical potentials) and a stronger one for a narrow parametric regime. For the former, it was indicated that, as a result of its manifestation, the vortex dipole appears to remain intact through rotation and it was argued that it can be thought of as structurally stable, although dynamically unstable. These results are worthy of a close inspection and comparison with the bottom panel of Fig. 7.4. In fact, there, we also observe an extremely weak (of the order of 10^{-3} or smaller) but apparently systematically occurring (for all μ 's) unstable eigenmode of imaginary eigenfrequency. However, based on physical grounds, we argue that this mode is likely to be a manifestation of the accuracy of the numerical eigenvalue computations involved herein (cf. Ref. [286]). The underlying physical principle of the rotational invariance of the vortex dipole and of its neutrality clearly suggest the presence of a vanishing eigenfrequency pair. We should note here that we have confirmed that higher accuracy (smaller grid spacing) computations reduce the magnitude of the relevant eigenvalues, although their convergence to zero is slow. A more detailed computational investigation of this effect and its convergence to the physically relevant and symmetry mandated zero eigenvalue pair, while worthwhile in its own right is outside the scope of the present manuscript. Thus, we conclude that the sole genuinely unstable mode is due to the relevant eigenfrequency collisions and occurs over a narrow parametric regime.

7.2.3 The Vortex Tripole State

The case of the vortex tripole is illustrated in Fig. 7.5. The top panel of the figure shows the density and the phase of this three vortex state for $\mu = 3$. The vortices are oriented along a line with adjacent vortices having opposite vorticity. The bottom panel shows the BdG spectrum for $\mu > 0.98$ (where the three vortex state bifurcates into existence).

The real part of the spectrum looks similar to the case of the vortex dipole. However, in this case, the anomalous mode decreasing from the dipolar one and the mode departing from zero cross without creating an oscillatory instability. The spectrum contains two zero modes, as in the case of the vortex dipole. The one among them which is (numerically) very weakly nonzero is due to the rotational invariance of the tripole and the corresponding neutrality of this equilibrium (cf. the relevant discussion above and also the discussion of Ref. [172] about the second instability mode therein). Furthermore, as argued above on the basis of the general bifurcation approach to this problem, there is always a purely imaginary mode. The magnitude of the purely imaginary mode is comparable to the magnitude of the trap frequency showing that the state is highly unstable, as it inherits the already strong instability of the dark soliton stripe at the chemical potential value where the tripole arises. This is consonant with the discussion of Ref. [172] about a “dominating mode which is roughly an order of magnitude larger” than the other one.

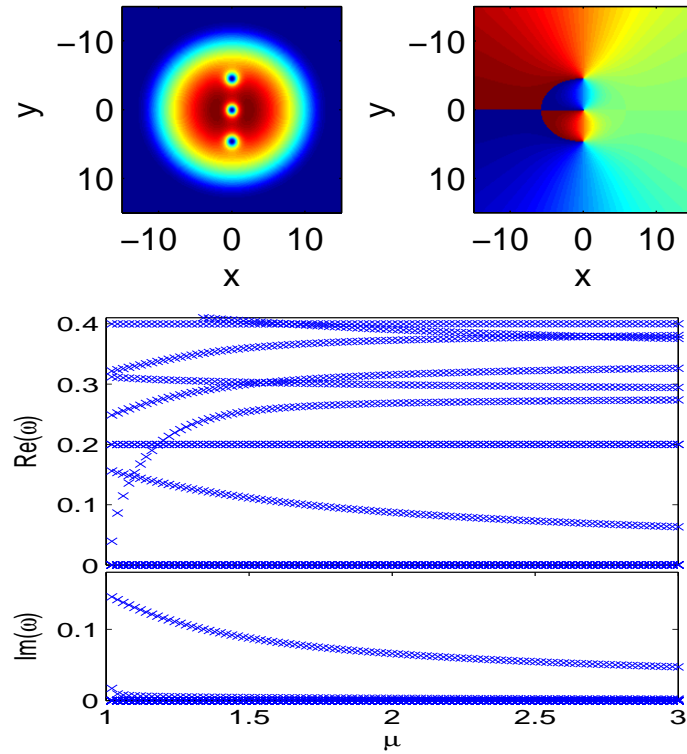


Figure 7.5: The three vortex state for a trap strength $\Omega = 0.2$. The top panels show contour plots of the density (left) and phase (right) of the wave function for $\mu = 3$, while the bottom panel shows the eigenfrequencies ω (real and imaginary parts) of the BdG spectrum as a function of the chemical potential μ .

One can extend the vortex particle approach described in section 7.1.2 to the three vortex state by adding the corresponding interaction term. The Jacobian matrix of the linearization around the equilibrium positions of the vortex tripole leads to the following eigenmodes. One of the modes has a vanishing eigenfrequency, similar to the case of the vortex dipole state, corresponding to the “rotational freedom” of the vortex tripole state. Of the other two pairs of eigenmodes, one is real and one is imaginary with respective eigenfrequencies

$$\omega_{\text{pr}1}^{\text{3v}} = \pm \sqrt{5}\omega_{\text{pr}}, \quad (7.12)$$

$$\omega_{\text{pr}2}^{\text{3v}} = \pm i\sqrt{7}\omega_{\text{pr}}. \quad (7.13)$$

The former corresponds to the anomalous mode leading to an oscillation of the vortices around their equilibrium positions, and the latter corresponds to the imaginary mode inducing the instability of the system. The modes agree qualitatively with our numerical findings.

7.2.4 The Aligned Quadrupole State

We now briefly turn to the case of four vortices aligned along the nodal line of the former dark soliton stripe. As in previous figures, Fig. 7.6 shows some of the characteristics of the four vortex (4v) aligned state. The bottom panel of the figure shows once again the BdG spectrum for $\mu > 1.26$ (where the four vortex state exists). Naturally, the real part of the

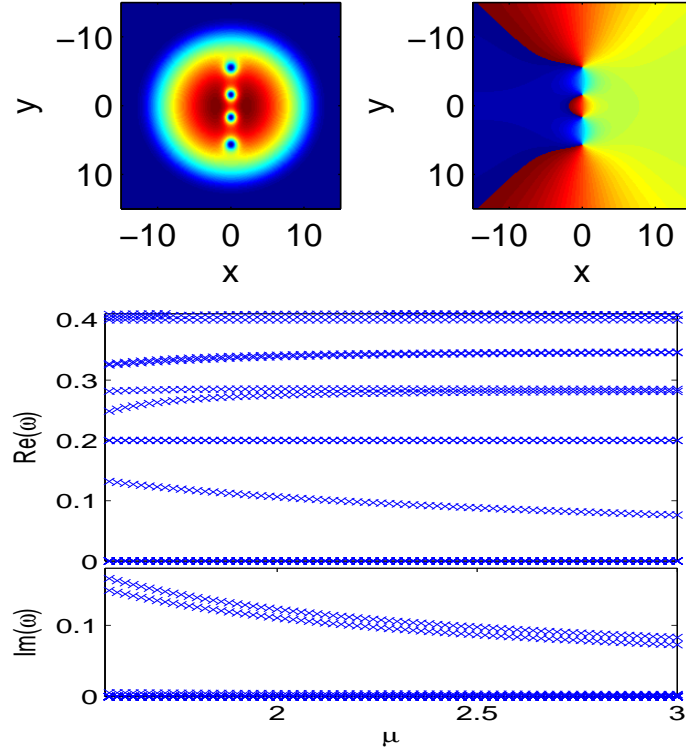


Figure 7.6: The aligned quadrupole state for a trap strength $\Omega = 0.2$. The top panels show contour plots of the density (left) and phase (right) of the wave function for $\mu = 3$, while the bottom panel shows the (real and imaginary) eigenfrequencies ω of the BdG spectrum as a function of the chemical potential μ .

spectrum looks similar to the case of the three vortex state. As in the case of the vortex dipole and tripole, the rotational and gauge invariances account for the two zero modes. On the other hand, for this four vortex case, there still exists a single negative energy mode. However, as anticipated from the stability of the dark soliton stripe at the critical point of the four-vortex-line bifurcation, in this case there exist two purely imaginary eigenfrequencies in the spectrum. The magnitude of the two purely imaginary modes is comparable to the magnitude of the trap frequency showing that the state is highly unstable, similarly to its dark soliton stripe ancestor in this parametric regime.

It is interesting to observe the count of (stable and) unstable eigenfrequencies of the vortex system in connection to the vortex “particles” participating in the respective state. In the case of two vortices, the epicyclic precession and the vanishing rotational eigenmode accounted for the two-modes of the two-particle system. In the case of the tripole, we expect three modes out of the three pairs of ODEs, one of which accounts for the remnant of the epicycles, one for the rotational invariance and one for the mode instability (associated with the outward drift of the outermost vortices towards the condensate boundary). In the aligned quadrupole, there are four modes: the epicycle, neutral and two unstable eigenmodes. For five aligned vortices (see below), there exist three unstable modes, and so on. As another interesting aside, we note that in none of the earlier studies of Refs. [165, 171, 172, 174] does this aligned quadrupole state seem to be noted (although, as discussed earlier, its quadrupolar analog was illustrated in Refs. [165, 172, 281]). However, higher order (such as 5- and 6-vortices aligned)

were discussed in the anisotropic trap setting also involving rotation in Ref. [178].

7.2.5 The Vortex Quadrupole State

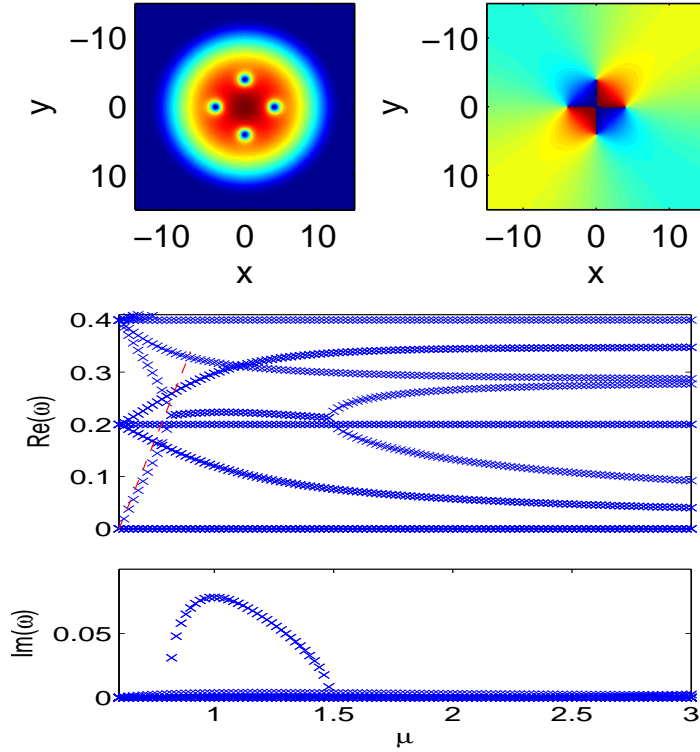


Figure 7.7: The vortex quadrupole state for a trap strength $\Omega = 0.2$. The top panels show contour plots of the density (left) and phase (right) of the wave function for $\mu = 3$, while the bottom panel shows the (real and imaginary parts of the) eigenfrequencies ω of the BdG spectrum as a function of the chemical potential μ . The dashed line shows the theoretical prediction for the mode departing from zero $\omega = \frac{4\sqrt{2}}{5}(\mu - 3\Omega)$.

We now make a brief interlude to discuss the quadrupole vortex state of Fig. 7.7, previously identified in Refs. [165, 172, 281], for completeness, although it does not structurally collide with or bifurcate from the dark soliton stripe (instead, as argued above, it emerges from the linear limit). Figure 7.7 shows density and phase plots of such a state. The bottom panel shows the real and imaginary eigenfrequencies of the BdG spectrum of the quadrupole state as a function of the chemical potential. At $\omega = \Omega$ and $\omega = 2\Omega$ one finds the dipolar and quadrupole mode of the condensate representing oscillations of the whole condensate. For the vortex quadrupole, negative energy modes bifurcate from both of the above locations. The one departing from the dipolar mode is two-fold degenerate, crosses the mode departing from zero, and thus becomes the lowest excitation of the state. The mode departing from the quadrupole limit collides with the mode departing from zero, and thus forms an instability band associated with eigenfrequency quartets, as illustrated in the middle and bottom panels of Fig. 7.7. For larger chemical potentials, this degeneracy is lifted and the negative energy mode crosses the dipolar mode and becomes the second smallest excitation frequency of the state. Similar to the single vortex state one can predict the behavior of the mode departing

from zero using a small parameter expansion as described in Sec. V.B of Ref. [273] yielding

$$\omega = \sqrt{2}(\mu - 3\Omega)\sqrt{\frac{C - D}{C + D}}, \quad (7.14)$$

with the overlap integrals of the one dimensional harmonic oscillator eigenfunctions $C = \int dx\psi_0(x)^4 \int dx\psi_2(x)^4$ and $D = (\int dx\psi_0(x)^2\psi_2(x)^2)^2$. Evaluation of the integrals yields

$$\omega = \frac{4\sqrt{2}}{5}(\mu - 3\Omega), \quad (7.15)$$

which is found to be in good agreement with the corresponding numerical result (see dashed line in the real BdG spectrum of Fig. 7.7).

7.2.6 The Vortex Quintopole State

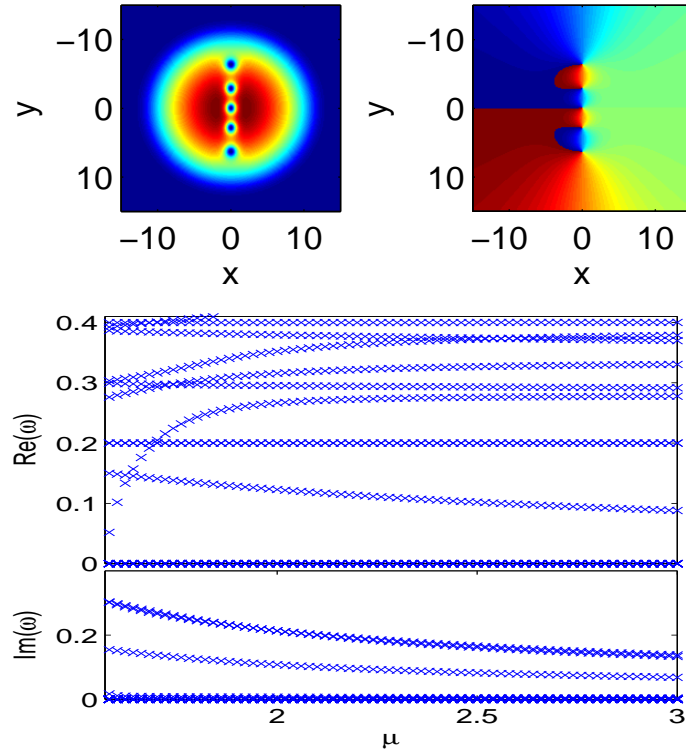


Figure 7.8: The five vortex state for a trap strength $\Omega = 0.2$. The top panels show contour plots of the density (left) and phase (right) of the wave function for $\mu = 3$, while the bottom panel shows the real and imaginary parts of the eigenfrequencies ω of the BdG spectrum as a function of the chemical potential μ .

Lastly, we briefly mention the five vortex state in Fig. 7.8. The presentation of the mode is similar to the earlier ones, with density and phase of a typical representative of this family of solutions being shown in the top panel and real and imaginary eigenfrequencies being demonstrated in the middle and bottom panels. The spectrum looks similar to the spectrum of the earlier states, but as argued above, it possesses three purely imaginary eigenfrequencies

with two of them being essentially degenerate, as is illustrated in the bottom panel of Fig. 7.8. Of course, once again the large magnitude of the corresponding eigenfrequencies illustrates the strong dynamical instability of the pertinent structure.

7.3 Vortex Dynamics: Numerical Results

7.3.1 Microscopical Displacements

In this section we show results obtained by direct numerical integration of Eq. (6.2), using as initial conditions stationary states perturbed along the direction of eigenvectors associated with particular eigenfrequencies. Since we are interested in the dynamics of the position of the vortex center we choose eigenfrequencies associated with instabilities or negative Krein sign eigenmodes. We should recall at this point that anomalous modes are connected to the oscillation frequencies of the vortices therefore a perturbation along the direction of an eigenvector associated to an anomalous mode leads to a precessional motion of the vortices. In order to determine the position of the vortex as a function of time we first compute the fluid velocity (see previous chapter)

$$\mathbf{v}_s = -\frac{i}{2} \frac{u^* \nabla u - u \nabla u^*}{|u|^2}. \quad (7.16)$$

The fluid vorticity is then defined as $\omega_{\text{vor}} = \nabla \times \mathbf{v}_s$. Due to our setup, the direction of the fluid vorticity is always the z -direction and, therefore, we can treat this quantity as a scalar. For well separated vortices, each vortex leads to a maximum of the absolute value of the fluid vorticity at its location. This allows us to determine the position of the vortices by determining the maxima of the absolute value of the fluid vorticity ω_{vor} . Notice the significant advantages of the above definition over alternative techniques such as those discussed in Ref. [174] which attempt to deal with phases and identifying plaquettes of 2π windings. This is evident in the figures illustrated below in comparison to the coarse features observed in Figs. 7 and 8 of Ref. [174].

The left panel of Fig. 7.9 shows the time evolution of the center of the vortices when the vortex dipole state is perturbed by the eigenvector corresponding to the anomalous mode for $\mu = 1.5$. Both vortices are initially shifted in the x -direction from the equilibrium position towards the center of the trap and in the y -direction both were shifted in the same direction namely in the positive half plane. So the vortices are still equi-distant from the center of the trap leading to the same value of the background density. During the time evolution the vortices perform an epicyclic (counter-rotating) motion around their respective equilibrium points.

The right panel shows the time evolution of the centers of the vortices for the state being perturbed by the eigenvector associated to the (near-) vanishing eigenfrequency corresponding to the rotational invariance at $\mu = 1.5$. Both vortices are displaced symmetrically from the fixed points in such a way that the distance to the origin and the distance between the vortices remains constant. Subsequently they rotate around the center of the trap. After a rotation of $\phi = \pi/2$ they rotate backwards. The forward- and backward-trajectories deviate slightly despite that the trajectories are closed. One of the vortices rotates forwards on the outer- and the other on the inner-trajectory and backwards vice-versa.

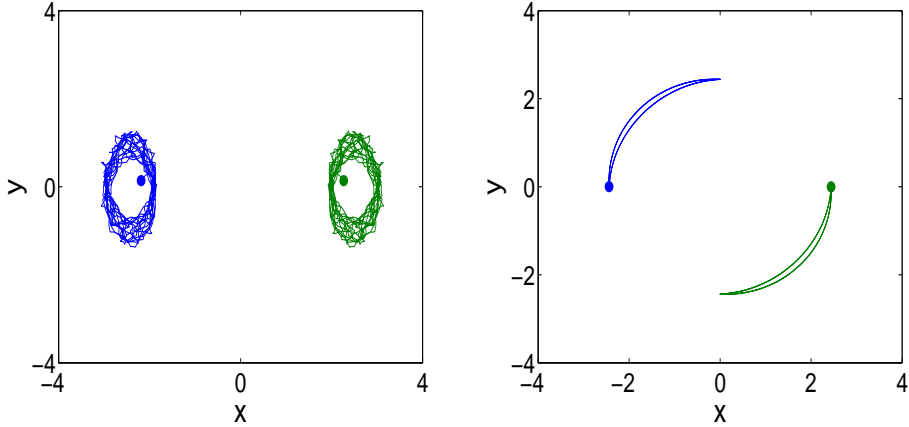


Figure 7.9: Time evolution of the center of the vortices for the two vortex state perturbed by the eigenvector of the anomalous mode (left panel) and the eigenvector associated to the zero eigenvalue connected to the rotational invariance (right panel) at $\mu = 1.5$. The filled circles represent the initial positions of the vortices.

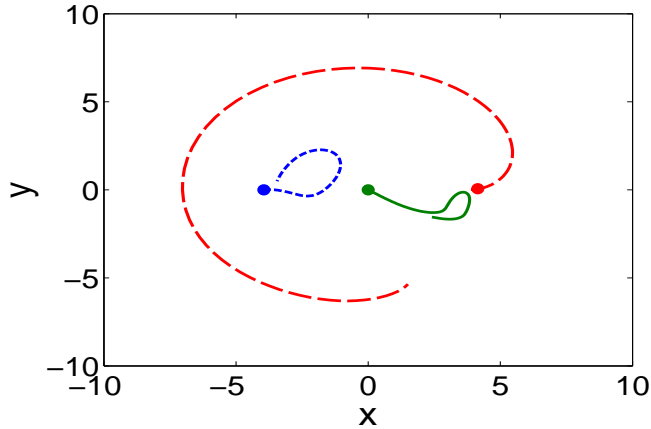


Figure 7.10: Time evolution of the center of the vortices for the three vortex state perturbed by the eigenvector of the purely imaginary mode at $\mu = 2.0$. The Initial positions of the vortices are depicted by the filled circles.

In the case of the three vortex state, on the other hand, there exists an imaginary eigenfrequency mode. Hence, we expect a dynamical manifestation of this strong instability. Figure 7.10 shows the time evolution of the center of the vortices for the vortex tripole being perturbed by the eigenvector of the imaginary eigenfrequency mode. One of the vortices immediately moves towards the outer regions of the background density (cf. with the corresponding dynamical description of Ref. [172]). The negative energy and anomalous modes of the states with the vortices oriented along a line lead to similar dynamical evolutions as the corresponding cases discussed here. As an aside, we note that among the rest of the considered states, the one containing a higher multiplicity of anomalous modes is the vortex quadrupole. The twofold degenerate mode with smaller magnitude leads to an in-phase oscillation of adjacent vortices around the fixed points whereas the anomalous mode with larger magnitude leads to an out-of-phase oscillation of the adjacent vortices.

7.3.2 Macroscopical Displacements

In this section we show the dynamical evolution of vortices placed at different initial positions, and compare the results obtained by direct time integration of Eq. (6.2) with the results obtained by integrating the corresponding ODEs. We will restrict the investigation in this subsection to two vortices with different vorticities since higher vortex states are unstable. In order to place a vortex at a certain point we use the following procedure. We define the pure vortex wave function as quotient of the single vortex state in a trap and the background density profile. This pure vortex wave function is then placed at the corresponding point. This procedure excites the background density as well, leading to a small amplitude oscillation of the vortices around a trajectory with large amplitude and frequency.

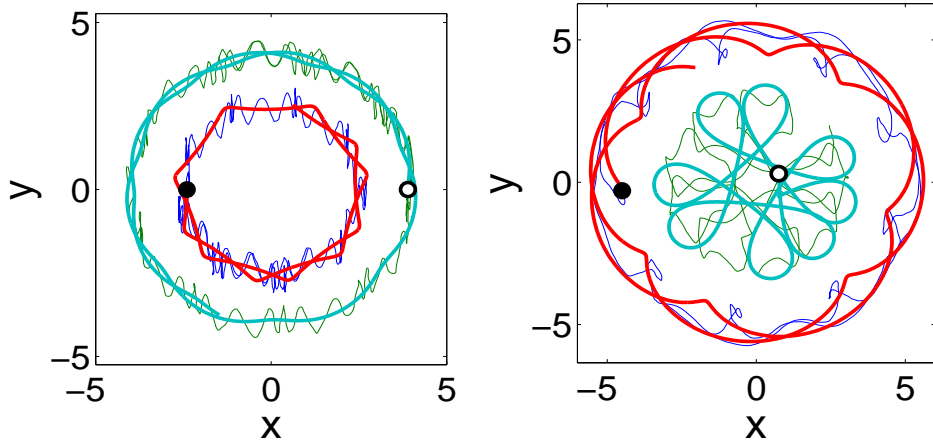


Figure 7.11: Time evolution of the centers of two vortices for a vortex with positive vorticity and one with negative vorticity initially placed at $(x_0, y_0) = (3.9, 0)$ (white circle) and $(x_0, y_0) = (-2.4, 0)$ (black circle), respectively (left panel) and $(x_0, y_0) = (0.75, 0.3)$ (white circle) and $(x_0, y_0) = (-4.5, -0.3)$ (black circle), respectively (right panel) for $\mu = 3$. The solid lines depict the predictions of Eqs. (7.7-7.8) and the thin solid lines the predictions of Eq. (6.2).

The left panel of Fig. 7.11 shows the time evolution of two vortices initially placed at $(x_0, y_0) = (3.9, 0)$ (white circle) and $(x_0, y_0) = (-2.4, 0)$ (black circle), respectively. The vortices oscillate around the center of the trap with an approximately constant distance to the trap center. The thick solid lines denote the predictions of Eqs. (7.7-7.8). They agree very well with the trajectories obtained by integrating Eq. (6.2) (depicted by thin solid lines). However the latter results perform an additional small amplitude oscillation due to the excitation of the background condensate as explained above. The right panel of Fig. 7.11 shows the time evolution for vortices initially placed at $(x_0, y_0) = (0.75, 0.3)$ (white circle) and $(x_0, y_0) = (-4.5, -0.3)$ (black circle), respectively. Due to the non-zero displacement in the y -direction one does not obtain an oscillation with constant amplitude around the origin but more complicated trajectories of the vortices with varying distances to the trap center. However the trajectories of the vortices are well separated, i.e., they do not cross. The predictions of Eqs. (7.7-7.8) (thick solid lines) agree qualitatively well with the corresponding results of the PDE (6.2) (thin solid lines) however the oscillation frequency deviates due to the dependence of the integration constants (A, B) on the position of the vortices. The left panel of Fig. 7.12 shows the evolution for $(x_0, y_0) = (4.5, 0)$ (white circle) and $(x_0, y_0) = (-4.5, 0)$

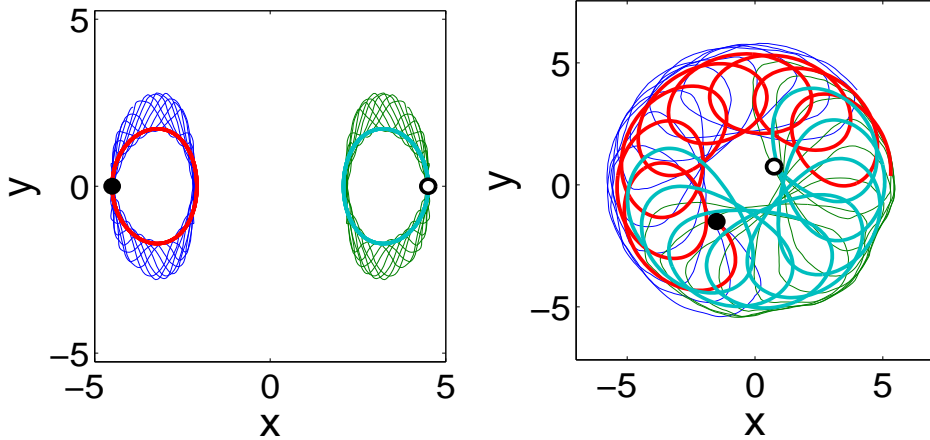


Figure 7.12: Time evolution of the center of two vortices for a vortex with positive vorticity and one with negative vorticity initially placed at $(x_0, y_0) = (4.5, 0)$ (white circle) and $(x_0, y_0) = (-4.5, 0)$ (black circle), respectively (left panel) and $(x_0, y_0) = (0.75, 0.75)$ (white circle) and $(x_0, y_0) = (-1.5, -1.5)$ (black circle), respectively (right panel) for $\mu = 3$. The thick solid lines depict the predictions of Eqs. (7.7-7.8) and the thin solid lines the predictions of Eq. (6.2).

(black circle). Due to the symmetrical displacement of the vortices with respect to the center of the trap, they perform oscillations around their fixed points. The right panel of Fig. 7.12 shows the evolution for $(x_0, y_0) = (0.75, 0.75)$ (white circle) and $(x_0, y_0) = (-1.5, -1.5)$ (black circle). Both vortices are shifted with respect to their fixed points towards the center of the trap. They perform complicated oscillations around the center of the trap. Once again the qualitative agreement of the prediction by the ODE (7.7-7.8) is good however the exact oscillation frequency cannot be predicted.

In conclusion the trajectories of the two vortices depend strongly on the initial conditions. The qualitative predictions by the ODE agree remarkably well with the PDE results however they cannot predict the exact oscillation frequencies. Here, we have attempted to explore, at both the PDE and ODE level, some of the salient features of such “choreographies”, as associated with instability and anomalous or invariant modes of the system. Clearly, a more detailed investigation of the possible orbits is warranted and will be forthcoming.

7.4 Conclusions

In this chapter, we have considered the existence, stability and dynamics of states associated with a dark soliton stripe, as well as of the related vortex quadrupole state. We have unveiled a systematic cascade of bifurcations from the former state into aligned vortex clusters (or crystals). The symmetry-breaking, supercritical pitchfork nature of the bifurcations was elucidated and a few-mode expansion was employed to identify the corresponding critical points. Although satisfactory approximations to the first four bifurcations were given, the approach is especially successful in the vicinity of the linear limit (and the bifurcation of the vortex dipole state). A complementary viewpoint was also formulated based on a particle picture enabling the development of an ordinary differential equation framework for the evolution of the vortex centers. This approach not only allowed the identification of the equilibrium

positions of the vortex clusters, but also assisted in the formulation of the vortex linearization problem and the analytical approximation of the vortex epicyclic near-equilibrium motions (e.g., for the vortex dipole), as well as that of the unstable eigenmodes of states such as the tripole. These results were systematically corroborated by existence and numerical linear stability techniques offering good agreement between the analytical approximations and the numerical findings in the relevant regimes.

Chapter 8

Dynamics of Dark-Bright Solitons in Cigar-Shaped Bose-Einstein Condensates

In chapter 4 and 5 we have investigated solitonic solutions in quasi-1D BECs. For repulsive interaction dark solitons exist as solutions of the 1D GPE whereas for attractive interactions bright solitons are solutions of the 1D GPE. Let us now investigate a two-component system, i.e., a BEC consisting of atoms in two different internal states. In a two component BEC dark-bright (DB) solitons exist for repulsive interaction between the atoms. DB solitons are symbiotic objects which do not exist in one-component systems. In a DB soliton the wave function of one component can be described as a dark soliton and the wave function of the second component as the wave function of a bright soliton. The bright soliton would not be stable without the other component due to the repulsive inter-atomic interaction. It gets stabilized by the interaction with the component supporting the dark soliton.

In this chapter we explore the stability and dynamics of DB solitons in two-component elongated Bose-Einstein condensates. For this purpose we will use both effectively 1D mean-field models and the full 3D GPE. We first develop in section 8.1 the Gerbier equation (GE) for two-component BECs. In section 8.2 we introduce DB solitons as solutions of the 1D GPE and then investigate the DB soliton statics and dynamics in section 8.3 using the non-polynomial Schrödinger equation (NPSE), the GE and the 3D GPE. Moreover, we analyze the interaction between multi-DB solitons and the role of their relative phase. Our results pertain to the hyperfine states $|1, -1\rangle$ and $|2, 0\rangle$ of ^{87}Rb , as in the experiment of Ref. [108], and also for the states $|1, -1\rangle$ and $|2, -2\rangle$ of ^{87}Rb in an optical dipole trap. For the latter states, we present experimental results concerning the DB soliton oscillations and multi-DB soliton interactions in section 8.4. Finally, we summarize our results in section 8.5. The results of this chapter are partly published in Ref. [287].

8.1 Effective 1D Theory

The macroscopic wave functions of Bose condensed atoms in two different internal states obey the following vector GPEs [3]:

$$i\hbar \frac{\partial \psi_k}{\partial t} = \left(-\frac{\hbar^2 \nabla^2}{2M} + U + g_{kk}|\psi_k|^2 + g_{12}|\psi_{3-k}|^2 \right) \psi_k, \quad (8.1)$$

where $\psi_k(\mathbf{r})$ are the macroscopic wave functions ($k = 1, 2$), of atoms in the internal state k , $g_{ij} = 4\pi\hbar^2 a_{ij}/M$ are the effective nonlinear coefficients due to the s -wave scattering for $i, j = 1, 2$, and $U(\mathbf{r})$ is the confining potential. Note, Eq. (8.1) conserves the atom numbers of the individual components separately (cf. the spinor GPE in chapter 9 where the individual atom numbers are not conserved). Therefore there should not be any transition between the

internal states k by inter atomic scattering in order to ensure that the vector GPE are valid. This is for example the case for states in different hyperfine manifolds.

For a single species, quasi-1D descriptions of cigar-shaped BECs rely on the non-polynomial Schrödinger equation (NPSE) (2.40) and the Gerbier equation (GE) (2.34); cf. section 2.2.3. However, in multi-component settings only the NPSE equation has been derived [288]. Therefore we use at first a similar scheme for the dimensionality reduction of Eq. (8.1) to an effective 1D equation, as described in section 2.2.3 for the scalar GPE, in order to obtain a multi-component version of the GE.

For a highly anisotropic trap, we first factorize the wave function as [141, 142, 144]

$$\psi_k(\mathbf{r}, t) = \phi_k(\mathbf{r}_\perp; x) f_k(x, t) \exp(-i\gamma t/\hbar), \quad (8.2)$$

where γ is the chemical potential defining the time dependence of the overall phase. Substitution of this ansatz in Eq. (8.1), multiplication by $\phi_k^*(\mathbf{r}_\perp; x)$ and, finally, integration over the transverse directions; leads to the following effective 1D model:

$$\left[i\hbar \frac{\partial}{\partial t} + \frac{\hbar^2}{2M} \frac{\partial^2}{\partial x^2} - V(x) \right] f_k = \mu_{\perp k}[f_k] f_k, \quad (8.3)$$

where $V(x) = M\omega_x^2 x^2/2$ is the axial potential and the transverse chemical potential $\mu_{\perp k} = \mu_{\perp k}[f_k(x, t)]$ is a functional of f_k :

$$\begin{aligned} \mu_{\perp k}[f_k] = & \int d^2 \mathbf{r}_\perp \phi_k^* \left(-\frac{\hbar^2}{2M} \nabla_\perp^2 + \frac{1}{2} M \omega_\perp^2 r_\perp^2 - \gamma \right. \\ & \left. + g_{kk} |\phi_k|^2 |f_k|^2 + g_{12} |\phi_{3-k}|^2 |f_{3-k}|^2 \right) \phi_k, \end{aligned} \quad (8.4)$$

where (ω_x, ω_\perp) are the trap frequencies along the longitudinal (axial) and transverse directions. We have neglected derivatives of ϕ_k with respect to time and to the axial variable x . For an effectively 1D system, we assume that the transverse wave function remains in its Gaussian ground-state,

$$\phi_k = \frac{1}{\sqrt{\pi} \sigma_k} \exp\left(-\frac{r_\perp^2}{2\sigma_k^2}\right). \quad (8.5)$$

To account for axial effects, we allow the width σ_k to be a variational parameter, $\sigma_k = \sigma_k[f_k(x, t)]$; this yields:

$$\mu_{\perp k} = \frac{\hbar^2}{2M} \sigma_k^{-2} + \frac{M}{2} \omega_\perp^2 \sigma_k^2 + \frac{g_{kk} |f_k|^2}{2\pi} \sigma_k^{-2} + \frac{g_{12} |f_{3-k}|^2}{\pi(\sigma_1^2 + \sigma_2^2)}. \quad (8.6)$$

Here we have set the constant offset shift $\gamma = 0$. In order to determine σ_k we minimize the chemical potential $\mu_{\perp k}$ with respect to σ_k for given $f_k(x, t)$ leading to

$$\sigma_k^4 = \frac{\hbar^2}{\omega_\perp^2 M^2} + \frac{g_{kk} |f_k|^2}{A \pi M \omega_\perp^2} + \frac{2g_{12} |f_{3-k}|^2}{\pi M \omega_\perp^2 (\sigma_1^2 + \sigma_2^2)^2} \sigma_k^4, \quad (8.7)$$

with $A = 1$. For the one component case f_{3-k} one obtains a one to one correspondence of σ and f and consequently Eq. (2.34). However for the two component case one cannot determine σ_k analytically due to the last summand in Eq. (8.7) which depends on σ_k, σ_{3-k} .

An alternative approach for defining σ_k is to use the Euler-Lagrange equations from the Lagrangian associated to Eq. (8.3) following Ref. [288] and thereby minimizing the total energy. This leads to Eq. (8.7) for σ_k with $A = 2$. Below we refer to $A = 1$ as the GE system and $A = 2$ as the NPSE system.

In the low density limit $g_{kl}f_m \ll 1$ (for $k, l, m = 1, 2$) equation (8.7) reduces to the constant, density independent width

$$\sigma_k^{\text{GP}} = \sqrt[4]{\frac{\hbar^2}{\omega_{\perp}^2 M^2}} \quad (8.8)$$

defined by the harmonic oscillator length in the transversal direction and subsequently Eq. (8.3) is reduced to the standard 1D vector GPE. The latter is given by Eq. (8.1) with modified coupling coefficients, in complete analog to the scalar 1D GPE. However in general one has to solve the following system of equations:

$$i\hbar \frac{\partial}{\partial t} f_k = \left[-\frac{\hbar^2}{2M} \frac{\partial^2}{\partial x^2} + V(x) + \mu_{\perp k}[f_k] \right] f_k, \quad (8.9)$$

$$\mu_{\perp k} = \frac{\hbar^2}{2M} \sigma_k^{-2} + \frac{M}{2} \omega_{\perp}^2 \sigma_k^2 + \frac{g_{kk}|f_k|^2}{2\pi} \sigma_k^{-2} + \frac{g_{12}|f_{3-k}|^2}{\pi(\sigma_1^2 + \sigma_2^2)}, \quad (8.10)$$

$$\sigma_k^4 = \frac{\hbar^2}{\omega_{\perp}^2 M^2} + \frac{g_{kk}|f_k|^2}{A\pi M \omega_{\perp}^2} + \frac{2g_{12}|f_{3-k}|^2}{\pi M \omega_{\perp}^2 (\sigma_1^2 + \sigma_2^2)} \sigma_k^4. \quad (8.11)$$

Notice that Eqs. (8.9-8.11) constitute a set of coupled nonlinear equations which have to be solved consistently in order to obtain $f_k(x, t)$ and $\sigma_k[f_k(x, t)]$. In Appendix B we describe in detail how one can solve these coupled nonlinear equations.

8.2 Dark Bright Solitons

Using the above approach, we will investigate the trapped dynamics of a DB soliton in a quasi-1D condensate. For the GP 1D case without a trap in the axial direction ($V(x) = 0$), and assuming that all scattering lengths are equal, there exists an analytical DB soliton solution [121]. This can be expressed in the following dimensionless form (in units so that $\hbar = M = 1$),

$$\psi_D = i\sqrt{\mu} \sin \alpha + \sqrt{\mu} \cos \alpha \tanh [\kappa[x - q(t)]], \quad (8.12)$$

$$\psi_B = \sqrt{\frac{N_B \kappa}{2}} e^{i(\phi + \omega_B t + x \kappa \tan \alpha)} \operatorname{sech} [\kappa[x - q(t)]]. \quad (8.13)$$

Here, ψ_D is the dark soliton (on top of a constant background with chemical potential $\mu = \mu_D$), with an inverse width $\kappa = \sqrt{\mu \cos^2 \alpha + (N_B/4)^2} - N_B/4$, position $q(t) = q(0) + t\kappa \tan \alpha$ and phase angle α , whereas ψ_B is the bright soliton that is symbiotically supported by the dark one with the same width and position. Note, one speaks about a dark and a bright soliton since the functional form described in Eqs. (8.12-8.13) is reminiscent of the functional form of a dark and a bright soliton (cf. section 2.3.2), respectively. However pure bright solitons exist only for an attractive interaction and not for a repulsive one. In this case the bright soliton gets stabilized by the dark soliton and would not exist without the dark one. In

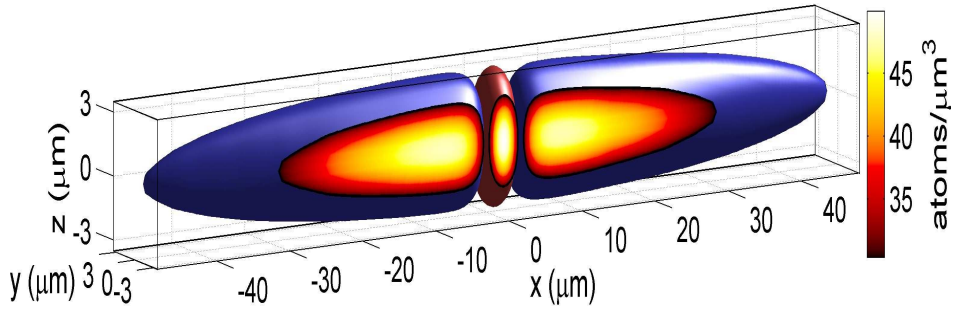


Figure 8.1: Iso-level contours at 2/5 of the maximal density (dark/bright soliton depicted in blue/red) of a DB soliton as a result of 3D GPE simulations ($N_D = 93\,367$, $N_B = 7\,926$). The transverse cut ($y = \text{const.}$) shows the atom density with the scale depicted by the colorbar.

the realistic case of the hyperfine states $|1, -1\rangle$ and $|2, 0\rangle$ of ^{87}Rb , the scattering lengths are different ($a_{11} = 100.86a_0$, $a_{22} = 94.57a_0$ and $a_{12} = 98.98a_0$). Nevertheless, in the quasi-1D setting (with the trap), we have found that there exists a stationary DB state [cf. Eqs. (8.12–8.13) with $\alpha = 0$] located at the trap center. We identify this state, f_k^{stat} , using a fixed-point algorithm, and then perform a Bogoliubov-de-Gennes (BdG) analysis to determine its linear stability by using the ansatz

$$f_k = f_k^{\text{stat}} + [u_k(x) \exp(i\omega t) + v_k^*(x) \exp(-i\omega^* t)]. \quad (8.14)$$

For a detailed description of the technical details of the BdG analysis we refer the interested reader to Appendix B. The eigenfrequencies ω and amplitudes (u_k, v_k) of the ensuing BdG linearization operator encode the dynamical stability of the system: for vanishing imaginary part ω_i of $\omega = \omega_r + i\omega_i$, the system is dynamically stable and $\omega_i \neq 0$ implies dynamical instability. We also note that the eigenfrequency of the anomalous (negative energy) mode of the spectrum (see below) coincides with the oscillation frequency of the DB soliton, similarly to dark solitons in one-species BECs cf. chapter 5 or Refs. [110, 112, 140].

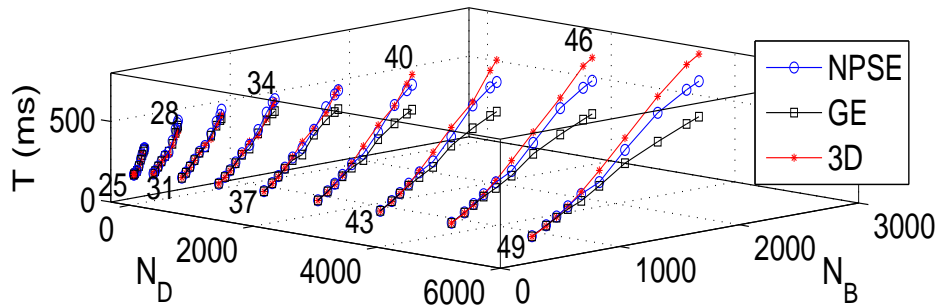


Figure 8.2: DB soliton oscillation period vs. N_D and N_B for fixed μ_D indicated by the numbers in the panel. Circles (blue) and squares (black) depict the results from the BdG analysis of the GE and NPSE, respectively; small red dots represent results of the 3D GPE.

8.3 Numerical Results

8.3.1 Comparison of quasi-1D and 3D Results

We have chosen a cylindrical trap with frequencies $\omega_{\perp} = 2\pi \times 133$ Hz and $\omega_x = 2\pi \times 5.9$ Hz, similar to the ones used in the experiment of Ref. [108]. In Fig. 8.1 we show iso-level contours of a DB soliton resulting from numerical integration of the 3D GPE, while in Fig. 8.2 we compare the oscillation period derived by the effective 1D model against results of the 3D GPE. The figure illustrates the dependence of the period of the DB soliton on the number of atoms (N_D, N_B) of the two components. It is clear that variation of the number of atoms, especially in the bright component by a factor of 2, may lead to a significant (approximately two-fold) variation of the DB soliton frequency. The agreement between 1D and 3D generally becomes worse when N_B is increased and, to a lesser extent, when N_D is increased. Notice that the NPSE model yields generally more accurate predictions than the GE one.

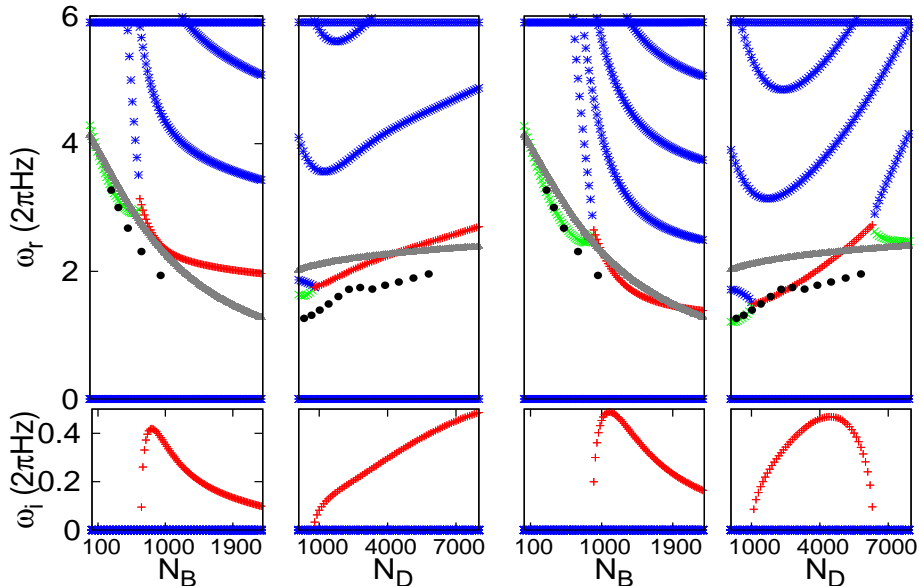


Figure 8.3: BdG analysis of GE (left) and NPSE (right) [real ω_r and imaginary ω_i parts of the eigenfrequencies]: Anomalous mode (green), dynamically unstable mode (red), analytical 1D result of Ref. [121] (gray), and 3D GPE results (black points).

The panels of Fig. 8.3 show the DB soliton spectrum. When the anomalous mode collides with a mode of positive energy, the DB soliton becomes dynamically unstable, i.e., the amplitude of its oscillation increases. Such collisions are present in the DB soliton spectrum, and denote a critical difference in comparison with the case of dark solitons in single-species BECs. Furthermore, as observed in the right-most panel of Fig. 8.3 and also corroborated by our 3D GPE simulations, this oscillatory instability disappears for sufficiently large N_D .

From Fig. 8.3, we infer that for progressively larger atomic populations, a departure from the quasi-1D behavior emerges and a larger (smaller) oscillation frequency is obtained, if N_D (N_B) is increased.

According to Fig. 8.2, the atom numbers used in Ref. [108] (up to $N_B \sim 8000$ and $N_D \sim 92000$) are out of the realm of validity of the effective 1D equations; thus, in this case, the 3D

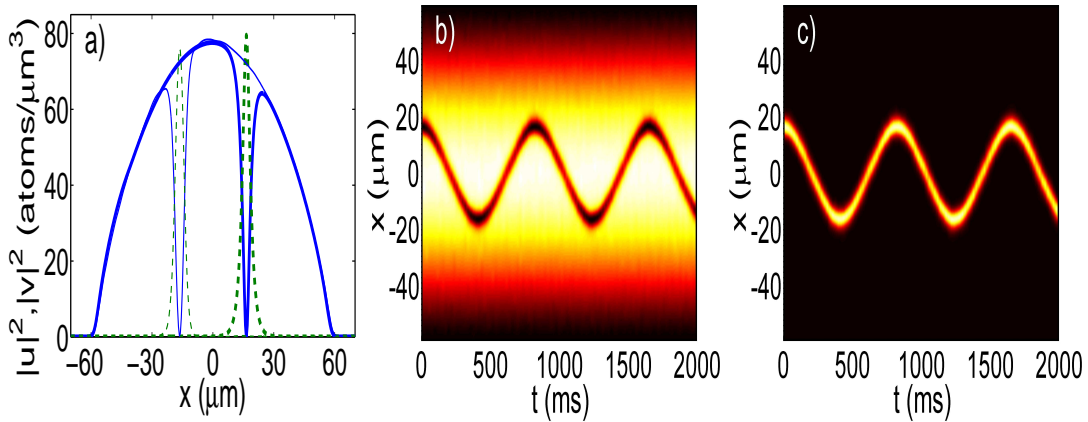


Figure 8.4: An oscillating DB soliton with period $T = 827$ ms in the 3D GPE approach. Left panel: Transversal ($y = z = 0$) cut of the density at $t = 0$ (thick lines) and $t = T/2$ (thin lines). Solid (dashed) line depicts the density for the dark (bright) component. Middle/right panels: Contour plots showing the evolution of the (y, z) -integrated density of the dark and bright solitons.

GPE has to be applied. Figure 8.4 illustrates the oscillating DB soliton for trap frequencies and atom numbers comparable to those used in Ref. [108]. This 3D simulation results in an oscillating DB period of about 827 ms that is comparable with the period observed in Ref. [108] (slightly larger than 1 s). Possible sources for the discrepancy between the numerical and experimental oscillation periods include (i) high sensitivity of the period on the N_D to N_B ratio, (ii) sensitivity of the dynamics to uncertainties in the measured scattering lengths, and, perhaps more importantly, (ii) our numerics confirm that the oscillations are not harmonic and tend to have increasing periods for higher oscillating amplitudes.

8.3.2 Departure from the quasi-1D Behavior

The departure from the effective 1D description can be noticed, e.g., in panels (a) and (b) of Fig. 8.5. It is clear both from the oscillation snapshots Fig. 8.5a and from the evolution of the bright soliton center in the transverse direction (Fig. 8.5b top panel), that the DB soliton starts exploiting the transverse degrees of freedom shortly after release. Up to $t < 200$ ms the soliton is at rest with respect to the transverse direction. For $t > 200$ ms an oscillation of the soliton occurs in the transversal direction leading at the same time to a reduction of the oscillation frequency in the axial direction (cf. thick (black) solid line in the bottom panel of Fig. 8.5b).

8.3.3 Interaction of Dark-Bright Solitons

We also showcase 3D GPE simulations, in Fig. 8.6, depicting the interaction between *two* DB solitons [217]. The left panel shows a stationary DB pair with *in-phase*, i.e. mutually repulsive, bright soliton components (also, the dark ones always repel) that is balanced by the pull of the harmonic trap. The middle panel depicts the evolution of the same initial DB pair as in the left one, but with *out-of-phase*, i.e. mutually attractive, bright solitons, which yields an oscillatory dynamics. The right panel depicts the oscillations and collisions for in-phase

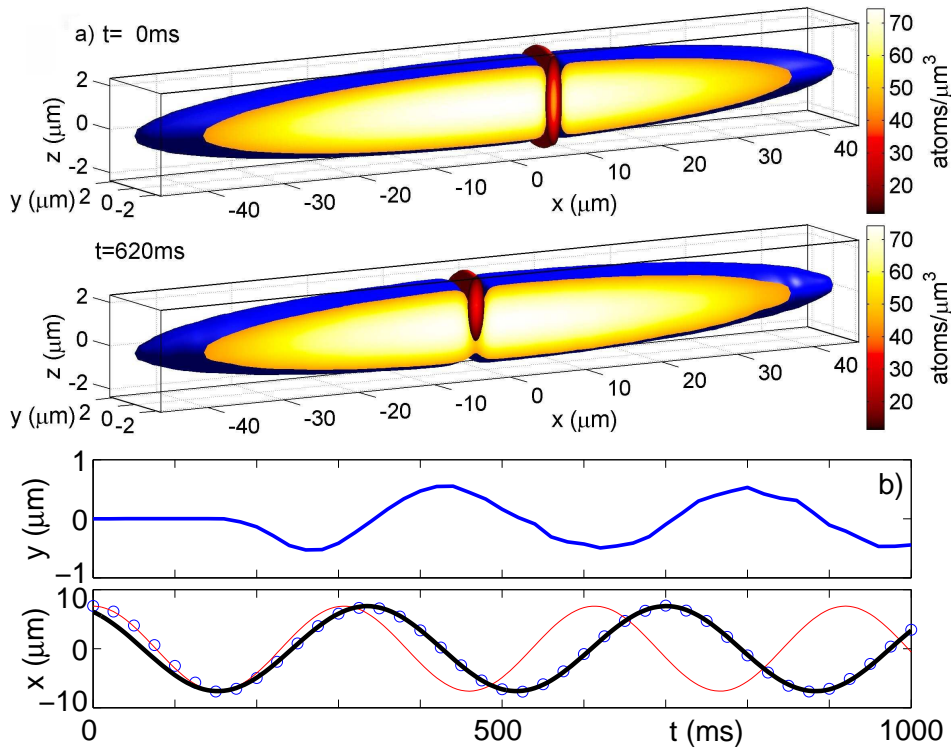


Figure 8.5: (a) Transverse oscillations of the DB soliton for $(N_D, N_B) = (88181, 1058)$. Top subpanel: initial condition. Bottom subpanel: a snapshot of the oscillating DB soliton at $t = 620$ ms. (b) Transverse (top) and longitudinal (bottom) oscillations for the bright soliton. The thin (red) and thick (black) solid lines are sinusoidal fits to the longitudinal oscillations (circles) yielding periods $T = 306$ ms (for $t < 200$ ms) and $T = 365$ ms (for $t > 200$ ms), respectively.

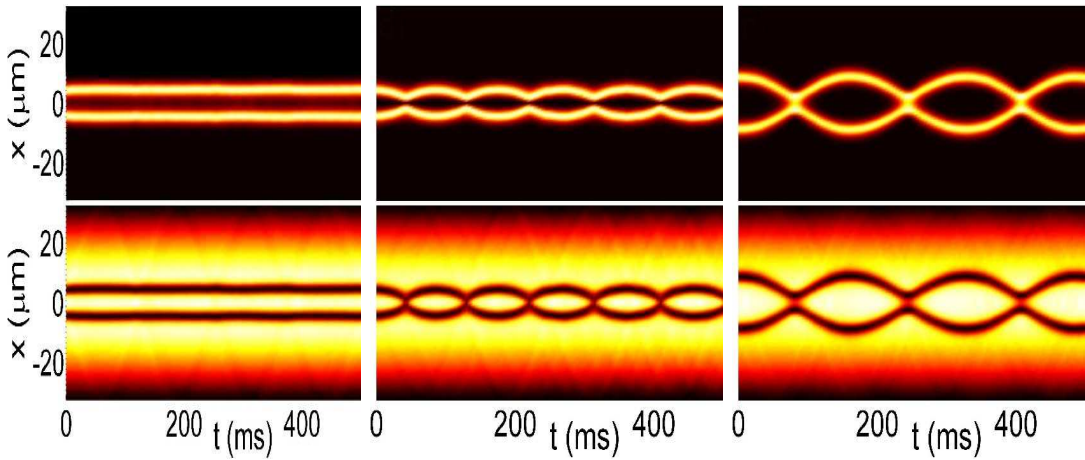


Figure 8.6: Interaction of two DB solitons [top (bottom) subpanels depicting the bright (dark) component]. Left panel: In-phase (i.e. repulsive among bright) solitons close to their equilibrium position. Middle panel: Out-of-phase (i.e. attractive among bright) solitons starting at the same location as in panel c). Right panel: Multiple collisions for in-phase solitons.

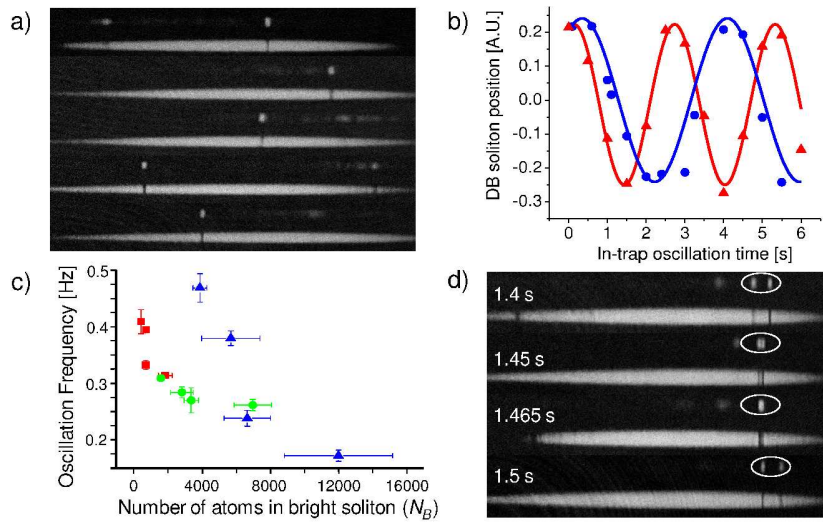


Figure 8.7: (a) Experimental images showing the oscillation of the DB soliton at the in-trap evolution times indicated. (b) In-trap DB soliton oscillation. Triangles (red) and squares (blue) correspond to, respectively, $(N_B, N_D) \approx (680, 27\,000)$ and $(N_B, N_D) \approx (9\,000, 650\,000)$. Solid lines correspond to fitted harmonic oscillations with frequencies 0.39 Hz and 0.27 Hz respectively. (c) Oscillation frequency vs. N_B for different number of atoms in the dark component: squares (red): $N_D \approx 30\,000$, triangles (green): $N_D \approx 200\,000$, and circles (blue): $N_D \approx 430\,000$. (d) Experimental expansion images showing the oscillation and collision (in circled regions) of two DB solitons. Images in (a) and (d) are taken after 7 ms and 8 ms of free expansion for the bright and dark component, respectively. The components are vertically overlapped prior to expansion.

bright solitons that were released at larger distances from the trap center and thus cannot avoid colliding despite their mutual repulsion. It is noteworthy that the DB collisions are apparently nearly elastic as the DB solitons retain their shape even after multiple collisions.

8.4 Experimental Results

Finally, we present experimental data corroborating some principal points of our analysis (Fig. 8.7). Nonlinear effects in the counterflow of two BEC components are exploited to generate individual DB solitons [289]. The dark and bright component are formed by ⁸⁷Rb atoms in the $|1, -1\rangle$ and $|2, -2\rangle$ state, respectively, for which $a_{11} = 100.4 a_0$, $a_{22} = 98.98 a_0$, and $a_{12} = 98.98 a_0$ [290]. The atoms are held in an elongated optical dipole trap with trapping frequencies $\omega_{x,y,z} = 2\pi \times \{1.3, 163, 116\}$ Hz. While the lack of exact cylindrical symmetry as well as the large atom number in the experiment preclude a direct comparison with our analytic results, the experiment clearly shows the anticipated decrease of oscillation frequency with increasing number of atoms in the bright and decreasing number of atoms in the dark component. Experimental results of the collision between two DB solitons are presented in Fig. 8.7d, confirming their near-elastic nature.

8.5 Conclusions

In this chapter we investigated DB solitons in two-component elongated BECs. We characterized the effectively 1D dynamics of DB solitons and showcased their potential dynamical

instability. We demonstrated experimentally and theoretically the tunability of the oscillation frequency of a DB soliton. Varying the atom number of either the dark or the bright component, we find that in a harmonic trap the soliton oscillation period may change by nearly one order of magnitude; most notably, the bright component is shown to slow down the oscillation of the dark one. Our investigation revealed a feature absent in the dark soliton dynamics in one-component BECs, namely that a single DB soliton may become dynamically unstable. Increasing N_D and N_B reveals a deviation from the effective 1D description: specifically, an increase of N_D leads to a spontaneous breaking of the cylindrical symmetry, manifested in a transversal oscillation of the bright component, and a subsequent decrease of the axial DB oscillation frequency. Moreover, we analyzed the interaction between multi-DB solitons and observed a strong phase dependence of the collisional dynamics of DB solitons.

Chapter 9

Interaction Induced Trapping and Pulsed Emission of a Magnetically Insensitive Bose-Einstein Condensate

In the previous chapter we investigated a two component BEC described by the vector GPEs. These do not allow a population transfer between the individual components. In this chapter we present the spinor GPEs describing a BEC consisting of atoms in the different hyperfine states of one hyperfine manifold. The spinor GPEs allow explicitly a population transfer between the components. We derive basic properties resulting from the spinor GPEs and subsequently apply the spinor GPEs to demonstrate that atoms in magnetically insensitive hyperfine states ($m = 0$) can be trapped efficiently by a Bose-Einstein condensate of the same atomic species occupying a different hyperfine state. The latter is trapped magnetically. We show that for a large BEC density in the $m \neq 0$ state the atoms in the $m = 0$ state behave as if they were confined by a potential which is constituted by the condensate density. Hyperfine state changing collisions, and therefore loss of the trapped ($m = 0$) atoms, are shown to be strongly inhibited in case of a low density of the confined atomic cloud. We monitor the transition from a 'soft' to a 'hard' effective potential by studying the backaction of the trapped ($m = 0$) atoms onto the condensate which provides their confinement. The controlled outcoupling of the trapped atoms by shaping the condensate's wave function is explored. We observe a pulsed emission of atoms from the trapping region reminiscent of an atom laser. This method complements current methods to outcouple atoms from a BEC, e.g., radio frequency [291] or Raman transitions [292] and facilitates the creation of an atom laser for $m = 0$ atoms. The results of this chapter are partly published in Ref. [293].

The chapter is structured in the following way. In section 9.1 and 9.2 we present the 3D and effective 1D spinor GPEs, respectively. In section 9.3 we provide our setup for trapping magnetically insensitive atoms. How the trapping mechanism works is demonstrated in section 9.4, whereas section 9.5 is devoted to loss mechanism. Finally, we investigate backaction of the $m = 0$ component on the $m = 1$ component, which provides the trapping, and demonstrate an outcoupling of parts of the trapped $m = 0$ component.

9.1 Spinor Equations

We investigate the case of a $F = 1$ spinor BEC consisting of atoms with mass M confined in a spin dependent potential V_m . The Hamiltonian of the system is given by [199, 294]

$$\begin{aligned} H = & \int d\mathbf{r} \sum_m \Psi_m^\dagger(\mathbf{r}) \left[-\frac{\hbar^2}{2M} \nabla^2 + V_m(\mathbf{r}) \right] \Psi_m(\mathbf{r}) \\ & + \sum_{m_1, 2, 3, 4} \Psi_{m_1}^\dagger(\mathbf{r}) \Psi_{m_2}^\dagger(\mathbf{r}) \left[\frac{g_0}{2} \delta_{m_1 m_4} \delta_{m_2 m_3} \right. \\ & \left. + \frac{g_1}{2} \mathbf{F}_{m_1 m_4} \mathbf{F}_{m_2 m_3} \right] \Psi_{m_1}(\mathbf{r}) \Psi_{m_2}(\mathbf{r}) \end{aligned} \quad (9.1)$$

where Ψ_m is the field operator of the atom in the magnetic sublevel m and \mathbf{F} is the spin-1 angular momentum operator. The spin independent and spin dependent interactions are characterized by $g_0 = \frac{4\pi\hbar^2(a_0+2a_2)}{3M}$ and $g_1 = \frac{4\pi\hbar^2(a_2-a_0)}{3M}$ with a_S being the s-wave scattering length for the scattering channel with total spin S . From the Hamiltonian (9.1) one can derive the multicomponent Gross-Pitaevskii equations in the same manner as we derived scalar GPE in section 2.1 and obtains with suppressed arguments in the wave functions [294]

$$\begin{aligned} i\hbar\partial_t \Psi_0 = & \left[-\frac{\hbar^2}{2M} \nabla^2 + V_0(\mathbf{r}) + g_0 n \right] \Psi_0 + \frac{g_1}{\sqrt{2}} (F_+ \Psi_1 + F_- \Psi_{-1}) \\ i\hbar\partial_t \Psi_{\pm 1} = & \left[-\frac{\hbar^2}{2M} \nabla^2 + V_{\pm 1}(\mathbf{r}) + g_0 n \right] \Psi_{\pm 1} + g_1 \left(\frac{1}{\sqrt{2}} F_{\mp} \Psi_0 \pm F_z \Psi_{\pm 1} \right). \end{aligned} \quad (9.2)$$

Ψ_m is the macroscopic wave function describing the internal state m , $n = \sum_m |\Psi_m|^2$ the total density, $F_z = |\Psi_1|^2 - |\Psi_{-1}|^2$, and $F_+ = F_-^* = \sqrt{2}(\Psi_1^* \Psi_0 + \Psi_0^* \Psi_{-1})$. These Eqs. can alternatively be derived by the variational principle $i\hbar\partial_t \Psi_m = \delta E / \delta \Psi_m^*$ with the energy functional

$$\begin{aligned} E[\Psi_{-1}, \Psi_0, \Psi_1] = & \int d\mathbf{r} \sum_{i,j,k,l} \left[-\frac{\hbar^2}{2M} |\nabla \Psi_i|^2 + V_i(\mathbf{r}) |\Psi_i|^2 \right. \\ & \left. + \frac{g_0}{2} \Psi_i^* \Psi_j^* \Psi_j \Psi_i + \frac{g_1}{2} \Psi_i^* \Psi_j^* \mathbf{F}_{ik} \mathbf{F}_{jl} \Psi_l \Psi_k \right] \end{aligned} \quad (9.3)$$

The total energy $E = E[\Psi_{-1}, \Psi_0, \Psi_1]$ is conserved for time-independent potentials. However, in contrary to the scalar and vector GPEs, the spinor GPEs (9.2) do not conserve the atom numbers $N_i = \int d\mathbf{r} |\Psi_i(\mathbf{r})|^2$ of the individual components but only the total atom number $N_{\text{tot}} = \sum_i N_i$ is conserved. The latter can be seen by investigating the time evolution of the different atom numbers. Therefore let us investigate the time evolution of the density distributions of the individual spin components

$$\partial_t \rho_m = \Psi_m^* \partial_t \Psi_m + \Psi_m \partial_t \Psi_m^*. \quad (9.4)$$

Substitution of Eqs. (9.2) and their complex conjugates in Eq. (9.4) leads to

$$\partial_t \rho_0 = \frac{i}{\hbar} \left(\Psi_0^* \frac{\hbar^2}{2M} \nabla^2 \Psi_0 - \Psi_0 \frac{\hbar^2}{2M} \nabla^2 \Psi_0^* \right) + \frac{2g_1}{i\hbar} (\Psi_0^{*2} \Psi_1 \Psi_{-1} - \Psi_0^2 \Psi_1^* \Psi_{-1}^*) \quad (9.5)$$

$$\partial_t \rho_{\pm 1} = \frac{i}{\hbar} \left(\Psi_{\pm 1}^* \frac{\hbar^2}{2M} \nabla^2 \Psi_{\pm 1} - \Psi_{\pm 1} \frac{\hbar^2}{2M} \nabla^2 \Psi_{\pm 1}^* \right) + \frac{g_1}{i\hbar} (\Psi_0^2 \Psi_{\pm 1}^* \Psi_{\mp 1}^* - \Psi_0^{*2} \Psi_{\pm 1} \Psi_{\mp 1}) \quad (9.6)$$

One can then define the probability current in the standard way

$$\mathbf{j}_m = \frac{\hbar}{2M} \frac{1}{i} (\Psi_m^* \nabla \Psi_m - (\nabla \Psi_m^*) \Psi_m) \quad (9.7)$$

and a particle flux for each component

$$S_0 = \frac{2g_1}{i\hbar} (\Psi_0^{*2} \Psi_1 \Psi_{-1} - \Psi_0^2 \Psi_1^* \Psi_{-1}^*), \quad (9.8)$$

$$S_1 = S_{-1} = \frac{g_1}{i\hbar} (\Psi_0^2 \Psi_{\pm 1}^* \Psi_{\mp 1}^* - \Psi_0^{*2} \Psi_{\pm 1} \Psi_{\mp 1}). \quad (9.9)$$

The particle flux of the $m = 1$ and the $m = -1$ component are equal. The flux of the $m = 0$ component has got twice the magnitude of the other components and an opposite sign. Thus the total flux is zero. With the particles fluxes (9.8-9.9) and the probability current (9.7) one obtains the following continuity equations for the individual components:

$$\partial_t \rho_m + \nabla j_m = S_m \quad (9.10)$$

Spatial integration of the continuity equation leads finally to the time evolution of the occupation number of the single components

$$\partial_t N_m = \int d\mathbf{r} S_m. \quad (9.11)$$

The integral of the probability current vanishes for square integrable functions as can be seen by integration in parts. Since the sum of the particle fluxes vanishes, the total atom number is conserved. Moreover, the change of the atom number in the $m = 1$ and $m = -1$ is equal and has got half of the magnitude of the change of the population of the $m = 0$ component. This can be understood by the fact that the only allowed spin changing process is the process where an atom with $m = 1$ and an atom with $m = -1$ collide and change into two atoms with $m = 0$ or vice versa.

9.2 Effective 1D Equations

In the following, we restrict ourselves to an effective one-dimensional description accounting only for the longitudinal dynamics. The transversal confinement may be provided by an isotropic harmonic potential with a sufficiently large spin independent trap frequency ω_\perp (associated with the harmonic oscillator length a_\perp) such that the transversal dynamics is frozen out. The dimensionality reduction can be done in the same manner as for the scalar GPE (cf. section 2.2.2). The longitudinal motion takes place in the x -direction and consequently the corresponding mean field equations for the evolution of the spinor components $\Psi_m = \Psi_m(x, t)$

are given by

$$\begin{aligned} i\hbar\partial_t\Psi_0 &= \left[-\frac{\hbar^2}{2M}\partial_x^2 + V_0(x) + g_0n\right]\Psi_0 + \frac{g_1}{\sqrt{2}}[F_+\Psi_{+1} + F_-\Psi_{-1}] \\ i\hbar\partial_t\Psi_{\pm 1} &= \left[-\frac{\hbar^2}{2M}\partial_x^2 + V_{\pm 1}(x) + g_0n\right]\Psi_{\pm 1} + g_1\left[\frac{1}{\sqrt{2}}G_{\mp}\Psi_0 \pm F_z\Psi_{\pm 1}\right] \end{aligned} \quad (9.12)$$

with the atomic mass M , the total atomic density $n = \sum_{m=-1}^1 |\Psi_m|^2$, $G_z = |\Psi_{+1}|^2 - |\Psi_{-1}|^2$ and $G_+ = G_-^* = \sqrt{2}[\Psi_1^*\Psi_0 + \Psi_0^*\Psi_{-1}]$. The coupling constants are $g_0 = 2\hbar^2(a_0+2a_2)/(3Ma_{\perp}^2)$ and $g_1 = 2\hbar^2(a_2-a_0)/(3Ma_{\perp}^2)$ where $a_{0/2}$ are the s-wave scattering lengths for the scattering-channels with total spin 0 and 2. Note, we used the same notation for the coupling coefficients as in Eq. (9.2) despite the fact that these are effective 1D coupling coefficients. The same holds for the density which depends in Eq. (9.2) on x . The particle number in the respective hyperfine state is calculated according to $N_m = \int dx |\Psi_m|^2$. In this chapter we consider ^{23}Na with the respective scattering lengths $a_0 = 2.43$ nm and $a_2 = 2.75$ nm. The transversal trap frequency is chosen $\omega_{\perp} = 2$ kHz which gives rise to a transverse oscillator length $a_{\perp} = 2.97 \times 10^3$ nm.

9.3 Setup

The spin-dependent potential under consideration is of the form $V_m(x) = mV(x)$ with $V(x)$ forming a double-well. As shown in Refs. [32, 33] such a potential can be created using a standard magnetic trap of Ioffe-Pritchard type which is dressed by a homogeneous radio-frequency field. Instead of using the actual form of $V(x)$ which is provided in Ref. [33] we rather model the double-well as $V(x) = \gamma + \eta \exp(-x^2/\sigma^2) + (1/2)M\omega^2x^2$. This model potential, which is easily implemented numerically, covers the important features of the exact potential and can be made to match the experimental situation by tuning the parameters γ , η , σ and ω . For our calculations we choose $\gamma = 0$, $\eta = 1.05 \times 10^{30}$ J, $\sigma = 28$ μm and $\omega = 71$ Hz. A sketch of this potential is shown in Fig. 9.1. While atoms in the $m = 1$ state are subjected to an overall confining double well potential, atoms in the state $m = -1$ can be trapped only temporarily in metastable states of a single well which is unbounded from below. We assume this state to be stable over the timescale of interest. Additionally, the atom numbers and well separations are chosen such that there is negligible initial overlap between the three atomic clouds located in the three wells. The initial state for our investigations is created by transferring the entire population of the $m = -1$ into the $m = 0$ state which experiences no confining potential. Such a transfer can be achieved experimentally by two sufficiently broad banded microwave or laser pulses providing a Raman transition via intermediate excited states.

We prepare our initial state by relaxation, i.e., imaginary time propagation of a trial wave function. Since there is no initial overlap between the wave packets each of them can be prepared independently. We therefore introduce the number of particles confined in the left and right well by $N_{1L} = \int_{-\infty}^0 dx |\Psi_1|^2$ and $N_{1R} = \int_0^{\infty} dx |\Psi_1|^2$, respectively (see Fig. 9.1). They obey $N_{1L} + N_{1R} = N_1$. After having obtained the ground states in each potential well we set $\Psi_0 = \Psi_{-1}$ and subsequently put $\Psi_{-1} = 0$ assuming a perfect population transfer. Then the system is evolved in time according to Eqs. (9.12) using the Adams-Bashforth-Moulton

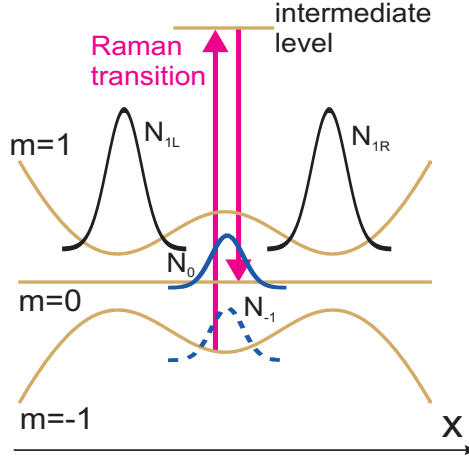


Figure 9.1: Preparation of the initial state: BECs prepared in the two wells of the $m = 1$ manifold and the single well of the $m = -1$ potential. All $m = -1$ atoms are transferred by a Raman transition to the $m = 0$ state.

predictor-corrector method (cf. Appendix A).

9.4 Trapping of the $m = 0$ Component

Throughout this work we will consider the regime of low densities of the $m = 0$ atoms and a small maximum overlap region of the $m = 0$ and $m = 1$ wave packets in which case $\partial_t N_{-1}$ becomes negligibly small. For analytical considerations we therefore make the very good approximation $\Psi_{-1} = 0$ for all times (see below for a corresponding discussion) and arrive at the two equations of motion:

$$i\hbar\partial_t\Psi_0=\left[-\frac{\hbar^2}{2M}\partial_x^2+g_0|\Psi_0|^2+(g_0+g_1)|\Psi_1|^2\right]\Psi_0 \quad (9.13)$$

$$i\hbar\partial_t\Psi_1=\left[-\frac{\hbar^2}{2M}\partial_x^2+V(x)+(g_0+g_1)(|\Psi_0|^2+|\Psi_1|^2)\right]\Psi_1, \quad (9.14)$$

i.e., the $m = -1$ component is not involved in the time-evolution at all. From Eq. (9.13) we observe that, although there is no external trap acting on Ψ_0 , we can identify the term $V_{\text{eff}}(x) = (g_0 + g_1)|\Psi_1|^2$ as an effective potential. However, this potential depends explicitly on the $m = 1$ density and implicitly on the $m = 0$ density as seen from Eq. (9.14). In order to demonstrate that $V_{\text{eff}}(x)$ can provide trapping we prepare an initial state with $N_{1R} = N_{1L} = (1/2) \times 10^5$ and $N_0 = 10^3$ as shown in Fig. 9.2. During the first several milliseconds the non-stationary $m = 0$ wave packet broadens until parts of it hit the atoms in the $m = 1$ state and Ψ_1 and Ψ_0 overlap. The situation at this instant of time is depicted in Fig. 9.3. The $m = 0$ atoms are reflected back completely and are thus eventually trapped as displayed in Fig. 9.4, where the $m = 0$ density over a time interval of 100 ms is shown. As can be seen the atoms are effectively confined to the interval $-50 \mu\text{m} < x < 50 \mu\text{m}$. Eq. (9.13) shows that the trapping is rooted in the density-density interaction between atoms in different spin states. A similar behavior is therefore expected for ^{87}Rb and for any other atomic species whose

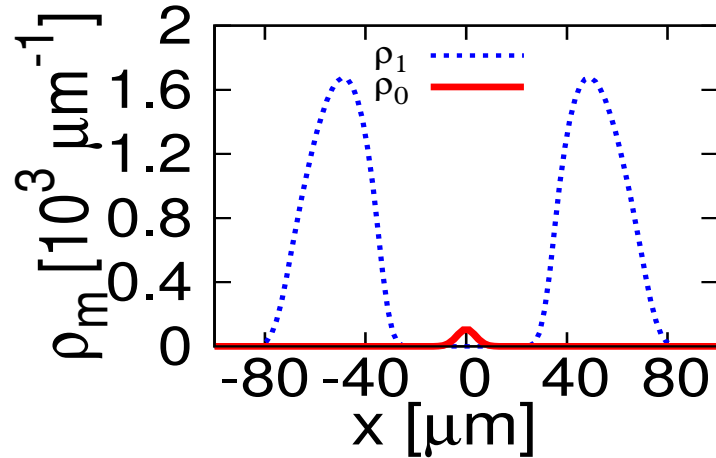


Figure 9.2: Density of the individual m components ($m = 1$ dashed line, $m = 0$ solid line) of the initial state with $N_1 = 10^5$ ($N_{1R} = N_{1L}$) and $N_0 = 10^3$.

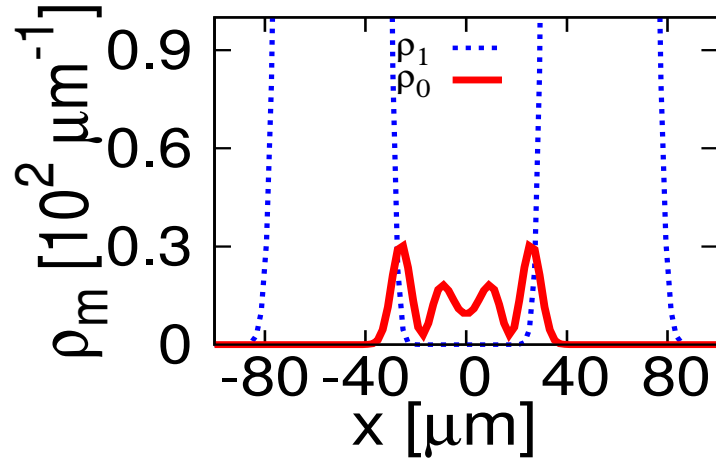


Figure 9.3: Density snapshot after the time $t = 13$ ms.

scattering lengths obey $g_0 + g_1 > 0$. Moreover, the density-density interaction implies that the demonstrated trapping effect should also be observable if two different atomic species are employed instead of two different spin states of the same atom. This, of course, requires that the atomic density of one of the species is shaped accordingly.

9.5 Loss Mechanism

Let us now return to the question of particle loss due to the scattering process $(m, m') = (0, 0) \rightarrow (1, -1)$. In Fig. 9.5 we show the temporal evolution of the relative change of the particle number $\Delta N_m(t) = \frac{N_m(t) - N_m(0)}{N_0(0)}$ in each of the three m -channels for $N_0(0) = 10^3$. The relative particle loss from the trapped atoms in the $m = 0$ state is negligibly small for the time interval 100 ms and therefore Eqs. (9.13,9.14) provide an accurate approximation. The scattering process $(0, 0) \rightarrow (1, -1)$, and thus the loss of $m = 0$ atoms, is strongly suppressed.

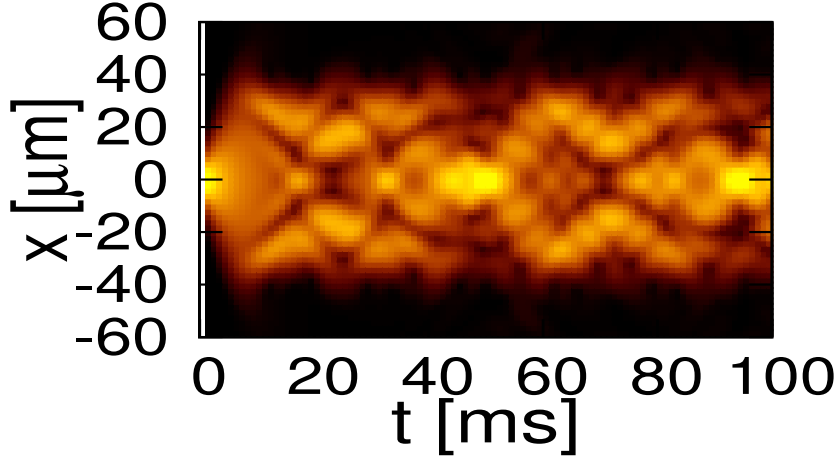


Figure 9.4: Time evolution of the density of the $m = 0$ component.

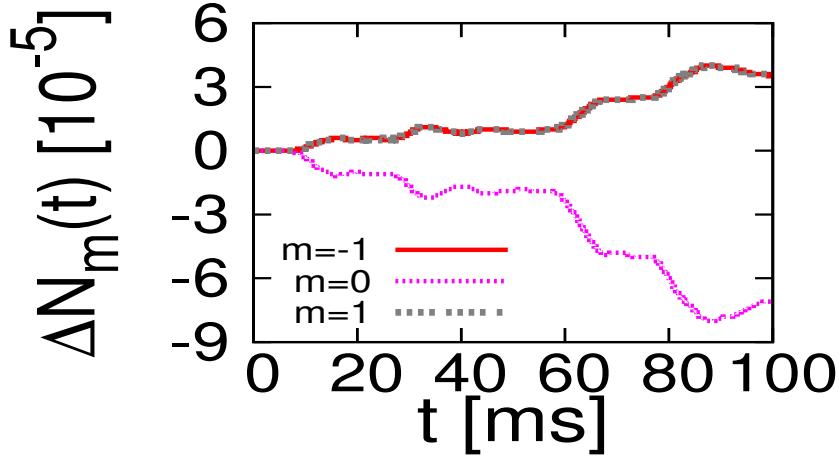


Figure 9.5: Relative change of the number of particles $\Delta N_m(t) = \frac{N_m(t) - N_m(0)}{N_0(0)}$ for $N_0(0) = 10^3$. The change of the particle number of the $m = 1$ and $m = -1$ components are equal (upper lines) which is a direct consequence of the conservation of magnetization in spinor condensates. The lower line denotes the change of the particle number of the $m = 0$ component.

For vanishing $m = 1$ and $m = -1$ components Eqs. (9.12) reduce to the Gross-Pitaevskii equation for the $m = 0$ component only and spin exchange processes are therefore absent. The microscopic spin exchange process can therefore in the mean field picture only occur if there is an overlap of at least two different spin components. In our situation this overlap is negligibly small. In order to see this more quantitatively we derive an upper bound for the population rate of the $m = -1$ component on the basis of Eq. (9.12). A combination of the 1D versions of Eqs. (9.9) and (9.11) leads to

$$\partial_t N_{-1} = \int dx [\partial_t \Psi_{-1} \Psi_{-1}^* + \partial_t \Psi_{-1}^* \Psi_{-1}] \quad (9.15)$$

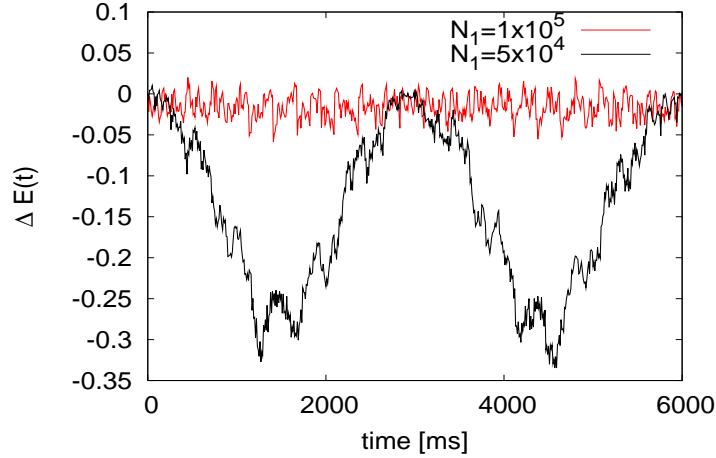


Figure 9.6: Relative energy change $\Delta E(t) = \frac{E_{\text{eff}}(t) - E_{\text{eff}}(0)}{E_{\text{eff}}(0)}$ of the $m = 0$ component for $N_0 = 10^3$, $N_1 = 10^5$ and 5×10^4 and $N_{1R} = N_{1L}$.

for the change of the atom number in the $m = -1$ component. For short times the evolution of Ψ_{-1} is governed by

$$\partial_t \Psi_{-1} = -i \frac{g_1}{\hbar} \Psi_0^2 \Psi_1^*. \quad (9.16)$$

Assuming the r.h.s. to be constant leads then to $\Psi_{-1}(t) \approx \partial_t \Psi_{-1} t$. Considering exclusively the process that populates Ψ_{-1} we find

$$\partial_t N_{-1} \approx \int dx \partial_t \Psi_{-1} \partial_t \Psi_{-1}^* t \approx (g_1/\hbar)^2 \int dx |\Psi_0|^4 |\Psi_1|^2 t. \quad (9.17)$$

Introducing a typical overlap region Δx between the $m = 0$ and $m = 1$ wave functions and the corresponding maximal values for the densities $n_{0,\max}$, $n_{1,\max}$ inside this region, we find the following upper bound for the particle number increase in the $m = -1$ mode:

$$\partial_t N_{-1} < \left(\frac{g_1}{\hbar}\right)^2 \Delta x n_{0,\max}^2 n_{1,\max} t. \quad (9.18)$$

Estimating the increase of the particle number in the $m = -1$ according to Eq. (9.18) we find with $n_{0,\max} = 25 \mu\text{m}^{-1}$, $n_{1,\max} = 100 \mu\text{m}^{-1}$ and an overlap of $\Delta x \approx 20 \mu\text{m}$ a rate of $\partial_t N_{-1} < 0.02t / (\text{ms})^2$ which is consistent with our numerical data. Beyond this estimate Fig. 9.5 shows a step-like increase of N_{-1} which is due to the time-dependence of the overlap of Ψ_0 and Ψ_1 .

9.6 Backaction of the $m = 0$ Component on the $m = 1$ Component

Let us now address the question of a backaction of the $m = 0$ atoms onto the $m = 1$ atoms. As demonstrated above the effective potential $V_{\text{eff}}(x) = (g_0 + g_1) |\Psi_1|^2$ can grant efficient confinement of the $m = 0$ atoms. However, according to the coupled Eqs. (9.13,9.14) Ψ_1 does not evolve independently of Ψ_0 . Hence it is expected that the trapped atoms act back

on the atoms in the $m = 1$ state and thereby modify the trapping potential itself. In order to quantify this effect we calculate the effective energy

$$E_{\text{eff}} = \int dx \left(-\frac{\hbar^2}{2M} |\partial_x^2 \Psi_0|^2 + \frac{(a_0 + 2a_2)\hbar^2}{3Ma_\perp^2} |\Psi_0|^4 + \frac{2a_2\hbar^2}{Ma_\perp^2} |\Psi_0|^2 |\Psi_1|^2 \right) \quad (9.19)$$

which is the energy contained in the $m = 0$ component itself plus a contribution arising due to the interaction of the $m = 0$ with the $m = 1$ density. If $|\Psi_1|^2$ was static, i.e., it did not change its shape as a function of time, $E_{\text{eff}} = E_{\text{eff}}(t)$ would be conserved. Conversely, energy exchange between the spin components will be reflected in a variation of E_{eff} over time. In Fig. 9.6 we illustrate the time-dependence of the quantity $\Delta E(t) = \frac{E_{\text{eff}}(t) - E_{\text{eff}}(0)}{E_{\text{eff}}(0)}$ for $N_0 = 10^3$ and two different particle numbers $N_1 = 10^5$ and 5×10^4 . The shape of the initial state is the same as discussed before, i.e., symmetric occupation of the $m = 1$ double-well potential (see Fig. 9.2). We observe that for $N_1 = 10^5$ the relative energy change is of the order of 5 % over the shown time interval of 10^4 ms. Here the effective potential can be approximately considered as static. The situation changes if N_1 is lowered. More concrete, for $N_1 = 5 \times 10^4$ we observe large oscillations of ΔE with peak values up to 35 % and the effective potential picture breaks down.

9.7 Outcoupling of Atoms

So far we have been focusing on an initial state with a symmetric occupation of the $m = 1$ double well. We will now investigate the situation $N_{1L} \neq N_{1R}$ where N_{1R} is not large enough to provide a complete confinement of the $m = 0$ atoms. In Fig. 9.7 the evolution of the $m = 0$

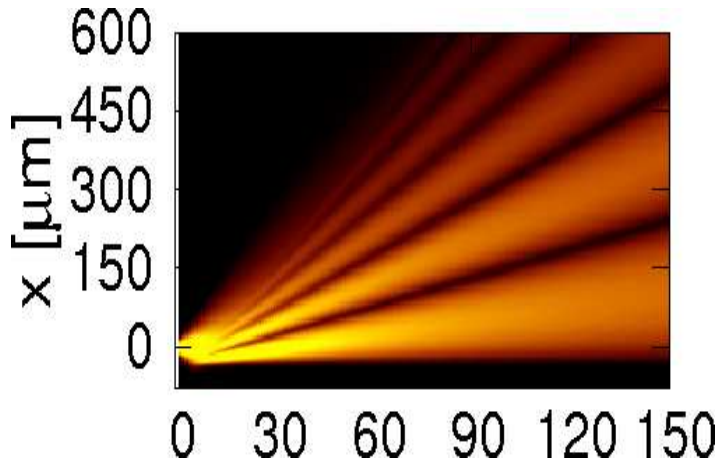


Figure 9.7: The time evolution of the $m = 0$ density for 150 ms and an initial state with $N_0 = 10^3$, $N_{1L} = 10^5$, $N_{1R} = 0$. Atoms are released from the trap region and escape to the $x > 0$ halfspace.

density is shown for the particle numbers $N_0 = 10^3$, $N_{1L} = 10^5$ and $N_{1R} = 0$. In the case, where there is no occupation of the right hand well, the atoms are free to leave the trapping region to the $x > 0$ halfspace. Escape to the opposite direction is prevented by the $m = 1$ wave packet in the left well (N_{1L}) and thus atoms which are initially going to the left are reflected. They interfere with the atoms initially going to the right thereby giving rise to an

emission of a sequence of distinct wave packets. In case of an initial occupation of the right

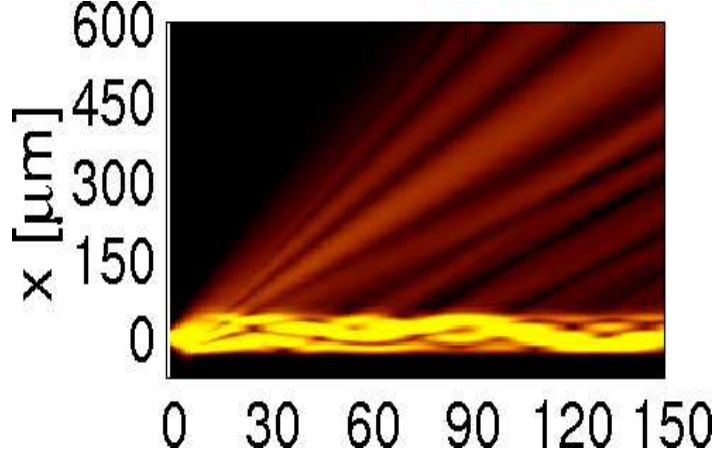


Figure 9.8: The time evolution of the $m = 0$ density for 150 ms and an initial state with $N_0 = 10^3$, $N_{1L} = 10^5$, and $N_{1R} = 7 \times 10^3$. Atoms are released from the trap region and escape to the $x > 0$ halfspace.

hand well, i.e., $N_{1R} \neq 0$ the situation becomes more complex. An example is shown in Fig. 9.8 where $N_{1R} = 7 \times 10^3$. Here N_{1R} is not sufficiently large in order to provide confinement for all $m = 0$ atoms, and a fraction of them escape to the $x > 0$ halfspace. This emission recedes drastically as soon as a sufficient number of atoms has escaped and the number of $m = 0$ atoms in the trapping region has become so small that confinement can eventually be granted by the $m = 1$ atoms in the right well. This behavior is studied in more detail in Fig.

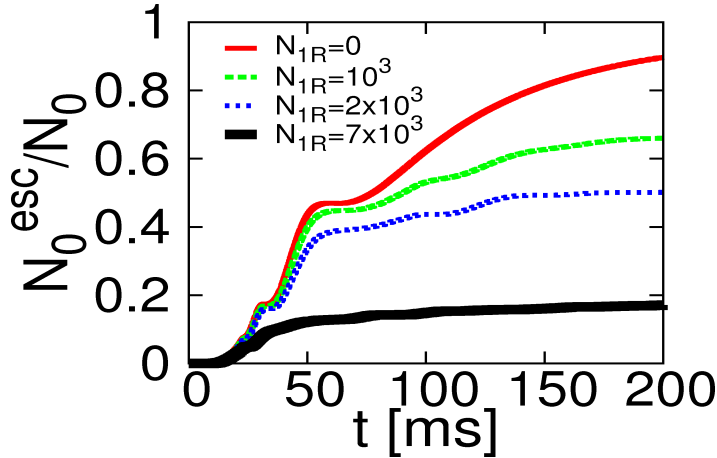


Figure 9.9: Time evolution of the relative number of escaped $m = 0$ atoms for (from top to bottom) $N_{1R} = \{0, 10^3, 2 \times 10^3, 7 \times 10^3\}$.

9.9 where we plot the time evolution of the number of escaped atoms $N_0^{esc} = \int_{x_0}^{\infty} dx |\Psi_0|^2$ for different values of the atom number N_{1R} keeping $N_0 = 10^3$ and $N_{1L} = 10^5$ constant. In the case at hand we define $x_0 = 80 \mu\text{m}$ thereby ensuring that the considered atoms are definitely not trapped any longer since the density of the $m = 1$ component beyond x_0 is sufficiently small. The number of escaped atoms increases monotonously as time passes. For

$t < 60\text{ ms}$ periods of a steep increase are followed by plateaus where almost no emission is observed. During the latter time intervals those atoms which are reflected from the $m = 1$ wave packet localized in the left well destructively interfere with the atoms that initially went to the right, causing the emission to cease for a while. This is reflected in the pulsed release of $m = 0$ atoms from the trapping region that is clearly seen in Figs. 9.7 and 9.8. This situation is strongly reminiscent of a pulsed atom laser. For large times N_0^{esc}/N_0 saturates since the number of remaining atoms in the $m = 0$ state is small enough to be confined. The number of confined atoms $N_0^{\text{tr}} = N_0 - N_0^{\text{esc}}$ after $t = 150\text{ ms}$ is plotted in Fig. 9.10

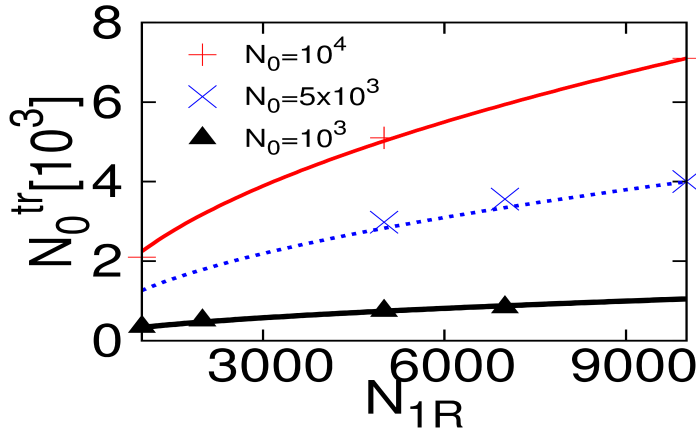


Figure 9.10: Number of trapped atoms $N_0^{\text{tr}} = N_0 - N_0^{\text{esc}}$ after $t = 150\text{ ms}$ as function of N_{1R} for $N_0 = 10^4$ (+), $N_0 = 5 \times 10^3$ (×) and $N_0 = 10^3$ (△). The lines were generated by fitting $N_0^{\text{tr}} = \kappa\sqrt{N_{1R}}$.

as a function of the occupation number of the right well for different N_0 . As expected the final number of trapped atoms increases with increasing N_{1R} . The energy E_0 of the $m = 0$ component is approximately proportional to the square of the occupation number N_0 in case of the nonlinear term being dominant. Furthermore, if one regards the $m = 1$ component in the right well to act as a potential then the height V_{1R} of this potential is proportional to N_{1R} . The energy $E_0 \propto N_0^2$ of trapped $m = 0$ atoms should be less than the height of the potential $V_{1R} \propto N_{1R}$ created by the $m = 1$ atoms. This yields the scaling $N_0^{\text{tr}} \propto \sqrt{N_{1R}}$ which is reproduced in Fig. 9.10. The constant of proportionality depends on the initial occupation of the $m = 0$ component. A larger initial occupation number leads to a larger amount of atoms with a small kinetic energy. As a consequence more atoms remain trapped reminiscent of the mechanism of evaporative cooling.

In the present study the focus was set on a 1d system but the results translate also to higher dimensions: For confinement in 2 and 3 dimensions ring [31–33] and shell-like [295] traps can be employed. Even more complex setups like arrays of BECs which provide a periodic ‘soft’ or ‘hard’ trapping potential are conceivable. Such a scenario, which is reminiscent of the self-assembled lattices presented in Ref. [296] can be realized via multi-well radio-frequency traps (see Ref. [295]).

Chapter 10

Creating Versatile Atom Traps by Applying Near Resonant Laser Light in Magnetic Traps

In the previous chapter we demonstrated how one can trap the magnetically insensitive $m = 0$ component due to interaction with the $m = 1$ component. In this chapter, we present a way of trapping atoms by applying external fields. Therefore we derive the potential for an atom exposed simultaneously to an inhomogeneous magnetic field in a Ioffe-Pritchard trap like configuration and two lasers in a Raman configuration. In this case, the non-trivial combination of the magnetic and the laser fields can no longer be reduced to a potential resulting from an effective magnetic field. A direct consequence of this fact is that the potential surfaces for different hyperfine components of an atom do not only differ by a global factor but can be substantially different. Thus, it is possible to confine the different components of a multi-component BEC in traps of different frequencies or different types, e.g., one component in a double well trap and another one in a single well trap located at the barrier of the double well. Our approach is complementary to the setup described in Ref. [37], where the authors create state dependent potentials by applying spatially dependent microwave fields in the near field regime on magnetic traps on an atom chip. Thereby, the microwaves couple the hyperfine manifolds of the ground state. In our case the most prominent features of the trapping potentials stem from the interplay of the simultaneous coupling of the ground state to two hyperfine manifolds of an electronically excited state. Furthermore, an advantage of using lasers in a Raman configuration instead of microwave or radio frequency fields is their larger flexibility in tuning the spatial shape of the laser profiles or changing the polarization of the lasers. Moreover, due to the availability of additional parameters, flexibility is gained in shaping the potentials compared to conventional traps. For example, one can smoothly convert a single well potential into a double well potential or drive a double well potential by varying an offset magnetic field. Furthermore, it is possible to rotate the potential around one axis by changing the phase between the Raman lasers. The content of this chapter is published in Ref. [297]. In this chapter we investigate a setup where Raman laser are applied in a magnetic trap. In appendix E we consider the complementary setup where Raman lasers are applied in an optical trap.

The chapter is structured as follows. In section 10.1, we derive the effective Hamiltonian. In section 10.2 our numerical results are presented. Specifically, we provide an overview of the potential surfaces of the different components and investigate the transition of a double well to a single well potential as well as the rotation of a double well potential for one component in detail. In section 10.3 we derive a semi-analytical expression for the potential surfaces; in section 10.4 loss mechanisms are discussed. Finally, we summarize our results in section 10.5 and mention possible applications of the trapping potential.

10.1 Analytical Considerations

10.1.1 Hamiltonian and Setup

The Hamiltonian of an (alkali) atom simultaneously exposed to magnetic and laser fields reads

$$H = -\frac{\hbar^2}{2M} \nabla_{\mathbf{R}}^2 + H^e(\mathbf{r}) + V^{IP}(\mathbf{r}, \mathbf{R}) + V^{AF}(\mathbf{r}, \mathbf{R}). \quad (10.1)$$

Here, \mathbf{R} denotes the center of mass coordinate of the atom and \mathbf{r} the coordinate of the valence electron relative to the center of mass position; M is the total mass of the atom. $H^e(\mathbf{r})$ accounts for the field-free electronic structure of the atom; for the scope of this chapter, we use ^{87}Rb as a paradigm. $V^{AF}(\mathbf{r}, \mathbf{R})$ and $V^{IP}(\mathbf{r}, \mathbf{R})$ denote the contributions of the Raman lasers and the magnetic field, respectively. In order to solve the coupled Schrödinger equation associated with Hamiltonian (10.1), we employ a Born-Oppenheimer separation of the center of mass motion and the electronic degrees of freedom. We are thereby led to an effective electronic Hamiltonian that parametrically depends on the center of mass position,

$$H^{\text{eff}}(\mathbf{R}) = H^e(\mathbf{r}) + V^{IP}(\mathbf{r}; \mathbf{R}) + V^{AF}(\mathbf{r}; \mathbf{R}). \quad (10.2)$$

Its solutions $V_\kappa(\mathbf{R})$ serve as adiabatic potential energy surfaces for the center of mass motion of the atom; each of these (trapping) potentials is then associated with a given internal state κ of the atom.

Regarding the magnetic field configuration, we consider the setup of a Ioffe-Pritchard trap [298] which is given by a two-dimensional quadrupole field in the x_1, x_2 -plane together with a perpendicular offset (Ioffe-) field in the x_3 -direction; it can be parameterized as $\mathbf{B}(\mathbf{x}) = Gx_1\mathbf{e}_1 - Gx_2\mathbf{e}_2 + B_I\mathbf{e}_3$. G denotes the magnetic gradient of the two-dimensional quadrupole field and B_I the constant offset field oriented along the x_3 -axis. The quadratic term $\mathbf{B}_q \propto (x_3^2 - \rho^2/2)\mathbf{e}_3$ that usually arises for a Ioffe-Pritchard configuration can be exactly zeroed by geometry, which we are considering in the following. In actual experimental setups, \mathbf{B}_q provides a weak confinement also in the x_3 -direction. Omitting \mathbf{B}_q , the magnitude of the magnetic field at a certain position \mathbf{x} in space is given by $|\mathbf{B}(\mathbf{x})| = \sqrt{B^2 + G^2\rho^2}$, which yields a linear asymptote $|\mathbf{B}(\mathbf{x})| \rightarrow G\rho$ for large values of the coordinates ($\rho = \sqrt{x_1^2 + x_2^2} \gg B/G$) and a harmonic behavior $|\mathbf{B}(\mathbf{x})| \approx B + \frac{1}{2}\frac{G^2}{B}\rho^2$ close to the origin ($\rho \ll B/G$). The magnetic field interaction within the Born-Oppenheimer approximation reads

$$V^{IP}(\mathbf{r}; \mathbf{R}) = g_F\mu_B \mathbf{F} \cdot \mathbf{B}(\mathbf{R}). \quad (10.3)$$

The Raman configuration of the excitation lasers is depicted in Fig. 10.1. It consists of two oppositely circular polarized lasers that are close to resonance with the D_1 transition line, i.e., being blue-detuned by Δ with respect to the transition from the $5S_{1/2}, F = 1$ ground state manifold to the $5P_{1/2}, F = 1$ excited state of ^{87}Rb . The propagation direction of the lasers is chosen to coincide with the direction of the constant Ioffe Field B_I . The overall setup is shown in Fig. 10.2

Within the dipole approximation, the potential of an atom exposed to the laser fields is given by

$$V^{AF}(\mathbf{r}; \mathbf{R}) = -e\mathbf{r} \cdot \mathbf{E}(\mathbf{R}, t), \quad (10.4)$$

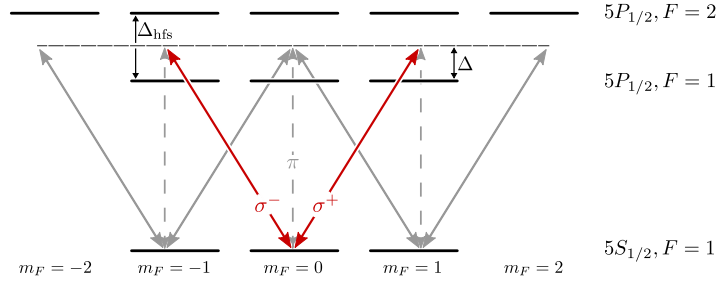


Figure 10.1: State linkage diagram of the unperturbed atom. The solid arrows denote the transitions allowed for σ^+ and σ^- light, whereas the dashed arrows indicate allowed transitions with π polarized light. The energy gap between the $5P_{1/2}, F = 1$ and $5P_{1/2}, F = 2$ manifold is $\Delta_{\text{hfs}} = 2\pi\hbar \times 0.8 \text{ GHz}$ [299].

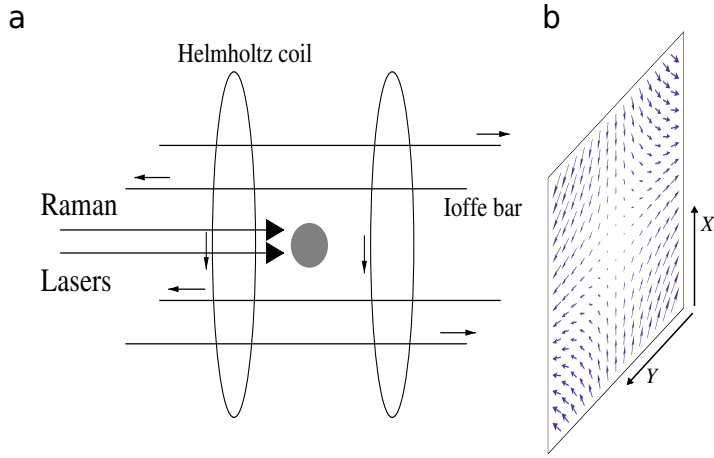


Figure 10.2: (a) Setup showing the propagation direction of the laser beams (large arrows) and the configuration of the magnetic trap. The Helmholtz coils generate the homogeneous Ioffe field oriented along the Z direction and the Ioffe bars the quadrupole field in the $X - Y$ plane, shown in subfigure (b).

$\mathbf{E}(\mathbf{R}, t)$ denoting the electric field of the lasers. The latter can be expressed as

$$\mathbf{E}(\mathbf{R}, t) = \frac{1}{2} \sum_{i=1}^2 [\mathbf{E}_i(\mathbf{R}, t) + \mathbf{E}_i^*(\mathbf{R}, t)] \quad (10.5)$$

with $\mathbf{E}_i(\mathbf{R}, t) = \epsilon_i \varepsilon_i(\mathbf{R}) e^{-i(\mathbf{k}_i \cdot \mathbf{R} - \omega_i t + \phi_i(t))}$ being the electric field associated with the i th laser. The amplitudes $\varepsilon_i(\mathbf{R})$ of the electric fields are spatially dependent in order to account for the focussing and shape of the laser beams. The factors ϵ_i are the unit polarization vectors given by $\epsilon_1 = \frac{1}{\sqrt{2}}(\mathbf{e}_1 + i\mathbf{e}_2)$ (σ^+ light) and $\epsilon_2 = \frac{1}{\sqrt{2}}(\mathbf{e}_1 - i\mathbf{e}_2)$ (σ^- light), respectively. $\phi_i(t)$ take into account the phases of the lasers, which additionally can depend on time. Expanding the atom field interaction in the basis $|\alpha\rangle$, defined as the eigenfunctions of the field free atom, leads to

$$V^{\text{AF}}(\mathbf{r}; \mathbf{R}) = \frac{1}{2} \sum_{i=1}^2 \sum_{\alpha, \gamma} (\omega_{i, \alpha\gamma}^{(+)} + \omega_{i, \alpha\gamma}^{(-)}) |\gamma\rangle \langle \alpha| + \text{h.c.} \quad (10.6)$$

with $\omega_{i,\alpha\gamma}^{(+)} = e\langle\alpha|\mathbf{E}_i(t)\mathbf{r}|\gamma\rangle$ and $\omega_{i,\alpha\gamma}^{(-)} = e\langle\alpha|\mathbf{E}_i^*(t)\mathbf{r}|\gamma\rangle$.

10.1.2 Rotating Wave Approximation

We employ the rotating wave approximation [300] in order to remove the time-dependence of Hamiltonian (10.2) that arises due to the laser interaction. For reasons of simplicity we assume that both lasers have the same frequency $\omega_i \equiv \omega$ and the same profile $\varepsilon_i(\mathbf{R}) \equiv \varepsilon(\mathbf{R})$. Since the magnetic field interaction term is block diagonal, i.e., does not mix states with different total angular momenta, $V^{\text{IP}}(\mathbf{r}; \mathbf{R})$ is not affected by the transformation into the rotated frame. The transformed Hamiltonian reads

$$H_{\text{RWA}} = V^{\text{IP}} + V_{\text{RWA}}^{\text{e}} + V_{\text{RWA}}^{\text{AF}}, \quad (10.7)$$

where

$$V_{\text{RWA}}^{\text{e}} = \sum_{\alpha} E_{\alpha} |\alpha\rangle\langle\alpha| + \sum_l (E_l - \hbar\omega) |l\rangle\langle l| \quad (10.8)$$

$$V_{\text{RWA}}^{\text{AF}} = \frac{1}{2} \sum_{i=1}^2 \sum_{\alpha, l} \varepsilon(\mathbf{R}) e^{-i(\mathbf{k}_i \cdot \mathbf{R} + \phi_i(t))} \langle l | \boldsymbol{\epsilon}_i \cdot \mathbf{r} | \alpha \rangle |l\rangle\langle\alpha| + \text{h.c.} \quad (10.9)$$

(for clarity, we omit the arguments \mathbf{r} and \mathbf{R} of the potentials in the following). Here, α labels the different states of the ground state manifold and l labels the excited states. Since the lasers are close to resonance to the D_1 transition line, we can restrict our basis to states close to the ground state and the first excited state. Using as a basis all hyperfine states of the $5S$ and $5P$ manifolds leads to an effective 32×32 matrix that will be diagonalized.

10.1.3 Van Vleck Perturbation Theory

In the last subsection we derived the Hamiltonian expanded in the eigenfunctions of the unperturbed atom. One can use *van Vleck perturbation theory* [301] to adiabatically eliminate the excited $5P$ levels that serve as intermediate states for the Raman transitions. In this manner, the Hamiltonian can be reduced to an operator acting only on the ground state manifold (i.e., all states $|\alpha\rangle = |5S_{1/2}, F=1, m_F\rangle$ with $m_F \in \{0, \pm 1\}$),

$$H_{\text{VV}} = V^{\text{IP}} + \sum_{\alpha} E_{\alpha} |\alpha\rangle\langle\alpha| + \sum_{\alpha, \beta} \mathcal{W}_{\beta\alpha} |\beta\rangle\langle\alpha|, \quad (10.10)$$

with

$$\mathcal{W}_{\beta\alpha} = \frac{1}{2} \sum_l \mathcal{V}_{\beta l} \mathcal{V}_{l\alpha} \left(\frac{1}{E_{\alpha} - E_l} + \frac{1}{E_{\beta} - E_l} \right), \quad (10.11)$$

being the effective interaction within the ground state manifold. Here, the index l labels the excited states, which have been eliminated. For a detailed derivation of Eq. (10.11), we refer the reader to Appendix D. Employing

$$\mathcal{V}_{l\alpha} = \frac{1}{2} \sum_{i=1}^2 \sum_{\alpha, l} \varepsilon(\mathbf{R}) e^{-i(\mathbf{k}_i \cdot \mathbf{R} + \phi_i(t))} \langle l | \boldsymbol{\epsilon}_i \cdot \mathbf{r} | \alpha \rangle. \quad (10.12)$$

for the block off-diagonal matrix elements of $V_{\text{RWA}}^{\text{AF}}$ yields the effective interaction W within the ground state manifold whose matrix representation correspondingly reads

$$W_{\beta\alpha} = \frac{1}{8}\varepsilon(\mathbf{R})^2 \sum_{i,i'=1}^2 \sum_l e^{i[\phi_i(t) - \phi_{i'}(t)]} \langle \beta | \epsilon_i \mathbf{r} | l \rangle \langle l | \epsilon_{i'} \mathbf{r} | \alpha \rangle \\ \times \left(\frac{1}{E_\alpha - E_l + \hbar\omega} + \frac{1}{E_\beta - E_l + \hbar\omega} \right). \quad (10.13)$$

If one restricts the sum over the intermediate states to the $5P_{1/2}$ hyperfine sublevels, which represent a good approximation, one obtains the compact form

$$\mathcal{W} = \frac{|\langle 5S_{1/2} | er | 5P_{1/2} \rangle|^2}{72c\epsilon_0\Delta} \begin{pmatrix} A & 0 & C \\ 0 & B & 0 \\ C^* & 0 & A \end{pmatrix} \quad (10.14)$$

for the atom laser interaction, with

$$A = \left(1 + \frac{7}{1 - \frac{\Delta_{\text{hfs}}}{\Delta}} \right) I(\mathbf{R}), \quad (10.15)$$

$$B = 2 \left(1 + \frac{3}{1 - \frac{\Delta_{\text{hfs}}}{\Delta}} \right) I(\mathbf{R}), \quad (10.16)$$

$$C = - \left(1 - \frac{1}{1 - \frac{\Delta_{\text{hfs}}}{\Delta}} \right) e^{i\Delta\phi(t)} I(\mathbf{R}), \quad (10.17)$$

$\Delta = E_{5S_{1/2},F=1} - E_{5P_{1/2},F=1} - \hbar\omega$ being the detuning of the transition lasers and $\Delta\Phi(t) = \phi_1(t) - \phi_2(t)$ their phase difference. $I(\mathbf{R}) = c\epsilon_0|\varepsilon(\mathbf{R})|^2/2$ denotes the intensity of the laser, ϵ_0 being the dielectric constant and c the speed of light. The radial matrix element in Eq. (10.14) can be deduced from the measured lifetime of the excited state which yields in our case $\langle 5S_{1/2} | er | 5P_{1/2} \rangle = \sqrt{3}(2.9919 \pm 0.0030) ea_0$ [302, 303]. Note, that the factor of $\sqrt{3}$ stems from the angular integration since we consider the radial matrix element in our calculations. The individual contributions of the matrix (10.14) can be interpreted as follows. The diagonal elements stem from the light shift potential of the lasers, i.e., the off-resonant coupling of a m_F component of the ground state to an excited state. The off-diagonal elements arise due to the coupling of the $m_F = 1$ ($m_F = -1$) component via an intermediate (excited) state to the $m_F = -1$ ($m_F = 1$) component. These off-diagonal matrix elements are not present in radio frequency traps. The specific form of the matrix occurs since the laser light is circularly polarized. Other polarizations would lead to a coupling of different states, i.e., different off-diagonal entries of the matrix \mathcal{W} . Furthermore, we should note at this point that the matrix is expanded in the field-free basis of the atom. In this basis, the contribution of the magnetic field interaction V^{IP} for the ground state manifold is represented by the spin matrices for total spin $F = 1$, giving rise to off-diagonal matrix elements as well. As a result, the combined action of the magnetic and laser fields leads to the mutual coupling of all magnetic sublevels of the $5S_{1/2}, F = 1$ manifold, represented by a fully occupied matrix. In section 10.3 we tackle this issue by performing a principal axis transformation that diagonalizes the magnetic

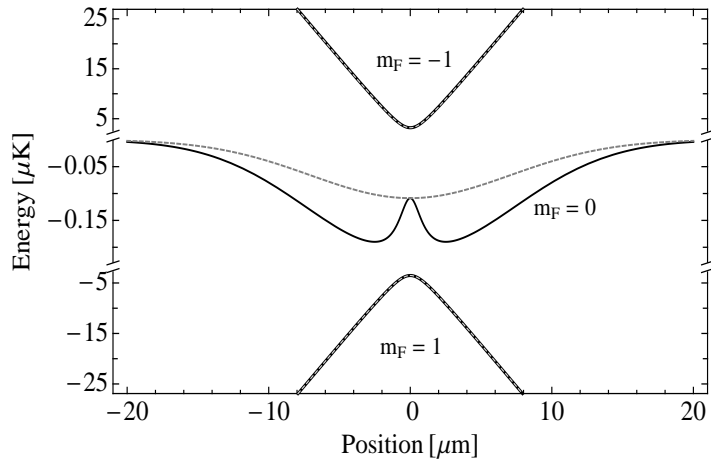


Figure 10.3: Potential curves for $Y = 0$ (solid line) and for $X = 0$ (dashed line). Two components show an attractive potential in two dimensions whereas one component is exposed to a repulsive potential. The individual potential surfaces are well separated.

field interaction and thus provides us with a more suitable basis for the interpretation of the underlying physics.

10.2 Numerical Results

We restrict our investigations to both lasers having a Gaussian profile with a width σ in the X, Y plane and assume that they have a constant intensity in the propagation direction Z ,

$$I(\mathbf{R}) = I_0 \exp\left(-\frac{X^2 + Y^2}{\sigma^2}\right). \quad (10.18)$$

Since the magnetic field interaction term is independent of Z as well, we find a total potential that is constant in the Z -direction. In order to provide a confinement in the Z -direction one can, e.g., utilize an additional laser or make use of the defocusing of the laser beams. If not stated otherwise, we fix the detuning of the lasers to $\Delta = -\Delta_{\text{hfs}}/2$, i.e., right in the middle between the $5P_{1/2}, F = 1$ and the $5P_{1/2}, F = 2$ excited states as depicted in Fig. 10.1, and the intensity to $I_0 = 10 \text{ W/m}^2$.

10.2.1 Overview Over All Components

Diagonalizing the Hamiltonian matrix (10.10) leads to the adiabatic potential surfaces $V_\kappa(\mathbf{R})$ for the center of mass motion as a function of the center of mass coordinate \mathbf{R} . As expected from the magnetic field interaction, we find one trapped and one anti-trapped component, according to the quantum numbers $m_F = +1$ and $m_F = -1$, respectively. Interestingly, the $m_F = 0$ component – that is untrapped in a pure Ioffe-Pritchard field – now shows an attractive potential with a double-well structure along the X -axis. Note that the quantum number m_F is only valid in a rotated frame of reference that we are going to introduce in Sec. 10.3. Nevertheless, we continue to use m_F as a label for the different states in

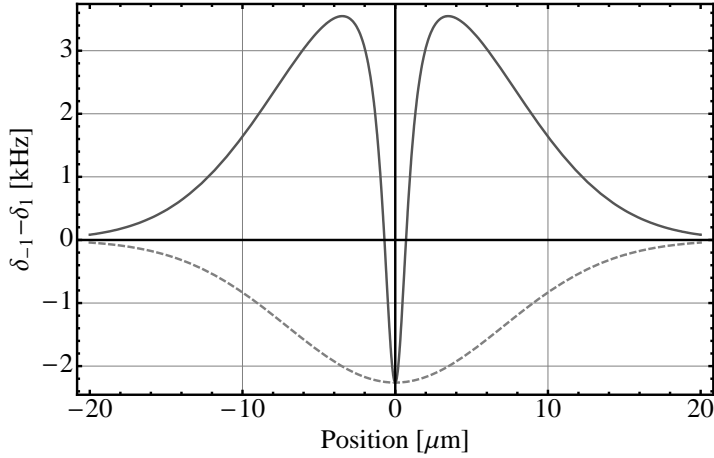


Figure 10.4: Difference of the potential differences for adjacent components for $X = 0$ (solid line) and $Y = 0$ (dashed line). The deviation between the transition frequencies of adjacent potential surfaces is non-zero and depends on the center of mass position of the atom.

the laboratory frame in order to avoid confusion. Since the different potential surfaces are separated, one can uniquely assign to each state one particular surface.

For investigating the energy spectrum further, let us define the radio transition frequencies $\delta_{-1}(\mathbf{R}) = V_{m_F=-1}(\mathbf{R}) - V_{m_F=0}(\mathbf{R})$ and $\delta_1(\mathbf{R}) = V_{m_F=0}(\mathbf{R}) - V_{m_F=1}(\mathbf{R})$ between the $m_F = 0$ and the $m_F = \mp 1$ states, respectively. Figure 10.4 provides a measure for the deviation of both transition frequencies by showing the difference $\delta_{-1}(\mathbf{R}) - \delta_1(\mathbf{R})$ for $X = 0$ (solid line) and $Y = 0$ (dashed line). The fact that the transition frequencies do not coincide, i.e., the difference being non-zero, can be used to mutually couple two components without coupling to the third component. This allows for example a transfer of atoms from the $m_F = -1$ component to the $m_F = 0$ component without coupling to the untrapped $m_F = 1$ component. Moreover, the radio transition frequencies depend on the center of mass position \mathbf{R} and thus on the absolute value of the potentials. Therefore, one may couple energy-selectively one component to another one, i.e., couple atoms of the $m_F = 0$ or $m_F = -1$ component at a certain position to the untrapped $m_F = 1$ component. Such a scheme can be used to evaporatively cool the $m_F = 0$ or the $m_F = -1$ component [304].

10.2.2 $m_F = 0$ Component

We start our detailed investigations of the individual components with the potential surface for the $m_F = 0$ component. Note that this component is not confined in a pure magnetic trap. Figure 10.5 shows the contour plot of its trapping potential for $\Delta\Phi = 0$, $\sigma = 10 \mu\text{m}$, $G = 0.1\text{G}/\mu\text{m}$, and (a) $B_I = 10 \text{ G}$, (b) $B_I = 1 \text{ G}$, (c) $B_I = 0.5 \text{ G}$, and (d) $B_I = 0.1 \text{ G}$. The shape of the potential correspondingly changes from (a) close to being rotationally symmetric to (b) a cigar shaped potential in the X -direction, and finally to (c,d) a double well in the X -direction. Thus, one can change the shape of the potential from a single- to a double well potential by changing the magnitude of the Ioffe field. Alternatively, one may also drive the double or single well potential by modulating the magnitude of the Ioffe field. The parameters of the double well trap can be tuned in different ways. The height of the

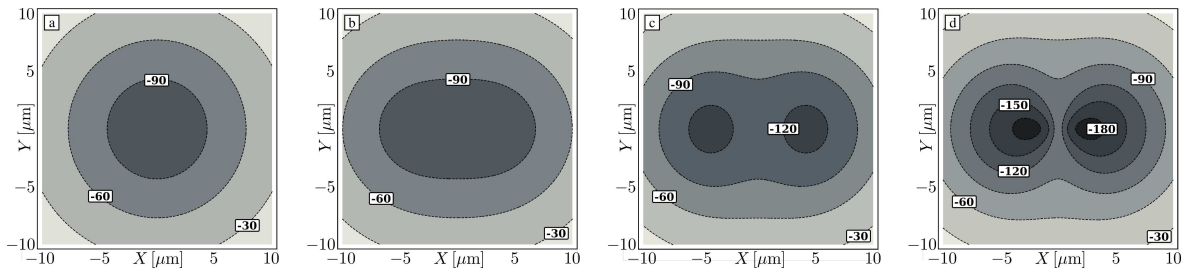


Figure 10.5: Contour plot of the potential surface for the $m_F = 0$ component for $\Delta\Phi = 0$, $\sigma = 10 \mu\text{m}$, $G = 0.1 \text{G}/\mu\text{m}$, and (a) $B_I = 10 \text{ G}$, (b) $B_I = 1 \text{ G}$, (c) $B_I = 0.5 \text{ G}$, and (d) $B_I = 0.1 \text{ G}$. The grey coded values of the potential are given in nK. By modulating the magnitude of the Ioffe field one can transform the potential smoothly from a single well to a double well potential.

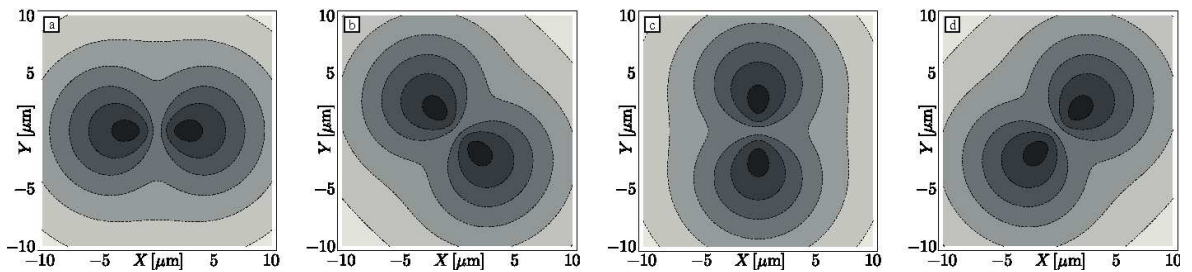


Figure 10.6: Contour plot of the potential surface for the $m_F = 0$ component for $G = 0.1 \text{ G}/\mu\text{m}$, $\sigma = 10 \mu\text{m}$, $B_I = 0.1 \text{ G}$, and for (a) $\Delta\Phi = 0$, (b) $\Delta\Phi = \pi/2$, (c) $\Delta\Phi = \pi$, and (d) $\Delta\Phi = 3\pi/2$. A phase difference of $\Delta\Phi$ between the Raman lasers leads to rotation of $\Delta\Phi/2$ of the potential surface around the Z -axis.

barrier can be tuned by changing the ratio $\xi = G/B$. This is shown in detail in Fig. 10.9 in Sec. 10.3. The position of the minima can be controlled by changing the width of the lasers. This leads at the same time to a change of the height of the barrier and consequently to a change in the number of trapped states within each well. For a more detailed discussion of the properties of the double well potential, we refer the reader to Sec. 10.3 where a semi-analytical expression for the potential surface is derived. By displacing the center of the laser beams in the X -direction with respect to the Ioffe Pritchard trap, one can create in addition a tilted double well potential.

Figure 10.6 shows the effects of a phase difference between the two excitation lasers on the potential surface. A phase difference $\Delta\Phi$ leads to a rotation of the whole potential surface about the Z -axis by $\Delta\Phi/2$. For a zero phase difference one can add the electric fields of the lasers, resulting in an effective electric field which is polarized linearly along the X -axis, whereas a phase difference of π leads to an effective electric field which is polarized linearly along the Y -axis. In general, a phase difference of $\Delta\Phi$ leads to a rotation of the polarization vector of the total electric field by $\Delta\Phi/2$. The sensitivity of the alignment of the double well potential on the orientation of the polarization vector seems at first glance surprising, given the azimuthal symmetry of a pure Ioffe-Pritchard trap. It is rooted in the spatially varying quantization axis of the Ioffe-Pritchard trap. This issue is analyzed further in Sec. 10.3, to which we refer the reader at this point.

Figure 10.7 shows the potential surface for the same setup as in Fig. 10.6 but for the case of a single σ^- -polarized laser instead of a pair of σ^+/σ^- polarized lasers. The potential is

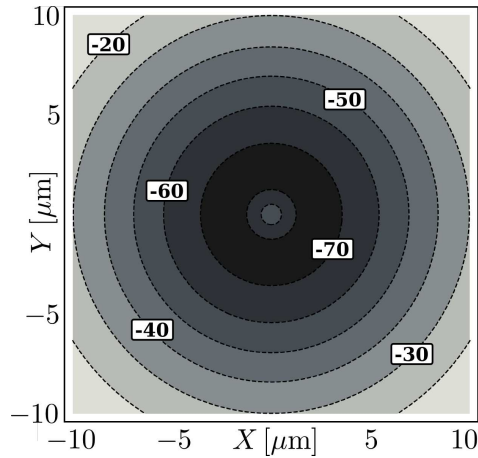


Figure 10.7: Potential surface for the case of a single σ^- polarized laser for $\sigma = 10\mu\text{m}$, $G = 0.1 \text{ G}/\mu\text{m}$, and $B_I = 0.1 \text{ G}$. The potential is ring shaped.

rotationally symmetric with a local maximum at the origin. Therefore it can be used as a ring shaped trap. The absolute value of the potential scales with the laser intensity. Hence, one can increase the height of the barrier by increasing the laser intensity. The position of the local minimum can be varied by changing the ratio B/G or the width of the laser σ .

10.2.3 $m_F = -1$ Component

The potential of the $m_F = -1$ component is dominated by the contribution of the magnetic field and therefore resembles the attractive potential of a pure Ioffe-Pritchard trap, namely a single well with a minimum at the origin. Without lasers, the confinement in the X - and Y -directions is equal, leading to an isotropic potential. The contributions of the lasers break this symmetry, giving rise to a slightly ellipsoidal potential. The value of the eccentricity depends on the intensity of the lasers. A phase difference between the lasers leads to a rotation of the (anisotropic) potential surface about the Z -axis.

10.3 Semi-Analytical Interpretation of the Potential

10.3.1 Principal Axis Transformation

In the previous sections we investigated the system in the laboratory frame of reference where the quantization axis for the atom is determined by the direction of the constant Ioffe field. However, because of the inhomogeneity of the magnetic field, a more adequate description of our system is to define the quantization axis along the *local* magnetic field vector $\mathbf{B}(\mathbf{R})$. In this chapter, we tackle this issue by introducing the spatially dependent unitary transformation

$$U_r = \exp(-i\alpha F_x) \exp(-i\beta F_y) \quad (10.19)$$

that rotates the local magnetic field vector into the z -direction of the laboratory frame of reference with the total spin vector $\mathbf{F} = \mathbf{L} + \mathbf{S} + \mathbf{I}$ consisting of the sum of the electronic orbital angular momentum vector \mathbf{L} , the electronic spin vector \mathbf{S} , and the nuclear spin vector \mathbf{I} .

The corresponding rotation angles are defined by $\sin \alpha = -GY/\sqrt{B^2 + G^2(X^2 + Y^2)}$, $\sin \beta = GX/\sqrt{B^2 + G^2X^2}$, $\cos \alpha = \sqrt{B^2 + G^2X^2}/\sqrt{B^2 + G^2(X^2 + Y^2)}$, and $\cos \beta = B/\sqrt{B^2 + G^2X^2}$. This rotation diagonalizes the magnetic field contribution in Hamiltonian (10.2), giving rise to

$$U_r V^{\text{IP}} U_r^\dagger = g_F \mu_B F_z |\mathbf{B}(\mathbf{R})|. \quad (10.20)$$

Note that in the rotated frame of reference without lasers m_F remains a good quantum number even in the presence of the inhomogeneous Ioffe-Pritchard field. In absence of the Raman lasers, the trapping potentials correspondingly read $V_\kappa = g_F \mu_B m_F |\mathbf{B}(\mathbf{R})|$.

In order to solve the time-dependent Schrödinger equation associated with Hamiltonian (10.2), the Hamiltonian for the atom in the Ioffe-Pritchard trap and the laser interaction must be expressed in the same frame of reference. Hence, the unitary transformation U_r must be applied to V^{AF} as well. We find

$$U_r \mathbf{r} U_r^\dagger = \begin{pmatrix} x \cos \beta + y \sin \alpha \sin \beta - z \cos \alpha \sin \beta \\ y \cos \alpha + z \sin \alpha \\ x \sin \beta - y \sin \alpha \cos \beta + z \cos \alpha \cos \beta \end{pmatrix}. \quad (10.21)$$

Therefore, the σ^+ and σ^- laser transitions that are depicted in Fig. 10.1 become

$$\begin{aligned} \epsilon_\pm \cdot U_r \mathbf{r} U_r^\dagger &= \frac{1}{\sqrt{2}} [x \cos \beta + y \sin \alpha \sin \beta \\ &\quad - z \cos \alpha \sin \beta \pm i(y \cos \alpha + z \sin \alpha)]. \end{aligned} \quad (10.22)$$

Equation (10.22) can be rewritten in terms of the polarization vectors $\tilde{\epsilon}_\pm$ and $\tilde{\epsilon}_0$ defined in the rotated frame of reference, showing that in a Ioffe-Pritchard trap contributions of all polarizations emerge away from the trap center [305–307]. This changes drastically the simple transition scheme caused by the σ^+ and σ^- light as depicted in Fig. 10.1, leading to a spatially dependent coupling between the involved ground- and excited states.

10.3.2 Effective Potential for the $m_F = 0$ Component

For our setup as depicted in Fig. 10.1 and zero relative phase $\Delta\Phi = 0$, the operator describing the interaction between the laser field and the atom reads in the rotated frame of reference

$$\begin{aligned} \hat{O}(X, Y) &\equiv (\epsilon_+ + \epsilon_-) \cdot U_r \mathbf{r} U_r^\dagger \\ &= \sqrt{2}x \cos \beta + \sqrt{2}y \sin \alpha \sin \beta - \sqrt{2}z \cos \alpha \sin \beta. \end{aligned} \quad (10.23)$$

Note that the dependence of $\hat{O}(X, Y)$ on the center of mass coordinates X and Y stems from the dependence of the rotation angles α and β on these coordinates. One finds the following limits. At the origin, the transformation is given by unity, providing $\hat{O}(0, 0) = \sqrt{2}x$, i.e., π -polarized light in the x -direction. For $X = 0$, $\hat{O}(X, Y)$ is invariant under U_r which results in $\hat{O}(0, Y) = \hat{O}(0, 0) = \sqrt{2}x$. For $Y = 0$ and $X \rightarrow \infty$ the gradient field dominates and the operator corresponds to the operator of π -polarized light in the z -direction $\hat{O}(\infty, 0) = \sqrt{2}z$. A non-zero relative phase between the lasers leads to a different polarization of the total electric field in the laboratory frame, giving rise to a rotation of the operators in the rotated frame. This explains the rotation of the potential as seen in Fig. 10.6. Since it is straightforward to

generalize our results to non-zero relative phases, we will restrict our analytical considerations to a zero relative phase in the following.

Within van Vleck perturbation theory as introduced in section 10.1.3, the effective interaction in the rotated frame of reference becomes

$$\begin{aligned} \mathcal{W}_{\beta\alpha} = & \frac{1}{8}\varepsilon(\mathbf{R})^2 \sum_{i,i'=1}^2 \sum_l \langle \beta | \epsilon_i U_r \mathbf{r} U_r^\dagger | l \rangle \langle l | \epsilon_i U_r \mathbf{r} U_r^\dagger | \alpha \rangle \\ & \times \left(\frac{1}{E_\alpha - E_l + \hbar\omega} + \frac{1}{E_\beta - E_l + \hbar\omega} \right), \end{aligned} \quad (10.24)$$

cf. Eq. 10.13. Note, that we assumed once more that the shapes and frequencies of both lasers are identical. We are interested in the regime of large enough magnetic fields (adjustable by the homogeneous Ioffe field component B_I) where the Zeeman splitting overcomes the light shifts of the laser fields, i.e., $|\mathcal{W}_{\beta\alpha}| \ll g_F \mu_B |\mathbf{B}(\mathbf{R})|$. Hence, we can approximate the fully occupied effective interaction matrix $\mathcal{V}^{1P} + \mathcal{W}$ by omitting the off-diagonal matrix elements $\mathcal{W}_{\beta\alpha}, \alpha \neq \beta$, that couple the Zeeman-splittered m_F components. This procedure leaves us with the diagonal matrix elements of the effective interaction,

$$\begin{aligned} \mathcal{W}_{\alpha\alpha} = & \frac{1}{2}\varepsilon(\mathbf{R})^2 \sum_l \left[\cos^2 \beta |\langle \alpha | x | l \rangle|^2 \right. \\ & + \sin^2 \alpha \sin^2 \beta |\langle \alpha | y | l \rangle|^2 \\ & \left. + \cos^2 \alpha \sin^2 \beta |\langle \alpha | z | l \rangle|^2 \right] / (E_\alpha - E_l + \hbar\omega). \end{aligned} \quad (10.25)$$

Employing $|\langle \alpha | x | l \rangle|^2 = |\langle \alpha | y | l \rangle|^2$ and performing the sum over all intermediate states $|l\rangle$ eventually yields for the $m_F = 0$ component the effective potential

$$V_{\text{eff}} = V_0 + \frac{X^2}{\xi^2 + X^2 + Y^2} (V_\infty - V_0), \quad (10.26)$$

where

$$V_0 = - \frac{I(\mathbf{R})}{36c\epsilon_0} \left(\frac{1}{\Delta} + \frac{3}{\Delta + \Delta_{\text{hfs}}} \right) |\langle 5S_{1/2} | |er| |5P_{1/2} \rangle|^2, \quad (10.27)$$

$$V_\infty = - \frac{I(\mathbf{R})}{9c\epsilon_0} \frac{|\langle 5S_{1/2} | |er| |5P_{1/2} \rangle|^2}{\Delta + \Delta_{\text{hfs}}} \quad (10.28)$$

are the light shifts at the origin and in the limit $Y = 0, X \rightarrow \infty$, respectively. $\xi = B/G$ is a length scale characterizing the particular configuration of the Ioffe-Pritchard trap. Numerical comparison of the effective potential (10.26) with the corresponding eigenvalue of the full problem (10.7) shows a excellent agreement for small laser intensities. We observe a maximal relative deviation of less then 1% for $I = 10 \text{ W/m}^2$. For larger intensities, the agreement gets worse since the off-diagonal matrix elements $\mathcal{W}_{\beta\alpha}$ increase in magnitude. However, even for $I = 100 \text{ W/m}^2$ the deviation is less than 5 %.

10.3.3 Discussion of the Effective Potential

The analytical prediction of the effective potential V_{eff} for the $m_F = 0$ component allows us to deduce its basic properties by a simple analysis of Eq. (10.26). The effects of the magnetic field creating the double well potential described in the previous section, are included in the second term in Eq. (10.26). In order to obtain the double well structure this term needs to be negative. This is the case for laser light which is red detuned with respect to the $F = 2$ state and blue detuned with respect to the $F = 1$ state, i.e., $0 > \Delta > -\Delta_{\text{hfs}}$. An interesting case occurs for $\Delta = -\Delta_{\text{hfs}}/4$. Then the offset potential V_0 vanishes and the height of the barrier is equal to the maximal depth of the potential. For $0 > \Delta > -\Delta_{\text{hfs}}/4$ the barrier-height is larger than the depth of the wells with respect to the continuum and for $\Delta_{\text{hfs}} < \Delta < -\Delta_{\text{hfs}}/4$ the height of the barrier is smaller than the depth of the wells with respect to the continuum. In the following, we restrict our investigations again to the case $\Delta = -\Delta_{\text{hfs}}/2$. Since the double well only occurs for $0 > \Delta > -\Delta_{\text{hfs}}$, this choice leads to a maximal detuning with respect to the $F = 1$ and $F = 2$ states. As expected from the numerical solutions provided in section 10.2, V_{eff} shows a double well structure that is centered at the origin. The positions (X_0, Y_0) of the two local minima are given by

$$X_0 = \pm \frac{\xi}{2} \sqrt{\sqrt{1 + 8 \frac{\sigma^2}{\xi^2}} - 3} \quad (10.29)$$

and $Y_0 = 0$. It is obvious from Eq. (10.29) that the double well only exists if the discriminant is positive, giving rise to the condition $\xi < \sigma$. For $\xi > \sigma$ one finds a single well potential, whereas for decreasing $\xi < \sigma$ the double well starts to build up. Starting in the limit $\xi \rightarrow 0$ from a double well with a barrier with finite height but width going to zero, the distance between the minima increases with ξ up to a local maximum $\Delta X_0^{\max} = 2(\sqrt{2} - 1)\sigma$ at $\xi_{\max} = \sqrt{3\sqrt{2} - 4}\sigma$ and decreases for even larger ξ up to $\xi_{\text{cr}} = \sigma$ where the minima vanish, thus transforming the energy surface to a single well potential. This behavior is illustrated in Fig. 10.8a where a contour plot of the effective potential along the X -axis as function of ξ is shown for a fixed width $\sigma = 10 \mu\text{m}$ of the lasers; the dashed line indicates the positions of the minima. Figure 10.8b shows a similar contour plot of the effective potential along the X -axis, but now as a function of σ for fixed $\xi = 1 \mu\text{m}$. In this case, the shape of the barrier close to the origin is approximately conserved but the position of the minima increases with increasing σ .

The height of the barrier is given by $\Delta V = V_{\text{eff}}(0, 0) - V_{\text{eff}}(X_0, 0)$ and is directly proportional to the intensity of the lasers. Figure 10.9 shows the dependence of ΔV on the parameter ξ for different values of σ and fixed laser intensity $I = 10 \text{ W/m}^2$. The behavior of ΔV for different σ is qualitatively very similar: the height of the barrier decreases with increasing ξ monotonically. For fixed ξ , a more narrow laser entails a more shallow double well. Since the range of ξ is determined by the condition $\xi < \sigma$, a more narrow laser necessitates furthermore tighter magnetic traps, i.e., smaller ξ . Note that the positions of the minima do not depend on the intensity of the lasers. Thus, by increasing the laser intensities one can increase the height of the barrier without changing the position of the minima. In this way, the number of trapped states in each well can be controlled.

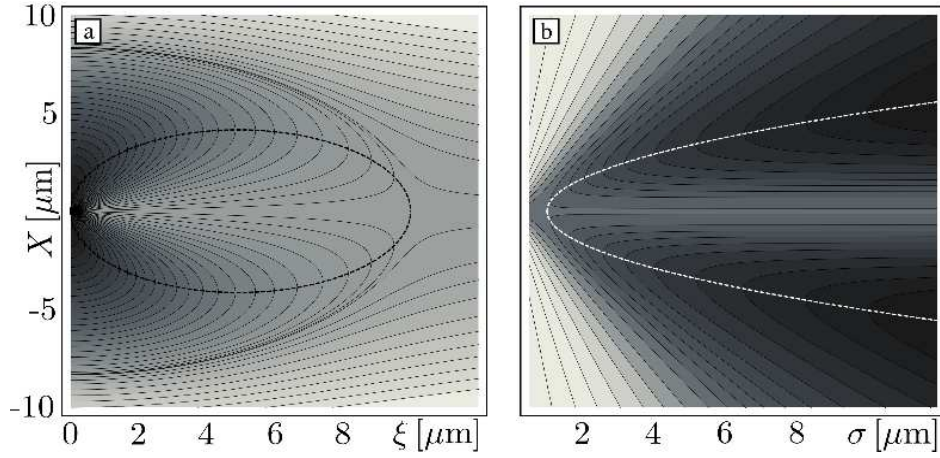


Figure 10.8: (a) Contour plot of the effective potential for $Y = 0$ for fixed $\sigma = 10 \mu\text{m}$ as a function of ξ . With increasing ξ the barrier gets lower and broader. (b) Same potential for fixed $\xi = 1 \mu\text{m}$ and as a function of σ . For $\sigma > \xi$, the shape of the barrier close to the origin is almost conserved. However, the position of the minima increases with increasing σ . In both subfigures, the dashed line indicates the positions of the minima.

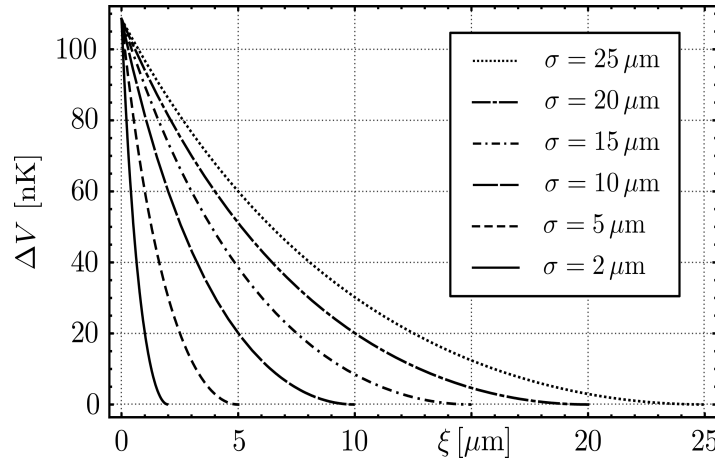


Figure 10.9: Dependence of the height of the barrier ΔV on ξ for different σ . For increasing ξ the height of the barrier decreases monotonically.

10.3.4 Effective Potential for a Single Laser

One can use the same semi-analytical procedure as above in order to predict the effective potential for a single laser. One finds

$$V_{\text{eff}}^1 = \frac{1}{2}V_0 + \frac{1}{8} \left(1 - \frac{\xi^2}{\xi^2 + R^2} \right) V_\infty \quad (10.30)$$

where $R^2 = X^2 + Y^2$. The comparison of the effective potential (10.30) and the corresponding numerical solutions shows again an excellent agreement. As opposed to the Raman setup involving two lasers, in the case of a single laser the resulting trapping potential for the $m_F = 0$ component is rotationally symmetric. The ring-shaped minimum is located at

$$R_0 = \sqrt{-\frac{5}{6}\xi^2 + \frac{1}{6}\xi^2\sqrt{1 + 12\sigma^2\xi^2}} \quad (10.31)$$

and exists for $\sigma > \sqrt{2}\xi$. Starting at a barrier with arbitrarily small width with maximal height for $\xi \rightarrow 0$, the barrier at the origin gets lower as ξ increases and eventually vanishes as $\xi = \sigma/\sqrt{2}$. The distance of the minimum to the origin increases with ξ up to the local maximum at $\xi_{\text{max}} = \sqrt{5\sqrt{3}/2 - 6\sigma}$ with a value $R_{\text{max}} = (\sqrt{3} - \sqrt{2})\sigma$. Then it decreases again and becomes zero at $\xi_{\text{cr}} = 1/\sqrt{2}\sigma$ thereby transforming the potential into a single well. Note that the potential is not a simple superposition of a magnetic single well potential and a repulsive potential created by the laser. The spatial structure is a direct consequence of the spatially dependent light shift potential of the laser, giving rise to a barrier which is smaller than the width of the laser.

10.4 Loss Mechanisms

In the previous sections we have shown that for appropriate parameters the discussed combination of external fields leads to a confinement for two components of the ground state manifold. Let us discuss in this section possible loss mechanism for these potentials.

10.4.1 Lifetime of the Intermediate State

One loss channel results from the coupling of the ground manifold of states to the excited $5P_{1/2}$ states. Despite the fact that the Raman lasers are detuned with respect to the excited state, there is a finite probability to excite the atom to this state due to the width of the state and the width of the lasers. The excited atom can subsequently decay spontaneously to the untrapped ground state. The resulting lifetime of the dressed state can be estimated by applying perturbation theory, leading to $\tau_{\text{eff}} = \tau(\Delta/\omega_{\text{cp}})^2$ with τ being the lifetime of the unperturbed excited state and ω_{cp} the coupling matrix element of the ground state to the excited state. For our parameters ($\Delta = -\Delta_{\text{hfs}}/2$, $I_1 = I_2 = 10 \text{ W/m}^2$, and $\tau = 27 \text{ ns}$) we get an effective lifetime of $\tau_{\text{eff}} \sim 27 \text{ ms}$. The latter can be increased by decreasing the intensities of the lasers. However, one has to bear in mind that this will reduce the depth of the trapping potentials as well.

10.4.2 Inelastic Collisions

Another loss mechanism occurs if more than one atom is loaded into the potential due to the mutual interaction of the atoms. This mechanism can be estimated on a mean field level, incorporating an effective coupling coefficient that determines the interaction between the atoms. In the field-free case one gets a population transfer from one component to another due to interaction when there is an overlap between the wave functions of two components. For our setup, however, one obtains new dressed states that are superpositions of the field-free states. Hence, one obtains a state changing contribution due to interaction even if only one dressed state is occupied. However, for the above discussed parameters this additional term can be neglected.

10.5 Conclusions and Physical Applications

We investigated the trapping potentials for ^{87}Rb ground state atoms simultaneously exposed to a magnetic trap in a Ioffe-Pritchard like configuration and an optical trap in a Raman setup. The Raman lasers were detuned between the two excited $5P_{1/2}$ hyperfine states, the $F = 1$ and the $F = 2$ state. By varying the offset field of the Ioffe-Pritchard trap, we demonstrated that the trapping potential of the $m_F = 0$ component can be tuned from a rotationally symmetric single well to a double well trap; in the intermediate regime, one finds a cigar shaped trapping potential. By applying a phase difference between the two Raman lasers, the resulting trapping potentials can be rotated about the propagation direction of the laser beams. A semi-analytical formula for the potential surfaces has been derived. All relevant properties of the double well potential have been determined analytically as a function of the various trap parameters. For a single excitation laser, the proposed scheme results in a ring-shaped trap for the $m_F = 0$ component.

In order to exploit the unique features of the above discussed potentials, one can think of various experiments. For example, one might trap the $m_F = 0$ component in a double well potential which gives for the $m_F = -1$ component a single well potential located at the center of the barrier. For an asymmetric occupation of the wells one can then observe tunneling of atoms trapped in the double well potential through the atoms trapped in the single well potential. The oscillation frequency of the tunneling can thus be investigated as a function of the occupation number of the second component located at the barrier, which is reminiscent of a single atom transistor [308]. We performed corresponding numerical simulations of the Spinor Gross Pitaevskii equation and observed indeed an increase of the oscillation period with increasing occupation number of the second component.

In a similar setup as mentioned above (one component is exposed to a double well potential with a narrow barrier and one component to single well potential centered at the position of the barrier) one might trap atoms in the component exposed to the single well potential and then transfer all atoms by an rf-pulse in the “double-well” component that feels a sharp potential maximum at this point. Depending on the energy of the atoms the condensate wave function would consequently either split into two parts or the whole wave function would move into one direction, which could be used as a test of the validity of the Gross Pitaevskii equation [309]. Moreover, the possibility to rotate an anisotropic single well trap (which arises for the $m_F = -1$ component) opens up a new possibility to study superfluids under rotation [5, 146, 310]. The possibility to rotate the double well potential

allows one to create an effective ring potential by rotating the potential fast enough so that the atoms feel a time averaged potential [295]. In this way the transition of a double well to a ring-shaped potential can be investigated. Moreover, one can exploit the feature that one can drive the potential surface of the $m_F = 0$ component by modulating the Ioffe field strength to investigate non-equilibrium driven systems [311, 312].

Chapter 11

Conclusions

One focal point of this thesis is the investigation of effects of a spatially inhomogeneous scattering length on Bose Einstein condensates for various setups. Due to recent experimental progress in controlling the scattering length on a nanometer length scale [79] studying effects of a spatially inhomogeneous scattering length has become a contemporary issue. Firstly, we demonstrate the effects of a spatially inhomogeneous scattering length on quasi-one-dimensional condensates trapped in a double-well potential. The corresponding bifurcation diagram depicting the stationary states depends crucially on the strength of the nonlinearity. Moreover, the threshold of transition from Josephson matter-wave oscillation to nonlinearly induced self-trapping is shifted due to the collisionally inhomogeneity. We developed an adjusted two-mode model which describes these effects accurately.

In a second step, we explore the effects of a collisionally inhomogeneity on dark and bright matter-wave solitons. By applying a relevant transformation the problem of a spatially dependent nonlinear problem is converted into one of spatially uniform nonlinearity, at the expense of introducing two perturbative terms: One of the form of a linear potential, while the other constitutes a non-potential type of perturbation, being proportional to the spatial derivative of the field. We focus on the case where the previous one vanishes thus the pure effects of the non-standard terms are reflected. Applying soliton perturbation theory allows us to derive simple ordinary differential equations describing the time evolution of the solitons.

It has been shown that modulating the interaction can be used to stabilize vortices against excitations due to finite temperature effects. This can be extremely useful for setups which require stable vortex states for a long period of time as, e.g., in the recent work of Ref. [278] which suggests the use of a superposition of two counter rotating Bose Einstein condensates as a gyroscope.

A second focal point of this thesis was the investigation of coherent excited states of Bose Einstein condensates, i.e., solitonic and vortex states. The existence and stability of single and multiple dark soliton states in quasi-one-dimensional condensates trapped in a double-well potential has been investigated systematically. An important finding of our analysis is that the optical lattice (which sets the barrier in the double-well setting) results in the emergence of nonlinear states that do not have a linear counterpart, such as dark soliton states, with solitons located in one well of the double-well potential. Such a study is particularly relevant, as many dark solitons can be experimentally created by means of the matter-wave interference method, as demonstrated in Refs. [110, 112]. By applying soliton perturbation theory we derived effective potentials for describing the motion of the solitons.

In a second step single and multiple vortex states in quasi-two-dimensional condensates have been investigated. We illustrated the connection of dark soliton stripes and multiple vortex states. A systematic cascade of bifurcations from the former state into aligned vortex clus-

ters (or crystals) has been unveiled. The symmetry-breaking, supercritical pitchfork nature of the bifurcations was elucidated and a few-mode expansion was employed to identify the corresponding critical points. Using a quasi-particle approach we were able to predict the motion of multiple vortices on an inhomogeneous background by simple ordinary differential equations. This approach not only allowed the identification of the equilibrium positions of the vortex clusters, but also assisted in the formulation of the vortex linearization problem and the analytical approximation of the vortex epicyclic near-equilibrium motions, e.g., for the vortex dipole, as well as that of the unstable eigenmodes of states such as the tripole. We have explored the time evolution of vortex dipole states with the vortices being located at different position and confirmed the validity of the ordinary differential equations. These results turn out to be extremely relevant due to the recent experimental observation of robust vortex dipoles [190, 191] and three-vortex states [192].

As an extension to the investigations of dark and bright solitons, we have studied dark bright solitons in two component Bose Einstein condensates. Stable dark bright solitons were observed experimentally [108], leading to a renewed interest in this area. A dark bright soliton is a symbiotic object consisting of a dark soliton in one component and a bright soliton in the other component and does not exist in single component Bose Einstein condensates. We have demonstrated a strong dependence of the oscillation frequency of the dark bright soliton in a trapped condensate on the atom number of the individual components (N_D , N_B). Varying the atom number of either the dark or the bright component, we find that in a harmonic trap the soliton oscillation period may change by nearly one order of magnitude; most notably, the bright component is shown to slow down the oscillation of the dark one. Our investigation revealed a feature absent in the dark soliton dynamics in one-component Bose Einstein condensates, namely that a single dark bright soliton may become dynamically unstable. Increasing N_D and N_B , the occupation numbers of the dark and bright component, respectively, reveals a deviation from the effective 1D description: specifically, an increase of N_D leads to a spontaneous breaking of the cylindrical symmetry, manifested in a transversal oscillation of the bright component, and a subsequent decrease of the axial dark bright oscillation frequency. Moreover, we analyzed the interaction between multi-dark bright solitons and observed a strong phase dependence of the collisional dynamics of dark bright solitons.

In an independent project of this thesis a specific method for trapping of ultracold atoms has been developed. We depicted a way of trapping magnetically insensitive atoms by inter atomic collisions with atoms of the same species which are trapped magnetically. Hyperfine state changing collisions, and therefore loss of the trapped atoms, were shown to be strongly inhibited in case of a low density of the confined atomic cloud. We monitored the transition from a 'soft' to a 'hard' effective potential by studying the backaction of the trapped atoms onto the condensate which provides their confinement. The controlled outcoupling of the trapped atoms by shaping the condensate's wave function was explored leading to a pulsed emission of atoms from the trapping region reminiscent of an atom laser.

Moreover, we have presented a way of trapping atoms by applying near resonant laser light in a Raman configuration on magnetic traps leading to versatile atom traps. The emerging potential surfaces are widely tunable and can be used for trapping two internal states. By varying an offset magnetic field, the trapping potential of the former magnetically insensitive component can be tuned from a rotationally symmetric single well to a double-well trap; in the intermediate regime, one finds a cigar shaped trapping potential. By applying a phase difference between the two Raman lasers, the resulting trapping potentials can be

rotated about the propagation direction of the laser beams. A semi-analytical formula for the potential surfaces has been derived. All relevant properties of the double-well potential have been determined analytically as a function of the various trap parameters.

There are various directions to which one can continue the studies of this thesis motivated by recent developments. Due to the experimental observation of multiple dark bright solitons and their collisions [287] it is relevant to extend the quasi-particle description we used for describing dark solitons to dark bright solitons. Thereby one can derive at first effective equations of motions describing the motion of dark bright solitons on an inhomogeneous background. In a second step one could include an interaction potential for the mutual scattering of dark bright soliton in a similar way as we did for dark solitons. Subsequently, it would be natural to investigate the existence and stability of multiple dark bright soliton states. Moreover, it is extremely relevant to connect the findings concerning the vortex dipoles and their motion to the recent experimental findings [190, 191]. This includes comparisons of the fixed points and of the trajectories of the vortices. Moreover, one can extend the bifurcation diagram showing the occurrence of vortex states from dark soliton stripes into various directions. On the one hand one can include states with multiple dark solitons stripes. On the other hand one can include ring dark soliton states as well. Taking into account these states and importantly the state bifurcating from these states should provide a complete picture of the occurrence and stability of multiple vortex states in the case of non-rotating traps. Another direction would be to include non-stationary states with a running phase as the state described in Ref. [192]. A further direction of experimental relevance would be a systematic study of the effects of anisotropic traps on the stability multi vortex states. First results suggest that a slightly anisotropic trap can stabilize or destabilize aligned multi vortex states depending on the orientation of the aligned vortex state.

As higher dimensional generalizations of dark bright solitons one can investigate vortex bright solitons, i.e., symbiotic objects consisting of a vortex in one component and a bright soliton in the other component. The proof of existence of these symbiotic objects was already granted in Ref. [218]. However, extremely interesting would be the investigation of the existence and stability of dipole states consisting of vortex bright solitons. Subsequently, one can derive equations of motions for vortex bright solitons in a similar fashion as for vortices and solitons.

Appendix A

Numerical Methods for Solving the Gross Pitaevskii Equation

One of the central equations in this thesis is the 1D GPE

$$i\hbar \frac{\partial f(z, t)}{\partial t} = \left[-\frac{\hbar^2}{2M} \frac{\partial^2}{\partial z^2} + V(z) + g_{1D} |f(z, t)|^2 \right] f(z, t), \quad (\text{A.1})$$

where the transversal coordinates have been integrated out and $V(z)$ is the axial potential. In this appendix we discuss methods for solving the 1D GPE. Generalizations of these methods to the 2D and 3D GPE are in principle straightforward, however one has to bear in mind that the numerical efforts increases drastically for higher dimensions. It is convenient to rescale Eq. (A.1) in order to make it dimensionless. Therefore we measure lengths in units of a_{scal} and frequencies in $\omega_{\text{scal}} = \frac{\hbar}{Ma_{\text{scal}}^2}$, i.e., $t' = \omega_{\text{scal}}t$, $z' = z/a_{\text{scal}}$. Energy is correspondingly measured in units of $\hbar\omega_{\text{scal}}$. Note, one often chooses as scaling length the harmonic oscillator length in the transversal or axial direction. Omitting the primes leads to the dimensionless Eq.

$$i \frac{\partial f(z, t)}{\partial t} = \left[-\frac{1}{2} \frac{\partial^2}{\partial z^2} + V(z) + g|f(z, t)|^2 \right] f(z, t). \quad (\text{A.2})$$

A.1 Representing the Derivative Term

Let us discuss in this section two possible ways of representing the derivative term. The problem of representing the derivative term is not restricted to nonlinear equations but occurs in many quantum mechanical problems. The easiest way to deal with the derivative term is to represent the wave function on a grid and represent the derivation using finite differences

$$\partial_z^2 f \rightarrow (f_{n-1} - 2f_n + f_{n+1})/\Delta^2, \quad (\text{A.3})$$

where Δ is the spacing between the grid points and f_n is the wave function at the grid point n . The advantage of using finite differences is that the derivative term is represented by a band matrix and has got an easy representation. The drawback is that the spacing between the grid points Δ needs to be small for an accurate representation of the derivative.

Another possible representation of the derivative term can be achieved by using a Discrete Variable Representation (DVR) [313]. For this purpose one represents the wave function as a linear combination of given interpolation functions ϕ_n

$$f(z) \approx \sum_{n=0}^{N-1} a_n \phi_n(z) \quad (\text{A.4})$$

in such a way that for given points $z_i = z_0, \dots, z_N$

$$f(z_i) = \sum_{n=0}^{N-1} a_n \phi_n(z_i). \quad (\text{A.5})$$

This allows an exact representation of the derivative term of the interpolated wave function (A.4) for differentiable functions ϕ_n . The advantage of this representation is that one needs less grid points in comparison to the case of finite differences. The drawback is that the derivative term is in this case represented by a fully occupied matrix. Moreover, one needs to approximate the representations of the potential terms and has to divide the wave function by spatial dependent weights resulting in more complicated numerical codes. For a detailed discussion of DVRs we refer the interested reader to the appendix of Ref. [313]. In this work we use both representations for the derivative term. Of course, the results do not depend on the kind of the representation. Therefore this is a good test for the convergence of the grid, i.e., whether the spacing of the grid is fine enough in the case of finite differences or whether one has taken enough basis functions in the case of a DVR. In the following we assume that the derivative term is in one of the above representations.

A.2 Time Propagation

Let us at this point discuss how one can propagate a given wave function in time using Eq. (A.2). In the case of linear differential equations, one can 'simply' integrate the right hand side of the equation and obtains thus a solution. The so-called predictor-corrector methods apply a similar scheme. We present here schematically how these work. For a more detailed description we refer to Ref. [314]. In order to obtain the wave function at the next time step, predictor-corrector methods integrate the right hand side of the equation and use for the nonlinear term the wave function of the current time step. This is called the predictor step. Since the wave function at the 'wrong' time is used in the nonlinear term a corrector step is performed afterwards, i.e., the same step is calculated with the wave function resulting from the predictor step as input in the nonlinear term. The resulting wave function serves as new result of the predictor step. This iterative scheme is continued until convergence of the wave function of the predictor and corrector step is reached. We used in this work the Adams-Bashforth-Moulton predictor corrector method.

Alternatively, we use a standard Runge-Kutta method for time integration. In the Runge Kutta algorithm the right hand side of the equation is treated as a function and evaluated at different points in time (cf. Ref. [314] for a detailed description and a possible way of implementation).

A.3 Methods for Finding Eigenstates

Moreover we are interested in eigenstates of Eq. (A.2), i.e., states of the form

$$f(z, t) = \exp(-\imath \mu t) f(z) \quad (\text{A.6})$$

with $f(z)$ being a time independent function. We have chosen the same name for the time dependent and the time independent function. However it should be clear from the context which function is referred to.

A.3.1 Relaxation

Relaxation or imaginary time propagation can be used to find the ground state of an equation. It makes use of the fact that the ground state is the lowest energy state. As the name indicates one replaces for imaginary time propagation the time variable by the imaginary unit times the time variable and propagates the corresponding equation. As initial state for the time propagation one should choose a state looking similar to the expected ground state, however this is not necessary but reduces the time needed for finding the ground state. The only condition the initial state must fulfill is that the state is not orthogonal to the ground state. Then one can represent the initial state in the basis of the eigenstates $f_i(z, t)$

$$\psi(z, t) = \sum_i c_i(t) f_i(z, t) \quad (\text{A.7})$$

with non-zero c_0 for f_0 being the ground state. The time evolution of the eigenstates obey Eq. (A.6). Consequently, one obtains by replacing $t \rightarrow -i\tau$

$$f_j(z, \tau) = \exp(-\mu_j \tau) f_j(z). \quad (\text{A.8})$$

This leads to an exponential damping of the coefficients. Note, the differential equation in imaginary time does not conserve the norm of the wave function. Therefore one has to renormalize the wave function after every (imaginary) time-step. However, importantly the damping scales with the energy μ_j of the eigenstate. Therefore the contributions of states with higher energy get damped out earlier and one obtains after a certain time only contributions of the lowest energy state, i.e., the ground state. It is worth mentioning that one can obtain higher excited states as well by either projecting out the ground state (which is possible if the ground state is perpendicular to the excited state) or shifting the energy in such a way that the excited state becomes the lowest energy state. The drawback of relaxation is that it takes rather long to obtain the eigenstate and getting excited states is complicated. The advantage is that relaxation is easy to implement.

A.3.2 The Newton Algorithm

Let us present now a much faster and more elegant way of obtaining eigenfunctions. Using Eq. (A.6) we can rewrite Eq. (A.2) as a root finding problem

$$F[f(z)] = 0 \quad (\text{A.9})$$

with

$$F[f(z)] = \left[-\frac{1}{2} \frac{\partial^2}{\partial z^2} + V(z) + g|f(z)|^2 - \mu \right] f(z). \quad (\text{A.10})$$

An effective way to solve such a root finding problem is the Newton algorithm. Note, F is a functional $F[f]$. So, if one represents f on a grid F will depend on a vector. The Newton

algorithm is then given by

$$f(z)^{(n+1)} = f(z)^{(n)} - (J[f(z)^{(n)}])^{-1} F[f(z)^{(n)}] \quad (\text{A.11})$$

with the Jacobian matrix $J[f^{(n)}]$ defined as

$$J[f(z)^{(n)}] = \frac{\partial F[f(z)^{(n)}]}{\partial f(z)^{(n)}} \quad (\text{A.12})$$

$$= -\frac{1}{2} \frac{\partial^2}{\partial z^2} + V(z) - \mu + 3g|f(z)^{(n)}|^2 \quad (\text{A.13})$$

Thereby we can determine the Jacobian matrix for given $f^{(n)}$ and μ . This allows us to find an eigenstate of Eq. (A.2) for fixed chemical potentials μ . One varies the shape and the norm of f in order to obtain a solution. The numerical efforts lies in the inversion of the Jacobian and the multiplication of the corresponding matrix with the functional F . The hard thing from the physical perspective is finding an initial state that converges to the eigenstate one is looking for.

Appendix B

Numerical Methods for Solving the Vector Gross Pitaevskii Equation

In chapter 8 we derived the following system of equations

$$i\hbar \frac{\partial f_k(z, t)}{\partial t} = \left[-\frac{\hbar^2}{2M} \frac{\partial^2}{\partial z^2} + V(z) + \mu_{\perp k} \right] f_k(z, t) \quad (\text{B.1})$$

$$\mu_{\perp k} = \frac{\hbar^2}{2M} \sigma_k^{-2} + \frac{1}{2} M \omega_{\perp}^2 \sigma_k^2 + g_{kk} \frac{|f_k(z, t)|^2}{2\pi} \sigma_k^{-2} + g_{12} \frac{|f_{3-k}(z, t)|^2}{\pi(\sigma_1^2 + \sigma_2^2)} \quad (\text{B.2})$$

$$\sigma_k^4 = \frac{\hbar^2}{\omega_{\perp}^2 M^2} + g_{kk} \frac{|f_k(z, t)|^2}{\pi M \omega_{\perp}^2} + 2g_{12} \frac{|f_{3-k}(z, t)|^2}{\pi M \omega_{\perp}^2 (\sigma_1^2 + \sigma_2^2)^2} \sigma_k^4 \quad (\text{B.3})$$

for $k = 1, 2$; with the axial trapping potential $V(z) = \frac{1}{2} M \omega^2 z^2$, the transversal trap frequency ω_{\perp} and the coupling coefficients g_{ij} describing the interatomic collisions. In this appendix we demonstrate different ways of solving the above system of Eqs. and derive the corresponding BdG equations. Let us at first rescale the Eqs. in order to make them dimensionless. We rescale lengths by a_{scal} , frequencies by $\omega_{\text{scal}} = \frac{\hbar}{Ma_{\text{scal}}^2}$ and energies by $\hbar\omega_{\text{scal}}$, i.e., $t' = \omega_{\text{scal}} t$, $z' = z/a_{\text{scal}}$, $\mu'_{\perp k} = \mu_{\perp k}/\hbar\omega_{\text{scal}}$. Omitting the primes leads to the dimensionless Eqs.

$$i \frac{\partial f_k(z, t)}{\partial t} = \left[-\frac{1}{2} \frac{\partial^2}{\partial z^2} + \frac{1}{2} \omega^2 z^2 + \mu_{\perp k} \right] f_k(z, t) \quad (\text{B.4})$$

$$\mu_{\perp k} = \frac{1}{2} \sigma_k^{-2} + \frac{1}{2} \omega_{\perp}^2 \sigma^2 + 2a_{kk} |f_k(z, t)|^2 \sigma_k^{-2} + 4a_{12} \frac{|f_{3-k}(z, t)|^2}{\sigma_1^2 + \sigma_2^2} \quad (\text{B.5})$$

$$\sigma_k^4 = \frac{1}{\omega_{\perp}^2} + 4a_{kk} \frac{|f_k(z, t)|^2}{\omega_{\perp}^2} + 8 \frac{a_{12} |f_{3-k}(z, t)|^2}{\omega_{\perp}^2} \frac{\sigma_k^4}{(\sigma_1^2 + \sigma_2^2)^2}. \quad (\text{B.6})$$

B.1 Methods for Finding Eigenstates

We are interested in eigenstates of Eq. (B.4), i.e., states of the form

$$f_k(z, t) = \exp(-i\mu_k t) f_k(z) \quad (\text{B.7})$$

with $f_k(z)$ being a time independent function. We have chosen the same name for the time dependent and the time independent function. However, it should be clear by the context which function is referred to. In the following we omit the arguments of the wave functions.

B.1.1 Relaxation

Probably the easiest way for finding eigenstates of Eqs. (B.4-B.6) is to use relaxation. Therefore one propagates the equation in imaginary time leading to a damping of the modes corresponding to the different eigenstates which depends on the energy of the eigenstate (cf. Appendix A). We performed the imaginary time propagation by the Adams-Basforth-Moulton predictor-corrector method. The drawback of relaxation is that it is rather slow and it is hard to obtain excited states. We used relaxation to benchmark our results obtained by the Newton solvers described below.

B.1.2 The Newton Algorithm

Using Eq. (B.7) we can rewrite Eq. (B.4) as a root finding problem

$$F_k = 0 \quad (\text{B.8})$$

with

$$F_k = \left(-\frac{1}{2} \frac{\partial^2}{\partial z^2} + \frac{1}{2} \omega^2 z^2 + \mu_{\perp k} - \mu_k \right) f_k \quad (\text{B.9})$$

An effective way to solve such an Eq. is the Newton algorithm.

$$f^{(n+1)} = f^{(n)} - (J[f_1^{(n)}, f_2^{(n)}])^{-1} F[f_1^{(n)}, f_2^{(n)}] \quad (\text{B.10})$$

where $f = (f_1, f_2)^\top$ and $F = (F_1, F_2)^\top$. One has to take into account that $\mu_{\perp k}$ depends on σ_k which itself depends on f_k . The Jacobian matrix is defined as

$$J_{i,j} = \frac{\partial F_i}{\partial f_j} \quad (\text{B.11})$$

with $i, j = 1, 2$ and reads

$$J(i, i) = -\frac{1}{2} \frac{\partial^2}{\partial z^2} + \frac{1}{2} \omega^2 z^2 + \mu_{\perp i} - \mu_i + f_i \frac{\partial \mu_{\perp i}}{\partial f_i} \quad (\text{B.12})$$

$$J(1, 2) = f_1 \frac{\partial \mu_{\perp 1}}{\partial f_2} \quad (\text{B.13})$$

$$J(2, 1) = f_2 \frac{\partial \mu_{\perp 2}}{\partial f_1}. \quad (\text{B.14})$$

Here we assume that the derivative term is in one of the matrix representation discussed in appendix A. There is no obvious mathematical reason that the Jacobian matrix is symmetric. However from a physical point of view it should be. Evaluation of the partial derivatives of μ_{\perp} with respect to f_k yields

$$\begin{aligned} \frac{\partial \mu_{\perp 1}}{\partial f_1} &= \left(-\frac{1}{\sigma_1^3} + \omega_{\perp}^2 \sigma_1 - 4a_{11} \frac{|f_1|^2}{\sigma_1^3} \right) \frac{\partial \sigma_1}{\partial f_1} + 4a_{11} \frac{f_1}{\sigma_1^2} \\ &\quad - 8a_{12} \frac{|f_2|^2}{(\sigma_1^2 + \sigma_2^2)^2} \left(\sigma_1 \frac{\partial \sigma_1}{\partial f_1} + \sigma_2 \frac{\partial \sigma_2}{\partial f_1} \right) \end{aligned} \quad (\text{B.15})$$

$$\begin{aligned} \frac{\partial \mu_{\perp 2}}{\partial f_2} = & \left(-\frac{1}{\sigma_2^3} + \omega_{\perp}^2 \sigma_2 - 4a_{22} \frac{|f_2|^2}{\sigma_2^3} \right) \frac{\partial \sigma_2}{\partial f_2} + 4a_{22} \frac{f_2}{\sigma_2^2} \\ & - 8a_{12} \frac{|f_1|^2}{(\sigma_1^2 + \sigma_2^2)^2} \left(\sigma_1 \frac{\partial \sigma_1}{\partial f_2} + \sigma_2 \frac{\partial \sigma_2}{\partial f_2} \right) \end{aligned} \quad (\text{B.16})$$

$$\begin{aligned} \frac{\partial \mu_{\perp 1}}{\partial f_2} = & \left(-\frac{1}{\sigma_1^3} + \omega_{\perp}^2 \sigma_1 - 4a_{11} \frac{|f_1|^2}{\sigma_1^3} \right) \frac{\partial \sigma_1}{\partial f_2} + 8a_{12} \frac{f_2}{\sigma_1^2 + \sigma_2^2} \\ & - 8a_{12} \frac{|f_2|^2}{(\sigma_1^2 + \sigma_2^2)^2} \left(\sigma_1 \frac{\partial \sigma_1}{\partial f_2} + \sigma_2 \frac{\partial \sigma_2}{\partial f_2} \right) \end{aligned} \quad (\text{B.17})$$

$$\begin{aligned} \frac{\partial \mu_{\perp 2}}{\partial f_1} = & \left(-\frac{1}{\sigma_2^3} + \omega_{\perp}^2 \sigma_2 - 4a_{22} \frac{|f_2|^2}{\sigma_2^3} \right) \frac{\partial \sigma_2}{\partial f_1} + 8a_{12} \frac{f_1}{\sigma_1^2 + \sigma_2^2} \\ & - 8a_{12} \frac{|f_1|^2}{(\sigma_1^2 + \sigma_2^2)^2} \left(\sigma_1 \frac{\partial \sigma_1}{\partial f_1} + \sigma_2 \frac{\partial \sigma_2}{\partial f_1} \right). \end{aligned} \quad (\text{B.18})$$

So, what remains to be done, is to determine the partial derivatives of σ_k with respect to f_k . These can be calculated by differentiation of Eq. (B.6) with respect to f_k leading to the following systems of equations

$$\begin{aligned} \frac{2a_{11}f_1}{\sigma_1^3 \omega_{\perp}^2} = & \left(1 + 8 \frac{a_{12}|f_2|^2}{\omega_{\perp}^2} \frac{\sigma_1^2}{(\sigma_1^2 + \sigma_2^2)^3} - 8 \frac{a_{12}|f_2|^2}{\omega_{\perp}^2} \frac{1}{(\sigma_1^2 + \sigma_2^2)^2} \right) \frac{\partial \sigma_1}{\partial f_1} \\ & + 8 \frac{a_{12}|f_2|^2}{\omega_{\perp}^2} \frac{\sigma_1 \sigma_2}{(\sigma_1^2 + \sigma_2^2)^3} \frac{\partial \sigma_2}{\partial f_1} \end{aligned} \quad (\text{B.19})$$

$$\begin{aligned} \frac{4a_{12}\sigma_2 f_1}{(\sigma_1^2 + \sigma_2^2)^2 \omega_{\perp}^2} = & \left(1 + 8 \frac{a_{12}|f_1|^2}{\omega_{\perp}^2} \frac{\sigma_2^2}{(\sigma_1^2 + \sigma_2^2)^3} - 8 \frac{a_{12}|f_1|^2}{\omega_{\perp}^2} \frac{1}{(\sigma_1^2 + \sigma_2^2)^2} \right) \frac{\partial \sigma_2}{\partial f_1} \\ & + 8 \frac{a_{12}|f_1|^2}{\omega_{\perp}^2} \frac{\sigma_1 \sigma_2}{(\sigma_1^2 + \sigma_2^2)^3} \frac{\partial \sigma_1}{\partial f_1} \end{aligned} \quad (\text{B.20})$$

$$\begin{aligned} \frac{4a_{12}\sigma_1 f_2}{(\sigma_1^2 + \sigma_2^2)^2 \omega_{\perp}^2} = & \left(1 + 8 \frac{a_{12}|f_2|^2}{\omega_{\perp}^2} \frac{\sigma_1^2}{(\sigma_1^2 + \sigma_2^2)^3} - 8 \frac{a_{12}|f_2|^2}{\omega_{\perp}^2} \frac{1}{(\sigma_1^2 + \sigma_2^2)^2} \right) \frac{\partial \sigma_1}{\partial f_1} \\ & + 8 \frac{a_{12}|f_2|^2}{\omega_{\perp}^2} \frac{\sigma_1 \sigma_2}{(\sigma_1^2 + \sigma_2^2)^3} \frac{\partial \sigma_2}{\partial f_1} \end{aligned} \quad (\text{B.21})$$

$$\begin{aligned} \frac{2a_{22}f_2}{\sigma_2^3 \omega_{\perp}^2} = & \left(1 + 8 \frac{a_{12}|f_1|^2}{\omega_{\perp}^2} \frac{\sigma_2^2}{(\sigma_1^2 + \sigma_2^2)^3} - 8 \frac{a_{12}|f_1|^2}{\omega_{\perp}^2} \frac{1}{(\sigma_1^2 + \sigma_2^2)^2} \right) \frac{\partial \sigma_2}{\partial f_1} \\ & + 8 \frac{a_{12}|f_1|^2}{\omega_{\perp}^2} \frac{\sigma_1 \sigma_2}{(\sigma_1^2 + \sigma_2^2)^3} \frac{\partial \sigma_1}{\partial f_1}. \end{aligned} \quad (\text{B.22})$$

Eqs. (B.19-B.22) represent a coupled system of equations for the partial derivatives of σ_k , which can be solved easily for given σ_k and f_k . Moreover, σ_k can be determined by applying Eq. (B.6) for given f_k using a standard Newton algorithm. As initial guess for the Newton algorithm one can use the solution for $g_{11} = g_{22} = g_{12} = g$ and assume $\sigma_1 = \sigma_2$ leading to

$$\sigma_k^{\text{appr}} = a_{\text{ho}} \sqrt[4]{1 + 4a(|f_1|^2 + |f_2|^2)}, \quad (\text{B.23})$$

where $a_{\text{ho}} = \sqrt{1/(\omega_{\perp})}$ is the dimensionless harmonic oscillator length in the transversal direction. Thus we can determine the Jacobian matrix for a given f_k and use the Newton

algorithm (B.10) to determine a solution of Eq. (B.8) whereby we have to update σ_k and its derivatives in each step. This allows us to find an eigenstate of Eq. (B.4) for fixed chemical potentials μ_1, μ_2 .

B.1.3 Newton Augmented

In most experimental situations it is easier to determine the number of atoms than the chemical potential. Therefore it is useful to have a method which determines the eigenstate for a fixed number of atoms instead of a fixed chemical potential. This can be realized by adding Lagrangian multipliers in the above scheme. Let us assume that the functional F_k can be derived from a Lagrangian L in the following way

$$F_k = \frac{\partial L(f_1, f_2)}{\partial f_k}. \quad (\text{B.24})$$

Then we have to augment the Lagrangian by the additional conditions

$$L_{\text{aug}}(f_1, f_2, \tilde{\mu}_1, \tilde{\mu}_2) = L(f_1, f_2) + \tilde{\mu}_1 \left(\int |f_1|^2 dz - N_1 \right) + \tilde{\mu}_2 \left(\int |f_2|^2 dz - N_2 \right), \quad (\text{B.25})$$

leading to the new functionals

$$F_{\text{aug}1} = F_1 + 2\tilde{\mu}_1 \int f_1 dz \quad (\text{B.26})$$

$$F_{\text{aug}2} = F_2 + 2\tilde{\mu}_2 \int f_2 dz \quad (\text{B.27})$$

$$F_{\text{aug}3} = \int |f_1|^2 dz - N_1 \quad (\text{B.28})$$

$$F_{\text{aug}4} = \int |f_2|^2 dz - N_2 \quad (\text{B.29})$$

which should vanish. One can calculate then the Jacobian matrix

$$J(i, j)_{\text{aug}} = \frac{\partial F_i}{\partial x_j} \quad (\text{B.30})$$

with $x_1 = f_1, x_2 = f_2, x_3 = \tilde{\mu}_1$ and $x_4 = \tilde{\mu}_2$. Performing the Newton algorithm with the augmented Jacobian and the two additional equation F_3, F_4 leads to eigenstates f_k of Eq. (B.4). Hereby we can fix the number of atoms N_1, N_2 in the individual components.

B.2 Bogoliubov de Gennes Analysis

Let us now determine the Bogoliubov de Gennes equations of Eqs. (B.4-B.6). Therefore we rewrite Eq. (B.4) as

$$\imath \partial_t f_k = F_k(f_1, f_1^*, f_2, f_2^*) \quad (\text{B.31})$$

with

$$F_k = \left(-\frac{1}{2} \frac{\partial^2}{\partial z^2} + \frac{1}{2} \omega^2 z^2 + \mu_{\perp k} - \mu_k \right) f_k. \quad (\text{B.32})$$

We want to investigate the effects of small perturbations around a solution f_k^0 of Eq. (B.31) and consequently make the ansatz

$$f_k = f_k^0 + \epsilon[u_k \exp(-\omega t) + v_k^* \exp(\omega^* t)], \quad (\text{B.33})$$

where ϵ is a small parameter. Insertion of this ansatz in Eq. (B.31) and performing a Taylor expansion of F_k around $\epsilon = 0$ leads in linear order in ϵ to

$$\begin{aligned} i\partial_t f_k^0 + \epsilon[u_k \omega \exp(-\omega t) - v_k^* \omega^* \exp(\omega^* t)] &= F_k(f_1^0, f_1^{0*}, f_2^0, f_2^{0*}) \\ &+ \epsilon \left[\frac{\partial F_k}{\partial f_1} \right]_{f_1=f_1^0} [u_1 \exp(-\omega t) + v_1^* \exp(\omega^* t)] + \frac{\partial F_k}{\partial f_1^*} \Big|_{f_1^*=f_1^{0*}} [u_1^* \exp(\omega^* t) + v_1 \exp(-\omega t)] \\ &+ \frac{\partial F_k}{\partial f_2} \Big|_{f_2=f_2^0} [u_2 \exp(-\omega t) + v_2^* \exp(\omega^* t)] + \frac{\partial F_k}{\partial f_2^*} \Big|_{f_2^*=f_2^{0*}} [u_2^* \exp(\omega^* t) + v_2 \exp(-\omega t)]. \end{aligned} \quad (\text{B.34})$$

Note, deriving the BdG equations by a Taylor expansion is completely equivalent to the approach described in section 2.4. For reasons of clarity, we omit the positions where one evaluates the derivative in the following. Comparing the terms oscillating with ω and those oscillating with $-\omega^*$ separately, leads to

$$u_k \omega = \frac{\partial F_k}{\partial f_1} u_1 + \frac{\partial F_k}{\partial f_1^*} v_1 + \frac{\partial F_k}{\partial f_2} u_2 + \frac{\partial F_k}{\partial f_2^*} v_1 \quad (\text{B.35})$$

$$v_k \omega = -\frac{\partial F_k^*}{\partial f_1^*} v_1 - \frac{\partial F_k^*}{\partial f_1} u_1 - \frac{\partial F_k^*}{\partial f_2^*} v_2 - \frac{\partial F_k^*}{\partial f_2} u_2. \quad (\text{B.36})$$

These equation can be written as an eigenvalue problem

$$\begin{pmatrix} u_1 \\ v_1 \\ u_2 \\ v_2 \end{pmatrix} \omega = \begin{pmatrix} \frac{\partial F_1}{\partial f_1} & \frac{\partial F_1}{\partial f_1^*} & \frac{\partial F_1}{\partial f_2} & \frac{\partial F_1}{\partial f_2^*} \\ -\frac{\partial F_1^*}{\partial f_1} & -\frac{\partial F_1^*}{\partial f_1^*} & -\frac{\partial F_1^*}{\partial f_2} & -\frac{\partial F_1^*}{\partial f_2^*} \\ \frac{\partial F_2}{\partial f_1} & \frac{\partial F_2}{\partial f_1^*} & \frac{\partial F_2}{\partial f_2} & \frac{\partial F_2}{\partial f_2^*} \\ -\frac{\partial F_2^*}{\partial f_1} & -\frac{\partial F_2^*}{\partial f_1^*} & -\frac{\partial F_2^*}{\partial f_2} & -\frac{\partial F_2^*}{\partial f_2^*} \end{pmatrix} \begin{pmatrix} u_1 \\ v_1 \\ u_2 \\ v_2 \end{pmatrix}. \quad (\text{B.37})$$

The second and fourth row can be derived from the first and third one, so one only needs to calculate the following elements of the matrix:

$$\frac{\partial F_k}{\partial f_k} = -\frac{1}{2} \frac{\partial^2}{\partial z^2} + \frac{1}{2} \omega^2 z^2 + \mu_{\perp 1} - \mu_k + f_k \frac{\partial \mu_{\perp k}}{\partial f_k}, \quad (\text{B.38})$$

$$\frac{\partial F_k}{\partial f_k^*} = f_k \frac{\partial \mu_{\perp k}}{\partial f_k^*}, \quad (\text{B.39})$$

$$\frac{\partial F_k}{\partial f_{3-k}} = f_k \frac{\partial \mu_{\perp k}}{\partial f_{3-k}}, \quad (\text{B.40})$$

$$\frac{\partial F_k}{\partial f_{3-k}^*} = f_k \frac{\partial \mu_{\perp k}}{\partial f_{3-k}^*}. \quad (\text{B.41})$$

The partial derivatives of $\mu_{\perp k}$ are given by

$$\begin{aligned} \frac{\partial \mu_{\perp 1}}{\partial f_1} &= \left(-\frac{1}{\sigma_1^3} + \omega_{\perp}^2 \sigma_1 - 4 \frac{a_{11}}{\sigma_1^3} |f_1|^2 \right) \frac{\partial \sigma_1}{\partial f_1} + 2 \frac{a_{11}}{\sigma_1^2} f_1^* \\ &\quad - 8 \frac{a_{12}}{(\sigma_1^2 + \sigma_2^2)^2} |f_2|^2 \left(\sigma_1 \frac{\partial \sigma_1}{\partial f_1} + \sigma_2 \frac{\partial \sigma_2}{\partial f_1} \right) \end{aligned} \quad (\text{B.42})$$

$$\begin{aligned} \frac{\partial \mu_{\perp 1}}{\partial f_2} &= \left(-\frac{1}{\sigma_1^3} + \omega_{\perp}^2 \sigma_1 - 4 \frac{a_{11}}{\sigma_1^3} |f_1|^2 \right) \frac{\partial \sigma_1}{\partial f_2} + 4 \frac{a_{12}}{\sigma_1^2 + \sigma_2^2} f_2^* \\ &\quad - 8 \frac{a_{12}}{(\sigma_1^2 + \sigma_2^2)^2} |f_2|^2 \left(\sigma_1 \frac{\partial \sigma_1}{\partial f_2} + \sigma_2 \frac{\partial \sigma_2}{\partial f_2} \right) \end{aligned} \quad (\text{B.43})$$

$$\begin{aligned} \frac{\partial \mu_{\perp 2}}{\partial f_1} &= \left(-\frac{1}{\sigma_2^3} + \omega_{\perp}^2 \sigma_2 - 4 \frac{a_{22}}{\sigma_2^3} |f_2|^2 \right) \frac{\partial \sigma_2}{\partial f_1} + 2 \frac{a_{22}}{\sigma_2^2} f_2^* \\ &\quad - 8 \frac{a_{12}}{(\sigma_1^2 + \sigma_2^2)^2} |f_1|^2 \left(\sigma_1 \frac{\partial \sigma_1}{\partial f_2} + \sigma_2 \frac{\partial \sigma_2}{\partial f_2} \right) \end{aligned} \quad (\text{B.44})$$

$$\begin{aligned} \frac{\partial \mu_{\perp 2}}{\partial f_1} &= \left(-\frac{1}{\sigma_2^3} + \omega_{\perp}^2 \sigma_2 - 4 \frac{a_{22}}{\sigma_2^3} |f_2|^2 \right) \frac{\partial \sigma_2}{\partial f_1} + 4 \frac{a_{12}}{\sigma_1^2 + \sigma_2^2} f_1^* \\ &\quad - 8 \frac{a_{12}}{(\sigma_1^2 + \sigma_2^2)^2} |f_1|^2 \left(\sigma_1 \frac{\partial \sigma_1}{\partial f_1} + \sigma_2 \frac{\partial \sigma_2}{\partial f_1} \right) \end{aligned} \quad (\text{B.45})$$

and since $\mu_{\perp k}$ is real $\frac{\partial \mu_{\perp i}}{\partial f_j^*} = \left(\frac{\partial \mu_{\perp i}}{\partial f_j} \right)^*$. The partial derivatives of σ_k with respect to f_k can again be calculated by differentiation of Eq. (B.6) with respect to f_k . Note that they differ from the derivatives in the previous section since we treat f_k and f_k^* as independent.

$$\begin{aligned} \frac{a_{11} f_1^*}{\sigma_1^3 \omega_{\perp}^2} &= \left(1 + 8 \frac{a_{12} |f_2|^2}{\omega_{\perp}^2} \frac{\sigma_1^2}{(\sigma_1^2 + \sigma_2^2)^3} - 8 \frac{a_{12} |f_2|^2}{\omega_{\perp}^2} \frac{1}{(\sigma_1^2 + \sigma_2^2)^2} \right) \frac{\partial \sigma_1}{\partial f_1} \\ &\quad + 8 \frac{a_{12} |f_2|^2}{\omega_{\perp}^2} \frac{\sigma_1 \sigma_2}{(\sigma_1^2 + \sigma_2^2)^3} \frac{\partial \sigma_2}{\partial f_1} \end{aligned} \quad (\text{B.46})$$

$$\begin{aligned} \frac{2a_{12}\sigma_2 f_1^*}{(\sigma_1^2 + \sigma_2^2)^2 \omega_{\perp}^2} &= \left(1 + 8 \frac{a_{12} |f_1|^2}{\omega_{\perp}^2} \frac{\sigma_2^2}{(\sigma_1^2 + \sigma_2^2)^3} - 8 \frac{a_{12} |f_1|^2}{\omega_{\perp}^2} \frac{1}{(\sigma_1^2 + \sigma_2^2)^2} \right) \frac{\partial \sigma_2}{\partial f_1} \\ &\quad + 8 \frac{a_{12} |f_1|^2}{\omega_{\perp}^2} \frac{\sigma_1 \sigma_2}{(\sigma_1^2 + \sigma_2^2)^3} \frac{\partial \sigma_1}{\partial f_1} \end{aligned} \quad (\text{B.47})$$

$$\begin{aligned} \frac{2a_{12}\sigma_1 f_2^*}{(\sigma_1^2 + \sigma_2^2)^2 \omega_{\perp}^2} &= \left(1 + 8 \frac{a_{12} |f_2|^2}{\omega_{\perp}^2} \frac{\sigma_1^2}{(\sigma_1^2 + \sigma_2^2)^3} - 8 \frac{a_{12} |f_2|^2}{\omega_{\perp}^2} \frac{1}{(\sigma_1^2 + \sigma_2^2)^2} \right) \frac{\partial \sigma_1}{\partial f_1} \\ &\quad + 8 \frac{a_{12} |f_2|^2}{\omega_{\perp}^2} \frac{\sigma_1 \sigma_2}{(\sigma_1^2 + \sigma_2^2)^3} \frac{\partial \sigma_2}{\partial f_1} \end{aligned} \quad (\text{B.48})$$

$$\begin{aligned} \frac{a_{22} f_2^*}{\sigma_2^3 \omega_{\perp}^2} &= \left(1 + 8 \frac{a_{12} |f_1|^2}{\omega_{\perp}^2} \frac{\sigma_2^2}{(\sigma_1^2 + \sigma_2^2)^3} - 8 \frac{a_{12} |f_1|^2}{\omega_{\perp}^2} \frac{1}{(\sigma_1^2 + \sigma_2^2)^2} \right) \frac{\partial \sigma_2}{\partial f_1} \\ &\quad + 8 \frac{a_{12} |f_1|^2}{\omega_{\perp}^2} \frac{\sigma_1 \sigma_2}{(\sigma_1^2 + \sigma_2^2)^3} \frac{\partial \sigma_1}{\partial f_1} \end{aligned} \quad (\text{B.49})$$

Since we know, for a given solution f_k^0 , σ_k (and μ_k) we can set up the matrix (B.37) and evaluate the corresponding eigenvalues and eigenvectors.

Appendix C

Two-Mode Approximation

In this appendix we derive equations describing the time evolution of the population and phase difference in the different wells of a double-well potential by applying a two mode approximation for a spatially dependent coupling coefficient. Let us therefore at first recall the Gross-Pitaevskii equation with a collisional inhomogeneity $g(x)$

$$i\partial_t \Psi = -\frac{1}{2}\partial_x^2 \Psi + V(x)\Psi + g(x)|\Psi|^2\Psi. \quad (\text{C.1})$$

We expand the GP wave function using the eigenfunctions $u_i(x)$ of the linear problem

$$\Psi(x, t) = \sum_i c_i(t)u_i(x). \quad (\text{C.2})$$

Applying the two mode approximation we make the ansatz that only two modes contribute to the wave function

$$\Psi(x, t) = c_L(t)\Phi_L(x) + c_R(t)\Phi_R(x), \quad (\text{C.3})$$

where

$$\Phi_R(x) = \frac{1}{\sqrt{2}}[u_0(x) + u_1(x)], \quad (\text{C.4})$$

$$\Phi_L(x) = \frac{1}{\sqrt{2}}[u_0(x) - u_1(x)], \quad (\text{C.5})$$

are superpositions of the eigenfunctions of the linear problem. Consequently, u_0, u_1 obey the equation

$$\mu_i u_i(x) = -\frac{1}{2}\partial_x^2 u_i(x) + V(x)u_i(x). \quad (\text{C.6})$$

u_0 is the symmetric ground state and u_1 the antisymmetric first excited state. Then Φ_R and Φ_L are localized in the right and left well, respectively. In conclusion, one obtains for the total wave function expressed as superposition of the eigenfunctions of the linear problem

$$\Psi(x, t) = c_R(t)\frac{1}{\sqrt{2}}[u_0(x) + u_1(x)] + c_L(t)\frac{1}{\sqrt{2}}[u_0(x) - u_1(x)]. \quad (\text{C.7})$$

We should emphasize at this point that c_L and c_R are time dependent $c_{L,R} = c_{L,R}(t)$ complex numbers. The absolute value of $c_{L,R}$ denotes the occupation of the localized mode $\phi_{L,R}$. u_0 and u_1 are time independent real functions defined by the linear problem (C.6). In the following we will suppress the spatial argument x in the wave functions. Substitution of the

two-mode ansatz (C.7) in Eq. (C.1) leads to

$$\begin{aligned}
i\partial_t c_R(t)(u_0 + u_1) + i\partial_t c_L(t)(u_0 - u_1) &= c_R(t)(\mu_0 u_0 + \mu_1 u_1) + c_L(t)(\mu_0 u_0 - \mu_1 u_1) \\
&\quad + g(x) \left[\frac{|c_R|^2}{2}(u_0^2 + 2u_0 u_1 + u_1^2) + \frac{|c_L|^2}{2}(u_0^2 - 2u_0 u_1 + u_1^2) \right. \\
&\quad \left. + \frac{c_R c_L^*}{2}(u_0^2 - u_1^2) + \frac{c_R^* c_L}{2}(u_0^2 - u_1^2) \right] [c_R(u_0 + u_1) + c_L(u_0 - u_1)] \\
&= c_R(t)(\mu_0 u_0 + \mu_1 u_1) + c_L(t)(\mu_0 u_0 - \mu_1 u_1) \\
&\quad + \frac{g(x)}{2} \left[|c_R|^2 c_R(u_0^3 + 3u_0^2 u_1 + 3u_0 u_1^2 + u_1^3) \right. \\
&\quad \left. + |c_L|^2 c_L(u_0^3 - 3u_0^2 u_1 + 3u_0 u_1^2 - u_1^3) \right. \\
&\quad \left. + [2|c_R|^2 c_L + c_R^2 c_L^*](u_0^3 + u_0^2 u_1 - u_0 u_1^2 - u_1^3) \right. \\
&\quad \left. + [2|c_L|^2 c_R + c_R^* c_L^*](u_0^3 - u_0^2 u_1 - u_0 u_1^2 + u_1^3) \right] \quad (C.8)
\end{aligned}$$

Let us now define the integral

$$I_{m,n} = \int_{-\infty}^{\infty} dx g(x) u_0^m(x) u_1^n(x) \quad (C.9)$$

and project the previous equation to the localized modes ϕ_L and ϕ_R . Multiplication by $\frac{1}{2}(u_0 + u_1)$ and subsequent integration over x leads to an differential equation for c_R due to the orthonormality of u_0 and u_1 :

$$\begin{aligned}
i\partial_t c_R &= \frac{c_R}{2}(\mu_0 + \mu_1) + \frac{c_L}{2}(\mu_0 - \mu_1) \\
&\quad + \frac{|c_R|^2 c_R}{4} (I_{4,0} + 3I_{3,1} + 3I_{2,2} + I_{1,3} + I_{3,1} + 3I_{2,2} + 3I_{1,3} + I_{0,4}) \\
&\quad + \frac{|c_L|^2 c_L}{4} (I_{4,0} - 3I_{3,1} + 3I_{2,2} - I_{1,3} + I_{3,1} - 3I_{2,2} + 3I_{1,3} - I_{0,4}) \\
&\quad + \frac{2|c_R|^2 c_L + c_R^2 c_L^*}{4} (I_{4,0} + I_{3,1} - I_{2,2} - I_{1,3} + I_{3,1} + I_{2,2} - I_{1,3} - I_{0,4}) \\
&\quad + \frac{2|c_L|^2 c_R + c_R^* c_L^2}{4} (I_{4,0} - I_{3,1} - I_{2,2} + I_{1,3} + I_{3,1} - I_{2,2} - I_{1,3} + I_{0,4}) \\
&= \frac{c_R}{2}(\mu_0 + \mu_1) + \frac{c_L}{2}(\mu_0 - \mu_1) \\
&\quad + \frac{|c_R|^2 c_R}{4} (I_{4,0} + 4I_{3,1} + 6I_{2,2} + 4I_{1,3} + I_{0,4}) \\
&\quad + \frac{|c_L|^2 c_L}{4} (I_{4,0} - 2I_{3,1} + 2I_{1,3} - I_{0,4}) \\
&\quad + \frac{2|c_R|^2 c_L + c_R^2 c_L^*}{4} (I_{4,0} + 2I_{3,1} - 2I_{1,3} - I_{0,4}) \\
&\quad + \frac{2|c_L|^2 c_R + c_R^* c_L^2}{4} (I_{4,0} - 2I_{2,2} + I_{0,4}) \quad (C.10)
\end{aligned}$$

A multiplication by $\frac{1}{2}(u_0 - u_1)$ followed by spatial integration leads similarly to a differential equation for c_L :

$$\begin{aligned}
\imath \partial_t c_L &= \frac{c_R}{2}(\mu_0 - \mu_1) + \frac{c_L}{2}(\mu_0 + \mu_1) \\
&\quad + \frac{|c_R|^2 c_R}{4} (I_{4,0} + 3I_{3,1} + 3I_{2,2} + I_{1,3} - I_{3,1} - 3I_{2,2} - 3I_{1,3} - I_{0,4}) \\
&\quad + \frac{|c_L|^2 c_L}{4} (I_{4,0} - 3I_{3,1} + 3I_{2,2} - I_{1,3} - I_{3,1} + 3I_{2,2} - 3I_{1,3} + I_{0,4}) \\
&\quad + \frac{2|c_R|^2 c_L + c_R^2 c_L^*}{4} (I_{4,0} + I_{3,1} - I_{2,2} - I_{1,3} - I_{3,1} - I_{2,2} + I_{1,3} + I_{0,4}) \\
&\quad + \frac{2|c_L|^2 c_R + c_R^* c_L^2}{4} (I_{4,0} - I_{3,1} - I_{2,2} + I_{1,3} - I_{3,1} + I_{2,2} + I_{1,3} - I_{0,4}) \\
&= \frac{c_R}{2}(\mu_0 - \mu_1) + \frac{c_L}{2}(\mu_0 + \mu_1) \\
&\quad + \frac{|c_R|^2 c_R}{4} (I_{4,0} + 2I_{3,1} - 2I_{1,3} - I_{0,4}) \\
&\quad + \frac{|c_L|^2 c_L}{4} (I_{4,0} - 4I_{3,1} + 6I_{2,2} - 4I_{1,3} + I_{0,4}) \\
&\quad + \frac{2|c_R|^2 c_L + c_R^2 c_L^*}{4} (I_{4,0} - 2I_{2,2} + I_{0,4}) \\
&\quad + \frac{2|c_L|^2 c_R + c_R^* c_L^2}{4} (I_{4,0} - 2I_{3,1} + 2I_{3,1} - I_{0,4}) \tag{C.11}
\end{aligned}$$

c_L and c_R are complex numbers. Therefore let us now introduce amplitude and phase variables $c_i = \rho_i e^{i\phi_i}$ $i = R, L$ and the phase difference $\Delta\phi = \phi_L - \phi_R$ of the complex numbers c_L and c_R . This allows us to rewrite the above equations in the following way

$$\begin{aligned}
&- \rho_R \partial_t \phi_R + \imath \partial_t \rho_R \\
&= \rho_R \left[\frac{\mu_0}{2} + \frac{\mu_1}{2} + \frac{\rho_R^2}{4} (I_{4,0} + 4I_{3,1} + 6I_{2,2} + 4I_{1,3} + I_{0,4}) + \frac{\rho_L^2}{2} (I_{4,0} - 2I_{2,2} + I_{0,4}) \right] \\
&\quad + \rho_L e^{i\Delta\phi} \left[\left(\frac{\mu_0}{2} - \frac{\mu_1}{2} + \frac{\rho_L^2}{4} (I_{4,0} - 2I_{3,1} + 2I_{1,3} - I_{0,4}) \right) + \frac{\rho_R^2}{2} (I_{4,0} + 2I_{3,1} - 2I_{1,3} - I_{0,4}) \right] \\
&\quad + \frac{\rho_R^2 \rho_L e^{-i\Delta\phi}}{4} (I_{4,0} + 2I_{3,1} - 2I_{1,3} - I_{0,4}) + \frac{\rho_R \rho_L^2 e^{2i\Delta\phi}}{4} (I_{4,0} - 2I_{2,2} + I_{0,4}), \tag{C.12}
\end{aligned}$$

$$\begin{aligned}
&- \rho_L \partial_t \phi_L + \imath \partial_t \rho_L \\
&= \rho_L \left[\frac{\mu_0}{2} + \frac{\mu_1}{2} + \frac{\rho_L^2}{4} (I_{4,0} - 4I_{3,1} + 6I_{2,2} - 4I_{1,3} + I_{0,4}) \right] + \frac{\rho_R^2}{2} (I_{4,0} - 2I_{2,2} + I_{0,4}) \\
&\quad + \rho_R e^{-i\Delta\phi} \left[\left(\frac{\mu_0}{2} - \frac{\mu_1}{2} + \frac{\rho_R^2}{4} (I_{4,0} + 2I_{3,1} - 2I_{1,3} - I_{0,4}) \right) + \frac{\rho_L^2}{2} (I_{4,0} - 2I_{3,1} + 2I_{3,1} - I_{0,4}) \right] \\
&\quad + \frac{\rho_R^2 \rho_L e^{-2i\Delta\phi}}{4} (I_{4,0} - 2I_{2,2} + I_{0,4}) + \frac{\rho_R \rho_L^2 e^{i\Delta\phi}}{4} (I_{4,0} - 2I_{3,1} + 2I_{3,1} - I_{0,4}). \tag{C.13}
\end{aligned}$$

Considering phase and amplitude separately leads for the phases to

$$\begin{aligned} -\partial_t \phi_R = & \frac{\mu_0}{2} + \frac{\mu_1}{2} + \frac{\rho_R^2}{4} (I_{4,0} + 4I_{3,1} + 6I_{2,2} + 4I_{1,3} + I_{0,4}) + \frac{\rho_L^2}{2} (I_{4,0} - 2I_{2,2} + I_{0,4}) \\ & + \frac{\rho_L}{\rho_R} \cos(\Delta\phi) \left[\frac{\mu_0}{2} - \frac{\mu_1}{2} + \frac{\rho_L^2}{4} (I_{4,0} - 2I_{3,1} + 2I_{1,3} - I_{0,4}) + \frac{\rho_R^2}{2} (I_{4,0} + 2I_{3,1} - 2I_{1,3} - I_{0,4}) \right] \\ & + \frac{\rho_R \rho_L \cos(\Delta\phi)}{4} (I_{4,0} + 2I_{3,1} - 2I_{1,3} - I_{0,4}) + \frac{\rho_L^2 \cos(2\Delta\phi)}{4} (I_{4,0} - 2I_{2,2} + I_{0,4}), \end{aligned} \quad (\text{C.14})$$

$$\begin{aligned} -\partial_t \phi_L = & \frac{\mu_0}{2} + \frac{\mu_1}{2} + \frac{\rho_L^2}{4} (I_{4,0} - 4I_{3,1} + 6I_{2,2} - 4I_{1,3} + I_{0,4}) + \frac{\rho_R^2}{2} (I_{4,0} - 2I_{2,2} + I_{0,4}) \\ & + \frac{\rho_R}{\rho_L} \cos(\Delta\phi) \left[\frac{\mu_0}{2} - \frac{\mu_1}{2} + \frac{\rho_R^2}{4} (I_{4,0} + 2I_{3,1} - 2I_{1,3} - I_{0,4}) + \frac{\rho_L^2}{2} (I_{4,0} - 2I_{3,1} + 2I_{1,3} - I_{0,4}) \right] \\ & + \frac{\rho_R^2 \cos(2\Delta\phi)}{4} (I_{4,0} - 2I_{2,2} + I_{0,4}) + \frac{\rho_R \rho_L \cos(\Delta\phi)}{4} (I_{4,0} - 2I_{3,1} + 2I_{1,3} - I_{0,4}), \end{aligned} \quad (\text{C.15})$$

and for the amplitudes to

$$\begin{aligned} \partial_t \rho_R = & \rho_L \sin(\Delta\phi) \left[\frac{\mu_0}{2} - \frac{\mu_1}{2} + \frac{\rho_L^2}{4} (I_{4,0} - 2I_{3,1} + 2I_{1,3} - I_{0,4}) + \frac{\rho_R^2}{2} (I_{4,0} + 2I_{3,1} - 2I_{1,3} - I_{0,4}) \right] \\ & - \frac{\rho_R^2 \rho_L \sin(\Delta\phi)}{4} (I_{4,0} + 2I_{3,1} - 2I_{1,3} - I_{0,4}) + \frac{\rho_R \rho_L^2 \sin(2\Delta\phi)}{4} (I_{4,0} - 2I_{2,2} + I_{0,4}) \end{aligned} \quad (\text{C.16})$$

$$\begin{aligned} \partial_t \rho_L = & -\rho_R \sin(\Delta\phi) \left[\frac{\mu_0}{2} - \frac{\mu_1}{2} + \frac{\rho_R^2}{4} (I_{4,0} + 2I_{3,1} - 2I_{1,3} - I_{0,4}) + \frac{\rho_L^2}{2} (I_{4,0} - 2I_{3,1} + 2I_{1,3} - I_{0,4}) \right] \\ & - \frac{\rho_R^2 \rho_L \sin(2\Delta\phi)}{4} (I_{4,0} - 2I_{2,2} + I_{0,4}) + \frac{\rho_R \rho_L^2 \sin(\Delta\phi)}{4} (I_{4,0} - 2I_{3,1} + 2I_{1,3} - I_{0,4}). \end{aligned} \quad (\text{C.17})$$

Let us now define sum and difference of the squares of the amplitudes $z = \rho_R^2 - \rho_L^2$, $N = \rho_L^2 + \rho_R^2$. Note, N and z are within the two mode approximation the total atom number and the occupation difference of the two wells, respectively. This yields for the time evolution of

the phase difference

$$\begin{aligned}
\partial_t \Delta\phi = & \frac{z}{4} (I_{4,0} + 6I_{2,2} + I_{0,4}) + N(I_{3,1} + I_{1,3}) - \frac{z}{2} (I_{4,0} - 2I_{2,2} + I_{0,4}) \\
& + \cos(\Delta\phi) \left[\left(\frac{\rho_L}{\rho_R} - \frac{\rho_R}{\rho_L} \right) \left(\frac{\mu_0}{2} - \frac{\mu_1}{2} \right) + \left(\frac{\rho_L^3}{4\rho_R} - \frac{\rho_R^3}{4\rho_L} \right) (I_{4,0} - I_{0,4}) \right. \\
& \left. - \left(\frac{\rho_L^3}{4\rho_R} + \frac{\rho_R^3}{4\rho_L} \right) (2I_{3,1} - 2I_{1,3}) + 2\rho_R\rho_L(I_{3,1} - I_{1,3}) \right] \\
& + \cos(\Delta\phi)\rho_L\rho_R(I_{3,1} - I_{1,3}) - \frac{z}{4} \cos(2\Delta\phi)(I_{4,0} - 2I_{2,2} + I_{0,4}) \\
= & -\frac{z}{4} (I_{4,0} - 10I_{2,2} + I_{0,4}) + N(I_{3,1} + I_{1,3}) \\
& - \cos(\Delta\phi) \frac{z}{\sqrt{N^2 - z^2}} \left[\mu_0 - \mu_1 + \frac{N}{2} (I_{4,0} - I_{0,4}) \right] \\
& + \cos(\Delta\phi) \frac{N^2 - 2z^2}{\sqrt{N^2 - z^2}} (I_{3,1} - I_{1,3}) \\
& - \cos(2\Delta\phi) \frac{z}{4} (I_{4,0} - 2I_{2,2} + I_{0,4}),
\end{aligned} \tag{C.18}$$

and for the time evolution of the difference of the squares of the amplitudes: $\partial_t z = 2\rho_R\partial_t\rho_R - 2\rho_L\partial_t\rho_L$

$$\begin{aligned}
\partial_t z = & \rho_R\rho_L \sin(\Delta\phi) \left[2\mu_0 - 2\mu_1 + \frac{N}{2} (I_{4,0} - I_{0,4}) + z(I_{3,1} - I_{1,3}) + N(I_{4,0} - I_{0,4}) + 2z(I_{3,1} - I_{1,3}) \right] \\
& - \rho_R\rho_L \sin(\Delta\phi) \left[\frac{N}{2} (I_{4,0} - I_{0,4}) + z(I_{3,1} - I_{1,3}) \right] \\
& + \rho_L^2\rho_R^2 \sin(2\Delta\phi)(I_{4,0} - 2I_{2,2} + I_{0,4}) \\
= & \sqrt{N^2 - z^2} \sin(\Delta\phi) \left[\mu_0 - \mu_1 + \frac{N}{2} (I_{4,0} - I_{0,4}) + z(I_{3,1} - I_{1,3}) \right] \\
& + \frac{N^2 - z^2}{4} \sin(2\Delta\phi)(I_{4,0} - 2I_{2,2} + I_{0,4}).
\end{aligned} \tag{C.19}$$

In conclusion, we obtain the following system of equations for the phase and atom differences between the two wells

$$\begin{aligned}
\partial_t \Delta\phi = & -\frac{z}{4} (I_{4,0} - 10I_{2,2} + I_{0,4}) + N(I_{3,1} + I_{1,3}) - \cos(\Delta\phi) \frac{z}{\sqrt{N^2 - z^2}} \left[\mu_0 - \mu_1 + \frac{N}{2} (I_{4,0} - I_{0,4}) \right] \\
& + \cos(\Delta\phi) \frac{N^2 - 2z^2}{\sqrt{N^2 - z^2}} (I_{3,1} - I_{1,3}) - \cos(2\Delta\phi) \frac{z}{4} (I_{4,0} - 2I_{2,2} + I_{0,4})
\end{aligned} \tag{C.20}$$

$$\begin{aligned}
\partial_t z = & \sqrt{N^2 - z^2} \sin(\Delta\phi) \left[\mu_0 - \mu_1 + \frac{N}{2} (I_{4,0} - I_{0,4}) + z(I_{3,1} - I_{1,3}) \right] \\
& + \frac{N^2 - z^2}{4} \sin(2\Delta\phi)(I_{4,0} - 2I_{2,2} + I_{0,4}).
\end{aligned} \tag{C.21}$$

Eqs. (C.20-C.21) have got a Hamiltonian structure and can therefore be derived from a Hamiltonian by $\partial_t z = -\partial_\phi H$ and $\partial_t \phi = \partial_z H$ with the Hamiltonian

$$H = ANz - Bz^2 + C\sqrt{N^2 - z^2} \cos(\Delta\phi) + Dz\sqrt{N^2 - z^2} \cos(\Delta\phi) + E(N^2 - z^2) \cos(2\Delta\phi), \quad (\text{C.22})$$

where $A = I_{3,1} + I_{1,3}$, $B = \frac{1}{8}(I_{4,0} - 10I_{2,2} + I_{0,4})$, $C = \mu_0 - \mu_1 + \frac{N}{2}(I_{4,0} - I_{0,4})$, $D = I_{3,1} - I_{1,3}$ and $E = \frac{1}{8}(I_{4,0} - 2I_{2,2} + I_{0,4})$. Note, for a homogeneous coupling coefficient $g = \text{const.}$ one can exploit the orthonormality of u_0 and u_1 which enter in the integrals $I_{m,n}$ and obtains $A = 0$ and $D = 0$.

Appendix D

Van Vleck Perturbation Theory

In this appendix we follow the lines of the appendix of Ref. [307]. We consider the regime where the intermediate levels p are only weakly coupled to the ground state manifold s . Such a scenario allows us to adiabatically eliminate the intermediate state p from the excitation dynamics, as we are going to show in the following. One can rewrite the Hamiltonian Matrix \mathcal{H}_{rwa} in a matrix \mathcal{H}_0 which is block diagonal in each F manifold plus a matrix \mathcal{V} which couples different F manifolds. The previous one contains the contributions of the magnetic field and the energy of the unperturbed atom. The latter one results from the off diagonal contributions of the laser atom interaction coupling different F manifolds. In this picture, \mathcal{V} represents a perturbation that couples the “model space” $\{s\}$ to the one-dimensional orthogonal subspace $\{p\}$. If the energy spacing between the different F manifolds is much larger than the magnitude of the coupling of the F manifolds, quasi degenerate van Vleck perturbation theory allows us to introduce a unitary transformation e^{-G} that block diagonalizes \mathcal{H}_{rwa} . In this manner, the subspace $\{p\}$ is decoupled from the dynamics of the model space $\{s\}$, yielding an effective Hamiltonian $H_{2l} = H_0 + W$ for the latter. Our goal is to determine the unitary transformation e^{-G} and hence the effective interaction W within the model space $\{s\}$.

The formalism to calculate G and accordingly W is derived in [301], which we briefly summarize in the following. We consider a general Hamiltonian H that can be divided into a zero-order part H_0 and a perturbation V , i.e., $H = H_0 + V$, with zero-order eigenfunctions $H_0|t\rangle = \varepsilon_t|t\rangle$. The set of eigensolutions of H_0 can then be partitioned into two subsets $\{t, u, \dots\} = \{\alpha, \beta, \dots\} \cup \{i, j, \dots\}$, defining the model space $\{\alpha, \beta, \dots\}$ and its orthogonal complement. The projection operator into the model space and its orthogonal complement read $P = \sum_{\alpha} |\alpha\rangle\langle\alpha|$ and $Q = 1 - P = \sum_i |i\rangle\langle i|$, respectively. Any operator A can be partitioned into a block diagonal part A_D and a block off-diagonal part A_X , $A = A_D + A_X$, where $A_D = PAP + QAQ$ and $A_X = PAQ + QAP$. Since H_0 is diagonal, we have for the Hamiltonian in general

$$H_D = H_0 + V_D, \quad (\text{D.1})$$

$$H_X = V_X. \quad (\text{D.2})$$

Within the canonical form of van Vleck perturbation theory, we require $G = G_X$, i.e., $G_D = 0$ for the operator determining the unitary transformation e^{-G} . Moreover, G is an anti-Hermitian operator, $G = -G^{\dagger}$. It is defined order by order via

$$[H_0, G^{(1)}] = -V_X, \quad (\text{D.3})$$

$$[H_0, G^{(2)}] = -[V_D, G^{(1)}]. \quad (\text{D.4})$$

For higher orders, see ; the zeroth order contribution vanishes, i.e., $G^{(0)} = 0$. The order-by-

order computation of the effective interaction W follows as

$$W^{(1)} = V_D, \quad (\text{D.5})$$

$$W^{(2)} = \frac{1}{2}[V_X, G^{(1)}]. \quad (\text{D.6})$$

Explicit equations for the $G^{(n)}$ can be gained from (D.3-D.4) using the resolvent formalism. The resolvent operator $R_\alpha^{(0)}$ is defined as

$$R_\alpha^{(0)} = \frac{Q}{\varepsilon_\alpha - H_0} = \sum_i \frac{|i\rangle\langle i|}{\varepsilon_\alpha - \varepsilon_i}. \quad (\text{D.7})$$

Employing $G|\alpha\rangle = G_X|\alpha\rangle = (PGQ + QGP)|\alpha\rangle = \sum_i |i\rangle\langle i|G|\alpha\rangle$, we find

$$\begin{aligned} -R_\alpha^{(0)}[H_0, G]|\alpha\rangle &= -\sum_i \frac{|i\rangle\langle i|}{\varepsilon_\alpha - \varepsilon_i} [H_0, G]|\alpha\rangle \\ &= \sum_i |i\rangle\langle i|G|\alpha\rangle = G|\alpha\rangle. \end{aligned} \quad (\text{D.8})$$

Equating (D.8) order by order and utilizing (D.3) yields for $G^{(1)}$ the matrix representation

$$\mathcal{G}_{j\alpha}^{(1)} = \frac{\mathcal{V}_{j\alpha}}{\varepsilon_\alpha - \varepsilon_j}. \quad (\text{D.9})$$

Note that per definition there are no block diagonal contributions to \mathcal{G} . The second order matrix elements of the effective interaction W correspondingly read

$$\mathcal{W}_{\beta\alpha}^{(2)} = \frac{1}{2} \sum_i \mathcal{V}_{\beta i} \mathcal{V}_{i\alpha} \left(\frac{1}{\varepsilon_\alpha - \varepsilon_i} + \frac{1}{\varepsilon_\beta - \varepsilon_i} \right), \quad (\text{D.10})$$

where we made use of (D.3) and (D.8) as well as $G^\dagger = -G$, and assumed $V_X^\dagger = V_X$. We can use this result to simplify our Hamiltonian. The model space constitutes of the ground state manifold, and its orthogonal complement is defined by the intermediate excited levels p . The zero-order energies are given by the diagonal and read for the ground state manifold $\varepsilon_\alpha = E_\alpha$ and for the excited states $\varepsilon_i = E_i - \hbar\omega$. The perturbation V only possesses block off-diagonal matrix elements, i.e., $V_D = 0$ and $\mathcal{V}_{i\alpha} = \sum_m \frac{1}{2}\varepsilon(\mathbf{R}) \exp(i\phi_m(t)) \langle i|\epsilon_{\mathbf{m}}\mathbf{r}| \alpha \rangle$, $\mathcal{V}_{\beta i} = \sum_m \frac{1}{2}\varepsilon(\mathbf{R}) \exp(-i\phi_m(t)) \langle \beta|\epsilon_{\mathbf{m}}\mathbf{r}| i \rangle$. Hence, the first order of the effective interaction vanishes, $W^{(1)} = 0$, cf. (D.5). The first non-vanishing order is the second one, whose matrix representation within the model space reads

$$\begin{aligned} W_{\beta\alpha} &= \frac{1}{8}\varepsilon(\mathbf{R})^2 \sum_{i,i'=1}^2 \sum_l e^{i[\phi_{i'}(t) - \phi_i(t)]} \langle \beta|\epsilon_{i'}\mathbf{r}| l \rangle \langle l|\epsilon_{i'}\mathbf{r}| \alpha \rangle \\ &\times \left(\frac{1}{E_\alpha - E_l + \hbar\omega} + \frac{1}{E_\beta - E_l + \hbar\omega} \right). \end{aligned} \quad (\text{D.11})$$

Appendix E

Spinor Condensate Exposed to Raman Lasers

In this appendix we consider an interesting modification to the 'standard' spinor BEC setup. We assume that one applies laser in a Raman setup on an optically trapped spinor BEC. The setup is complementary to the setup investigated in Chapter 10, where we investigated effects of applying Raman lasers on a magnetically trapped condensate. In Chapter 10 we included the effects of the Raman lasers into the trapping potential and expressed the atomic wave function as eigenfunction of this combined effective external potential. Thus the Raman potential was diagonal. In contrary to this approach we express the atomic wave function in this appendix as eigenfunction of the pure optical potential and include the effects of the Raman lasers as off-diagonal potential in the equations of motion. For an optical trap the individual components are exposed to the same external potential. Therefore one obtains due to the overlap of the wave functions of the different components a population transfer between the $m = 0$ and the $m = \pm 1$ components caused by interatomic hyperfine state changing collisions. Moreover, the Raman lasers are polarized in such a way that they couple the $m = 1$ and the $m = -1$ component inducing a population transfer between these components. We derive in this appendix the equations describing a spinor BEC which is exposed to Raman lasers but do not present solutions of the equations. This is still work in progress.

E.1 Multicomponent Gross-Pitaevskii Equations

Let us at first recall the 'standard' spinor GPE in an optical trap. Therefore we investigate the dynamics of a $F = 1$ spinor BEC consisting of atoms with mass M confined in a spin independent potential V . The Hamiltonian of the system is given by [199, 294]

$$\begin{aligned} H = & \int d\mathbf{r} \sum_m \Psi_m^\dagger(\mathbf{r}) \left[\left(-\frac{\hbar^2}{2M} \nabla^2 + V(\mathbf{r}) \right) \Psi_m(\mathbf{r}) \right. \\ & + \sum_{m_1, 2, 3, 4} \Psi_{m_1}^\dagger(\mathbf{r}) \Psi_{m_2}^\dagger(\mathbf{r}) \left[\frac{g_0}{2} \delta_{m_1 m_4} \delta_{m_2 m_3} \right. \\ & \left. \left. + \frac{g_1}{2} \mathbf{F}_{m_1 m_4} \cdot \mathbf{F}_{m_2 m_3} \right] \Psi_{m_3}(\mathbf{r}) \Psi_{m_4}(\mathbf{r}), \right] \end{aligned} \quad (\text{E.1})$$

where Ψ_m is the field operator of the atom in the magnetic sublevel m and \mathbf{F} is the spin-1 angular momentum operator. The spin independent and spin dependent interactions are characterized by $g_0 = \frac{4\pi\hbar^2(a_0+2a_2)}{3M}$ and $g_1 = \frac{4\pi\hbar^2(a_2-a_0)}{3M}$ with a_S being the s-wave scattering length for the scattering channel with total spin S . The Hamiltonian (E.1) commutes with the total number of atoms $N = \int d\mathbf{r} \sum_m |\Psi_m|^2$ and the total magnetization $M = \int d\mathbf{r} (|\Psi_1|^2 - |\Psi_{-1}|^2)$ [205] leading to these quantities being constants of motion. From

the Hamiltonian (E.1) one can derive the multicomponent Gross-Pitaevskii equations, which read with suppressed arguments in the wave functions [294]

$$i\hbar \frac{\partial \Psi_0}{\partial t} = \left(-\frac{\hbar^2}{2M} \nabla^2 + V(\mathbf{r}) + g_0 n \right) \Psi_0 + \frac{g_1}{\sqrt{2}} (F_+ \Psi_1 + F_- \Psi_{-1}) \quad (\text{E.2})$$

$$i\hbar \frac{\partial \Psi_{\pm 1}}{\partial t} = \left(-\frac{\hbar^2}{2M} \nabla^2 + V(\mathbf{r}) + g_0 n \right) \Psi_{\pm 1} + g_1 \left(\frac{1}{\sqrt{2}} F_{\mp} \Psi_0 \pm F_z \Psi_{\pm 1} \right), \quad (\text{E.3})$$

where Ψ_m is the macroscopic wave function, $n = \sum_m |\Psi_m|^2$, $F_z = |\Psi_1|^2 - |\Psi_{-1}|^2$, and $F_+ = F_-^* = \sqrt{2}(\Psi_1^* \Psi_0 + \Psi_0^* \Psi_{-1})$.

E.2 Raman Potential

A single atom exposed to two lasers in a Raman configuration with the total electric field

$$\begin{aligned} \mathbf{E}(\mathbf{R}, t) = & \frac{1}{2} \left(\varepsilon_1(\mathbf{R}) e^{-i(\mathbf{k}_1 \mathbf{R} - \omega_1 t + \phi_1(t))} \epsilon_1 + \varepsilon_1^*(\mathbf{R}) e^{i(\mathbf{k}_1 \mathbf{R} - \omega_1 t + \phi_1(t))} \epsilon_1^* \right) \\ & + \frac{1}{2} \left(\varepsilon_2(\mathbf{R}) e^{-i(\mathbf{k}_2 \mathbf{R} - \omega_2 t + \phi_2(t))} \epsilon_2 + \varepsilon_2^*(\mathbf{R}) e^{i(\mathbf{k}_2 \mathbf{R} - \omega_2 t + \phi_2(t))} \epsilon_2^* \right) \end{aligned} \quad (\text{E.4})$$

is exposed to the potential

$$V^R(\mathbf{R}, \mathbf{r}, t) = \mathbf{d} \cdot \mathbf{E}(\mathbf{R}, t) \quad (\text{E.5})$$

with the dipole operator $\mathbf{d} = -er$. Here \mathbf{R} denotes the center of mass coordinate of the atom and \mathbf{r} is the relative coordinate of the electron with respect to the center of mass coordinate. We assume that the electric field is almost constant over the dimension of the atom. Therefore the electric field is independent on the electronic coordinate but depends only on the center of mass coordinate. This approximation is well justified for ground state atoms. The amplitudes $\varepsilon_{1,2}(\mathbf{R})$ are space dependent in order to account for the focussing and shape of the laser beams. They do not depend on time and can therefore not describe switching on and off effects. The factors $\epsilon_{1,2}$ are the unit polarization vectors.

The transitions occurring by the lasers are much faster than the center of mass motion of the atom. Therefore we can make a Born-Oppenheimer like approximation and neglect the kinetic energy for determining the electronic state with the center of mass coordinate as a parameter. Let us assume that the lasers emit circular polarized light and are detuned by Δ to the D_1 transition line. Then the lasers couple the $|m = -1\rangle$ and the $|m = 1\rangle$ state. In the case of ^{87}Rb and if one only takes into account the coupling to the p state with $j = 1/2$ one obtains

$$W = \frac{3\eta_0 e^2 a_0^2}{8h\Delta} \begin{pmatrix} A & 0 & D \\ 0 & B & 0 \\ D^* & 0 & C \end{pmatrix} \quad (\text{E.6})$$

$$A = I_1(\mathbf{R}) + (I_1(\mathbf{R}) + 6I_2(\mathbf{R})) \frac{1}{1 - \frac{\Delta_{\text{hfs}}}{\Delta}} \quad (\text{E.7})$$

$$\begin{aligned}
B &= (I_1(\mathbf{R}) + I_2(\mathbf{R})) \left(1 + \frac{3}{1 - \frac{\Delta_{\text{hfs}}}{\Delta}} \right) \\
C &= I_2(\mathbf{R}) + (I_2(\mathbf{R}) + 6I_1(\mathbf{R})) \frac{1}{1 - \frac{\Delta_{\text{hfs}}}{\Delta}} \\
D &= -\sqrt{I_1(\mathbf{R})I_2(\mathbf{R})} \left(1 - \frac{1}{1 - \frac{\Delta_{\text{hfs}}}{\Delta}} \right) e^{i\Delta\phi(\mathbf{t})}
\end{aligned}$$

(cf. Eq. (10.14)) for the atom laser interaction expanded into the eigenfunctions of the unperturbed ground state manifold. $I_i(\mathbf{R}) = |E_i|^2/2\eta$ denotes the intensity of the laser $i = \{1, 2\}$ and $\eta_0 = \frac{1}{\epsilon_0 c}$ with the electric constant ϵ_0 and the speed of light c . a_0 is the Bohr radius and $\Delta\phi(\mathbf{R})$ is the phase difference between the lasers. The potential constitutes out of a diagonal part corresponding to the light shift and additionally it couples the $|m = -1\rangle$ and the $|m = 1\rangle$ state. Note, in the following we express the center of mass coordinate with \mathbf{r} again.

E.3 Augmented Spinor Equations

Let us now shine two lasers in a Raman like configuration on a spinor BEC. We assume that one can determine the effective trapping potential V , confining the spinor BEC, independently on the Raman lasers, e.g., that the field creating the trap does not change the symmetry of the internal states the Raman potential utilizes and vice versa. This can for example be realized by an optical trap created by a far detuned laser leading to the potential [26]

$$V = \frac{3\pi c^2}{2\omega_0^3} \frac{\Gamma}{\Delta_{\text{trap}}} I_{\text{trap}}, \quad (\text{E.8})$$

where ω_0 is the transition frequency between the ground state and an excited state, Γ the width of the excited state, Δ_{trap} the detuning of the laser frequency with respect to the transition frequency, and finally I_{trap} the intensity of the laser creating the trap. A typical order of magnitude for such a potential is $V \sim 10^{-12} I [\text{W/m}^2] \text{eV}$ leading for large laser intensities to trapping potentials in the MHz regime. In order to get the full Hamiltonian one can simply add the Raman potential to the Hamiltonian (E.1) leading to:

$$\begin{aligned}
H &= \int d\mathbf{r} \sum_m \Psi_m^\dagger(\mathbf{r}) \left(-\frac{\hbar^2}{2M} \nabla^2 + V(\mathbf{r}) \right) \Psi_m(\mathbf{r}) \\
&\quad + \sum_{m_1, m_2} \Psi_{m_1}^\dagger(\mathbf{r}) V^R(\mathbf{r}) \Psi_{m_2}(\mathbf{r}) \\
&\quad + \sum_{m_1, 2, 3, 4} \Psi_{m_1}^\dagger(\mathbf{r}) \Psi_{m_2}^\dagger(\mathbf{r}) \left(\frac{g_0}{2} \delta_{m_1 m_4} \delta_{m_2 m_3} \right. \\
&\quad \left. + \frac{g_1}{2} \mathbf{F}_{m_1 m_4} \cdot \mathbf{F}_{m_2 m_3} \right) \Psi_{m_3}(\mathbf{r}) \Psi_{m_4}(\mathbf{r})
\end{aligned} \quad (\text{E.9})$$

$\Psi_m(\mathbf{r})$ is again the field operator of the atom in the magnetic sublevel m . Therefore it constitutes out of two different parts, the spatial dependent part and the part describing the

internal state, acting on different Hilbert spaces. Since both Hilbert spaces are independent the field operator can be factorized $\Psi_m = \phi_m(\mathbf{r})|m\rangle$.

$$\begin{aligned} H = & \int d\mathbf{r} \sum_m \phi_m^\dagger(\mathbf{r}) \left(-\frac{\hbar^2}{2M} \nabla^2 + V(\mathbf{r}) \right) \phi_m(\mathbf{r}) \\ & + \sum_{m_1, m_2} \phi_{m_1}^\dagger(\mathbf{r}) \langle m_1 | (\mathbf{r}) V^R(\mathbf{r}) | m_2 \rangle \phi_{m_2}(\mathbf{r}) \\ & + \sum_{m_{1,2,3,4}} \phi_{m_1}^\dagger(\mathbf{r}) \phi_{m_2}^\dagger(\mathbf{r}) \langle m_1 | \langle m_2 | \left(\frac{g_0}{2} \delta_{m_1 m_4} \delta_{m_2 m_3} \right. \\ & \left. + \frac{g_1}{2} \mathbf{F}_{m_1 m_4} \cdot \mathbf{F}_{m_2 m_3} \right) | m_3 \rangle | m_4 \rangle \phi_{m_3}(\mathbf{r}) \phi_{m_4}(\mathbf{r}) \end{aligned} \quad (\text{E.10})$$

$\phi_m(\mathbf{r})$ is the field operator describing an atom in the hyperfine state m at position \mathbf{r} and obeys the commutator relation $[\phi_m(\mathbf{r}), \phi_n^\dagger(\mathbf{r}')] = \delta_{m,n} \delta(\mathbf{r} - \mathbf{r}')$. The total number of atoms is still conserved. However, the total magnetization is not conserved any longer. Applying the commutator relations $[H, \phi_m]$ and performing the mean-field approximation leads to the following modified GPE with suppressed arguments in the wave functions

$$\begin{aligned} i\hbar \frac{\partial \phi_0}{\partial t} = & \left(-\frac{\hbar^2}{2M} \nabla^2 + V_0(\mathbf{r}) + g_0 n \right) \phi_0 + \frac{g_1}{\sqrt{2}} (F_+ \phi_1 + F_- \phi_{-1}) \\ & + \sum_m \langle 0 | V^R(\mathbf{r}) | m \rangle \phi_m \end{aligned} \quad (\text{E.11})$$

$$\begin{aligned} i\hbar \frac{\partial \phi_{\pm 1}}{\partial t} = & \left(-\frac{\hbar^2}{2M} \nabla^2 + V_{\pm 1}(\mathbf{r}) + g_0 n \right) \phi_{\pm 1} + g_1 \left(\frac{1}{\sqrt{2}} F_+ \phi_0 \pm F_z \phi_{\pm 1} \right) \\ & + \sum_m \langle \pm 1 | V^R(\mathbf{r}) | m \rangle \phi_m \end{aligned} \quad (\text{E.12})$$

with $F_z = |\phi_1|^2 - |\phi_{-1}|^2$, and $F_+ = F_-^* = \sqrt{2}(\phi_1^* \phi_0 + \phi_0^* \phi_{-1})$. One can rewrite these equations in a more instructive way by substitution of F_z , F_+ and F_-

$$\begin{aligned} i\hbar \frac{\partial \phi_0}{\partial t} = & \left(-\frac{\hbar^2}{2M} \nabla^2 + V_0(\mathbf{r}) + g_0 |\phi_0|^2 + (g_0 + g_1)(|\phi_1|^2 + |\phi_{-1}|^2) \right) \phi_0 \\ & + 2g_1 \phi_{-1} \phi_1 \phi_0^* + \langle 0 | V^R(\mathbf{r}) | 0 \rangle \phi_0 \end{aligned} \quad (\text{E.13})$$

$$\begin{aligned} i\hbar \frac{\partial \phi_{\pm 1}}{\partial t} = & \left(-\frac{\hbar^2}{2M} \nabla^2 + V_{\pm 1}(\mathbf{r}) + (g_0 + g_1)(|\phi_{\pm 1}|^2 + |\phi_0|^2) + (g_0 - g_1)|\phi_{\mp 1}|^2 \right) \phi_{\pm 1} + g_1 \phi_0^2 \phi_{\mp 1}^* \\ & + \langle \pm 1 | V^R(\mathbf{r}) | \pm 1 \rangle \phi_{\pm 1} + \langle \pm 1 | V^R(\mathbf{r}) | \mp 1 \rangle \phi_{\mp 1}. \end{aligned} \quad (\text{E.14})$$

In addition to the usual terms appearing in the spinor GPE one obtains another diagonal spatial dependent single atom term $V^{LS} = \langle m | V^R(\mathbf{r}) | m \rangle$, the so called light shift. This term acts as an additional trapping potential and is in the order of $V^{LS} \sim 10^{-12} I [W/m^2] eV$. Moreover, one obtains a spatial dependent non-diagonal term $V^{CP} = \langle \pm 1 | V^R(\mathbf{r}) | \mp 1 \rangle$ coupling the $m = 1$ and the $m = -1$ state being of the order $V^{CP} \sim 5 \times 10^{-13} \sqrt{I_1 I_2} [W/m^2] eV$. The total number of atoms $N = \sum N_m$ is conserved however the individual number of atoms N_m of each component is not conserved. Let us therefore calculate the continuity equation for

the single components

$$\frac{\partial \rho_m}{\partial t} = \phi_m^* \partial_t \phi_m + \phi_m \partial_t \phi_m^*. \quad (\text{E.15})$$

Substitution of the augmented spinor GPE (E.14) and their complex conjugates leads to

$$\frac{\partial \rho_0}{\partial t} = j_0 + \frac{2g_1}{i\hbar} (\phi_0^{*2} \phi_1 \phi_{-1} - \phi_0^2 \phi_1^* \phi_{-1}^*) \quad (\text{E.16})$$

$$\begin{aligned} \frac{\partial \rho_{\pm 1}}{\partial t} = & j_{\pm 1} + \frac{g_1}{i\hbar} (\phi_0^2 \phi_{\pm 1}^* \phi_{\mp 1}^* - \phi_0^{*2} \phi_{\pm 1} \phi_{\mp 1}) \\ & + \frac{1}{i\hbar} (\langle \pm 1 | V^R(\mathbf{r}) | \mp 1 \rangle \phi_{\pm 1}^* \phi_{\mp 1} - \langle \mp 1 | V^R(\mathbf{r}) | \pm 1 \rangle \phi_{\mp 1}^* \phi_{\pm 1}) \end{aligned} \quad (\text{E.17})$$

with the probability current $j_m = \frac{i}{\hbar} \left[\phi_m^* \frac{\hbar^2}{2M} \nabla^2 \phi_m + \phi_m \frac{\hbar^2}{2M} \nabla^2 \phi_m^* \right]$. The first term appears due to the fact that the scattering between two atoms does not conserve the individual magnetic quantum number, but only the sum of the quantum number, allowing the process $|m = 1\rangle, |m = -1\rangle \leftrightarrow |m = 0\rangle, |m = 0\rangle$. This process depends on the overlap of all three wave functions describing the different spin components. the second row of Eq. (E.17) stems from the Raman potential leading to a population transfer between the $|m = 1\rangle$ and the $|m = -1\rangle$ components. Since the Raman potential is spatial dependent for a laser beam with an inhomogeneous shape the magnitude of this transfer is spatial dependent as well. Estimating the magnitude of the different contribution leads for the scattering process to $\frac{g_1}{\hbar} \sim 10^{-13} \text{ m}^3/\text{s}$. For a density of $\phi_0^2 = 10^{15} \text{ 1/cm}^3$ one gains $\frac{g_1}{\hbar} \phi_0^2 \sim 10^{-4} \text{ 1/s}$. The corresponding value of the Raman transition is $V^R/\hbar \sim 10^3 I [\text{W/m}^2] \text{ 1/s}$. So the Raman transition leads already for small intensities to a large transfer of atoms between the $|m = 1\rangle$ and the $|m = -1\rangle$ components.

Bibliography

- [1] C. J. Pethick and H. Smith, *Bose-Einstein condensation in dilute gases*, Cambridge University Press, 2002.
- [2] L. P. Pitaevskii and S. Stringari, *Bose-Einstein Condensation*, Oxford University Press, 2003.
- [3] P. G. Kevrekidis, D. J. Frantzeskakis, and R. Carretero-González, *Emergent Nonlinear Phenomena in Bose-Einstein Condensates*, Springer Verlag, 2008.
- [4] F. Dalfovo, S. Giorgini, L. P. Pitaevskii, and S. Stringari, *Theory of Bose-Einstein condensation in trapped gases*, Rev. Mod. Phys. **71**, 463 (1999).
- [5] R. Carretero-González, D. J. Frantzeskakis, and P. G. Kevrekidis, *Nonlinear waves in Bose-Einstein condensates: physical relevance and mathematical techniques*, Nonlinearity , R139 (2008).
- [6] S. Bose, *Plancks Gesetz und Lichtquantenhypothese*, Z. Phys **26**, 178 (1926).
- [7] A. Einstein, *Quantentheorie des einatomigen idealen Gases*, Sitzungsber. Kgl. Preuss. Akad. Wiss. **22**, 261 (1924).
- [8] F. London, *The λ -Phenomenon of Liquid Helium and the Bose-Einstein Degeneracy*, Nature **141**, 643 (1938).
- [9] F. London, *On the Bose-Einstein Condensation*, Phys. Rev. **54**, 947 (1938).
- [10] O. Penrose and L. Onsager, *Bose-Einstein Condensation and Liquid Helium*, Phys. Rev. **104**, 576 (1956).
- [11] T. R. Sosnick, W. M. Snow, and P. E. Sokol, *Deep-inelastic neutron scattering from liquid He4*, Phys. Rev. B **41**, 11185 (1990).
- [12] D. M. Ceperley, *Path integrals in the theory of condensed helium*, Rev. Mod. Phys. **67**, 279 (1995).
- [13] M. H. Anderson, J. R. Ensher, M. R. Matthews, C. E. Wieman, and E. A. Cornell, *Observation of Bose-Einstein Condensation in a Dilute Atomic Vapor*, Science **269**, 198 (1995).
- [14] S. Chu, *Nobel Lecture: The manipulation of neutral particles*, Rev. Mod. Phys. **70**, 685 (1998).
- [15] C. N. Cohen-Tannoudji, *Nobel Lecture: Manipulating atoms with photons*, Rev. Mod. Phys. **70**, 707 (1998).
- [16] W. D. Phillips, *Nobel Lecture: Laser cooling and trapping of neutral atoms*, Rev. Mod. Phys. **70**, 721 (1998).

- [17] C. C. Bradley, C. A. Sackett, J. J. Tollett, and R. G. Hulet, *Evidence of Bose-Einstein Condensation in an Atomic Gas with Attractive Interactions*, Phys. Rev. Lett. **75**, 1687 (1995).
- [18] K. B. Davis, M. O. Mewes, M. R. Andrews, N. J. van Druten, D. S. Durfee, D. M. Kurn, and W. Ketterle, *Bose-Einstein Condensation in a Gas of Sodium Atoms*, Phys. Rev. Lett. **75**, 3969 (1995).
- [19] C. C. Bradley, C. A. Sackett, and R. G. Hulet, *Bose-Einstein Condensation of Lithium: Observation of Limited Condensate Number*, Phys. Rev. Lett. **78**, 985 (1997).
- [20] W. Ketterle, *Nobel lecture: When atoms behave as waves: Bose-Einstein condensation and the atom laser*, Rev. Mod. Phys. **74**, 1131 (2002).
- [21] E. A. Cornell and C. E. Wieman, *Nobel Lecture: Bose-Einstein condensation in a dilute gas, the first 70 years and some recent experiments*, Rev. Mod. Phys. **74**, 875 (2002).
- [22] R. Folman, P. Krüger, J. Schmiedmayer, J. Denschlag, and C. Henkel, Microscopic atom optics: From wires to an atomchip, volume 48 of *Advances In Atomic, Molecular, and Optical Physics*, pages 263 – 356, 2002.
- [23] C. E. Wieman, D. E. Pritchard, and D. J. Wineland, *Atom cooling, trapping, and quantum manipulation*, Rev. Mod. Phys. **71**, S253 (1999).
- [24] J. Fortagh and C. Zimmermann, *Magnetic microtraps for ultracold atoms*, Rev. Mod. Phys. **79**, 235 (2007).
- [25] J. Weiner, V. S. Bagnato, S. Zilio, and P. S. Julienne, *Experiments and theory in cold and ultracold collisions*, Rev. Mod. Phys. **71**, 1 (1999).
- [26] R. Grimm, M. Weidemüller, and Y. B. Ovchinnikov, Optical Dipole Traps for Neutral Atoms, volume 42 of *Advances In Atomic, Molecular, and Optical Physics*, pages 95 – 170, Academic Press, 2000.
- [27] M. Greiner, O. Mandel, T. Esslinger, T. W. Hansch, and I. Bloch, *Quantum phase transition from a superfluid to a Mott insulator in a gas of ultracold atoms*, Nature **415**, 39 (2002).
- [28] S. Fölling, S. Trotzky, P. Cheinet, M. Feld, R. Saers, A. Widera, T. Müller, and I. Bloch, *Direct observation of second-order atom tunnelling*, Nature **448**, 1029 (2007).
- [29] M. Albiez, R. Gati, J. Fölling, S. Hunsmann, M. Cristiani, and M. K. Oberthaler, *Direct Observation of Tunneling and Nonlinear Self-Trapping in a Single Bosonic Josephson Junction*, Phys. Rev. Lett. **95**, 010402 (2005).
- [30] R. Zhang, N. V. Morrow, P. R. Berman, and G. Raithel, *Laser cooling in an optical lattice that employs Raman transitions*, Phys. Rev. A **72**, 043409 (2005).
- [31] S. Hofferberth, I. Lesanovsky, B. Fischer, J. Verdu, and J. Schmiedmayer, *Radiofrequency-dressed-state potentials for neutral atoms*, Nat. Phys. **2**, 710 (2006).
- [32] I. Lesanovsky, S. Hofferberth, J. Schmiedmayer, and P. Schmelcher, *Manipulation of ultracold atoms in dressed adiabatic radio-frequency potentials*, Phys. Rev. A **74**, 033619 (2006).

- [33] I. Lesanovsky, T. Schumm, S. Hofferberth, L. M. Andersson, P. Krüger, and J. Schmiedmayer, *Adiabatic radio-frequency potentials for the coherent manipulation of matter waves*, Phys. Rev. A **73**, 033619 (2006).
- [34] S. Hofferberth, I. Lesanovsky, B. Fischer, T. Schumm, and J. Schmiedmayer, *Non-equilibrium coherence dynamics in one-dimensional Bose gases*, Nature **449**, 324 (2007).
- [35] T. Schumm, S. Hofferberth, L. M. Andersson, S. Wildermuth, S. Groth, I. Bar-Joseph, J. Schmiedmayer, and P. Krüger, *Matter-wave interferometry in a double well on an atom chip*, Nat. Phys. **1**, 57 (2005).
- [36] I. H. Deutsch and P. S. Jessen, *Quantum-state control in optical lattices*, Phys. Rev. A **57**, 1972 (1998).
- [37] P. Böhi, M. F. Riedel, J. Hoffrogge, J. Reichel, T. W. Hänsch, and P. Treutlein, *Coherent manipulation of Bose-Einstein condensates with state-dependent microwave potentials on an atom chip*, Nat. Phys. **5**, 592 (2009).
- [38] M. Andrews, C. Townsend, H. Miesner, D. Durfee, D. Kurn, and W. Ketterle, *Observation of interference between two Bose condensates*, Science **275**, 637 (1997).
- [39] S. Raghavan, A. Smerzi, S. Fantoni, and S. R. Shenoy, *Coherent oscillations between two weakly coupled Bose-Einstein condensates: Josephson effects, π oscillations, and macroscopic quantum self-trapping*, Phys. Rev. A **59**, 620 (1999).
- [40] S. Raghavan, A. Smerzi, and V. M. Kenkre, *Transitions in coherent oscillations between two trapped Bose-Einstein condensates*, Phys. Rev. A **60**, R1787 (1999).
- [41] A. Smerzi and S. Raghavan, *Macroscopic quantum fluctuations in the Josephson dynamics of two weakly linked Bose-Einstein condensates*, Phys. Rev. A **61**, 063601 (2000).
- [42] E. A. Ostrovskaya, Y. S. Kivshar, M. Lisak, B. Hall, F. Cattani, and D. Anderson, *Coupled-mode theory for Bose-Einstein condensates*, Phys. Rev. A **61**, 031601 (2000).
- [43] K. W. Mahmud, J. N. Kutz, and W. P. Reinhardt, *Bose-Einstein condensates in a one-dimensional double square well: Analytical solutions of the nonlinear Schrödinger equation*, Phys. Rev. A **66**, 063607 (2002).
- [44] V. S. Shchesnovich, B. A. Malomed, and R. A. Kraenkel, *Solitons in Bose-Einstein condensates trapped in a double-well potential*, Physica D **188**, 213 (2004).
- [45] D. Ananikian and T. Bergeman, *Gross-Pitaevskii equation for Bose particles in a double-well potential: Two-mode models and beyond*, Phys. Rev. A **73**, 013604 (2006).
- [46] P. Ziń, E. Infeld, M. Matuszewski, G. Rowlands, and M. Trippenbach, *Method for obtaining exact solutions of the nonlinear Schrödinger equation for a double-square-well potential*, Phys. Rev. A **73**, 022105 (2006).
- [47] T. Kapitula and P. G. Kevrekidis, *Bose-Einstein condensates in the presence of a magnetic trap and optical lattice: two-mode approximation*, Nonlinearity **18**, 2491 (2005).
- [48] G. Theocharis, P. G. Kevrekidis, D. J. Frantzeskakis, and P. Schmelcher, *Symmetry breaking in symmetric and asymmetric double-well potentials*, Phys. Rev. E **74**, 056608 (2006).

- [49] L. D. Carr, D. R. Dounas-Frazer, and M.-A. Garcia-March, *Dynamical Realization of Macroscopic Superposition States of Cold Bosons in a Tilted Double Well*, arXiv:quant-ph/0610166v2 (2010).
- [50] C. Cambournac, T. Sylvestre, H. Maillotte, B. Vanderlinden, P. Kockaert, P. Emplit, and M. Haelterman, *Symmetry-Breaking Instability of Multimode Vector Solitons*, Phys. Rev. Lett. **89**, 083901 (2002).
- [51] P. Kevrekidis, Z. Chen, B. Malomed, D. Frantzeskakis, and M. Weinstein, *Spontaneous symmetry breaking in photonic lattices: Theory and experiment*, Phys. Lett. A **340**, 275 (2005).
- [52] M. Ornigotti, G. D. Valle, D. Gatti, and S. Longhi, *Topological suppression of optical tunneling in a twisted annular fiber*, Phys. Rev. A **76**, 023833 (2007).
- [53] C. Wang, P. Kevrekidis, N. Whitaker, and B. Malomed, *Two-component nonlinear Schrödinger models with a double-well potential*, Physica D **237**, 2922 (2008).
- [54] O. E. Müstecaplıoğlu, M. Zhang, and L. You, *Tunneling of condensate magnetization in a double-well potential*, Phys. Rev. A **71**, 053616 (2005).
- [55] O. E. Müstecaplıoğlu, W. Zhang, and L. You, *Quantum dynamics of a spin-1 condensate in a double-well potential*, Phys. Rev. A **75**, 023605 (2007).
- [56] T. Köhler, K. Goral, and P. S. Julienne, *Production of cold molecules via magnetically tunable Feshbach resonances*, Rev. Mod. Phys. **78**, 1311 (2006).
- [57] S. Inouye, M. R. Andrews, J. Stenger, H.-J. Miesner, D. M. Stamper-Kurn, and W. Ketterle, *Observation of Feshbach resonances in a Bose-Einstein condensate*, Nature **392**, 151 (1998).
- [58] J. Stenger, S. Inouye, M. R. Andrews, H.-J. Miesner, D. M. Stamper-Kurn, and W. Ketterle, *Strongly Enhanced Inelastic Collisions in a Bose-Einstein Condensate near Feshbach Resonances*, Phys. Rev. Lett. **82**, 2422 (1999).
- [59] J. L. Roberts, N. R. Claussen, J. P. Burke, C. H. Greene, E. A. Cornell, and C. E. Wieman, *Resonant Magnetic Field Control of Elastic Scattering in Cold ^{85}Rb* , Phys. Rev. Lett. **81**, 5109 (1998).
- [60] S. L. Cornish, N. R. Claussen, J. L. Roberts, E. A. Cornell, and C. E. Wieman, *Stable ^{85}Rb Bose-Einstein Condensates with Widely Tunable Interactions*, Phys. Rev. Lett. **85**, 1795 (2000).
- [61] F. K. Fatemi, K. M. Jones, and P. D. Lett, *Observation of Optically Induced Feshbach Resonances in Collisions of Cold Atoms*, Phys. Rev. Lett. **85**, 4462 (2000).
- [62] M. Theis, G. Thalhammer, K. Winkler, M. Hellwig, G. Ruff, R. Grimm, and J. H. Denschlag, *Tuning the Scattering Length with an Optically Induced Feshbach Resonance*, Phys. Rev. Lett. **93**, 123001 (2004).
- [63] D. M. Bauer, M. Lettner, C. Vo, G. Rempe, and S. Durr, *Control of a magnetic Feshbach resonance with laser light*, Nat. Phys. **5**, 339 (2009).

- [64] K. E. Strecker, G. B. Partridge, A. G. Truscott, and R. G. Hulet, *Formation and propagation of matter-wave soliton trains*, Nature **417**, 150 (2002).
- [65] L. Khaykovich, F. Schreck, G. Ferrari, T. Bourdel, J. Cubizolles, L. D. Carr, Y. Castin, and C. Salomon, *Formation of a Matter-Wave Bright Soliton*, Science **296**, 1290 (2002).
- [66] S. L. Cornish, S. T. Thompson, and C. E. Wieman, *Formation of Bright Matter-Wave Solitons during the Collapse of Attractive Bose-Einstein Condensates*, Phys. Rev. Lett. **96**, 170401 (2006).
- [67] J. Herbig, T. Kraemer, M. Mark, T. Weber, C. Chin, H.-C. Nagerl, and R. Grimm, *Preparation of a Pure Molecular Quantum Gas*, Science **301**, 1510 (2003).
- [68] C. A. Regal, C. Ticknor, J. L. Bohn, and D. S. Jin, *Creation of ultracold molecules from a Fermi gas of atoms*, Nature **424**, 47 (2003).
- [69] M. Bartenstein, A. Altmeyer, S. Riedl, S. Jochim, C. Chin, J. H. Denschlag, and R. Grimm, *Crossover from a Molecular Bose-Einstein Condensate to a Degenerate Fermi Gas*, Phys. Rev. Lett. **92**, 120401 (2004).
- [70] T. Bourdel, L. Khaykovich, J. Cubizolles, J. Zhang, F. Chevy, M. Teichmann, L. Tar Russell, S. J. J. M. F. Kokkelmans, and C. Salomon, *Experimental study of the BEC-BCS crossover region in lithium 6*, Phys. Rev. Lett. **93**, 050401 (2004).
- [71] F. K. Abdullaev, J. G. Caputo, R. A. Kraenkel, and B. A. Malomed, *Controlling collapse in Bose-Einstein condensates by temporal modulation of the scattering length*, Phys. Rev. A **67**, 013605 (2003).
- [72] H. Saito and M. Ueda, *Dynamically Stabilized Bright Solitons in a Two-Dimensional Bose-Einstein Condensate*, Phys. Rev. Lett. **90**, 040403 (2003).
- [73] G. D. Montesinos, V. M. Pérez-García, and P. J. Torres, *Stabilization of solitons of the multidimensional nonlinear Schrödinger equation: matter-wave breathers*, Physica D **191**, 193 (2004).
- [74] P. G. Kevrekidis, G. Theocharis, D. J. Frantzeskakis, and B. A. Malomed, *Feshbach Resonance Management for Bose-Einstein Condensates*, Phys. Rev. Lett. **90**, 230401 (2003).
- [75] D. E. Pelinovsky, P. G. Kevrekidis, and D. J. Frantzeskakis, *Averaging for Solitons with Nonlinearity Management*, Phys. Rev. Lett. **91**, 240201 (2003).
- [76] D. E. Pelinovsky, P. G. Kevrekidis, D. J. Frantzeskakis, and V. Zharnitsky, *Hamiltonian averaging for solitons with nonlinearity management*, Phys. Rev. E **70**, 047604 (2004).
- [77] Z. X. Liang, Z. D. Zhang, and W. M. Liu, *Dynamics of a Bright Soliton in Bose-Einstein Condensates with Time-Dependent Atomic Scattering Length in an Expulsive Parabolic Potential*, Phys. Rev. Lett. **94**, 050402 (2005).
- [78] M. Matuszewski, E. Infeld, B. A. Malomed, and M. Trippenbach, *Fully Three Dimensional Breather Solitons Can Be Created Using Feshbach Resonances*, Phys. Rev. Lett. **95**, 050403 (2005).

- [79] R. Yamazaki, S. Taie, S. Sugawa, and Y. Takahashi, Nanometer-scale spatial modulation of an inter-atomic interaction in a Bose-Einstein condensate, arXiv:1005.3372v1.
- [80] G. Theocharis, P. Schmelcher, P. G. Kevrekidis, and D. J. Frantzeskakis, *Matter-wave solitons of collisionally inhomogeneous condensates*, Phys. Rev. A **72**, 033614 (2005).
- [81] F. K. Abdullaev and M. Salerno, *Adiabatic compression of soliton matter waves*, J. Phys. B **36**, 2851 (2003).
- [82] M. I. Rodas-Verde, H. Michinel, and V. M. Pérez-García, *Controllable Soliton Emission from a Bose-Einstein Condensate*, Phys. Rev. Lett. **95**, 153903 (2005).
- [83] A. V. Carpentier, H. Michinel, M. I. Rodas-Verde, and V. M. Pérez-García, *Analysis of an atom laser based on the spatial control of the scattering length*, Phys. Rev. A **74**, 013619 (2006).
- [84] G. Theocharis, P. Schmelcher, P. G. Kevrekidis, and D. J. Frantzeskakis, *Dynamical trapping and transmission of matter-wave solitons in a collisionally inhomogeneous environment*, Phys. Rev. A **74**, 053614 (2006).
- [85] J. Garnier and F. K. Abdullaev, *Transmission of matter-wave solitons through nonlinear traps and barriers*, Phys. Rev. A **74**, 013604 (2006).
- [86] G. Dong, B. Hu, and W. Lu, *Ground-state properties of a Bose-Einstein condensate tuned by a far-off-resonant optical field*, Phys. Rev. A **74**, 063601 (2006).
- [87] Y. V. Bludov, V. A. Brazhnyi, and V. V. Konotop, *Delocalizing transition in one-dimensional condensates in optical lattices due to inhomogeneous interactions*, Phys. Rev. A **76**, 023603 (2007).
- [88] P. Niarchou, G. Theocharis, P. G. Kevrekidis, P. Schmelcher, and D. J. Frantzeskakis, *Soliton oscillations in collisionally inhomogeneous attractive Bose-Einstein condensates*, Phys. Rev. A **76**, 023615 (2007).
- [89] F. K. Abdullaev and J. Garnier, *Propagation of matter-wave solitons in periodic and random nonlinear potentials*, Phys. Rev. A **72**, 061605 (2005).
- [90] H. Sakaguchi and B. A. Malomed, *Matter-wave solitons in nonlinear optical lattices*, Phys. Rev. E **72**, 046610 (2005).
- [91] M. A. Porter, P. Kevrekidis, B. A. Malomed, and D. Frantzeskakis, *Modulated amplitude waves in collisionally inhomogeneous Bose-Einstein condensates*, Physica D **229**, 104 (2007).
- [92] F. Abdullaev, A. Abdumalikov, and R. Galimzyanov, *Gap solitons in Bose-Einstein condensates in linear and nonlinear optical lattices*, Phys. Lett. A **367**, 149 (2007).
- [93] Y. V. Bludov and V. V. Konotop, *Localized modes in arrays of boson-fermion mixtures*, Phys. Rev. A **74**, 043616 (2006).
- [94] M. T. Primatarowa, K. T. Stoychev, and R. S. Kamburova, *Interaction of solitons with extended nonlinear defects*, Phys. Rev. E **72**, 036608 (2005).

- [95] V. M. Pérez-García and R. Pardo, *Localization phenomena in nonlinear Schrödinger equations with spatially inhomogeneous nonlinearities: Theory and applications to Bose-Einstein condensates*, Physica D **238**, 1352 (2009).
- [96] G. Fibich, Y. Sivan, and M. Weinstein, *Bound states of nonlinear Schrödinger equations with a periodic nonlinear microstructure*, Physica D **217**, 31 (2006).
- [97] Y. Sivan, G. Fibich, and M. I. Weinstein, *Waves in Nonlinear Lattices: Ultrashort Optical Pulses and Bose-Einstein Condensates*, Phys. Rev. Lett. **97**, 193902 (2006).
- [98] J. Belmonte-Beitia, V. M. Pérez-García, V. Vekslerchik, and P. J. Torres, *Lie Symmetries and Solitons in Nonlinear Systems with Spatially Inhomogeneous Nonlinearities*, Phys. Rev. Lett. **98**, 064102 (2007).
- [99] Z. Rapti, P. G. Kevrekidis, V. V. Konotop, and C. K. R. T. Jones, *Solitary waves under the competition of linear and nonlinear periodic potentials*, J. Phys. A **40**, 14151 (2007).
- [100] F. K. Abdullaev, Y. V. Bludov, S. V. Dmitriev, P. G. Kevrekidis, and V. V. Konotop, *Generalized neighbor-interaction models induced by nonlinear lattices*, Phys. Rev. E **77**, 016604 (2008).
- [101] D. J. Frantzeskakis, *Dark solitons in atomic Bose-Einstein condensates: from theory to experiments*, J. Phys. A **43**, 213001 (2010).
- [102] S. Burger, K. Bongs, S. Dettmer, W. Ertmer, K. Sengstock, A. Sanpera, G. V. Shlyapnikov, and M. Lewenstein, *Dark Solitons in Bose-Einstein Condensates*, Phys. Rev. Lett. **83**, 5198 (1999).
- [103] J. Denschlag, J. E. Simsarian, D. L. Feder, C. W. Clark, L. A. Collins, J. Cubizolles, L. Deng, E. W. Hagley, K. Helmerson, W. P. Reinhardt, S. L. Rolston, B. I. Schneider, and W. D. Phillips, *Generating Solitons by Phase Engineering of a Bose-Einstein Condensate*, Science **287**, 97 (2000).
- [104] Z. Dutton, M. Budde, C. Slowe, and L. V. Hau, *Observation of Quantum Shock Waves Created with Ultra-Compressed Slow Light Pulses in a Bose-Einstein Condensate*, Science **293**, 663 (2001).
- [105] B. P. Anderson, P. C. Haljan, C. A. Regal, D. L. Feder, L. A. Collins, C. W. Clark, and E. A. Cornell, *Watching Dark Solitons Decay into Vortex Rings in a Bose-Einstein Condensate*, Phys. Rev. Lett. **86**, 2926 (2001).
- [106] N. S. Ginsberg, J. Brand, and L. V. Hau, *Observation of Hybrid Soliton Vortex-Ring Structures in Bose-Einstein Condensates*, Phys. Rev. Lett. **94**, 040403 (2005).
- [107] P. Engels and C. Atherton, *Stationary and Nonstationary Fluid Flow of a Bose-Einstein Condensate Through a Penetrable Barrier*, Phys. Rev. Lett. **99**, 160405 (2007).
- [108] C. Becker, S. Stellmer, P. Soltan-Panahi, S. Dörscher, M. Baumert, E.-M. Richter, J. Kronjäger, K. Bongs, and K. Sengstock, *Oscillations and interactions of dark and dark-bright solitons in Bose-Einstein condensates*, Nat. Phys. **4**, 496 (2008).

- [109] S. Stellmer, C. Becker, P. Soltan-Panahi, E.-M. Richter, S. Dörscher, M. Baumert, J. Kronjäger, K. Bongs, and K. Sengstock, *Collisions of Dark Solitons in Elongated Bose-Einstein Condensates*, Phys. Rev. Lett. **101**, 120406 (2008).
- [110] A. Weller, J. P. Ronzheimer, C. Gross, J. Esteve, M. K. Oberthaler, D. J. Frantzeskakis, G. Theocharis, and P. G. Kevrekidis, *Experimental Observation of Oscillating and Interacting Matter Wave Dark Solitons*, Phys. Rev. Lett. **101**, 130401 (2008).
- [111] I. Shomroni, E. Lahoud, S. Levy, and J. Steinhauer, *Evidence for an oscillating soliton/vortex ring by density engineering of a Bose-Einstein condensate*, Nat. Phys. **5**, 193 (2009).
- [112] G. Theocharis, A. Weller, J. P. Ronzheimer, C. Gross, M. K. Oberthaler, P. G. Kevrekidis, and D. J. Frantzeskakis, *Multiple atomic dark solitons in cigar-shaped Bose-Einstein condensates*, Phys. Rev. A (in press, 2010), e-print arXiv:0909.2122v1.
- [113] W. H. Zurek, *Causality in Condensates: Gray Solitons as Relics of BEC Formation*, Phys. Rev. Lett. **102**, 105702 (2009).
- [114] B. Damski and W. H. Zurek, *Soliton Creation During a Bose-Einstein Condensation*, Phys. Rev. Lett. **104**, 160404 (2010).
- [115] J. Anglin, *Atomic dark solitons: Quantum canaries learn to fly*, Nat. Phys. **4**, 437 (2008).
- [116] A. Negretti and C. Henkel, *Enhanced phase sensitivity and soliton formation in an integrated BEC interferometer*, J. Phys. B **37**, L385 (2004).
- [117] A. Negretti, C. Henkel, and K. Mølmer, *Quantum fluctuations in the image of a Bose gas*, Phys. Rev. A **78**, 023630 (2008).
- [118] P. O. Fedichev, A. E. Muryshev, and G. V. Shlyapnikov, *Dissipative dynamics of a kink state in a Bose-condensed gas*, Phys. Rev. A **60**, 3220 (1999).
- [119] A. Muryshev, G. V. Shlyapnikov, W. Ertmer, K. Sengstock, and M. Lewenstein, *Dynamics of Dark Solitons in Elongated Bose-Einstein Condensates*, Phys. Rev. Lett. **89**, 110401 (2002).
- [120] D. L. Feder, M. S. Pindzola, L. A. Collins, B. I. Schneider, and C. W. Clark, *Dark-soliton states of Bose-Einstein condensates in anisotropic traps*, Phys. Rev. A **62**, 053606 (2000).
- [121] T. Busch and J. R. Anglin, *Motion of Dark Solitons in Trapped Bose-Einstein Condensates*, Phys. Rev. Lett. **84**, 2298 (2000).
- [122] D. J. Frantzeskakis, G. Theocharis, F. K. Diakonos, P. Schmelcher, and Y. S. Kivshar, *Interaction of dark solitons with localized impurities in Bose-Einstein condensates*, Phys. Rev. A **66**, 053608 (2002).
- [123] V. V. Konotop and L. Pitaevskii, *Landau Dynamics of a Grey Soliton in a Trapped Condensate*, Phys. Rev. Lett. **93**, 240403 (2004).
- [124] G. Theocharis, P. Schmelcher, M. K. Oberthaler, P. G. Kevrekidis, and D. J.

- Frantzeskakis, *Lagrangian approach to the dynamics of dark matter-wave solitons*, Phys. Rev. A **72**, 023609 (2005).
- [125] D. E. Pelinovsky, D. J. Frantzeskakis, and P. G. Kevrekidis, *Oscillations of dark solitons in trapped Bose-Einstein condensates*, Phys. Rev. E **72** (2005).
- [126] V. A. Brazhnyi, V. V. Konotop, and L. P. Pitaevskii, *Dark solitons as quasiparticles in trapped condensates*, Phys. Rev. A **73** (2006).
- [127] M. Coles, D. Pelinovsky, and P. Kevrekidis, Excited states in the Thomas-Fermi limit: a variational approach, arXiv:0910.5249v1.
- [128] N. G. Parker, N. P. Proukakis, M. Leadbeater, and C. S. Adams, *Soliton-sound interactions in quasi-one-dimensional Bose-Einstein condensates*, Phys. Rev. Lett. **90** (2003).
- [129] F. K. Abdullaev, B. B. Baizakov, S. A. Darmanyan, V. V. Konotop, and M. Salerno, *Nonlinear excitations in arrays of Bose-Einstein condensates*, Phys. Rev. A **64**, 043606 (2001).
- [130] A. V. Yulin and D. V. Skryabin, *Out-of-gap Bose-Einstein solitons in optical lattices*, Phys. Rev. A **67**, 023611 (2003).
- [131] G. L. Alfimov, V. V. Konotop, and M. Salerno, *Matter solitons in Bose-Einstein condensates with optical lattices*, EPL **58**, 7 (2002).
- [132] V. V. Konotop and M. Salerno, *Modulational instability in Bose-Einstein condensates in optical lattices*, Phys. Rev. A **65**, 021602 (2002).
- [133] P. J. Y. Louis, E. A. Ostrovskaya, and Y. S. Kivshar, *Matter-wave dark solitons in optical lattices*, Journal of Optics B: Quantum and Semiclassical Optics **6**, S309 (2004).
- [134] P. G. Kevrekidis, R. Carretero-González, G. Theocharis, D. J. Frantzeskakis, and B. A. Malomed, *Stability of dark solitons in a Bose-Einstein condensate trapped in an optical lattice*, Phys. Rev. A **68** (2003).
- [135] P. G. Kevrekidis, R. Carretero-González, G. Theocharis, D. J. Frantzeskakis, and B. A. Malomed, *Stability of dark solitons in a Bose-Einstein condensate trapped in an optical lattice* (vol 68, pg 035602, 2003), Phys. Rev. A **72** (2005).
- [136] N. G. Parker, N. P. Proukakis, C. F. Barenghi, and C. S. Adams, *Dynamical instability of a dark soliton in a quasi-one-dimensional Bose-Einstein condensate perturbed by an optical lattice*, J. Phys. B **37**, S175 (2004).
- [137] G. Theocharis, D. J. Frantzeskakis, R. Carretero-González, P. G. Kevrekidis, and B. A. Malomed, *Controlling the motion of dark solitons by means of periodic potentials: Application to Bose-Einstein condensates in optical lattices*, Phys. Rev. E **71** (2005).
- [138] G. Theocharis, D. J. Frantzeskakis, P. G. Kevrekidis, R. Carretero-González, and B. A. Malomed, *Dark soliton dynamics in spatially inhomogeneous media: Application to Bose-Einstein condensates*, Mathematics and Computers in Simulation **69**, 537 (2005).
- [139] C. Menotti and S. Stringari, *Collective oscillations of a one-dimensional trapped Bose-Einstein gas*, Phys. Rev. A **66**, 043610 (2002).

- [140] G. Theocharis, P. G. Kevrekidis, M. K. Oberthaler, and D. J. Frantzeskakis, *Dark matter-wave solitons in the dimensionality crossover*, Phys. Rev. A **76**, 045601 (2007).
- [141] F. Gerbier, *Quasi-1D Bose-Einstein condensates in the dimensional crossover regime*, EPL **66**, 771 (2004).
- [142] L. Salasnich, A. Parola, and L. Reatto, *Effective wave equations for the dynamics of cigar-shaped and disk-shaped Bose condensates*, Phys. Rev. A **65**, 043614 (2002).
- [143] A. M. Mateo and V. Delgado, *Ground-state properties of trapped Bose-Einstein condensates: Extension of the Thomas-Fermi approximation*, Phys. Rev. A **75**, 063610 (2007).
- [144] A. M. Mateo and V. Delgado, *Effective mean-field equations for cigar-shaped and disk-shaped Bose-Einstein condensates*, Phys. Rev. A **77**, 013617 (2008).
- [145] A. M. Mateo and V. Delgado, *Effective one-dimensional dynamics of elongated Bose-Einstein condensates*, Annals of Physics **324**, 709 (2009).
- [146] P. G. Kevrekidis, R. Carretero-González, D. J. Frantzeskakis, and I. G. Kevrekidis, *Vortices in Bose-Einstein condensates: Some recent developments*, Mod. Phys. B **18**, 1481 (2004).
- [147] A. L. Fetter and A. A. Svidzinsky, *Vortices in a trapped dilute Bose-Einstein condensate*, Journal Of Physics-Condensed Matter **13**, R135 (2001).
- [148] Y. S. Kivshar, J. Christou, V. Tikhonenko, B. Luther-Davies, and L. M. Pismen, *Dynamics of optical vortex solitons*, Optics Communications **152**, 198 (1998).
- [149] A. Dreischuh, S. Chervenkov, D. Neshev, G. G. Paulus, and H. Walther, *Generation of lattice structures of optical vortices*, Journal Of The Optical Society Of America B-Optical Physics **19**, 550 (2002).
- [150] Y. S. Kivshar and B. Luther-Davies, *Dark optical solitons: physics and applications*, Phys. Rep. **298**, 81 (1998).
- [151] A. S. Desyatnikov, Y. S. Kivshar, and L. Torner, *Optical vortices and vortex solitons*, Progress In Optics, Vol 47 **47**, 291 (2005).
- [152] L. M. Pismen, *Vortices in Nonlinear Fields*, Oxford University Press, 1999.
- [153] M. R. Matthews, B. P. Anderson, P. C. Haljan, D. S. Hall, C. E. Wieman, and E. A. Cornell, *Vortices in a Bose-Einstein Condensate*, Phys. Rev. Lett. **83**, 2498 (1999).
- [154] J. E. Williams and M. J. Holland, *Preparing topological states of a Bose-Einstein condensate*, Nature **401**, 568 (1999).
- [155] K. W. Madison, F. Chevy, W. Wohlleben, and J. Dalibard, *Vortex Formation in a Stirred Bose-Einstein Condensate*, Phys. Rev. Lett. **84**, 806 (2000).
- [156] A. Recati, F. Zambelli, and S. Stringari, *Overcritical Rotation of a Trapped Bose-Einstein Condensate*, Phys. Rev. Lett. **86**, 377 (2001).
- [157] S. Sinha and Y. Castin, *Dynamic Instability of a Rotating Bose-Einstein Condensate*, Phys. Rev. Lett. **87**, 190402 (2001).

- [158] K. W. Madison, F. Chevy, V. Bretin, and J. Dalibard, *Stationary States of a Rotating Bose-Einstein Condensate: Routes to Vortex Nucleation*, Phys. Rev. Lett. **86**, 4443 (2001).
- [159] C. Raman, J. R. Abo-Shaeer, J. M. Vogels, K. Xu, and W. Ketterle, *Vortex Nucleation in a Stirred Bose-Einstein Condensate*, Phys. Rev. Lett. **87**, 210402 (2001).
- [160] R. Onofrio, C. Raman, J. M. Vogels, J. R. Abo-Shaeer, A. P. Chikkatur, and W. Ketterle, *Observation of Superfluid Flow in a Bose-Einstein Condensed Gas*, Phys. Rev. Lett. **85**, 2228 (2000).
- [161] D. R. Scherer, C. N. Weiler, T. W. Neely, and B. P. Anderson, *Vortex Formation by Merging of Multiple Trapped Bose-Einstein Condensates*, Phys. Rev. Lett. **98**, 110402 (2007).
- [162] A. E. Leanhardt, A. Görlitz, A. P. Chikkatur, D. Kielpinski, Y. Shin, D. E. Pritchard, and W. Ketterle, *Imprinting Vortices in a Bose-Einstein Condensate using Topological Phases*, Phys. Rev. Lett. **89**, 190403 (2002).
- [163] Y. Shin, M. Saba, M. Vengalattore, T. A. Pasquini, C. Sanner, A. E. Leanhardt, M. Prentiss, D. E. Pritchard, and W. Ketterle, *Dynamical Instability of a Doubly Quantized Vortex in a Bose-Einstein Condensate*, Phys. Rev. Lett. **93**, 160406 (2004).
- [164] H. Pu, C. K. Law, J. H. Eberly, and N. P. Bigelow, *Coherent disintegration and stability of vortices in trapped Bose condensates*, Phys. Rev. A **59**, 1533 (1999).
- [165] M. Möttönen, S. M. M. Virtanen, T. Isoshima, and M. M. Salomaa, *Stationary vortex clusters in nonrotating Bose-Einstein condensates*, Phys. Rev. A **71**, 033626 (2005).
- [166] T. P. Simula, S. M. M. Virtanen, and M. M. Salomaa, *Stability of multiquantum vortices in dilute Bose-Einstein condensates*, Phys. Rev. A **65**, 033614 (2002).
- [167] E. Lundh, *Multiply quantized vortices in trapped Bose-Einstein condensates*, Phys. Rev. A **65**, 043604 (2002).
- [168] J. A. M. Huhtamäki, M. Möttönen, and S. M. M. Virtanen, *Dynamically stable multiply quantized vortices in dilute Bose-Einstein condensates*, Phys. Rev. A **74**, 063619 (2006).
- [169] E. Lundh and H. M. Nilsen, *Dynamic stability of a doubly quantized vortex in a three-dimensional condensate*, Phys. Rev. A **74**, 063620 (2006).
- [170] J. R. Abo-Shaeer, C. Raman, J. M. Vogels, and W. Ketterle, *Observation of Vortex Lattices in Bose-Einstein Condensates*, Science **292**, 476 (2001).
- [171] L.-C. Crasovan, V. Vekslerchik, V. M. Pérez-García, J. P. Torres, D. Mihalache, and L. Torner, *Stable vortex dipoles in nonrotating Bose-Einstein condensates*, Phys. Rev. A **68**, 063609 (2003).
- [172] V. Pietilä, M. Möttönen, T. Isoshima, J. A. M. Huhtamäki, and S. M. M. Virtanen, *Stability and dynamics of vortex clusters in nonrotated Bose-Einstein condensates*, Phys. Rev. A **74**, 023603 (2006).
- [173] A. Klein, D. Jaksch, Y. Zhang, and W. Bao, *Dynamics of vortices in weakly interacting Bose-Einstein condensates*, Phys. Rev. A **76**, 043602 (2007).

- [174] W. Li, M. Haque, and S. Komineas, *Vortex dipole in a trapped two-dimensional Bose-Einstein condensate*, Phys. Rev. A **77**, 053610 (2008).
- [175] T. Schulte, L. Santos, A. Sanpera, and M. Lewenstein, *Vortex-vortex interactions in toroidally trapped Bose-Einstein condensates*, Phys. Rev. A **66**, 033602 (2002).
- [176] D. M. Jezek, P. Capuzzi, M. Guilleumas, and R. Mayol, *Stationary rings of vortices in nonrotating Bose-Einstein condensates*, Phys. Rev. A **78**, 053616 (2008).
- [177] R. Geurts, M. V. Milošević, and F. M. Peeters, *Topologically trapped vortex molecules in Bose-Einstein condensates*, Phys. Rev. A **78**, 053610 (2008).
- [178] S. McEndoo and T. Busch, *Small numbers of vortices in anisotropic traps*, Phys. Rev. A **79**, 053616 (2009).
- [179] E. A. Kuznetsov and S. K. Turitsyn, *Soliton Instability And Collapse In Media With Defocusing Nonlinearity*, Zh. Eksp. Teor. Fys. **94**, 119 (1988).
- [180] V. Tikhonenko, J. Christou, B. LutherDavies, and Y. S. Kivshar, *Observation of vortex solitons created by the instability of dark soliton stripes*, Optics Letters **21**, 1129 (1996).
- [181] A. V. Mamaev, M. Saffman, and A. A. Zozulya, *Propagation of Dark Stripe Beams in Nonlinear Media: Snake Instability and Creation of Optical Vortices*, Phys. Rev. Lett. **76**, 2262 (1996).
- [182] G. Theocharis, D. J. Frantzeskakis, P. G. Kevrekidis, B. A. Malomed, and Y. S. Kivshar, *Ring dark solitons and vortex necklaces in Bose-Einstein condensates*, Phys. Rev. Lett. **90** (2003).
- [183] L. D. Carr and C. W. Clark, *Vortices and ring solitons in Bose-Einstein condensates*, Phys. Rev. A **74**, 043613 (2006).
- [184] G. Herring, L. D. Carr, R. Carretero-González, P. G. Kevrekidis, and D. J. Frantzeskakis, *Radially symmetric nonlinear states of harmonically trapped Bose-Einstein condensates*, Phys. Rev. A **77** (2008).
- [185] A. E. Muryshev, H. B. van Linden van den Heuvell, and G. V. Shlyapnikov, *Stability of standing matter waves in a trap*, Phys. Rev. A **60**, R2665 (1999).
- [186] P. G. Kevrekidis, G. Theocharis, D. J. Frantzeskakis, and A. Trombettoni, *Avoiding infrared catastrophes in trapped Bose-Einstein condensates*, Phys. Rev. A **70** (2004).
- [187] M. Ma, R. Carretero-González, P. G. Kevrekidis, D. J. Frantzeskakis, and B. A. Malomed, *Controlling the transverse instability of dark solitons and nucleation of vortices by a potential barrier*, arXiv:1004.3060v1.
- [188] J. Brand and W. P. Reinhardt, *Solitonic vortices and the fundamental modes of the “snake instability”: Possibility of observation in the gaseous Bose-Einstein condensate*, Phys. Rev. A **65**, 043612 (2002).
- [189] M. A. Hoefer, P. Engels, and J. J. Chang, *Matter-wave interference in Bose-Einstein condensates: A dispersive hydrodynamic perspective*, Physica D **238**, 1311 (2009).

- [190] T. W. Neely, E. C. Samson, A. S. Bradley, M. J. Davis, and B. P. Anderson, *Observation of Vortex Dipoles in an Oblate Bose-Einstein Condensate*, Phys. Rev. Lett. **104**, 160401 (2010).
- [191] D. Freilich, D.V. and Bianchi, A. Kaufman, T. Langin, and D. Hall, Experimental Visualization of Vortex Dynamics in a Bose-Einstein Condensate, submitted.
- [192] J. A. Seman, E. A. L. Henn, M. Haque, R. F. Shiozaki, E. R. F. Ramos, M. Caracanhas, C. Castelo Branco, G. Roati, K. M. F. Magalhães, and V. S. Bagnato, Three-vortex configurations in trapped Bose-Einstein condensates, arXiv:0907.1584v2.
- [193] T. W. B. Kibble, *Topology of cosmic domains and strings*, J. Phys. A **9**, 1387 (1976).
- [194] W. H. ZUREK, *Cosmological Experiments In Superfluid-Helium*, Nature **317**, 505 (1985).
- [195] W. H. Zurek, *Cosmological experiments in condensed matter systems*, Phys. Rep. **276**, 177 (1996).
- [196] C. N. Weiler, T. W. Neely, D. R. Scherer, A. S. Bradley, M. J. Davis, and B. P. Anderson, *Spontaneous vortices in the formation of Bose-Einstein condensates*, Nature **455**, 948 (2008).
- [197] C. J. Myatt, E. A. Burt, R. W. Ghrist, E. A. Cornell, and C. E. Wieman, *Production of Two Overlapping Bose-Einstein Condensates by Sympathetic Cooling*, Phys. Rev. Lett. **78**, 586 (1997).
- [198] J. Stenger, S. Inouye, D. M. Stamper-Kurn, H.-J. Miesner, A. P. Chikkatur, and W. Ketterle, *Spin domains in ground-state Bose-Einstein condensates*, Nature **396**, 345 (1998).
- [199] T.-L. Ho, *Spinor Bose Condensates in Optical Traps*, Phys. Rev. Lett. **81**, 742 (1998).
- [200] O. Zobay and B. M. Garraway, *Two-Dimensional Atom Trapping in Field-Induced Adiabatic Potentials*, Phys. Rev. Lett. **86**, 1195 (2001).
- [201] H.-J. Miesner, D. M. Stamper-Kurn, J. Stenger, S. Inouye, A. P. Chikkatur, and W. Ketterle, *Observation of Metastable States in Spinor Bose-Einstein Condensates*, Phys. Rev. Lett. **82**, 2228 (1999).
- [202] D. M. Stamper-Kurn, H.-J. Miesner, A. P. Chikkatur, S. Inouye, J. Stenger, and W. Ketterle, *Quantum Tunneling across Spin Domains in a Bose-Einstein Condensate*, Phys. Rev. Lett. **83**, 661 (1999).
- [203] H. Schmaljohann, M. Erhard, J. Kronjäger, M. Kottke, S. van Staa, L. Cacciapuoti, J. J. Arlt, K. Bongs, and K. Sengstock, *Dynamics of $F = 2$ Spinor Bose-Einstein Condensates*, Phys. Rev. Lett. **92**, 040402 (2004).
- [204] J. Kronjäger, C. Becker, M. Brinkmann, R. Walser, P. Navez, K. Bongs, and K. Sengstock, *Evolution of a spinor condensate: Coherent dynamics, dephasing, and revivals*, Phys. Rev. A **72**, 063619 (2005).
- [205] J. Mur-Petit, M. Guilleumas, A. Polls, A. Sanpera, M. Lewenstein, K. Bongs, and K. Sengstock, *Dynamics of $F = 1$ ^{87}Rb condensates at finite temperatures*, Phys. Rev. A **73**, 013629 (2006).

- [206] G. Modugno, M. Modugno, F. Riboli, G. Roati, and M. Inguscio, *Two Atomic Species Superfluid*, Phys. Rev. Lett. **89**, 190404 (2002).
- [207] G. Thalhammer, G. Barontini, L. De Sarlo, J. Catani, F. Minardi, and M. Inguscio, *Double Species Bose-Einstein Condensate with Tunable Interspecies Interactions*, Phys. Rev. Lett. **100**, 210402 (2008).
- [208] G. Thalhammer, G. Barontini, J. Catani, F. Rabatti, C. Weber, A. Simoni, F. Minardi, and M. Inguscio, *Collisional and molecular spectroscopy in an ultracold Bose-Bose mixture*, New Journal of Physics **11**, 055044 (12pp) (2009).
- [209] Y. S. Kivshar and G. P. Agrawal, *Optical Solitons: From Fibers to Photonic Crystals*, Academic Press, 2003.
- [210] M. Ablowitz, B. Prinari, and A. Trubatch, *Discrete and Continuous Nonlinear Schrödinger Systems*, Cambridge University Press, Cambridge, 2004.
- [211] Z. Chen, M. Segev, T. H. Coskun, D. N. Christodoulides, Y. S. Kivshar, and V. V. Afanasjev, *Incoherently coupled dark-bright photorefractive solitons*, Opt. Lett. **21**, 1821 (1996).
- [212] E. A. Ostrovskaya, Y. S. Kivshar, Z. Chen, and M. Segev, *Interaction between vector solitons and solitonic gluons*, Opt. Lett. **24**, 327 (1999).
- [213] D. S. Hall, M. R. Matthews, J. R. Ensher, C. E. Wieman, and E. A. Cornell, *Dynamics of Component Separation in a Binary Mixture of Bose-Einstein Condensates*, Phys. Rev. Lett. **81**, 1539 (1998).
- [214] D. M. Stamper-Kurn, M. R. Andrews, A. P. Chikkatur, S. Inouye, H.-J. Miesner, J. Stenger, and W. Ketterle, *Optical Confinement of a Bose-Einstein Condensate*, Phys. Rev. Lett. **80**, 2027 (1998).
- [215] H. E. Nistazakis, D. J. Frantzeskakis, P. G. Kevrekidis, B. A. Malomed, and R. Carretero-González, *Bright-dark soliton complexes in spinor Bose-Einstein condensates*, Phys. Rev. A **77**, 033612 (2008).
- [216] S. Rajendran, P. Muruganandam, and M. Lakshmanan, *Interaction of darkâ€“bright solitons in two-component Boseâ€“Einstein condensates*, J. Phys. B **42**, 145307 (2009).
- [217] C. Yin, N. G. Berloff, V. M. Pérez-García, V. A. Brazhnyi, and H. Michinel, Coherent Atomic Soliton Molecules, arXiv:1003.4617v1.
- [218] K. J. H. Law, P. G. Kevrekidis, and L. S. Tuckerman, Stable Vortex-Bright Soliton Structures in Two-Component Bose Einstein Condensates, arXiv:1001.4835v1.
- [219] O. Morsch and M. Oberthaler, *Dynamics of Bose-Einstein condensates in optical lattices*, Rev. Mod. Phys. **78**, 179 (2006).
- [220] C. Chin, R. Grimm, P. Julienne, and E. Tiesinga, *Feshbach resonances in ultracold gases*, Rev. Mod. Phys. **82**, 1225 (2010).
- [221] J. M. Gerton, D. Strekalov, I. Prodan, and R. G. Hulet, *Direct observation of growth and collapse of a Bose-Einstein condensate with attractive interactions*, Nature **408**, 692 (2000).

- [222] E. A. Donley, N. R. Claussen, S. L. Cornish, J. L. Roberts, E. A. Cornell, and C. E. Wieman, *Dynamics of collapsing and exploding Bose-Einstein condensates*, Nature **412**, 295 (2001).
- [223] M. J. Ablowitz and H. Segur, *Solitons and the Inverse Scattering Transform*, Philadelphia: SIAM, 1981.
- [224] V. E. Zakharov, *Kinetic Equation For Solitons*, Sov. Phys. JETP **33**, 538 (1971).
- [225] V. E. Zakharov and A. B. Shabat, *Interaction Between Solutions In A Stable Medium*, Zh. Eksp. Teor. Fys. **64**, 1627 (1973).
- [226] K. Blow and N. Doran, *Multiple dark soliton solutions of the nonlinear Schrödinger equation*, Phys. Lett. A **107**, 55 (1985).
- [227] N. Akhmediev and A. Ankiewicz, *First-order exact solutions of the nonlinear Schrödinger equation in the normal-dispersion regime*, Phys. Rev. A **47**, 3213 (1993).
- [228] L. Gagnon, *Solitons on a continuous-wave background and collision between two dark pulses: some analytical results*, J. Opt. Soc. Am. B **10**, 469 (1993).
- [229] R. S. MacKay and J. Meiss, *Hamiltonian Dynamical Systems*, Hilger, Bristol, 1987.
- [230] A. S. Rodrigues, P. G. Kevrekidis, M. A. Porter, D. J. Frantzeskakis, P. Schmelcher, and A. R. Bishop, *Matter-wave solitons with a periodic, piecewise-constant scattering length*, Phys. Rev. A **78**, 013611 (2008).
- [231] P. Krüger, personal communication.
- [232] C. Wang, P. G. Kevrekidis, N. Whitaker, D. J. Frantzeskakis, S. Middelkamp, and P. Schmelcher, *Collisionally inhomogeneous Bose-Einstein condensates in double-well potentials*, Physica D **238**, 1362 (2009).
- [233] T. Kapitula and P. G. Kevrekidis, *Bose-Einstein condensates in the presence of a magnetic trap and optical lattice*, Chaos: An Interdisciplinary Journal of Nonlinear Science **15**, 037114 (2005).
- [234] N. G. Vakhitov and A. A. Kolokolov, *Stationary solutions of the wave equation in a medium with nonlinearity saturation*, Radiophysics and Quantum Electronics **16**, 783 (1973).
- [235] I. M. Merhasin, B. V. Gisin, R. Driben, and B. A. Malomed, *Finite-band solitons in the Kronig-Penney model with the cubic-quintic nonlinearity*, Phys. Rev. E **71**, 016613 (2005).
- [236] M. Grillakis, *Linearized instability for nonlinear schrödinger and klein-gordon equations*, Communications on Pure and Applied Mathematics **41**, 747 (1988).
- [237] M. Grillakis, J. Shatah, and W. Strauss, *Stability theory of solitary waves in the presence of symmetry, I*, Journal of Functional Analysis **74**, 160 (1987).
- [238] J. Gomez-Gardeñes, B. A. Malomed, L. M. Floría, and A. R. Bishop, *Solitons in the Salerno model with competing nonlinearities*, Phys. Rev. E **73**, 036608 (2006).

- [239] S. Middelkamp, P. G. Kevrekidis, D. J. Frantzeskakis, and P. Schmelcher, *Matter-wave solitons in the presence of collisional inhomogeneities: Perturbation theory and the impact of derivative terms*, Phys. Lett. A **373**, 262 (2009).
- [240] Y. S. Kivshar and W. Królikowski, *Lagrangian approach for dark solitons*, Optics Communications **114**, 353 (1995).
- [241] P. Smereka, B. Birnir, and S. Banerjee, *Regular and chaotic bubble oscillations in periodically driven pressure fields*, Physics of Fluids **30**, 3342 (1987).
- [242] Y. S. Kivshar and B. A. Malomed, *Dynamics of solitons in nearly integrable systems*, Rev. Mod. Phys. **61**, 763 (1989).
- [243] C. Lee, E. A. Ostrovskaya, and Y. S. Kivshar, *Nonlinearity-assisted quantum tunnelling in a matter-wave interferometer*, J. Phys. B **40**, 4235 (2007).
- [244] R. Ichihara, I. Danshita, and T. Nikuni, *Matter-wave dark solitons in a double-well potential*, Phys. Rev. A **78**, 063604 (2008).
- [245] S. Middelkamp, G. Theocharis, P. G. Kevrekidis, D. J. Frantzeskakis, and P. Schmelcher, *Dark solitons in cigar-shaped Bose-Einstein condensates in double-well potentials*, Phys. Rev. A **81**, 053618 (2010).
- [246] F. G. Bass, V. V. Konotop, and S. A. Puzenko, *Dark solitary waves in a generalized version of the nonlinear Schrödinger equation*, Phys. Rev. A **46**, 4185 (1992).
- [247] Y. S. Kivshar, T. J. Alexander, and S. K. Turitsyn, *Nonlinear modes of a macroscopic quantum oscillator*, Phys. Lett. A **278**, 225 (2001).
- [248] P. G. Kevrekidis, V. V. Konotop, A. Rodrigues, and D. J. Frantzeskakis, *Dynamic generation of matter solitons from linear states via time-dependent scattering lengths*, J. Phys. B **38**, 1173 (2005).
- [249] G. L. Alfimov and D. A. Zezyulin, *Nonlinear modes for the Gross-Pitaevskii equation - a demonstrative computation approach*, Nonlinearity **20**, 2075 (2007).
- [250] Y. S. Kivshar and X. Yang, *Perturbation-induced dynamics of dark solitons*, Phys. Rev. E **49**, 1657 (1994).
- [251] S. H. Strogatz, *Nonlinear Dynamics And Chaos*, Westview Press; 1 edition, 2000.
- [252] R. Graham, *Decoherence of Bose-Einstein Condensates in Traps at Finite Temperature*, Phys. Rev. Lett. **81**, 5262 (1998).
- [253] M. D. Lee and C. W. Gardiner, *Quantum kinetic theory. VI. The growth of a Bose-Einstein condensate*, Phys. Rev. A **62**, 033606 (2000).
- [254] S. Choi, S. A. Morgan, and K. Burnett, *Phenomenological damping in trapped atomic Bose-Einstein condensates*, Phys. Rev. A **57**, 4057 (1998).
- [255] M. Tsubota, K. Kasamatsu, and M. Ueda, *Vortex lattice formation in a rotating Bose-Einstein condensate*, Phys. Rev. A **65**, 023603 (2002).

- [256] A. A. Penckwitt, R. J. Ballagh, and C. W. Gardiner, *Nucleation, Growth, and Stabilization of Bose-Einstein Condensate Vortex Lattices*, Phys. Rev. Lett. **89**, 260402 (2002).
- [257] I. Aranson and V. Steinberg, *Stability of multicharged vortices in a model of superflow*, Phys. Rev. B **53**, 75 (1996).
- [258] R. Šášik, L. M. A. Bettencourt, and S. Habib, *Thermal vortex dynamics in a two-dimensional condensate*, Phys. Rev. B **62**, 1238 (2000).
- [259] E. Madarassy and C. Barenghi, *Vortex Dynamics in Trapped Bose-Einstein Condensate*, J. Low Temp. Phys. **152**, 122 (2008).
- [260] R. Carretero-González, N. Whitaker, P. G. Kevrekidis, and D. J. Frantzeskakis, *Vortex structures formed by the interference of sliced condensates*, Phys. Rev. A **77**, 023605 (2008).
- [261] R. Carretero-González, B. P. Anderson, P. G. Kevrekidis, D. J. Frantzeskakis, and C. N. Weiler, *Dynamics of vortex formation in merging Bose-Einstein condensate fragments*, Phys. Rev. A **77** (2008).
- [262] N. P. Proukakis, N. G. Parker, C. F. Barenghi, Adams, and C. S., *Parametric Driving of Dark Solitons in Atomic Bose-Einstein Condensates*, Phys. Rev. Lett. **93**, 130408 (2004).
- [263] N. P. Proukakis and B. Jackson, *Finite-temperature models of Bose-Einstein condensation*, Journal Of Physics B: Atomic Molecular And Optical Physics **41** (2008).
- [264] S. Middelkamp, P. G. Kevrekidis, D. J. Frantzeskakis, R. Carretero-González, and P. Schmelcher, *Stability and dynamics of matter-wave vortices in the presence of collisional inhomogeneities and dissipative perturbations*, J. Phys. B **43**, 155303 (2010).
- [265] D. L. Feder, A. A. Svidzinsky, A. L. Fetter, and C. W. Clark, *Anomalous Modes Drive Vortex Dynamics in Confined Bose-Einstein Condensates*, Phys. Rev. Lett. **86**, 564 (2001).
- [266] T. Kapitula, P. G. Kevrekidis, and B. Sandstede, *Counting eigenvalues via the Krein signature in infinite-dimensional Hamiltonian systems (vol 201, pg 199, 2005)*, Physica D **201**, 199 (2005).
- [267] A. A. Svidzinsky and A. L. Fetter, *Stability of a vortex in a trapped Bose-Einstein condensate*, Phys. Rev. Lett. **84**, 5919 (2000).
- [268] A. L. Fetter and J. K. Kim, *Vortex precession in a rotating nonaxisymmetric trapped Bose-Einstein condensate*, J. Low Temp. Phys. **125**, 239 (2001).
- [269] B. Rubinstein and L. Pismen, *Vortex motion in the spatially inhomogenous conservative Ginzburg-Landau model*, Physica D **78**, 1 (1994).
- [270] S. A. McGee and M. J. Holland, *Rotational dynamics of vortices in confined Bose-Einstein condensates*, Phys. Rev. A **63**, 043608 (2001).
- [271] J. Dziarmaga and J. Meisner, *Quantum fluctuations of a vortex in a dilute Bose-Einstein condensate*, J. Phys. B **38**, 4211 (2005).

- [272] D. E. Pelinovsky and P. G. Kevrekidis, *Dark solitons in external potentials*, Zeitschrift für angewandte Mathematik und Physik **59**, 559 (2008).
- [273] T. Kapitula, P. G. Kevrekidis, and D. J. Frantzeskakis, *Disk-shaped Bose-Einstein condensates in the presence of an harmonic trap and an optical lattice*, Chaos **18** (2008).
- [274] K. J. H. Law, L. Qiao, P. G. Kevrekidis, and I. G. Kevrekidis, *Stability of quantized vortices in a Bose-Einstein condensate confined in an optical lattice*, Phys. Rev. A **77** (2008).
- [275] P. G. Kevrekidis, R. Carretero-González, G. Theocharis, D. J. Frantzeskakis, and B. A. Malomed, *Vortices in a Bose-Einstein condensate confined by an optical lattice*, Journal of Physics B: Atomic Molecular And Optical Physics **36**, 3467 (2003).
- [276] B. Jackson, J. F. McCann, and C. S. Adams, *Vortex Formation in Dilute Inhomogeneous Bose-Einstein Condensates*, Phys. Rev. Lett. **80**, 3903 (1998).
- [277] B. Jackson, N. P. Proukakis, C. F. Barenghi, and E. Zaremba, *Finite-temperature vortex dynamics in Bose-Einstein condensates*, Phys. Rev. A **79**, 053615 (2009).
- [278] S. Thanvanthri, K. T. Kapale, and J. P. Dowling, *Ultra-Stable Matter-Wave Gyroscopy with Counter-Rotating Vortex Superpositions in Bose-Einstein Condensates*, arXiv:0907.1138v1.
- [279] S. Middelkamp, P. G. Kevrekidis, D. J. Frantzeskakis, R. Carretero-González, and P. Schmelcher, *Bifurcations, stability, and dynamics of multiple matter-wave vortex states*, Phys. Rev. A **82**, 013646 (2010).
- [280] E. W. Kirr, P. G. Kevrekidis, E. Shlizerman, and M. I. Weinstein, *Symmetry-Breaking Bifurcation In Nonlinear Schrodinger/Gross-Pitaevskii Equations*, Siam Journal On Mathematical Analysis **40**, 566 (2008).
- [281] T. Kapitula, P. G. Kevrekidis, and R. Carretero-González, *Rotating matter waves in Bose-Einstein condensates*, Physica D **233**, 112 (2007).
- [282] A. J. Chorin and J. E. Marsden, *A Mathematical Introduction to Fluid Mechanics*, Springer-Verlag, New York, 1993.
- [283] P. G. Kevrekidis and D. J. Frantzeskakis, *Pattern forming dynamical instabilities of Bose-Einstein condensates*, Mod. Phys. B **18**, 173 (2004).
- [284] P. K. Newton and G. Chamoun, *Vortex Lattice Theory: A Particle Interaction Perspective*, Siam Review **51**, 501 (2009).
- [285] G. Theocharis, A. Weller, J. P. Ronzheimer, C. Gross, M. K. Oberthaler, P. G. Kevrekidis, and D. J. Frantzeskakis, *Multiple atomic dark solitons in cigar-shaped Bose-Einstein condensates*, arXiv:0909.2122v1.
- [286] C. Lobo and Y. Castin, *Nonclassical scissors mode of a vortex lattice in a Bose-Einstein condensate*, Phys. Rev. A **72**, 043606 (2005).
- [287] S. Middelkamp, J. J. Chang, C. Hamner, R. Carretero-González, P. G. Kevrekidis,

- V. Achilleos, D. J. Frantzeskakis, P. Schmelcher, and P. Engels, *Dynamics of dark-bright solitons in cigar-shaped Bose-Einstein condensates*, arXiv:1005.3789v2 (2010).
- [288] L. Salasnich and B. A. Malomed, *Vector solitons in nearly one-dimensional Bose-Einstein condensates*, Phys. Rev. A **74**, 053610 (2006).
- [289] C. Hamner, J. Chang, P. Engels, and M. A. Hoefer, Generation of inter-component dispersive shocks and dark-bright soliton trains in counterflowing superfluids, arXiv:1005.2610v1.
- [290] S. Kokkelmans, Private communication.
- [291] M.-O. Mewes, M. R. Andrews, D. M. Kurn, D. S. Durfee, C. G. Townsend, and W. Ketterle, *Output Coupler for Bose-Einstein Condensed Atoms*, Phys. Rev. Lett. **78**, 582 (1997).
- [292] E. W. Hagley, L. Deng, M. Kozuma, J. Wen, K. Helmerson, S. L. Rolston, and W. D. Phillips, *A Well-Collimated Quasi-Continuous Atom Laser*, Science **283**, 1706 (1999).
- [293] S. Middelkamp, I. Lesanovsky, and P. Schmelcher, *Interaction-induced trapping and pulsed emission of a magnetically insensitive Bose-Einstein condensate*, EPL **84**, 40011 (2008).
- [294] H. Saito, Y. Kawaguchi, and M. Ueda, *Breaking of Chiral Symmetry and Spontaneous Rotation in a Spinor Bose-Einstein Condensate*, Phys. Rev. Lett. **96**, 065302 (2006).
- [295] I. Lesanovsky and W. von Klitzing, *Time-Averaged Adiabatic Potentials: Versatile Matter-Wave Guides and Atom Traps*, Phys. Rev. Lett. **99**, 083001 (2007).
- [296] G. Pupillo, A. Griessner, A. Micheli, M. Ortner, D.-W. Wang, and P. Zoller, *Cold Atoms and Molecules in Self-Assembled Dipolar Lattices*, Phys. Rev. Lett. **100**, 050402 (2008).
- [297] S. Middelkamp, M. Mayle, I. Lesanovsky, and P. Schmelcher, *Creating versatile atom traps by applying near-resonant laser light in magnetic traps*, Phys. Rev. A **81**, 053414 (2010).
- [298] D. E. Pritchard, *Cooling Neutral Atoms in a Magnetic Trap for Precision Spectroscopy*, Phys. Rev. Lett. **51**, 1336 (1983).
- [299] E. Arimondo, M. Inguscio, and P. Violino, *Experimental determinations of the hyperfine structure in the alkali atoms*, Rev. Mod. Phys. **49**, 31 (1977).
- [300] M. O. Scully and M. S. Zubairy, *Quantum Optics*, Cambridge University Press; 1 edition, 1997.
- [301] I. Shavitt and L. T. Redmon, *Quasidegenerate perturbation theories. A canonical van Vleck formalism and its relationship to other approaches*, The Journal of Chemical Physics **73**, 5711 (1980).
- [302] R. Loudon, *The quantum Theory of Light*, Oxford, 1983.
- [303] U. Volz and H. Schmoranz, *Precision lifetime measurements on alkali atoms and on helium by beam-gas-laser spectroscopy*, Physica Scripta **T65**, 48 (1996).

- [304] C. L. Garrido Alzar, H. Perrin, B. M. Garraway, and V. Lorent, *Evaporative cooling in a radio-frequency trap*, Phys. Rev. A **74**, 053413 (2006).
- [305] M. Mayle, I. Lesanovsky, and P. Schmelcher, *Exploiting the composite character of Rydberg atoms for cold-atom trapping*, Phys. Rev. A **79**, 041403(R) (2009).
- [306] M. Mayle, I. Lesanovsky, and P. Schmelcher, *Erratum: Exploiting the composite character of Rydberg atoms for cold-atom trapping [Phys. Rev. A **79**, 041403 (2009)]*, Phys. Rev. A **80**, 029903(E) (2009).
- [307] M. Mayle, I. Lesanovsky, and P. Schmelcher, Dressing of Ultracold Atoms by their Rydberg States in a Ioffe-Pritchard Trap, arXiv:1002.2870v1.
- [308] A. Micheli, A. J. Daley, D. Jaksch, and P. Zoller, *Single Atom Transistor in a 1D Optical Lattice*, Phys. Rev. Lett. **93**, 140408 (2004).
- [309] A. I. Streltsov, O. E. Alon, and L. S. Cederbaum, *Role of Excited States in the Splitting of a Trapped Interacting Bose-Einstein Condensate by a Time-Dependent Barrier*, Phys. Rev. Lett. **99**, 030402 (2007).
- [310] A. L. Fetter, *Rotating trapped Bose-Einstein condensates*, Rev. Mod. Phys. **81**, 647 (2009).
- [311] F. Lenz, F. K. Diakonos, and P. Schmelcher, *Tunable Fermi Acceleration in the Driven Elliptical Billiard*, Phys. Rev. Lett. **100**, 014103 (2008).
- [312] F. Lenz, C. Petri, F. R. N. Koch, F. K. Diakonos, and P. Schmelcher, *Evolutionary phase space in driven elliptical billiards*, New Journal of Physics **11**, 083035 (2009).
- [313] M. H. Beck, A. Jäckle, G. A. Worth, and H.-D. Meyer, *The multiconfiguration time-dependent Hartree (MCDTH) method: A highly efficient algorithm for propagating wavepackets*, Phys. Rep. **324**, 1 (2000).
- [314] W. H. Press, S. A. Teukolsky, W. T. Vetterling, and B. P. Flannery, *Numerical Recipes*, Cambridge University Press, New York, 2007.

Acknowledgements

While there are a number of people whom I would like to express my utmost gratitude and appreciation to, below I would like to single out those who made the most valuable contribution.

My supervisor Prof. Peter Schmelcher for permanent assistance.

Prof. Panayotis Kevrekidis for a lake of knowledge I have inherited from him and for his hospitality.

My office-mates in Heidelberg Dr. Alexej Streltsov and Dr. Nicolas Sisourat for a fruitful working environment and many (controversial) discussions.

My office- and flat-mates in Hamburg.

Finally, I would like to express my sincere thanks to my family and friends.